DEVELOPMENT OF DYNAMIC PRESSURE SENSOR FOR HIGH TEMPERATURE APPLICATIONS

Alfin Leo

A Thesis
In the Department
of
Mechanical and Industrial Engineering

Presented in Partial Fulfillment of the Requirements
For the Degree of Doctor of Philosophy at
Concordia University
Montreal, Quebec, Canada

August 2010

© Alfin Leo, 2010

Library and Archives Canada

Published Heritage Branch

395 Wellington Street
Ottawa ON K1A 0N4
Canada

Bibliothèque et Archives Canada

Direction du Patrimoine de l'édition

395, rue Wellington
Ottawa ON K1A 0N4
Canada

Your file Votre référence
ISBN: 978-0-494-71155-2
Our file Notre référence
ISBN: 978-0-494-71155-2

NOTICE:

The author has granted a non-exclusive license allowing Library and Archives Canada to reproduce, publish, archive, preserve, conserve, communicate to the public by telecommunication or on the Internet, loan, distribute and sell theses worldwide, for commercial or non-commercial purposes, in microform, paper, electronic and/or any other formats.

The author retains copyright ownership and moral rights in this thesis. Neither the thesis nor substantial extracts from it may be printed or otherwise reproduced without the author's permission.

AVIS:

L'auteur a accordé une licence non exclusive permettant à la Bibliothèque et Archives Canada de reproduire, publier, archiver, sauvegarder, conserver, transmettre au public par télécommunication ou par l'Internet, prêter, distribuer et vendre des thèses partout dans le monde, à des fins commerciales ou autres, sur support microforme, papier, électronique et/ou autres formats.

L'auteur conserve la propriété du droit d'auteur et des droits moraux qui protège cette thèse. Ni la thèse ni des extraits substantiels de celle-ci ne doivent être imprimés ou autrement reproduits sans son autorisation.

In compliance with the Canadian Privacy Act some supporting forms may have been removed from this thesis.

While these forms may be included in the document page count, their removal does not represent any loss of content from the thesis.

Conformément à la loi canadienne sur la protection de la vie privée, quelques formulaires secondaires ont été enlevés de cette thèse.

Bien que ces formulaires aient inclus dans la pagination, il n'y aura aucun contenu manquant.

Abstract

DEVELOPMENT OF DYNAMIC PRESSURE SENSOR FOR HIGH TEMPERATURE APPLICATIONS

Alfin Leo
Concordia University

August 2010

Pressure measurement under high temperature environments is required in many engineering applications and it poses many practical problems. Pressure patterns are highly desirable for health monitoring for improved performance and accurate prediction of remaining life of systems used in various applications.

Data acquisition in harsh environments has always been a major challenge to the available technology. Sensing becomes more intricate in case if it has to operate under extreme conditions of temperature. Propulsion system applications represent one such area that requires a sensor that is absolutely accurate and has utmost sensitivity coupled with the ability to withstand high temperature. The need for such sensors is driven by the dependence of the performance of propulsion system on pressure pattern encountered along the gas path. Associated with that, high resolution, small size, low time dependent drift and stable range of measurement will complete the performance of such Microsystems

Sensors using the current technology are capable of reliable measurement for a limited time at an extremely high cost and are bulky thereby preventing online monitoring. Improvement in the durability of the sensors requires new technology and will definitely open new areas of research. A number of technologies have been lately

investigated, these technologies targeting specific applications and they are limited by the maximum operating temperature.

The objective of this research is to develop a dynamic pressure measurement system that would be capable of operating at high temperatures with the technology of the device based on Silicon Carbon Nitride (SiCN). The principle of operation is based on the drag effect.

Silicon carbon-nitride (SiCN) is a material that has been little explored. The service temperature of SiCN is in the range of 1400°C. The structure is produced from a liquid polymer precursor that could be originally formed into any shape.

The proposed micro sensor can measure dynamic pressure and detects flow which is very important to know as the flow continuity is critical in many applications. Furthermore pressure measurement can be used as a base for many aspects. For example the proposed micro sensor could be designed and packaged to be fitted in the gas turbine engine. The correlation of the acquired data from the sensors may provide valuable timely information on imminent instability in the gas flow, detect leakage, improve efficiency etc.

ACKNOWLEDGEMENTS

I wish to express my deepest gratitude to Prof. Dr. B.V.A. Rao, for showing me the way to Concordia University.

I should thank Prof. Rama Bhat and Prof. Ion Stiharu for their continuous support and encouragement during my research. If not for their presence, patience and guidance, completion of my thesis would just be a dream. They continuously conveyed a spirit of pursuit and zeal towards research and I learned a lot from them. Having them as role models, I will continue to work with confidence in my career.

Thanks are due to Dr. Sergey Andronenko who consistently provided me with a good sanity check and provided important unbiased audience and comments to discuss the problems associated with material synthesis and characterization that I faced during my research. He allowed me to interrupt his testing as we shared research space. Based on his experience, expertise and guidance, I was able to fabricate samples and gather data I needed for part of this research.

I will fail in my duty if I forget to acknowledge my seniors and colleagues, Dr. Gino Rinaldi, Dr. Anas Alazzam, Mr Arash Firoozrai, Mr. Vasudevan, Mr. Balasubramaniam, Mr.Murali, Mr. Shankar, Mr. Saif, Mr. Saeedi, Mr. Dacian and Mr. Amin with whom I have been privileged to work with.

I greatly appreciate the support of the technical personnel Henry, Brad, and Dan for their efforts to provide supplies and equipment expertise needed along the way.

Finally, my undying gratitude is directed to my parents and my siblings for their patience and support and for always being there for me when I needed them. Their confidence in my ability has been a crucial driving force in the pursuit of my goals.

DEDICATIONS

Dedicated to

My parents, the living legends who sacrificed their past and present for my future.

And also to

Prof. Dr. B.V.A. Rao

தொட்டனைத் தூறும் மணற்கேணி மாந்தர்க்குக்
கற்றனைத் தூறும் அறிவு.

- குறள்

As deep you dig the sand spring flows
As deep you learn the knowledge grows.

Table of contents

CHAPTER 1 : INTRODUCTION AND LITERATURE REVIEW **1**

1.1. Introduction 1
1.2. Motivation 3
1.3. Gas turbine engine – instabilities 8
1.4. Active control 11
1.5. Dynamic pressure measurements 16
1.6. Pressure measurement at high temperature and applications 19
1.6.1 High temperature regime 19
1.6.2 Sensors for high temperature applications 22
1.6.2.1 Thin film sensors 24
1.6.2.2 Optical sensors at high temperature 27
1.6.2.3 Microwave sensors 30
1.6.2.4 MEMS candidates for high temperature 32
1.7. High temperature considerations 37
1.7.1 Silicon carbon-nitride (SiCN) as sensor material 38
1.8. Objective of the proposed research 40
1.9. Organization of the dissertation 41

CHAPTER 2 : SILICON CARBON NITRIDE (SICN) FABRICATION PROCESSES, STRUCTURES AND PROPERTIES **45**

2.1. Introduction 45
2.2. State of the art 47
2.3. Fabrication of SiCN using liquid precursor CERASET™ 49
2.3.1 Mould preparation and polymer casting 50
2.3.2 Thermosetting 51
2.3.3 Cross linking and pyrolysis 54
2.4. SiCN in different forms 57
2.4.1 Thin film SiCN 58
2.4.2 Thick film SiCN 63
2.4.2.1 Shrinkage issue and mould design 66
2.4.3 Patterned SiCN 68
2.4.4 Machinability of SiCN 71
2.5. Elementary chemical analysis of SiCN 72
2.6. Influence of thermosetting temperature 74
2.7. Influence of catalyst 77
2.8. Influence of annealing temperature 80
2.9. X-ray powder diffractograms of SiCN ceramics 80
2.10. Summary 85

CHAPTER 3 : STATIC AND DYNAMIC PRESSURE MEASUREMENT USING DIAPHRAGMS **87**

3.1. Introduction 87
3.2. Pressure sensing by electrical transduction 87
3.3. Pressure sensing by optical transduction 89
3.4. Sensitive element configurations 91
3.4.1 Micro bellows / bourdon tube as sensitive element configuration 92
3.4.2 Diaphragm as sensitive element configuration 93

3.5. Static and dynamic analysis of diaphragm subjected to pressure loading 94
3.6. Stress analysis 99
3.7. Frequency response 101
3.8. Annular diaphragms for pressure measurement 105
3.9. Pneumatic capacitance 108
3.9.1 Pneumatic resistance 109
3.10. Response of the system 114
3.11. Summary 119

CHAPTER 4 : DIFFERENT CONFIGURATIONS OF SENSITIVE ELEMENT 120
4.1. Introduction 120
4.2. Analytical formulation using Bessel's function 121
4.2.1 Circular plate 124
4.2.1.1 Circular plate with clamped boundary condition 124
4.2.1.2 Annular plate with outer edge clamped and inner edge free 126
4.3. Analytical formulation using the Rayleigh Ritz method 128
4.3.1 Generation of boundary characteristic orthogonal polynomials 131
4.3.2 Coordinates of perforations in plates 132
4.4. Experimental Investigation 133
4.5. Test cases 135
4.5.1 Case 1 and 2 Full circular Plate and annular plate 135
4.5.2 Case 3: Disk with 1 perforation at its center and 8 perforations closer to the center (at a distance of 50 mm from the center) 138
4.5.3 Case 4: Disk with 1 perforation at center and 8 perforations closer to the outer edge (at a distance of 100 mm from the center) 139
4.5.4 Case 5: Disk with 1 perforation at center and 8 perforations at a distance of 50 mm from the center and 16 perforations at a distance of 100 mm from the center. 140
4.5.5 Discussion 141
4.6. Influence of temperature on sensitivity 141
4.6.1 Diaphragm 142
4.6.2 Cantilever beam 143
4.7. Drag based sensors 145
4.7.1 Cantilever beam as sensing element for dynamic pressure 146
4.8. Summary 149

CHAPTER 5 : ANALYSIS OF PROPOSED DRAG BASED SENSOR FOR DYNAMIC PRESSURE MEASUREMENT 150
5.1. Introduction 150
5.2. Sensor configuration 151
5.3. Experimental investigation 153
5.3.1 Jets – introduction 159
5.3.2 Jet characterization 160
5.3.3 Tip deflection measurement 165
5.3.4 Stress analysis 168
5.4. Overloading of the sensitive element 169
5.4.1 Deflection regime 172
5.4.2 Stress involved in overloading 175
5.5. Numerical study on the phenomenon 182
5.5.1 Problem definition 183
5.5.2 Meshing 184
5.5.3 Results and discussion 185

5.6. Summary 190

CHAPTER 6 : INTEGRATED DYNAMIC PRESSURE AND TEMPERATURE MEASUREMENT AT HIGH TEMPERATURE 191

6.1. Introduction 191
6.2. Need for integrated smart sensors 192
6.3. Integrated temperature and pressure measurements 195
6.3.1 Pressure sensing and cross sensitivity issues 196
6.3.2 Discussion on the integrated sensing scheme 197
6.4. Acoustic sensor for dynamic pressure and temperature measurements 198
6.4.1 Experimental setup 200
6.4.2 Time signal analysis 204
6.5. Sensing scheme as applied to GTE application 205
6.5.1 Temperature measurement 207
6.5.2 Frequency and amplitude measurement 208
6.6. Discussion on acoustic sensing scheme 213
6.7. Summary 214

CHAPTER 7 : IMPLEMENTATION ISSUES 215

7.1. Introduction 215
7.2. Sensor design and material 217
7.3. Forced vibration solution for sensitive element 218
7.4. Material consideration for gas turbine engines 223
7.5. Fiber optics for data acquisition 224
7.5.1 Sapphire as material for optical fibre 226
7.5.2 Installation of the fiber 228
7.5.3 Positioning of the sensor 230
7.6. Summary 234

CHAPTER 8 : CONCLUSIONS AND SUGGESTIONS FOR FUTURE WORK 235

8.1. Contributions 235
8.2. Conclusions 238
8.3. Suggestions for future work 240
8.3.1 Modeling of the Indirect Drag effect 240
8.3.2 Testing at high temperature – Indirect drag effect sensing scheme 240
8.3.3 Optical measurement at high temperature 241
8.3.4 Testing at high temperature – Acoustic sensing scheme 241

References 242

List of Figures

Figure 1.1: Working cycle of gas turbine engine [3] 3

Figure 1.2: Simplified Bryton cycle [3] 4

Figure 1.3: Performance map conditions [3] 9

Figure 1.4: The change in clearance due to the self weight of the engine 18

Figure 2.1: Ring structure of CERASET™ 46

Figure 2.2: Layout of SiCN fabrication 52

Figure 2.3: Thermally set polymer 53

Figure 2.4: Barnstead Thermolyne 21100 tube furnace used for thermosetting 54

Figure 2.5: Combined cross linking and pyrolysis temperature and pressure vs time 56

Figure 2.6: Custom built high-pressure, high temperature furnace (Thoughtventions Unlimited LLC) 57

Figure 2.7: The Laurell Spin-Coater, Model WS-400B 59

Figure 2.8: Microscopic image of the surface of thermally set polymer thin films 60

Figure 2.9: Image of the surface SiCN thin films X 100 61

Figure 2.10: Thin film SiCN with Canadian cent for size comparison 61

Figure 2.11: Surface roughness 63

Figure 2.12: PDMS mould used to cast CERASET™ 64

Figure 2.13: Thermally set polymer along with the ceramic 65

Figure 2.14: SiCN chips of different thickness 66

Figure 2.15: Mould design for thick SiCN 68

Figure 2.16: Patterned CERASET™ on the glass substrate 70

Figure 2.17: Laser ablation in SiCN ceramic using femtosecond laser 71

Figure 2.18: Hardness test performed using MST (CSEM) micro scratch tester 75

Figure 2.19: Image of Indentation marks on SiCN using Hysitron Nanoindentator 76

Figure 2.20: Chemical structure of Dicumyl peroxide [129] 77

Figure 2.21: Surface topology between SiCN without and with catalyst 78

Figure 2.22: Dicumyl peroxide on the (5 X 5 μm) surface of SiCN ceramic 78

Figure 2.23: Image of hardness test mark for the specimen with highest hardness. H = 28 GPa 80

Figure 2.24: XRD principle of operation 81

Figure 2.25: XRD peaks for a SICN at different temperatures 82

Figure 2.26: XRD peaks for a SICN annealed to a temperature of 1500°C 83

Figure 2.27: SEM image of SiCN ceramics annealed at 1500°C 85

Figure 3.1: Uniform pressure loading model on a fixed diaphragm 94

Figure 3.2: Deflection curve of a diaphragm under pressure 97

Figure 3.3: Thickness vs pressure for specific radius for SiCN diaphragm 98

Figure 3.4: Theoretical sensitivity for different radius for SICN diaphragm 99

Figure 3.5: Radial and tangential stresses for SiCN diaphragm 101

Figure 3.6: Theoretical natural frequency for SiCN diaphragm 104

Figure 3.7: Electrical analogy with capacitance and resistance 107

Figure 3.8: Flow through an orifice [172] 110

Figure 3.9: Resistance as a slope of pressure difference and mass flow rate 114

Figure 3.10: Resistance provided by orifices of different diameters 115

Figure 3.11: Time response of first order system of annular membrane 118

Figure 4.1: Top view of sensitive elements for lift force based sensing [174,175] 121

Figure 4.2: Coordinates of the perforation 132

Figure 4.3: Schematic layout of experimental setup 133

Figure 4.4: Experimental setup 134

Figure 4.5: Circular plate with 9 perforations close to center in clamped free boundary condition 138

Figure 4.6: Circular plate with 9 perforations in clamped free boundary condition.......... 139

Figure 4.7: Circular plate with 25 perforations in clamped free boundary condition.......... 140

Figure 4.8: Temperature sensitivity of cantilever and diaphragm configurations fabricated using same material.......... 145

Figure 5.1: Experimental configuration of sensor setup.......... 152

Figure 5.2: Front view of the tip of sensitive element before and after deflection.......... 152

Figure 5.3: Experimental setup.......... 154

Figure 5.4: Experimental setup – schematic layout.......... 155

Figure 5.5: Side view of the cantilever sensitive element as zoomed in the microscope 156

Figure 5.6: Graph (obtained experimentally) depicting deflection versus pressure.......... 158

Figure 5.7: Jet expansion zones [202].......... 159

Figure 5.8: Experimental layout for jet characterization.......... 162

Figure 5.9: Nozzle and pitot tube arrangement.......... 163

Figure 5.10: Jet velocity decay with distance.......... 164

Figure 5.11: Zoomed in view of figure 5.10 within the area of interest.......... 165

Figure 5.12: Deflection measurement set up.......... 166

Figure 5.13: Tip deflection at different velocities as measured from figure 5.12.......... 167

Figure 5.14: Stress at fixed end for different velocities.......... 169

Figure 5.15: Overloading protection strategy H slot along the thickness [215].......... 171

Figure 5.16: Deflection regimes of sensitive element.......... 173

Figure 5.17: Sensor scheme at over loading conditions.......... 174

Figure 5.18: ANSYS contact model ... 177

Figure 5.19: Sensitive element with applied pressure ... 178

Figure 5.20: Unsupported length of the sensitive element ... 179

Figure 5.21: Stress distribution along the sensitive element N/m^2 ... 181

Figure 5.22: Computational domain with boundary conditions (Sensitive element is not visible) ... 183

Figure 5.23: Zoomedin view of computational domain close to blocking / sensitive element ... 185

Figure 5.24: Velocity stream line with vortex formation behind the sensitive element. 186

Figure 5.25: Velocity vectors close to the blocking / sensitive element ... 187

Figure 5.26: Streams in flow during vortex formation [225,226] ... 188

Figure 6.1 : Smart sensor block diagram ... 193

Figure 6.2: Pressure and temperature measurement scheme used in the experiments ... 199

Figure 6.3: Experimental setup for dynamic pressure measurement ... 202

Figure 6.4: Schematic diagram with heating coil to heat the suction side of the fan (not to scale) ... 203

Figure 6.5: FFT analysis showing peak shift corresponding to temperature ... 204

Figure 6.6: Time signal for an rpm of 275 ... 205

Figure 6.7: Schematic diagram of implementation of acoustic sensing ... 206

Figure 6.8: Temperature and rpm frequency domain ... 207

Figure 6.9: Reflection and transmission of a plane wave normally incident on a wall .. 210

Figure 6.10: Non dimensionalized acoustic output obtained through walls of different thicknesses ... 212

Figure 7.1: Frequency Vs displacement for SiCN sensitive element ... 218

Figure 7.2: Loading scheme for 5 blade fan (Generalized) ... 218

Figure 7.3: Loading scheme on the sensitive element 220

Figure 7.4: Forced response for a sinusoidal load 223

Figure 7.5: Fibre optic sensing scheme.. 225

Figure 7.6: Integration of sapphire fibre on the shroud 229

Figure 7.7: Typical axial compressor stage: rotor with the tip clearance 230

Figure 7.8: Classification of loads contributing to clearance variation 232

Figure 7.9: Schematic representation of an axial flow compressor (with axial gaps) 233

List of Tables

Table 1-1: Physical properties of SiCN, SiC, Si_3N_4 and Si. 7

Table 1-2: Generic sensor requirements [13-17] 14

Table 2-1: Composition of SiCN ceramics (4^0C/min heating rate) 73

Table 2-2: Composition of SiCN ceramics (heating rate 1^0C/min) with different pyrolysis and annealing conditions.. 73

Table 2-3: Hardness of SiCN without catalyst (specimen 2) at different forces 75

Table 2-4: Comparison of properties of SiCN with and without catalyst at 2500 μN force 79

Table 4-1: Comparison of the dimensionless natural frequencies Ω of a circular plate with clamped boundary using M=10 orthogonal polynomials with Bessel function 136

Table 4-2: Comparison of the natural frequencies Ω of a circular annular plate (b /a =0.085*) in clamped free BC using M=10 orthogonal polynomials with experiment and Bessel function.. 136

Table 4-3: Comparison of the natural frequencies Ω of a circular plate with perforations case 3 (b /a =0.085*) in clamped free BC with experiment... 138

Table 4-4: Comparison of the natural frequencies Ω of a circular plate with perforations case 4 (b /a =0.085*) in clamped free BC with experiment... 139

Table 4-5: Comparison of the natural frequencies Ω of a circular plate with perforations case 5 (b /a =0.085*) in clamped free BC with experiment... 140

Table 5-1: Contact stress and distance.. 180

Table 7-1: Typical compressor stage frequency ranges in GTE.................................... 216

Table 7-2: Properties of SiCN.. 217

Table 7-3: Details of axial gaps between stator and rotor blades in GTE 232

Nomenclature

a	Outer radius (m)
A_1, A_2	Cross sectional area of flow at sections 1 and 2 (m^2)
A_o	Cross sectional area of orifice (m^2)
b	Radius of perforation (m)
C	Pneumatic capacitance (kg-m^2/N)
C_c	Coefficient of contraction
C_d	Coefficient of discharge
C_e	Thermal coefficient of modulus of elasticity per degree change in temperature ($^0C^{-1}$)
d	Maximum width of the bluff body (m)
D	Flexural rigidity (N-m^2)
e	Distance of the center of the perforation from the center of plate
E	Young's modulus (N/m^2)
f	Frequency of vortex shedding (Hz)
$f^{(L,T)}$	Standing wave frequency (Hz)
g	Gravitational constant (m/s^2)
h	Thickness (m)
I	Moment of inertia I_{zz} (m^4)
K	Wave number (m^{-1})
K_1 and K_2	Wave numbers in air and in the material of the wall (m^{-1})
l_r	Reduced length
L_{eff}	Effective length of the resonance tube (m)

m	**Mass of air (kg)**
m_p	**Mass loss due to crosslinking and pyrolysis (kg)**
m_t	**Mass loss due to thermosetting process (kg)**
M	**Bending moment (N-m)**
n	**Polytropic index**
n_b	**Number of blades**
P	**Pressure (N/m^2)**
P_m	**Peak amplitude of the sound pressure (Pa)**
$P(x)$	**Amplitude after the wave has propagated a distance x through the medium (Pa)**
q	**Flow (m^3/s)**
r	**Radial distance from the center (m)**
R	**Radius of diaphragm (m)**
R_c	**Unbalanced reaction (N)**
R_p	**Pneumatic resistance (N-s/kg-m^2)**
St	**Strouhal number**
T	**Temperature (^{o}C)**
T_{max}	**Maximum kinetic energy (N-m)**
u	**Streamwise velocity (m/s)**
U_{max}	**Maximum potential energy (N-m)**
v	**Flow velocity (m/s)**
$v_{air}^{(T)}$	**Velocity of sound in air at a given temperature T (m/s)**
v_c	**Volume of CERASET™ (m^3)**

v_t	**Volume of thermally set CERASET™ (m^3)**
v_{SiCN}	**Volume of SiCN (m^3)**
V	**Volume of chamber (m^3)**
w	**Load (N)**
X_1	**Distance travelled by the acoustic wave in air (m)**
Y_r	**Deflection of the diaphragm at radial distance (m)**
z	**Distance from neutral axis to outer surface where maximum stress occurs (m)**
α	**Coefficient of thermal expansion ($^0 C^{-1}$)**
γ	**Adiabatic index**
δ	**Gap between the blocking element and sensitive element**
μ	**Poisson ratio**
υ	**dynamic viscosity (Pa-s)**
ε	**Expansion factor**
ρ	**Mass density of gas (kg/m^3)**
ρ_c	**Density of CERASET™ (kg/m^3)**
ρ_t	**Density of thermally set CERASET™ (kg/m^3)**
σ_r	**Radial stress (N/m^2)**
σ_t	**Tangential stress (N/m^2)**
τ	**Time constant (s)**
ω	**Frequency (rad/s)**
$\phi(r)$	**Assumed deflection function**

Chapter 1 : Introduction and Literature Review

1.1. Introduction

Pressure plays a key role in many engineering applications. History of pressure measurement dates back to early 1643 when Evangelista Torricelli used mercury in tube to measure pressure for the first time. Later Blaise Pascal studied fluids, and clarified the concepts of pressure and vacuum by generalizing the work of Evangelista Torricelli. Torricelli also postulated Torricelli's Law, regarding the speed of a fluid flowing out of an orifice, which was later shown to be a particular case of Bernoulli's principle. Bernoulli addressed compressible and incompressible flows and established the base for modern day's pressure measurement. Present day instrumentation for pressure measurement has refined itself but still when technology changes the need for pressure measurement under complex environmental conditions and inaccessible spaces become acute.

Measurement of pressure becomes more complex if the zone of interest experiences high temperature. The gas turbine engine is an example where an extensive study of pressure patterns along the flow path of air is needed. Continuity of flow needs to be monitored closely since any interruption of flow would cause flow reversal that would require the engine to be stopped and started again.

Gas turbine engines employed in civilian and military aircrafts have been very important means of transportation which continues to demand outrageous amount of jet fuel. The increasing energy consumption attributed to this industry demands extension of operating envelopes of gas turbine engines to their limits to achieve higher thrust, better

efficiency, lower emissions, improved reliability and longer engine life. The industry consensus is that these goals can be achieved by strategic measurements at various locations in an engine for design optimization and real-time diagnosis during service [1].

Instrumentation at high temperatures has always challenged the available technology. Gas turbines used in the aerospace industry operate at very challenging levels of performance that require the stable operation of the compressor at all times. The operating environment within the engine is characterized by strong Electro Magnetic Interference (EMI) and high temperature, pressure, corrosion and turbulence, which greatly impede the implementation of most of the currently available sensors. However, during takeoff and landing, transient pressure fluctuations normally arise, resulting in surge that is propagated to adjacent blades through the various stages of the compressor which, in mere fractions of a second, leads to engine stall for high speed turbines, resulting in the destruction of the engine [2].

Compressor surge generally occurs as a result of unsteady pressure fluctuations, such as when the airflow on the airfoil has a positive angle of incidence. When this occurs, there is a tendency for flow to separate, which creates a constricted passage for further incoming air. As a result, reverse flow conditions are established and propagated back through the engine, giving rise to compressor surge [2]. These conditions emphasize the need for the study of these pressure fluctuations and means to measure them during operation.

1.2. Motivation

Gas turbine engine uses air as a working fluid to generate thrust. These engines have a superior thrust to weight ratio, unlike the IC engines and hence are used for aviation purposes. The basic components of this propulsion system are fan, compressor, combustion chamber, turbine and nozzle. There is a need to measure pressure at all these components.

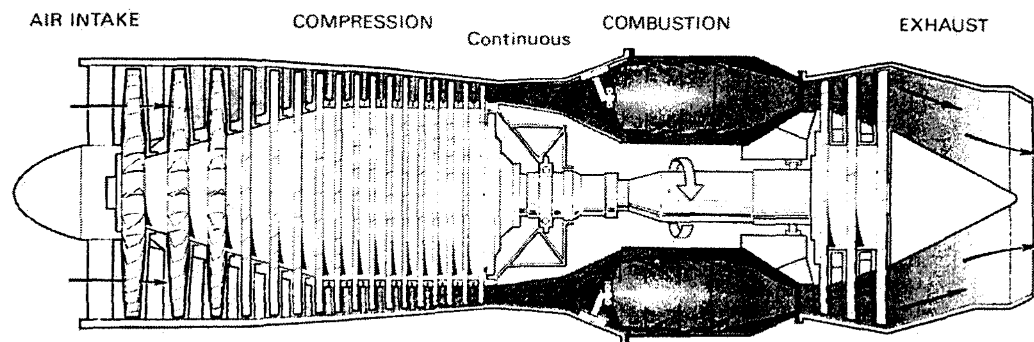

Figure 1.1: Working cycle of gas turbine engine [3]

A detailed description on design and components of gas turbine engine is available from various resources [3, 4]. Modern gas turbine engines are complex systems that handle large quantity of air that convert chemical potential energy into useful thrust safely, reliably and efficiently and it operates on Bryton cycle [3].

The working cycle of gas turbine engine in its simplest form is represented by the figure 1.2. Process 1-2 is isentropic compression where in the air from atmosphere is compressed by multi stage rotary compressor (500^0C, (965 kPa) 140 psi, 120 m/s at 2). Process 2-3 involves the addition of heat to the compressed air (flame temperature 2000^0C, Metal temperature 1100^0C, 110 psi (758 kPa), 90 m/s at 3). In process 3-4

(500^0C, 75 psi (517 kPa), 220 m/s at 4) the combusted gases expand through the turbine and exhaust to the atmosphere [3]. The values of temperature, pressure and velocity could vary based on the size, model and make of the engine, however, they follow the same trend.

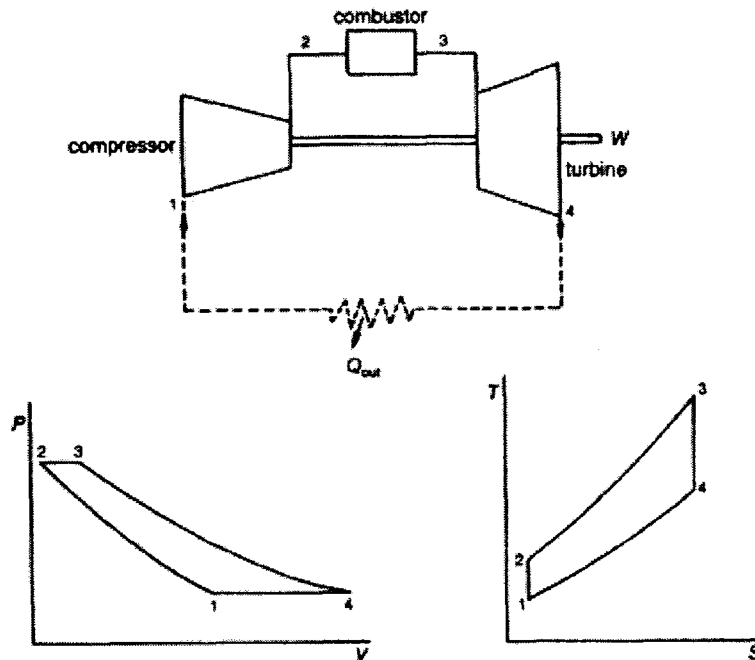

Figure 1.2: Simplified Bryton cycle [3]

In order to make gas turbine engine more intelligent, with online condition monitoring there is a need to embed more sensors to measure temperature, pressure (static and dynamic), vibration, emission species, tip clearance, flow and acquire data online. The present system has a control loop based on 6 sensors but the latest diagnostic, prognostic and health management (DPHM) requirements demand many more sensors to be incorporated. The measurement requirements for gas turbine engine applications are technically very challenging as the sensor environment is more hostile. Gas turbine engines are operated at increased pressure ratios, higher temperature, higher centrifugal and aerodynamic loads. A sensor that would suit such conditions should be durable as

they have to withstand extreme conditions, remain functional at all temperature and pressure cycles, minimize thermal drift and should be non-intrusive and easily installable and replaceable.

Present day development in Micro Electro Mechanical Systems (MEMS) opens up new rooms to embed micro sensors in complex systems such as gas turbine engines. The widely used semiconductor pressure sensors have several major drawbacks in terms of maximum possible operating temperature. MEMS is an enabling technology that yields micro-machines that have the size of a grain of salt, integrating mechanical elements such as those used for sensing and actuation, with electronics, such as those required for measurements and control circuits, on a common silicon substrate. This technology results in substantial cost benefits, directly through low unit pricing, or indirectly by cutting service and maintenance costs. However, conventional silicon-based technology produce components that cannot function at temperatures exceeding 200°C. Beyond this temperature, the doped impurities get diffused within the silicon. This would result in the failure of the electronic components of the sensor. At 600°C, silicon mechanically softens there-by failing structurally and is unsuitable for high temperature applications. Using silicon at temperatures of up to 250°C requires the utilization of long wires to connect the sheltered electronics to the hot area sensors. Both of these approaches result in serious setbacks in terms of implementation. Another drawback is the bulky packaging that would be required to keep a Si-MEMS device operating in high temperature environments since it would not only be impractical in cost but also in weight and size.

Just to push the limit of operation Silicon on Insulator (SoI) based sensors could go a little higher, however below 300°C [5]. SoI is based on the use of Silicon dioxide as insulator on silicon substrate instead of conventional silicon substrate. The insulator layer could be silicon oxide or (less commonly) sapphire. The primary barrier to SOI implementation is the drastic increase in substrate cost, which contributes an estimated 10 - 15% increase in total manufacturing costs due to additional insulator deposition [5]. This SoI implementation does not provide too much gain in operating temperature as well. Further SoI technology induces differential stress in the topmost silicon layer.

In order to overcome this drawback, extensive research is currently in progress to use Silicon Carbide MEMS technology (SiC-MEMS). A silicon carbide pressure transducer has been developed based on SiC-MEMS technology that can operate up to 500°C. However, the primary technique used to pattern SiC thin film is reactive ion etching (RIE) and this is known to be time consuming, expensive, and technically very challenging due to poor etch rate of SiC [6]

There is a vital need for sensor that would work in a high temperature regime. Adaptability to the operating environment without intervention in the normal operation is more important for online monitoring and hence mere capability to measure pressure at high temperature without size advantage will not be enough. Hence it is highly desirable that such a sensor is a micro sensor that would utilize the advantage of microsystems such as low mass, high reliability, low energy consumption, low cost and option to replace than to maintain. This is possible only when the sensor is made from a material that would withstand high temperature without the need for cooling and most importantly could be implemented with ease.

Recent results of research have overcome these problems by the exploitation of a new class of polymer-derived ceramics, which essentially consist of amorphous alloys of silicon, carbon and nitrogen, and is known as Silicon Carbon Nitride (SiCN). SiCN can be derived from powder or liquid precursor and could be moulded into any shape. SiCN has exceptional properties enabling it to be one of the best candidates for sensing application at higher temperature [7]

Table 1-1: Physical properties of SiCN, SiC, Si_3N_4 and Si.

	SiCN	SiC	Si_3N_4	Si
Max temperature (°C)	1900°	1100°	1500°	600°
Density (g/cm^3)	2.20	3.2	3.19	2.3
E modulus (GPa)	158	700	314	190
Poisson's ratio	0.17	0.19	0.24	0.27
Coefficient of thermal expansion CTE×10-6 (m/mK)	0.5	3.3	3.5	2.33
Hardness (GPa)	25	30	28	11.2
Fracture Strength (MPa)	500-1200	418	700	175
Fracture Toughness (MPa $m^{1/2}$)	3.5	4-6	5-8	0.9
Thermal Shock (Fom)	1100-5000	270	890	

It should be noted from table 1.1, that SiCN ceramics have good properties to suit high temperature applications and also they exhibit excellent creep and oxidation resistance, which makes it one of best materials for harsh working conditions. SiCN is a fullerene and resist oxidation to a greater extent. Hence, the main purpose of this work is

to enhance the knowledge of building a dynamic pressure sensor and develop a process for fabricating hard, crack-free SiCN ceramics, which can successfully serve as the body of pressure sensors, which could be used for online dynamic pressure monitoring in the harsh environment of a gas turbine engine.

1.3. Gas turbine engine – instabilities

In gas turbine engines compressor surge and stall events are problematic as they results in flow reversal, which requires the engine to be stopped completely to resume operation. Compressor surge is an instability that results in a sharp reduction of airflow handling ability of the engine or a flow reversal (flow reverses its direction and flows from exit to inlet for short time intervals). Surge, if allowed to survive would result in permanent damage to the engine. Surge may be accompanied by excessive vibration and audible sound, however, surge can damage the system even without these symptoms. Repeated compressor surge can result in the cracking of stator vanes and blades in the compressor. Compressor clearances can also be affected with a resulting decrease in efficiency and further reduction in engine stability. Stall consists of airflow instability in the area of several adjacent blades. Stall may precede surge and can be detected as precursors [1]

Performance map of a compressor (Figure 1.3) shows the variation of pressure ratio as a function of corrected mass flow rate through it for a series of corrected speed lines. The mass flow rate and speeds are corrected to compensate for variations in inlet temperature and pressure conditions. Relative equivalent flow in x-axis is the ratio of corrected mass flow rate to the real flow rate. Corrected flow is the mass flow rate that

would pass through a device if the inlet pressure and temperature correspond to ambient conditions. Complete avoidance of the initiation of conditions that will lead to surge or stall, requires engine designs to conservatively determine operational stability margins that are far from the stability limit of the compression system.

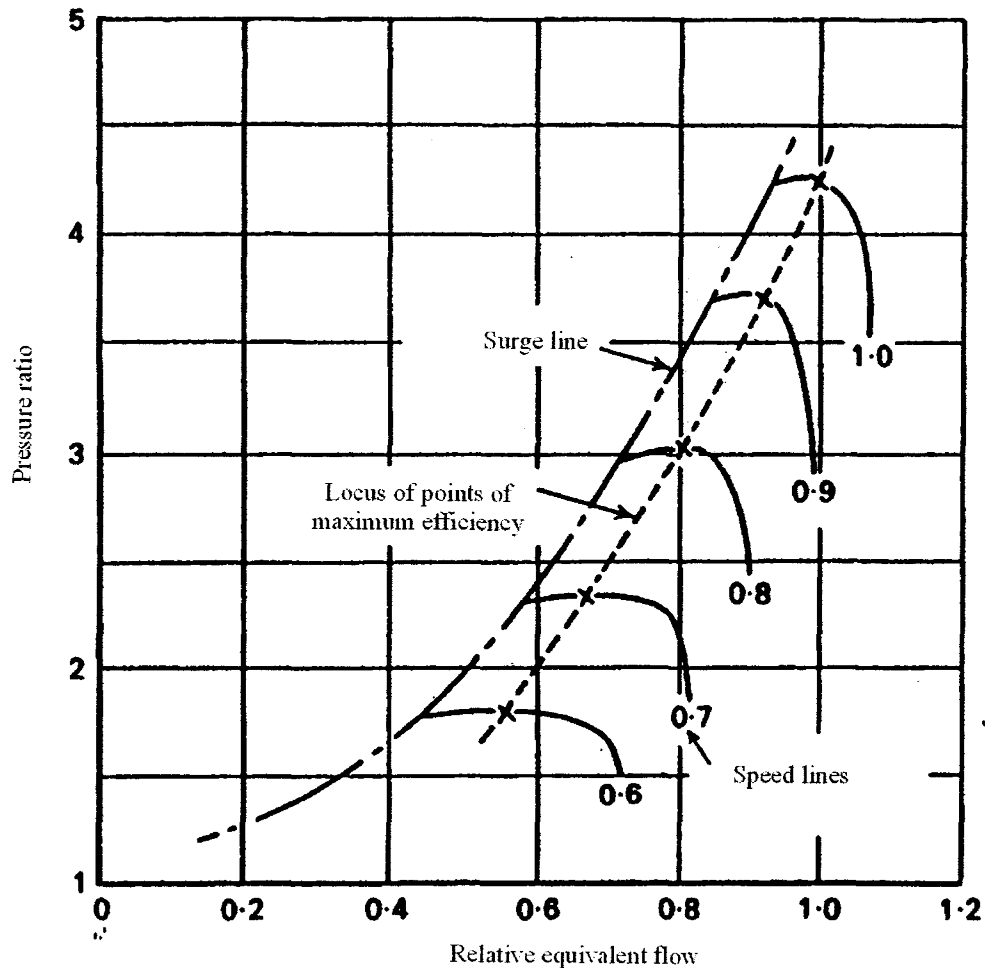

Figure 1.3: Performance map conditions [3]

The compressor operating line is the locus of points at which the compressor operates. The surge line is the locus of points above which the airflow is unstable and compressor surges. The locus of points that represents maximum efficiency operation point is the maximum possible efficiency that compressor could attain without initiating

stall/surge. Due to the proximity of the maximum efficiency line to the surge line and due to lack of real time monitoring to locate the point of the operation at any given time in air on the compressor map, compressors are normally operated at a point well below the maximum operating line.

Compressor has to operate at a point well below the maximum efficiency point so as to prevent the chance of slipping into surge line. The distance maintained to prevent surge between the compressor operating line and the surge line is known as compressor surge margin. These margins are achieved during compressor design so that the compressor can be safely operated close to but lower than the maximum efficiency point. The design of the compressor should include this margin that results in over design of the compressor. The total amount of margin is in the order of 35% [1]. This means that the engine is carrying 35% more compressor capacity by design than it needs for steady state operation. Compressor designers build in margin for engine acceleration, inlet distortion, clearance changes, engine deterioration, and other factors. The penalties associated with this extra margin are cost, weight, compressor length and number of parts.

Combustion instability is another type of instability that is prominent in gas turbine engines. Combustion processes are associated with intrinsic instabilities, In addition to this, combustion instability is also created in response to super-imposed oscillations among which pressure oscillations are the most common [8]. The combustion flames reach temperatures as high as 2000°C which is way higher than the capability of sensors. Combustion process heats up fluid element and the expansion due to addition of heat produces a weak wave that radiates around. This pressure wave could get reflected by the walls of combustion system to affect flames there-by serving as a source of

pressure disturbance. Combustion instability produces intense vibrations, structural damage, high burn rates and can propagate upstream to cause a change in atomization and vaporization process in the system [8].

1.4. Active control

Modern air-craft engines face challenging environment to satisfy customer needs and these are hostile and still out of reach of instrumentation. Gas turbine engines are expected to have high operational range while maintaining a very high level of operating efficiency at low operating cost. Real time control can help to meet future engine requirements by active improvement of the component's characteristics. This concept relies heavily on sensing of actual operating conditions and initiating actuator action. Real time control can improve engine characteristics such as performance, durability, emission control, and control of unsteady phenomenon that occurs mostly during exceptional operating conditions such as inlet distortion, combustion instability, flow separations, vibration and noise [9]. Current engines are open loop devices because of the existence of operating gap between current instrumentation and the conditions that prevails in some parts of the engine. Limited onboard computational capability and relatively poor sensor technology do not allow active control [10] and these engines are unable to respond to changing conditions during operation. This forces engine design to be governed by large safety margin and restricts the exploitation of the engine capability to the maximum possible extent. To minimize large safety margins it is necessary to make the engines more intelligent by installing sensors for active control. The concept of active control can be extended to different areas in gas turbine engine.

Active inlet control to control flow distortions at the engine intake can improve intake efficiency by minimizing inlet distortion problems and maintain flow conformity upstream of compressor. This could possibly reduce the chance of compressor stall [10].

Active flow control involves the control of the air flow and combustion gases through the engine to dynamically alter its performance during flight. This would make the engine more fuel-efficient, and would lower emission of gases. Active flow controls are yet to be realized as it requires further research on technologies to achieve intelligent and embedded control at strategic locations along the flow path. Some techniques that could be used for active flow control are pulsed jet (synthetic jets), vortex generator, air foil morphing with shape memory alloys [11].

Active clearance control is another area of importance as improper clearance has a negative impact on efficiency. Active clearance control helps to maintain stability and efficiency by maintaining optimum clearance. Current clearance control is based on thermal expansion of the casing which can be controlled by modulating cooling air [9]. But change of clearance with time is still an issue as this kind of control system does not measure the actual clearance. The thermal inertia of casing prevents the linking of the actual clearance and the amount of cooling air. Another type of active clearance system has been suggested in [11] where-in there will be sensor that would measure the clearance and an actuator that would adjust the position of the casing. The actuator may be thermal, mechanical/pneumatic system. It is possible to control compressor stability by the modification of local tip clearance using magnetic bearings [12]. The main advantage of clearance control would be the capability to react on any clearance change and counteract accordingly.

Active combustion instability control monitors combustion process and controls the input into the combustion process using a dynamic hardware component. Active control in realistic combustors can be done using off phase fuel injection, to suppress instability. A complete closed loop control of combustion instability suppression is possible only with sensors and actuators that would sense and act in appropriate places which is characterized by high temperature, high frequency vibration and corrosive environment.

Active surge control is possible by measuring high frequency pressure and velocity fluctuations as these waves or pressure spikes are the precursors of surge. Active surge control could give a direct benefit by enhancing stability of the compressor. In addition, it would reduce the surge margin by allowing the compressor to operate close to the maximum operating point. This additional margin could enhance overall performance and efficiency.

Gas turbine engine is no exception as any other application that comes with requirement to measure temperature, pressure at high temperature etc. Sensors play an inevitable role in real time control by providing a signal that characterizes the current condition of the system and provides input to the controller. This task could be accomplished only by placing sensors at correct locations that would provide a reliable measurement. Active control technology while sensing different parameters such as static pressure, dynamic pressure, temperature, distance, emissions, jet direction etc., is aimed at improving overall efficiency and reliability of the gas turbine engine. Active controls for different parts of the GTE are cited in table 1-2.

Table 1-2: Generic sensor requirements [13-17]

Technology / sensed variable	Required sensor specifications
Combustion instability control Thermo acoustic instabilities	~ ±1 psi (6.9 kPa)dynamic pressure measurements ~ 700 Hz bandwidth ± 5 % accuracy 1540 °C, + 400 psi (2759 kPa) combustor environment [13]
Emissions species monitoring	Array of emission species (CO,CO_2,NO) and dynamic pressure measurement (with above specs) [13, 14]
Active flow control Flow separation	~ ±5 psi (34.5 kPa) dynamic pressure measurements ~ 1 Hz bandwidth ± 0.5 % accuracy 95 °C, ~35 psi (241.3 kPa) environment [15]
Active stall control	±5 psi (34.5 Kpa) dynamic pressure measurement ~ 5 kHz bandwidth ± 0.196 % accuracy ~95 °C, ~35 psi (241.3 kPa) environment
Active turbine clearance control Blade to case clearance	0-100 mil (milli inch) distance measurement ~ ±1 mil accuracy 50 kHz bandwidth ~ 1370 °C HPT environment [13]
Burner pattern factor control	~ 1540 °C temperature measurement ± 2 % accuracy

	< I Hz bandwidth [13]
Structural health monitoring Vibration	Multiple low cost, light weight, vibration sensors Band widths up to 50 kHz [13]
Structural health monitoring Blade health	Tip clearance accuracy of 1 -5 mils (higher resolution as clearance is reduced). Temperature upto to 1540 °C in turbines stages. Band width of 100 – 500 kHz dependent on blade speed Vibration environment upto 300 g peak
Prognastics and life usage monitoring	Metal temperature sensors (1095°C in turbine section) Component stress strain measurement
Active inlet control	Pressure sensor array 37.5 psi (258.5 kPa) nominal operating pressure ± 0.1 % accuracy [16]
Performance diagnostics Gas path debris	Capability to detect debris of size 40 μ and larger. Inlet (-50 to +65 °C) [17]

Certain sensors for use in GTE have to satisfy high frequency and wide range requirements, and sensors available today can deal with those requirements to some extent. One of the problems is the exposure to high temperature that demands new materials and sensing scheme that would make real time control possible in certain areas facing high temperature above 500°C. Today's GTEs are reliable and safe but they are expensive to operate and maintain [18] .The sensors used in active control systems should

be affordable, light weight, readily installable and accessible. Real time or active control is expected to enhance engine functionality, reduce emissions and noise, however, this comes with increased complexity.

1.5. Dynamic pressure measurements

Dynamic pressure is one of the important information that is required for real time control. Dynamic pressure measured at various sections will give different information. For example in compressor section the pressure would provide details about the rpm of the compressor blades, the change in clearance between the blade and the shroud (change in shape of the shroud due to its self weight) and detect blade failure.

Dynamic pressure measurements in the compressor have a direct role in the detection of compressor stall events. The need for accurate high temperature dynamic pressure measurements is an integral step in implementing active control system for performance enhancement of gas turbine engines. Frequency response will be a major issue of such a sensor and the desired frequency response will be around 100 kHz. In today's large gas turbine engine the exit temperature of the compressor is as high as 650 °C – 760°C [1].

Dynamic pressure sensors for real time sensing and control are required at different parts of the gas turbine engine. In order to avoid catastrophic instabilities it is important to have a reliable control system for early detection of incipient surge. This generally relies on accurate pressure measurements using dynamic pressure transducers located on the stator of the various stages of the compressor. Stall margin management and active surge control requires measurement of dynamic pressures as high as 35 kPa

and combustion instability suppression requires 10 kPa dynamic pressure measurement [19]. There are sensors that would deal with the above requirements provided those measurements are done at ambient conditions but there are other environmental factors like high pressure and temperature that restricts the use of those sensors.

The normal technique to handle such a high temperature is air or water cooling. However, even with temperature compensation the accuracy of the pressure component is usually compromised [20]. In GTE a dynamic pressure transducer capable of operating at high temperature with a high bandwidth would have multiple applications of interest. for example i) surge/stall measurement ii) individual blade pressure iii) combustor instability and iv) pressure distributions on rotating hardware.

Weigl et al. [21] demonstrated that stable operation could be achieved over a wider range of flow conditions with a minimal loss in performance through active or passive control of the flow conditions. If active surge control could be achieved it is possible that a stage of compression could be eliminated from an engine with the following benefits for a typical military type of engine [22].

+ 5 % Thrust

-1.5 % Thrust specific fuel consumption

-3.2 % Acquisition cost

-1 % Operating cost

Surge free operation

Extension of maintenance intervals

Passive control incorporates a design that results in self-correcting flows as reported by Crook et al. [23] and Saha et al. [24]. On the other hand active suppression is

generally considered more effective being a response to a measured anomaly in the flow as reported by Paduano et al. [25] Weigl et al. [21] Suder et al. [20]. However, the effective implementation requires the use of sensors, actuators, and controllers to detect and rectify the incipient instabilities of the system. This would generally result in an increased weight and consequently cost offset any benefits derived from an enhanced engine performance.

Clearance management is also an important parameter that requires measurements between the blade and the shroud. Change in clearance can be caused by self weight of the engine under non operating conditions and could go intricate and highly time dependent due to thermal expansion of shroud and centrifugal forces due to rotation.

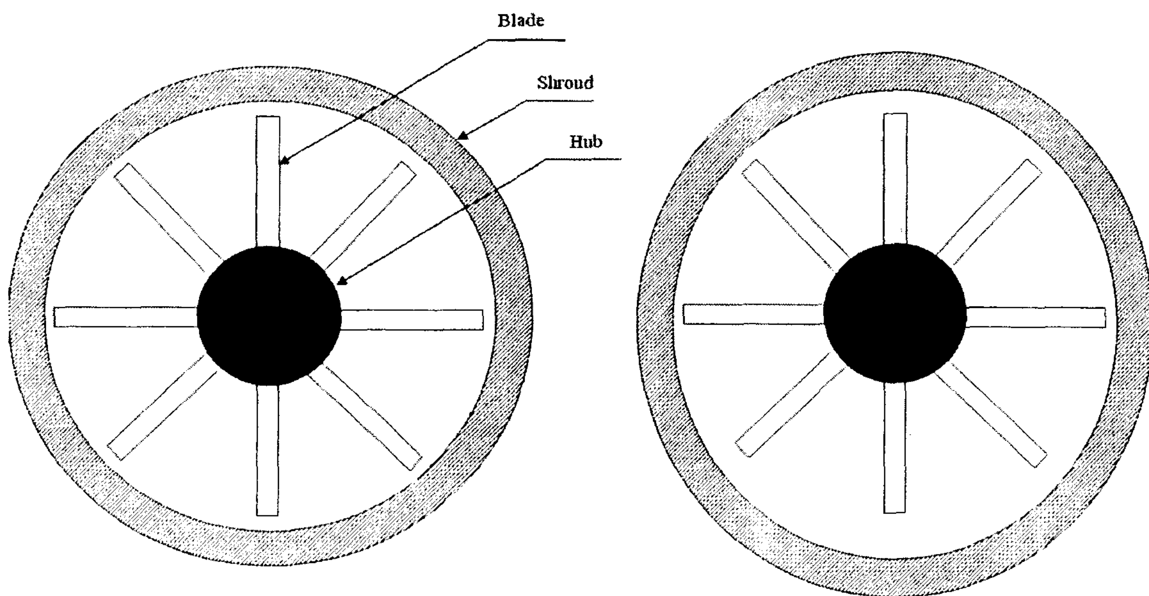

Figure 1.4: The change in clearance due to the self weight of the engine

Pressure and temperature measurement is thus of great importance as the first step towards active turbulence monitoring and control. Online condition monitoring of the gas turbine engine requires a sensing system that would withstand temperatures above 500°C

and it is highly desirable that it is a micro sensor. Once in place, the sensor relays information to a control system that can automatically adjust the engine for smoother operation, which will improve the engine operational performance and reliability.

1.6. Pressure measurement at high temperature and applications

Pressure is the second most sought parameter after temperature in various industrial applications and is one of the most important physical quantities that drives various engineering applications. Pressure measurement techniques have grown to a level where different sensing methodologies are available for different applications and different ranges of pressure. Pressure measurement has reached another dimension as some applications come with a harsh environment that impedes the use of traditional pressure measurement devices.

1.6.1 High temperature regime

Most of the applications demand measurement of temperature and pressure at the same time and at the same location. These locations often are under extreme conditions. Some of the applications require information at the operating temperatures exceeding the nominal limits (125°C or 155°C). Under such circumstances, there may be other challenges associated with the high operating temperatures.

High temperature is a general term that is benchmarked based on the application. For domestic purposes even 100°C could be considered as high temperature, whereas in gas turbine engines 500°C is quite common. The high temperature regime (at which the dynamic pressure is intended to be measured) targeted in this work is above 500°C which

is more than the sensing capability of most of the commercially available sensors. Leading sensor manufacturers like Kulite Inc and Vibrometer Inc have reached limited success in measuring pressure at 750°C but this sensor is bulky, expensive and restricted to one time use due to very high thermal drift. Pressure measurement at this temperature is performed using these expensive pressure sensors only in test rigs.

Pressure measurement, unlike temperature measurement, does not yield for non contact type measurement as in pyrometers for temperature measurement. Pressure measurement at high temperatures is extremely difficult due to the following factors

- ❖ Above 200°C lateral thermal diffusion affects micro electronics.
- ❖ Lack of existence of wires or need for high insulation to withstand high temperatures in flexible and compliant conductors.
- ❖ Thermal oxidation and scale formation.
- ❖ Excessive thermal expansion/mismatch challenges the integrity of the structure.
- ❖ Thermal stress and drift limits the operation.
- ❖ The signal transmission, wiring, packaging and maintenance issues.

Currently available technologies (like SoI, SiC) to measure pressure at high temperatures in the range of 300^0C – 500^0C [26] [27] do not satisfy the acceptable lifetime requirements to be used in engine environment. Also these pressure sensors designed to work at this temperature range cannot be used in temperature regimes and the harsh environment in engines due to issues related to implementation and packaging. In case the sensor is designed to address the above issues they become expensive, bulky and most of the time is restricted to single use.

Pressure measurement for active inlet control involves measurement at compressor inlet with impurities like ice, sand and dust. Also temperature is in the range of -60^{0}C to +65^{0}C [19] due to air preheating and exhaust gas recirculation. Pressure measurement is necessary to predict noise, complete / incomplete combustion and to study the inlet distortion detection in order to manage inlet stability etc.

Surge and stall detection requires dynamic pressure sensor with a frequency range of 5-40 kHz and 35 kPa, and these requirements could be met by currently available MEMS sensors [19]. But high temperature environment prevents the use of these sensors to ranges below 250^{0}C while temperatures can reach in the range of 500^{0}C and up to 700^{0}C depending on the type of compressor used [19]. Hence Si and SoI sensors cannot be used and there is a need for SiC or SiCN based sensors as these materials are compatible with MEMS technology and could be potentially embedded within the system.

In addition, thermo acoustic instability detection requires dynamic pressure sensors with a minimum of 10 kPa dynamic pressure, atleast 1 kHz bandwidth and operating temperature of 1700^{0}C [19]. Dealing with temperatures in the range of 1700^{0}C is out of discussion at this time. There is a gap in pressure measurement when it has to be extended to a high temperature application. This gap could be addressed by materials such as SiCN even though there are serious issues like sensing concepts that could operate at very high temperatures, data transmission from high temperature zones, wiring, packaging and high temperature electronics.

Pressure measurement at high temperature is not only an issue in engines, but also is important in oil industry as downhole pressure measurement is an important parameter

for oil reservoir prognosis. The conditions are high temperature (300^{0}C), high pressure, vibration, shock, confined space etc [28]. Other high temperature pressure measurement applications would include geo thermal power plants (300 -1000^{0}C), nuclear reactors (300-700^{0}C), coal gasification plants (500 -1000^{0}C) [29]. All these applications require drift and maintenance free sensors and are to be placed at locations that may not be easily accessible.

1.6.2 Sensors for high temperature applications

Aerospace industry has a great need for sensors that can be installed and practically operated at any location and temperature conditions on a modern engine for intelligent control and health monitoring [30]. It is highly desirable that the sensor is small, wireless, has little or no integration impact on the performance of the engine, power consumption is low, and is able to withstand high temperature and corrosion induced by flames apart from the regular requirements of a sensor in terms of accuracy, resolution, stability etc.

The above requirements could be met with advances in enabling technologies such as Micro Electro Mechanical Systems (MEMS) or MOEMS (Micro Optical Electro Mechanical Systems). As of today there is a void in MEMS based sensors that would operate at high temperatures and there are still significant technical challenges related to materials, fabrication technologies, data acquisition from zone of interest, packaging and high temperature electronics. The failure mechanisms normally found in micro systems such as material incompatibility, stiction, creep, and environmentally induced stress are aggravated with temperature [31]. Further screening, qualification and testing of MEMS

for these applications are very essential due to high factor of safety and reliability issues [31].

MOEMS uses optical techniques which can take the advantage of optical systems such as high temperature operation, immunity to Electro Magnetic Interference (EMI), high bandwidth, small size and weight. Currently the gas turbine engines do not have optical sensors integrated in it since controller for gas turbine engine Full Authority Digital Engine Control (FADEC) does not have an optical interface. The interest for such a sensor is so high that this technology cannot be ignored. The only issue in using optical means is that FADEC (Full Authority Digital Engine Control) would have to incorporate opto-electronic interface [32].

Locating internal sensors in various parts of engine may be labour intensive in terms of positioning while getting leads out of the engine might be intricate. Moreover significant work is required so as to enable engine hardware to permit applications and lead wire routing. Also wiring these sensors will be a real challenge as it needs special wires that would sustain extreme temperature conditions. Ni-30%cr-16%Si alloy is used as material for construction for these wires which could work at 815°C with insulation [33] but the wires themselves are bulky and in certain case the diameter would be larger than the size of sensor itself.

Telemetry system may be used to achieve trouble free data acquisition but transmitter frequency drifts with change in temperature and that poses a problem. In spite of compensation for thermal drift currently available telemetry systems can only transmit data from an environment that is exposed to temperature of around 290^0C [34]. Power supply to those systems is also a major problem which needs to be addressed in case of

using telemetry systems. Use of wireless sensors would reduce the complexity of lead wires and other means of data transportation accessories. This may exempt the engine from unnecessary instrumentation for wired data transfer system. Realising a data acquisition and transmission system would be an issue as aerospace components have to undergo meticulous qualification criteria. Various sensors that could be used for pressure measurement at high temperature are discussed below.

1.6.2.1 Thin film sensors

Thin film sensors are mostly used in view of their light weight, minimally intrusive nature and low power consumption. However due to high temperature conditions and cycles of temperature the use of these sensors is limited in gas turbine engines.

Thin film sensors were mostly used as gas sensors (which are based on adsorption by thin film oxides that produce a conductance change) and have a long history [35]. Also gallium and titanium oxide based thin film sensors could operate at higher temperatures in the range of 80^0C -120^0C for oxygen sensing [36].

Miniaturization of sensors and electronics eliminated large classical sensors in many applications related to aerospace. The thin film sensors have several advantages over classical sensors [37]. They are considerably thinner than wire/foil strain gauges. The thin film sensors offer fewer disturbances to the operating environment, and have a minimal impact on the physical characteristics of the supporting components. In addition several thin film sensors have been tested in different engine conditions up to a temperature of 1100°C in NASA Glenn research center [38].

Platinum deposited as thin film maintained the property of bulk material except for slight difference in density. Thin platinum films produce a very stable and constant resistivity over thermal cycles from 100^0C in steps of 100^0C for 1 hour up to 1400^0C. The results indicate that at 1200^0C the platinum film resistivity changes [39]. Aerospace applications have much more intense and transient cycles of temperature. Thermal scaling due to oxidation at high temperature is another issue that has to be addressed.

Metals may form thin films on their surface when exposed to high temperatures due to the reaction of the surface of hot metal with the atmosphere. Some metals like platinum are more resistant to oxidation. Film loss via oxidation on platinum thin films exposed to temperatures in the range of over 900°C is reported [40]. For temperatures above 900°C a film loss model was developed predicting a loss rate of 62 Å/hr at 1000°C and 2500 Å/hr at 1500°C through volatile oxidation. Volatile oxidation of metals at higher temperature poses serious issues if the body of the sensor is made up of metal. Hence it is desirable to fabricate the sensor with a material which is more resistant to high temperature oxidation.

Advanced thin film strain gauge and thermocouples are reported by Lei et.al. [41]. The strain gauges are made up of Palladium – 13% chromium alloy and the thermocouples are platinum – 13% rhodium versus platinum. PdCr dynamic strain gauge is stable and repeatable between thermal cycles of 1100°C. Also thin film thermocouple could provide surface temperatures up to 1100°C. However, in high pressure high temperature conditions, it is difficult to obtain temperature data [42]. Reliability and durability of these sensors have to be developed and the lead wire attachment techniques to both the thin films and substrate materials need to be improved.

Fabrication of thin films to suit high temperature application is discussed in [43]. Reactively sputtered process is used to develop a multilayer thin film strain sensor for large temperature range. Two multifunctional sensors were fabricated using Tantalum nitride (TaN) and palladium chromium (PdCr) thin films. The sensors are fabricated in fine line widths utilizing the sacrificial layer lift off process that is used for micro fabricated noble – metal sensors. These films are suggested to be suitable for temperature applications in the range of 20°C to 120°C due to the low temperature coefficient of resistance of the thin films.

The feasibility of utilizing photolithography techniques for durable measurement processing for patterning thin film sensors is discussed by Lisa C Martin et al. [44].

Rajanna et al. [45] have reported a pressure sensor with Au-Ni (89:11) alloy thin film strain gauge. With a thickness of around 650 Å it has been reported that maximum non-linearity and the hysteresis is improved from 0.92% FSO to 0.06% FSO after 1000 pressure cycles. But these sensors are intended to work in normal temperature conditions. Further, 1000 pressure cycles could be attained in few seconds in aerospace applications and a pressure sensor with higher capability to resist pressure cycles is desired.

Chung [46] reported a thin film pressure sensor for static pressure measurement based on chromium nitride Cr-N, and tested till 200°C. Cr-N sensor showed decrease in sensitivity from 1.21mV/V/Kgf/cm^2 at room temperature to 1.097mV/V/Kgf/cm^2 when temperature is increased to 200°C due to negative co efficient of resistance. Thin film loss would be a problem apart from thermal drift caused by change in resistance due to change in temperature.

Chromium silicide and Tantalum carbide $CrSi_2$ / TaC ceramics are better in terms of high stability and robustness [47]. $CrSi_2$ and TaC is used for 650°C and $CrSi_2$ and Pt is linear up to 600°C.

Thin film sensors have inherent advantages in terms of minimal interference, easy installation, good repeatability, and have disadvantages in terms of lead wires to transfer data from high temperature zone and loss of film thickness at extremely higher temperatures. Thin film loss even though in the range of 2500Å / hr at 1500°C is significantly higher and it is not suitable for prolonged use at high temperatures. The current work suggests the use of a polymer based SiCN based sensor.

1.6.2.2 Optical sensors at high temperature

Optical sensors employed for pressure measurement are based on various principles, among which the most common are

i) Reflection of light from an elastic element that deflects due to pressure signal.

ii) Fibre grating based sensors selectively reflects one wavelength while transmitting others. Under pressure there is a change in location of the filter band, specifically the peak in the spectrum reflected from the fibre grating.

Optical sensors use optical beams characterized by several variables such as intensity, spectrum phase, wavelength and state of polarization to measure an external physical quantity including temperature, pressure, strains etc. An optical measurement system consists of two parts. Optical sensors in reflection mode uses a fiber optic cable that could sense the deflection of a sensing element which deflects based on the intensity of pressure that has to be measured. Thus optical sensor needs a fibre optic cable and a

sensing element which is a diaphragm or a cantilever beam in most cases. The change in the property of optical beam has to be processed by signal conditioning unit.

Temperature is the most sought physical quantity followed by pressure. Optical sensors for measurement of high temperatures is an area of extensive research and new materials such as sapphire based fibre optic cable are used for this purpose [48]. Fibre optic sensors are characterized into major groups including intensity based fibre optic sensors, color modulated fibre optic sensors, phase modulated (interferometric) fibre optic sensors, polarization modulated fibre optic sensors.

Fibre optic based sensors are also used to measure pressure in view of the advantages they offer [49, 50] such as

Immunity to electromagnetic interference (EMI)

Low noise

Wide range of measurand

Remote sensing capability

High resolution and reliability

Safe operation as no chance of spark generation

High frequency response

In addition to these advantages due to improvement in MOEMS / MEMS technology the optical sensors also yield themselves to miniaturization [51]. Miniaturization also imposes the need for new / special materials that would withstand rugged conditions and yield itself for micro fabrication.

Fibre optic sensors have been demonstrated using different optical techniques such as interferometry [52], micro bend created by pressure [53] and photo elasticity [54]

and grating based sensor [55][56]. Even though fibre optic based sensing was mostly propagated for pressure measurements in room or low temperatures recent advances and industrial requirements have extended their use for higher temperatures.

For pressure measurement in various temperature levels different types of fibre optic cables are used. Metal (aluminum, stainless steel, nickel) coated fibre optic cables are used for pressure measurement in the range of room temperature to 600^0C and fused silica cladding with Germanium doped fused silica as core based fibre optic sensors are used for pressure measurement from 200^0C up to 700^0C [57][58]. This could be possibly extended to higher temperature by using different coating material. Also fiber optic cables based on sapphire and cubic zirconium could prove operable at 1093^0C and 1026^0C, respectively [59][60]. Sapphire has excellent optical qualities with a melting point of about 2000 °C. These fibre optic cables that could function at higher temperatures could effectively function as wires at high temperature that would carry optical signal [60].

Performance of fibre optic sensors has been tested for dynamic cylinder pressure measurement in spark ignition engine and the results are in good agreement with those from temperature compensated piezoelectric sensor [61]. The amplitude and frequency encountered in engine cylinders are up to 12 MPa and 20 kHz, respectively. However, the tests were done for a maximum of 4000 rpm with a peak pressure of 80 kPa. The use of optical sensors for dynamic pressure measurement is encouraged by using a diaphragm based high bandwidth optical sensor to measure rapidly changing pressures in an explosive air blast [62], thereby demonstrating the application of high band width fiber optic sensor for the measurement of explosive shock waves.

One of the major problems and limitations of fibre optic type of pressure sensor used for pressure measurement at higher temperature is the thermal expansion / thermal mismatch and creep of the material of the sensing element (mostly diaphragm). This induces thermal stress caused by thermal expansion since this stress fluctuates with ambient temperature and disturbs the sensor signal. In addition optical sensors require clean environment which is not achievable in most of the applications that comes with harsh conditions.

Research carried out in this area, for more than 30 years have greatly enhanced the capacity of optical sensors and have increased the application potential of these types of sensors. The cross sensitivity to temperature of fibre optic pressure sensor could be minimized by the use of single deeply corrugated diaphragm (SDCD) [63]. SDCD has a flat suspended region that is suspended all around with free side walls. SDCD consist of i) sensing region ii) corrugated region and iii) outer region. The corrugated region (suspending side walls) is to transform loads (especially thermal loads) at outer region into local transformations with a small impact on sensing region, thus having a stress releasing and buffering effect on the sensing region of the diaphragm. Even though SDCD could minimize the temperature effects when compared to normal diaphragm sensors, the thermal effects cannot be completely ignored. Hence materials to resist high temperatures have gained importance.

1.6.2.3 Microwave sensors

Microwaves are used for sensing applications in the form of transmission sensors, reflection sensors, radar sensors, radiometer sensors. The basic transmission sensor

consists of two horn antennas configured in such a way that microwaves pass through the object. The attenuation or phase shift is measured. The reflection sensors are based on the measurement of the reflection coefficient, for example from the open end of the transmission line. Radar sensors measure the flight time or the frequency of the echo from an object. The sensor may be a pulse, impulse, FM or Doppler radar or an interferometer or a combination of those. Microwave radiometers receive the blackbody radiation emitted from an object.

Micro wave sensors are a type of sensors that have grown with the industrial automation. Microwave sensors are used for a variety of applications in the industry, in medicine, and for research purposes. Microwave sensors are based on interaction between microwaves and matter. This interaction may be in the form of reflection, refraction, scattering, emission, absorption, or change of speed and phase which could classify them into different types. They can form different types like resonator sensor, transmission sensor, reflection sensors, radar sensors, radiometer sensors which have solved new measurement problems faced by modern industries [64]. Microwave sensors are used for various applications involving measurement of distance, measurement of movement, shape and particle size and measurements related to material properties. In general micro wave sensors have the following advantages and disadvantages [65]

Advantages

- They do not need mechanical contact which facilitates easier online measurements with minimum or no interference.
- Microwaves can penetrate all materials except metals
- They are selectively insensitive to environmental conditions such as water vapour, dust and high temperatures.

- They are less sensitive to build up than capacitive sensors.
- At power levels used for measurement with microwave sensors, microwaves (non ionizing radiation) are safer than radioactive radiation.
- They can have associated electronics away from the measurement zone.
- They do not affect the material under test in any way.

Disadvantages

- The electronic components that operate on high frequency are more expensive.
- Must be calibrated separately for different material and in addition every microwave sensor is specific with respect to a specific application.
- Sensitive to more than one variable and it has to be compensated in some cases.
- Achievable space resolution is limited due to its higher wave length.

Considering the advantages and disadvantages of micro wave sensors and its key characteristic of being insensitive to high temperature it is fair to expect this type of sensors to be used for high temperature applications. ASIC technology will make these sensors smaller, less expensive and more applicable for different fields. Falling prices and higher availability of components for higher frequencies will open new application for these sensors. The possibility of moving the signal processing units from the zone of measurement could make measurements in high temperature zone easier.

1.6.2.4 MEMS candidates for high temperature

Harsh environment applications represent an exciting new frontier, challenging the capabilities of micro technologies. Micro-machined sensors gained importance in sensor market due to the following advantages [66] apart from conventional benefits.

- ❖ Small form factor – Some applications have size and weight constraints, smaller systems tend to move more quickly than larger systems because of lower inertia of the mass. Minute sizes of small device encounter fewer problems in thermal distortion and resonant vibration of a system as natural frequency is inversely proportional to the mass. Smaller system has higher natural frequency.
- ❖ Leveraging from IC industry – Manufacturing processes are borrowed from IC industry, this ensures low cost of MEMS devices due to possibility of batch fabrication and monolithic integration – integrating electronics and micro sensors on same substrate.
- ❖ Low power consumption and low noise
- ❖ Possibility of wireless approach and energy harvesting.

MEMS based micro pressure sensors use capacitive [67] Piezo resistive [68] and optical [69] methods of pressure measurement. Even micro machined pirani gauge capable of measuring vacuum pressure down to 10^{-7} torr is reported [70]. Piezo resistive sensors as compared with other types of sensors are in high demand due to its enhanced performance. In spite of being successful in normal conditions of temperature, silicon based micro sensors fail at temperatures higher than 200^0C.

MEMS devices are mostly made of silicon and are capable of withstanding 200^0C. A novel high temperature sensor based on Silicon on Insulator (SoI) technology is developed by implantation of oxygen (SIMOX) and due to its good linearity it is recommended for pressure measurement in high temperature applications [71]. SoI technology makes possible monolithic integration of sensors with complex high performance electronics [72] which makes it a successful sensor technology. But SoI

technology is found to be ideal for applications with temperature in the range of 250^0C - 300^0C. Applications demanding more than this range have to be met with some other method of measurement. This triggered the research in the area of Silicon Carbide (SiC) to be used for sensing applications.

SiC based sensors have been found suitable for high temperature applications due to its excellent mechanical and electrical characteristics. SiC is a semi conductor which is also famous for its chemical inertness. This makes it very hard to etch. These properties make SiC based sensors suitable for use in i) high temperature applications ii) extremely harsh environments [73].

SiC is a semi conductor that also possesses excellent electrical characteristics such as wide band gap (3.0 eV) and high electron saturation velocity ($2x10^7$ cm/s) [74]. SiC apart from being body of sensor is also found suitable for transistors due to the above mentioned characteristics [75]. SiC sensors for various applications like drag force transducer, and gas sensing application has been successfully fabricated and tested in [76][77].

The problems (for example lateral thermal diffusion) associated with silicon based sensors when exposed to high temperature was minimized by having a layer of SiC uniformly deposited on silicon wafer and using phosphorous silicate glass (PSG) as an insulation layer as well as bonding material [78]. The pressure sensing diaphragm is made from SiC and the silicon substrate is isolated from the high temperature zone. This kind of approach could push the temperature limit to 400^0C with a linear response between 1100 and 1760 torr at 200^0C with a sensitivity of 7.7 fF / torr [79] for a capacitance based SiC diaphragm based pressure sensor. Poly–SiC films when doped

with nitrogen could exhibit piezo resistivity and this characteristic was used to make piezo resistive high temperature pressure sensor using silicon nitride as insulator between the piezo resistor and the diaphragm [80]. Piezo resistive SiC pressure sensors could withstand up to 400^0C and exhibit a sensitivity of 177.6 mV/V*psi at room temperature and 63.1 mV/V*psi at 400^0C. Detailed study of temperature dependency of output of piezoresistive SiC pressure sensor is reported in [81] in which temperature coefficient of resistance changes from -3.07 % / 38^0C at 82.5^0C to +4.24 % / 38^0C at 260^0C.

Electrical mode (measurement using electrical signals) of measurement is more suitable for dynamic pressure measurement as the data is time variant and may occur with high frequency. SiC piezo resistor that could operate at 500^0C is reported [82] for dynamic pressure measurement with a sensor natural frequency of 30 kHz. However, it is highlighted that the pressure sensor is sensitive to temperature. Detailed test for temperature sensitivity is described in [83], in which the SiC sensor is compared with a reference piezo electric pressure transducer, that is commercially available which is bulky, expensive and a single use type used for test rig measurements. It is reported that at highest temperature (420^0C) the output was lower than the reference transducer.

SiC films have been investigated for applications targeting high temperature, where most of these applications require SiC to be in contact with metal electrodes. Metals at high temperatures diffuse into SiC and control of quality in the interface is a crucial issue. Metallization contacts of a SiC based device intended for high temperature degrades because of factors like inter-diffusion between layers, compositional and structural changes, thermal and / or structural induced stress that can take place at the metal / semi conductor interface [84].

SiC sensor backed up by its material properties to withstand harsh conditions provides chances of direct insertion into high temperature environment with the need for external cooling. However devices of this capability fail with prolonged usage. There are two possible reasons for failure. The first is associated with changes in resistance at metallurgical junctions between sensors and wire bonds which weaken the bond, and also change in bridge resistance with temperature [85][86]. The second mode of failure is due to thermal stresses developed due to mismatch in coefficient of thermal expansion between the sensor and the package components [87]. These failure modes reduce the reliability of these sensors based on evaluation of SiC sensor to be in satisfactory operation for around 130 hours at 300^0C [88].

Although SiC based sensors pushed the limit of operation of pressure sensors to a higher temperature, they pose inherent problems in terms of high thermal stress due to higher CTE (table 1.1), and complex fabrication issues [89]. Many applications require sensing at temperatures beyond 500^0C and SiC cannot be used for pressure sensing in environments above 500^0C. Special technology and material is required for sensors to operate at a temperature higher than 500^0C. The challenge for a high temperature sensor resulted in the new class of ceramic Silicon Carbon Nitride (SiCN) made directly from liquid precursors called poly silazanes. SiCN with operating temperature of 1400^0C is comparable with pure chemically vapour deposited SiC in terms of oxidation resistance [90]. SiCN when compared with SiC provides advantages in terms of withstanding higher temperature, ease of fabrication as innovative precursor based processing leads to low cost and flexible manufacturing and reduced coefficient of thermal expansion. In addition

SiCN has the functional advantages over SiC such as chemical inertness, oxidation resistance, and corrosion resistance at higher temperature.

1.7. High temperature considerations

Pressure measurement in high temperature environment poses certain complex problems. A list of few is provided below

- Change in structural, electrical and mechanical properties of materials.
- Creep
- Thermal drift
- Thermal expansion and stress developed due to thermal expansion and thermal mismatch.
- Diffusion of doped impurities especially in micro electronics.
- Softening of materials thereby challenging structural integrity.
- Scale formation due to thermal oxidation

Most of the problems discussed above are related to the material that is used as the material for the sensor. This triggered the exploration of ceramics for high performance engineering. Ceramics are better in withstanding high temperature with low thermal expansion and negligible scale formation due to thermal oxidation and better resistance to corrosive environment. The main difficulties to overcome in using ceramics are brittleness of the material, fabrication complexities, and creep. The next section will discuss the possibility of using Silicon Carbon Nitride (SiCN) for high temperature applications, which is polymer derived ceramic that can be moulded into any shape.

1.7.1 Silicon carbon-nitride (SiCN) as sensor material

MEMS technology has not yet come up with sensors for high temperature (higher than 500^0C) or harsh corrosive environment applications, specifically for gas turbine engine applications. This is because MEMS technology uses materials that are not structurally stable at temperatures above 500^0C. High temperature requirement comes with challenges associated with thermal expansion, thermal shock, oxidation as temperature acts as a catalyst to corrosion and also promotes structural rearrangement. Ceramics could properly operate under these extreme situations. New MEMS systems to withstand higher temperatures are required that would be made from various materials including ceramics since they can withstand high temperature, are chemically inert and abrasive resistant, and have low degree of reactivity with oxygen and water.

Material that would form the body of the sensor to be used in high temperature application must have the following characteristics

- Chemical inertness and abrasive resistance
- Ability to stay functional at high temperature
- Low coefficient of thermal expansion
- High figure of merit value for thermal shock resistance

SiCN is a class off recently derived ceramics that remain mechanically stable at temperatures in the range well above 1000^0C. At high temperatures around 1000^0C SiCN is stable but there is a structural re-arrangement with negligible changes in chemical composition [90]. SiCN aroused interest due to its wide band gap and good field emission characteristics in addition to the high bond strength and short bond length of SiCN, which is comparable to those of diamond [91]. Chen et al. [92] have reported hardness and

effective modulus of crystalline SiCN to be 30, 321.7 GPa, respectively, and amorphous SiCN to be 22 and 164.7 GPa, the value of hardness of crystalline SiCN to be as high as cubic boron nitride. SiCN apart from being popular as a thin film, is also used as an etch stop due to chemical inertness exhibited by SiCN. The use of SiCN as an etch stop improves etch selectivity, manufacturability of etching processes and enables the use of thinner etch stop layers [93].

SiCN having high temperature capability could incorporate other features that are listed above that make them a suitable candidate for fabrication of

- MEMS that can operate in high temperature environment, such as sensors for gas turbine engines.
- MEMS that can handle high temperatures, such as micro mirrors for high energy laser systems.
- Micro combustor and micro power sources

SiCN has the advantage of fabrication using many methods based on the requirement (discussed in chapter 2). It was initially identified as SiCN thin films since they exhibited interesting properties. The electrical resistance of SiCN films changes with temperature and the presence of certain gas species change the resistance [94]. SiCN thin films was formed by plasma enhanced chemical vapor deposition at temperatures of 473–1173K (200-900^{0}C) using hexamethyldisilazane ($Si_2NH(CH_3)_6$), ammonia and helium. The crystalline structure was with grain size of about 2 nm above 700K (427^{0}C) and hardness 30 GPa [95].

If sensors have to be made out of SiCN it is highly desirable that it could be made of different thickness. The versatility of SiCN fabrication is enhanced by the fact that

SiCN can be obtained from liquid or powder-based polymer precursors. SiCN fabrication can be performed in many different ways:

- Thin film fabrication by deposition techniques
- Fabrication by photo polymerization of liquid precursor
- Sintering based fabrication from powder precursor

Mostly liquid based polymer precursors are used because powder based fabrication uses specific techniques that cannot be easily integrated along with the existing micro fabrication techniques. In addition powder based SiCN shows relatively low strength and hardness. The reason behind this inferior performance of powder route when compared to the liquid route is due to the high porosity of powder derived ceramic in the range of ~10% by volume porosity [71]. Another advantage of SiCN fabrication is that it can be formed to any shape because it could be moulded to any shape from the liquid precursor.

SiCN fabrication has three major sub processes i) Thermo setting ii) Cross linking iii) Pyrolysis. There are issues related to each process as it heavily depends on the specific temperature and pressure of the process phase. These issues will be addressed in the chapter 2 that would deal with the fabrication of SiCN.

1.8. Objective of the proposed research

Even though there are some sensors that could perform pressure measurements at 750°C that would operate under the conditions at the compressor intake, compressor exit and in few cases low pressure turbine of a gas turbine engine, do not satisfy other essential conditions such as longer lifespan, higher time between maintenance, reliability,

non intrusiveness and small volume and mass. Hence they are mostly present in test stands because of the fact that they are bulky, expensive and limited operating time [19].

The overall objective of the present thesis is to develop a SiCN based dynamic pressure sensor that would operate in a temperature range normally encountered in gas turbine engine applications and would be implementable without disturbing the normal operation of the engine. It is highly desirable that the sensor will be a micro sensor. The research work in this dissertation is focused on the following:

1) Development of Silicon Carbon Nitride (SiCN) as sensor material.
2) Testing of the sensor material and checking for the properties to evaluate the material as a candidate for high temperature application. One fundamental advantage of SiCN is that it does not initiate scale formation at the operating temperature condition that diminishes the dimensions of the sensor.
3) Analysis of various designs for sensing elements and sensing schemes, that would measure dynamic pressure in a high operating temperature capability providing adequate protection to sensing element.
4) Address integrated measurement scheme for dynamic pressure and temperature using acoustics sensing scheme for the same application.

1.9. Organization of the dissertation

The thesis is presented in 8 chapters. The layout of the thesis is provided below.

Chapter 1 is a detailed literature review that focuses on the conditions prevailing in different parts of the gas turbine engine (GTE) and the need for active control based on the input from the sensor. Sensor being the weak link of the control system for high

temperature application needs more attention and research effort. The discussion on the instabilities along with the temperature and pressure regimes associated with gas turbine engine provides an insight of the operating environment especially operating temperature that the sensor has to address.

In order to successfully measure in harsh environment regime, the sensor should be backed up with the enabling material. Silicon carbon nitride (SiCN) is the material of choice by virtue of its excellent properties and ease of fabrication.

Chapter 2 provides a detailed description of fabrication of SiCN and its characterization at high temperatures. SiCN is a polymer derived ceramic and could be made from liquid or powder precursor. SiCN fabrication consists of thermosetting, crosslinking and pyrolysis. All the three processes include precise control of temperature and pressure and the influence of these parameters on the mechanical and structural properties are studied.

Thin and thick films of SiCN are fabricated in rectangular and circular shapes. These shapes provide the flexibility to choose diaphragm or cantilever beam as the configuration of the sensitive element.

Chapter 3 addresses the rationale for choosing diaphragm as the preferred sensitive element for pressure sensing application. Dynamic pressure sensors operate with annular diaphragm as sensitive element. Study on the annular diaphragm as a prospective sensitive element demonstrates that the proposed sensor cannot be used for high frequency application.

As the annular diaphragm configuration that is used to measure dynamic pressure in oil wells in low frequency application cannot be used for high frequency application,

other option emerges towards using aero-elastic phenomenon for sensing application, which is further addressed.

In chapter 4 different aero-elastic phenomena are described and the possibility of using such phenomena for sensing application for high temperature high flow application is discussed. Diaphragms with multiple holes are analysed for their frequency response and it is studied and identified as a possible configuration. Even though it is proved that the natural frequency could be trimmed based on the location of the perforation, other parameters such as space limitation and thermal expansion limits the usage of perforated diaphragms as sensitive element.

Also there are over loading issues that have to be addressed, diaphragm based sensors might not handle high temperature due to issues like buckling associated with high temperature. Cantilever based sensors might not deal with high flow due to overloading issues. This calls for a new sensing scheme that would provide overload protection along with the possibility of handling high temperature.

Chapter 5 presents a new sensing scheme which uses indirect drag effect. This scheme has protection in the form of a blocking element, which would protect the sensing element from the possible impingement from suspension particles and over loading. This phenomenon of indirect drag effect that causes the deflection of sensitive element is experimentally studied.

Cantilever configuration that uses deflection as a means to measure pressure. There are some instances wherein insight of temperature would be very beneficial. An integrated sensing scheme to measure temperature and pressure is also investigated in the next chapter.

Chapter 6 provides a brief discussion on integrated measurements and describes a novel method to perform integrated measurements of temperature and pressure using acoustic signals. A resonant tube is used to indicate the temperature by measuring the shift in the resonant frequency of the tube as the resonant frequency depends on the velocity of sound in air, which in turn depends on the temperature. The strength of the acoustic signal captured by the microphone is proportional to the dynamic pressure and the FFT analysis on this signal would provide a measure of temperature. The solution to the proposed research problem would not be complete in case if the issues associated with implementation are not addressed

Chapter 7 enumerates different issues associated with implementation on GTE. Sapphire based optical measurement is suggested based on the capability of sapphire to withstand high temperatures in the range of 900^0C – 1000^0C. Problems associated with cladding of the fibre and bending loss is also included in the study.

Chapter 8 presents the conclusion of the work and scope of future work.

Chapter 2 : Silicon Carbon Nitride (SICN) Fabrication Processes, Structures and Properties

2.1. Introduction

Electromechanical systems subjected to high temperature have to overcome temperature induced problems which could fall under two main categories: i) problems associated with properties of materials ii) problems associated with integration and data transduction. None of these factors can be compromised in order for the sensor to successfully operate at high temperatures.

Properties related to materials can be classified as mechanical properties, (hardness, ultimate / yield stress, thermal expansion, creep resistance) micro-structural properties, (grain size, grain structure, crystallization) and chemical properties (oxidation resistance, corrosion resistance, chemical inertness). Integration issues are related to the space availability, shape of the sensitive element to achieve better functionality under geometrical constrains imposed by fabrication methodology, constraints provided by packaging issues (thermal mismatch between parts of sensor, usage of glues for joining materials etc). Data transduction issues include type of transduction methodology used to transmit data from high temperature zone (electrical / optical etc), problems associated with diffusion of doped elements that are associated with micro electronics.

Silicon Carbon Nitride (SiCN) as the sensor material is under present consideration due to the advantages in terms of fabrication and reliability offered when exposed to rugged conditions.

SiCN is a class of recently derived ceramics that remain mechanically stable at temperatures such as 1500°C, as well as in corrosive environment [96]. Fabrication

processes of SiCN comprises of three processes i) thermosetting, ii) cross linking and iii) pyrolysis.

For SiCN the commercially available CERASET™ from Kion Corporation is used as a starting polymer. CERASET™ is poly-urea-methyl-vinyl-silazane ("PUMVS") which has to undergo thermosetting, cross linking and pyrolysis during the process of conversion from liquid polymer to Ceramics. CERASET™ is a transparent, pale yellowish liquid inorganic thermosetting resin. The material contains repeating units of silicon atoms bonded in alternating sequence to nitrogen atoms, forming a ring structure. The ring structure is as shown in figure 2.1.

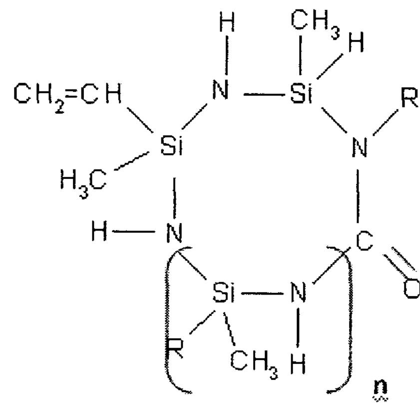

Figure 2.1: Ring structure of CERASET™

The material contains vinyl group (CH_2=CH-) bonded to Si outside of the ring structure through a vinyl cross linking mechanism that converts liquid CERASET™ into a solid upon the application of heat [97]. The thermosetting mechanism is ensured by reaction between vinylsilyl group (CH_2=CH-Si) and reactive hydrosilyl group (Si-H) [98]. During thermosetting the viscosity of the polymer increases continuously forming a gel like followed by rubber like and finally rigid solid. The process is accompanied by 1 - 3% weight loss. The weight loss is caused by evaporation of light isomers or rings

without vinyl group [98]. The ring structure in CERASET™ remains after thermosetting, but is broken in the cross linking reactions evidenced by the evaporation of NH_3 and H_2 gases at temperatures in the range of 400^0C - 500^0C as only the ring contains nitrogen. The reaction between the alkyl group R (basically hydro carbon group) and silane group (CH_3-Si) results in the evolution of methane gas during cross linking at 600^0C during the process of cross linking [98].

SiCN can be made from two different precursors, from liquid precursor / casting route or from powder precursor/powder route. Powder route, even though facilitates easy handling of CERASET™, poses problems in structural uniformity. In addition the density of casting route is higher than that of powder route [96]. SiCN developed from liquid precursor has shown superior properties in terms of strength and hardness than its powder-made counterpart [99]. Liquid precursor is widely used as it integrates easily to the existing micro fabrication techniques. Due to the inherent advantage of the casting route the casting route is used to fabricate the specimen.

2.2. State of the art

Silicon carbon nitrate (SiCN) is a polymer derived ceramic (PCD), which is a new class of ceramics derived from liquid precursors, called polysilazanes. The processing route for SiCN is micro casting that favours the fabrication of low cost, mass fabrication of MEMS devices [100]. The process consists of the following steps

Thermal Setting - The liquid precursor is cast into a mould of desired shape and undergoes thermal treatment (with or without thermal initiator) to create a rigid polymer

Crosslinking – Rigid polymer is crosslinked at higher temperature and pressure. Cross linking creates bonds that link one polymer chain to the other.

Pyrolysis – The free standing forms are pyrolyzed at 400^0C-1100^0C under a controlled atmosphere yielding SiCN at 1000^0C.

SiCN is suggested for high temperature applications mainly because of its oxidization resistance at high temperatures. The oxidation behaviour of SiCN is studied at temperature range of 900^0C -1200^0C [101] and the results suggest that at these temperatures the oxidation of SiCN is similar to that of Silicon Carbide (SiC) in spite of the presence of nitrogen in SiCN. The oxidation resistance of SiCN resulted in exploration of new type of PCD called silicoaluminum carbonitride (SiAlCN). SiAlCN possesses high resistance to oxidation and high corrosion [102]. Polyaluminasilazanes were used as the precursor for SiAlCN and tested for oxidation resistance upto 1400^0C [103]. The oxidation of SiCN is similar to SiAlCN till 900^0C, however, at higher temperature the oxidation rates of SiAlCN decrease with annealing time [104].

The electrical properties possessed by PCDs are also an important factor that enables PCDs to be used as body of the sensor. The addition of thermal initiator has significant effect on conductivity (thermal conductivity) which first increases and then decreases with increasing concentration of thermal initiator [105]. SiCN ceramic when doped with boron leads to p type conductivity which could be increased dramatically by annealing treatments [106,107]. Addition of manganese powder results in SiCN –Mn which has magnetic properties [108]. SiCN also exhibits piezoresistive behaviour with piezoresistive coefficient of ~ 1000-4000 which is much higher than that of any existing ceramic [109]. Piezoresistive coefficient is defined as $\frac{dR/R}{\varepsilon}$ where R is the resistance and

ε is the strain. It is also observed that the resistivity of SiCN decreases steeply with the applied stress (0-2 MPa) and then decreases slowly with higher applied stress (2-8 MPa) [110]. These characteristics of SiCN make it a valuable material for sensing at high temperatures. The proposed sensor application deal with dynamic pressure sensing and temperature regime addressed is above 500^0C.

2.3. Fabrication of SiCN using liquid precursor CERASET™

Sensors for high temperature applications require that all the parts of the sensor be made with a material capable of performing predictably at high temperatures. SiCN is one such material that qualifies for the purpose as discussed earlier. To be successfully implemented as the body of the sensor it is highly desirable that SiCN could be made and patterned in any size shape and thickness. The following section deals with how SiCN is fabricated as thick film, thin film and patterned film. There are differences in terms of mould preparation for thermo setting associated with thin film, thick film and patterned SiCN fabrication processes, as the process after thermosetting is the same except for temperature rate involved in crosslinking and pyrolysis.

The fabrication of SiCN using casting route can be outlined as follows

- ❖ Mould design and fabrication
- ❖ Polymer preparation and casting
- ❖ Thermosetting of polymer
- ❖ Cross linking of polymer
- ❖ Pyrolysis

The fabrication of a fully dense monolithic ceramics from liquid precursor involves high temperature and pressure and has the following major difficulties [111, 112]

i) Bubble formation / foaming during thermosetting

ii) Gas evolution during cross linking and pyrolysis

iii) Material shrinkage

Bubble formation occurs during evaporation of the liquid precursor, the extent of evaporation is limited by vinyl cross linking mechanism and is determined by the maximum temperature, rate of heating, polymer viscosity and pressure involved [113]. Evolution of gases mostly occurs in cross linking that contributes to the major weight loss. Both gas evolution and material shrinkage issues are discussed in the forthcoming sections in the same chapter.

2.3.1 Mould preparation and polymer casting

SiCN has an advantage of being fabricated into any shape as it is made from liquid. Thus successful fabrication of SiCN components depends heavily on the fabrication of the mould. The type of mould depends on the nature of the final product required. The proposed dynamic pressure sensor requires SiCN in terms of thin films with thickness in the range of 70 to 100 microns and thick films in the range of 2-3 mm. Further SiCN could be patterned by adding photo synthesizer by traditional photo lithography. Few types of moulds used to fabricate different specimens are as follows

- Poly dimethyl Siloxane (PDMS) based moulds – Thick SiCN
- Gelatine based sacrificial moulds on silicon substrate – Thin film SiCN

❖ Sacrificial gelatine coating on glass substrate – Patterned thin film SiCN

The mould fabrication defines the shape and thickness of the SiCN specimens, whereas other processes like thermosetting, crosslinking and pyrolysis yields the structure of the material that defines the mechanical and structural properties of the obtained specimen. The thermosetting, cross linking and pyrolysis are the same for all the specimens with minor differences in temperature rate, maximum temperature and pressure and are discussed in the subsequent sections in this chapter.

2.3.2 Thermosetting

CERASET™ is a clear, colorless, viscous inorganic thermosetting resin that has repeating units of Silicon atoms bonded in alternating sequence to nitrogen atoms, forming a ring structure as illustrated in figure 2.1. The vinyl group bonded to Si is important for thermosetting as these vinyl group reacts with hydrosilyl group to form solid polymer at the end of thermosetting process. CERASET™ can be thermally set in its raw form by heating it to a temperature in the range of 200°C – 240°C with a heating rate of up to 4°C/min in the presence of inert atmosphere (N_2 or Ar) to avoid reaction with oxygen at high temperature. Addition of heat increases the viscosity of the liquid polymer continuously forming a gel like, rubber like substance and then rigid solid polymer. The solidification is a function of temperature rate experienced by the liquid polymer, and is achieved as soon as the temperature reaches the desired range. Figure 2.3 shows the thermally set CERASET™, made from a mould made up of PDMS (poly dimethylsiloxane), and the resulting thermally set solid polymer is colorless, transparent and could be easily machined.

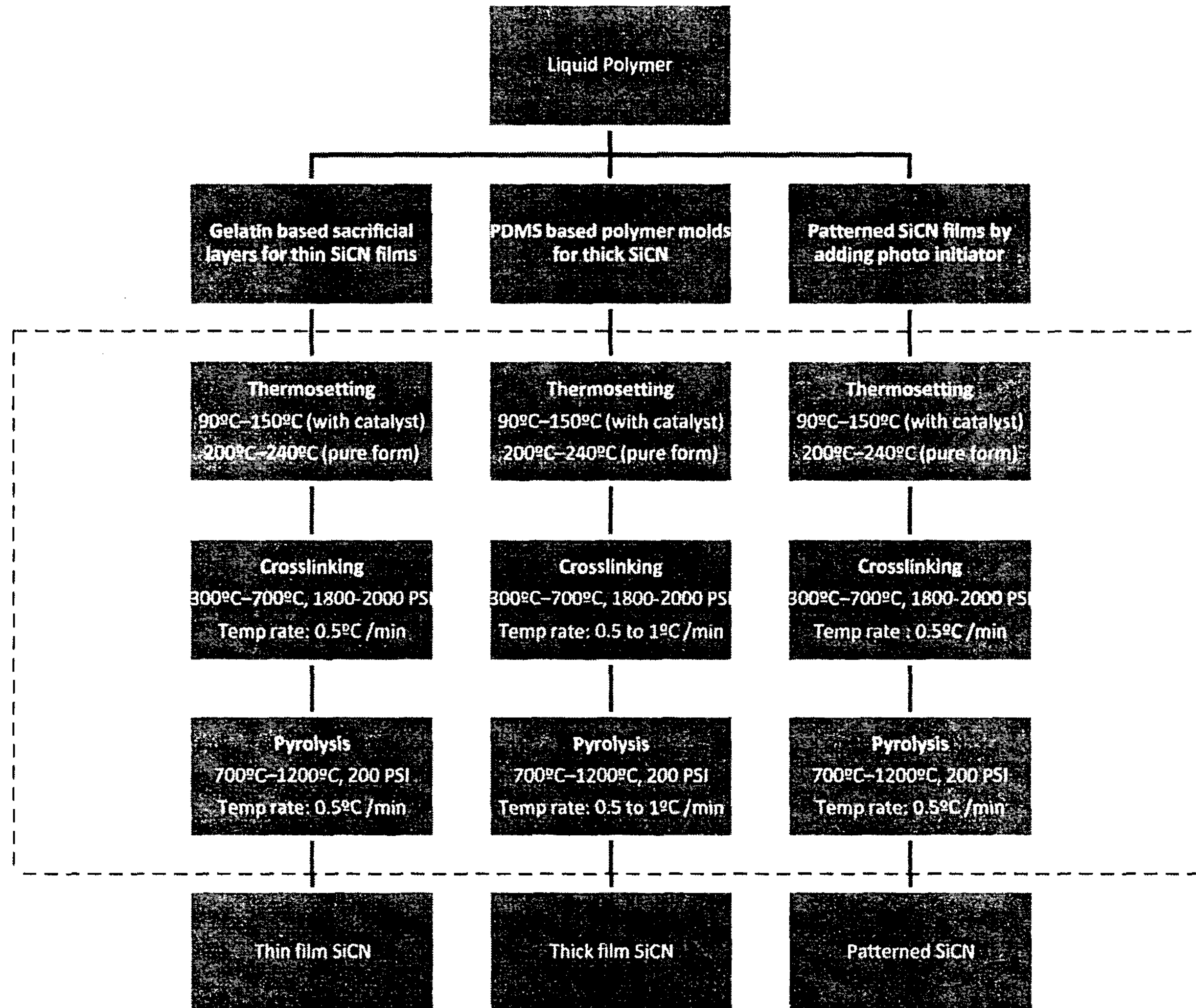

Figure 2.2: Layout of SiCN fabrication

Thermosetting temperature could be drastically reduced to 90°C – 150°C by adding a catalyst with free radical initiator such as dicumyl peroxide. The influence of the thermosetting temperature has a major influence on the properties like hardness which is discussed in the forth-coming section. Also addition of catalyst greatly reduces the temperature involved in thermosetting process there by reducing thermal stress developed between the mould that holds the liquid polymer before thermosetting and the solid thermally set polymer after thermosetting.

Figure 2.3: Thermally set polymer

Thermosetting process results in a weight loss of 1 - 3% in thermally set CERASET™ [98] while the volumetric shrinkage values of around 6 % [97] is caused by the evaporation of light isomer without vinyl group. The thermosetting process is carried out in a mould, which are made of different materials such as gelatine, PDMS, etc. Further to facilitate easy removal of the solid polymer aluminum foils are used on interior parts of the mould that is in contact with the liquid polymer. Only thermosetting process requires moulds and these moulds have to be made in a way so as to accommodate these volume losses.

Thermosetting was performed in a tube furnace in nitrogen atmosphere. The thermosetting temperature is reduced to 120^0C (while preparing the specimens) with the

addition of free radical initiator like dicumyl Peroxide. Normally dicumyl Peroxide is added 1 % by weight. This addition enables lower thermosetting temperatures thereby simplifying the mould design [114]. Higher temperature of thermosetting means higher stress due to thermal mismatch between the mould and the CERASET™, requiring more complex mould in order to withstand higher temperatures and a solid CERASET™ becomes more prone to micro pores and cracks.

The maximum temperature is based on the type of the specimen, and the temperature rate was selected as 1°C/min during heating and a dwell of 90 minutes was practiced once the temperature reaches the maximum (i.e. 120°C) while the cooling is furnace controlled. Thermosetting was performed using Barnstead thermolyne 21100 tube furnace with the specifications of maximum operating temperature of the furnace to be 1000^0C at the atmospheric pressure.

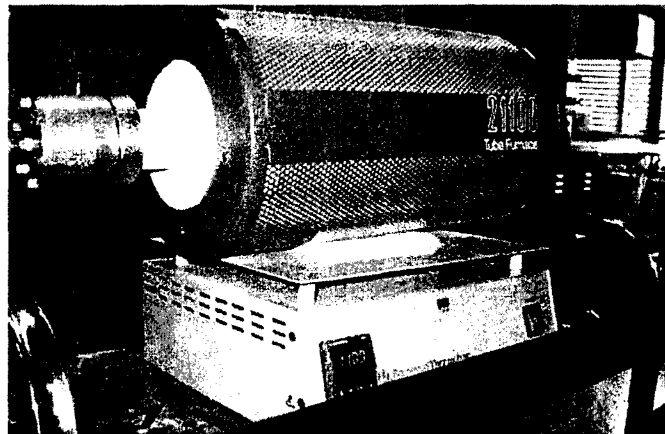

Figure 2.4: Barnstead Thermolyne 21100 tube furnace used for thermosetting

2.3.3 Cross linking and pyrolysis

Cross linking is a process of creating bonds that link one polymer chain to the other. Cross links are created by chemical reactions that are initiated by heat and /or pressure that result in the linking of polymer chains and are mostly performed in inert

atmosphere. When polymer chains are cross linked they lose some of their ability to move as individual polymer chains. Cross linking reaction could result in changing a liquid polymer to solid or could result in denser solid.

CERASET™ if heated to a temperature of around 400°C results in reaction within the polymer which is called cross linking. This process induces a change in physical properties and is irreversible. The ring structure of CERASET™ retains its shape after thermosetting but with higher temperature results in the breakage of ring structure during cross linking. The evaporation of NH_3 gas could be considered as an evidence for breakage of structural ring since only the ring contains nitrogen [98].

Cross linking is performed at a temperature in the range of 400^0C. This process releases NH_3 gas and could create micro pores in the specimen. The formation of micro pores could be avoided by applying isostatic pressure during cross linking. The pressure of about 2000 psi (13.789MPa) is maintained till the end of cross linking. At around 400^0C the cross linking is complete and the furnace is purged with fresh nitrogen along and the NH_3 gas is removed by scavenging. The obtained cross linked polymer is infusible, does not dissolve in any organic solvent and does not melt. However the cross linked material would not face temperatures higher than 180^0C. Further heating the cross linked specimen in an oxidizing environment would only result in burning. Hence in order to achieve further thermal decomposition it is necessary to perform pyrolysis.

Pyrolysis is a process of decomposition of a condensed substance by heating in atmosphere that lacks Oxygen. Pyrolysis of the specimen is performed in the presence of heat and in the absence of oxygen. Once the cross linking is performed and the temperature is further increased, the cross linked specimen undergoes thermal

decomposition and becomes a ceramic at 1000^0C [72]. With the rise of temperature the specimen's color changes from transparent to yellow between 500°C – 600°C, to red – brown between 650°C – 750°C, to dark brown above 800°C and finally becomes black at ~1000°C [98].

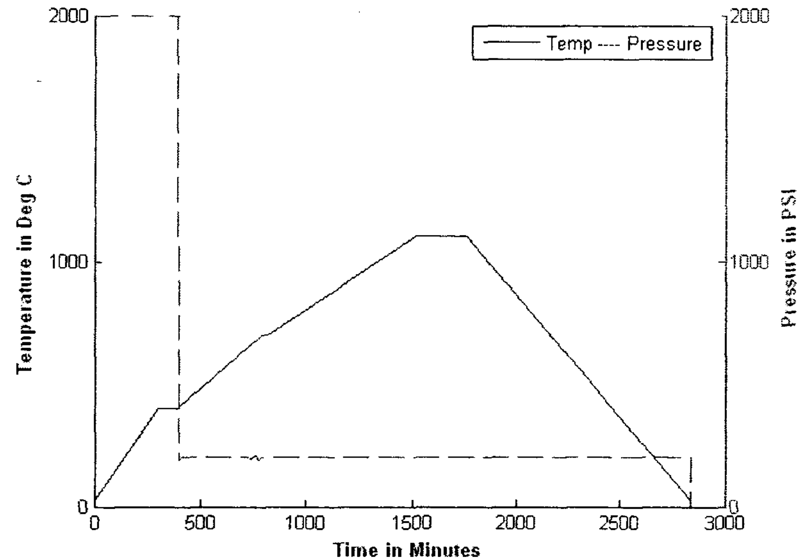

Figure 2.5: Combined cross linking and pyrolysis temperature and pressure vs time

Heating between 600^0C and 700^0C results in higher weight loss of the specimens, as gases like CH_4 and H_2 are released. Pyrolysis involves higher temperature as compared with thermosetting and cross linking and results in up to 25 % weight loss during pyrolysis [115] and linear shrinkage of 15% - 20% [116]. Scavenging is carried out between 600^0C and 700^0C using nitrogen to facilitate removal of the evolved gases. At around 1000^0C the pyrolysed specimen results in a black amorphous solid ceramic called SiCN. SiCN is stable up to 1600^0C in air. SiCN has excellent mechanical properties, qualifying it to be a suitable candidate for high temperature applications.

The furnace used for high temperature high pressure crosslinking and pyrolysis is custom made by Thoughtventions Unlimited LLC. The specifications of the furnace

are maximum pressure 2500 psi (17.24 MPa) and maximum temperature is 1200^0C. The furnace has a cubic boron nitride core along with alumina refractory and is water cooled at the exterior. The temperature rate of 0.5 – 4^0C/min is achievable and is electronically controlled. However the pressure control and purging of nitrogen is manually performed.

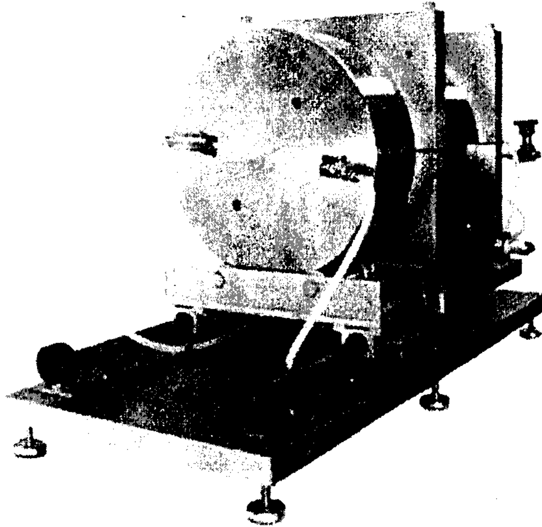

Figure 2.6: Custom built high-pressure, high temperature furnace (Thoughtventions Unlimited LLC)

2.4. SiCN in different forms

The proposed sensor whose details are described in detail in chapter 5 requires SiCN as thin film with thickness in the range of few microns for sensitive element as well as thick films of 2-3 mm thick that would be used as blocking element. Both the blocking and sensitive element are in shapes of flat strips (cantilever beam configuration). Further, in this case if SiCN has to be used to build micro sensors it is mandatory that it is batch fabricated so as to reduce the cost per unit. The following sections deal with the fabrication of SiCN in different forms as illustrated in figure 2.2 so as to form the body of sensing unit at higher temperature.

2.4.1 Thin film SiCN

Thin film SiCN would form the sensitive element of the proposed sensor. Thin film fabrication involves handling the samples in different stages, CERASET™ as liquid, thermally set solid polymer, and in its last stage as a SiCN ceramic.

Thin film SiCN needs thin moulds that would define the shape and thickness of the SiCN film. These micro moulds are made from different micro fabrication techniques. Photolithography using SU-8 photo resist on silicon substrate is popular [117]. The micro mould has to have the desired shape of the SiCN micro structure but should be larger than the SiCN microstructure so as to compensate for shrinkage during cross linking and pyrolysis.

Meanwhile thin films could be made as described below. Silicon wafers are used as the substrate for deposition of thin films, the substrate is coated with a thin layer of gelatine (Bovine skin type B). This gelatine coating acts as a sacrificial layer, which will assist in removing the thermally set CERASET™ from the silicon substrate. Further silicon wafer can easily withstand the thermosetting temperature. The major advantage of using gelatine based sacrificial layer is that it facilitates easy removal of the thermally set CERASET™ by melting the mould in warm water. Gelatine mould is prepared by spin coating of gelatine on a silicon wafer. This gelatine acts as a sacrificial layer which will assist in removing the polymerized CERASET™ from the silicon substrate. The gelatine hardens in air after less than one hour, at which point the CERASET™ can be applied on top of the gelatine. Both the gelatine and the CERASET™ are deposited onto the silicon substrates using a process called spin-coating, whereby a single wafer is held in place with a vacuum force and spun very quickly.

Droplets of gelatine are dropped onto the wafers, and the lid is closed. The spinning motion spreads the fluid evenly over the surface and excessive fluid flies off the edges. The speed of rotation, angular acceleration, duration and the viscosity of the fluid all affect the thickness of the film. The speed of rotation that is used for applying the gelatine is kept relatively low at 1000 rpm for 30 seconds in order to ensure that the wafer is well-coated.

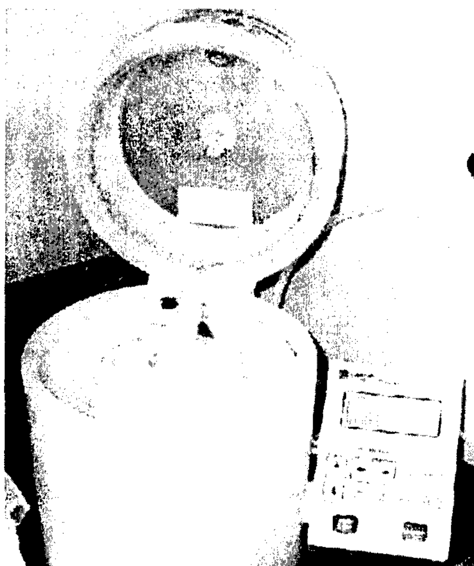

Figure 2.7: The Laurell Spin-Coater, Model WS-400B

On the other hand, the rotational speed for applying the CERASET™ is varied between 2000 rpm and 4000rpm for 60 seconds to obtain a very thin coating. Any speed higher than 4000 rpm produces thin SiCN film that is difficult to handle after thermosetting.

The substrate is subjected to thermal setting (60 min at 120°C in tube furnace in nitrogen gas flow) which makes the polymer solid and transparent. Substrate with gelatine sacrificial layer and CERASET™ polymer layer is immersed in warm /hot water which releases a thin film of CERASET™ in the order of desired thickness. Thermoset thin film is shown in Figure 2.8. The shown dimension of the films is 150 X 100 microns,

the surface impurities that are visible on the surface are the peroxide particles. The peroxide particles are ground manually to fine powder and these peroxide particles are mixed with liquid CERASET™ so as to reduce the thermosetting temperature. The mixing is done by mechanical stirrer and it is found that the dispersion of the particles is not uniform. A regular industrial process would overcome this defect.

Figure 2.8: Microscopic image of the surface of thermally set polymer thin films

The resulting thin film CERASET™ is crosslinked and pyrolysed to produce a thin film SiCN ceramic. One major problem during this process is warping of thin film. Warping occurs due to high temperature involved and also because of high rate of heating. Thinner samples experience warping more than crack development [113]. Different approaches were followed to reduce warping. When placed on flat graphite block with the top surface open to the controlled environment in the furnace specimen showed warping into a dish shape. Hence thin films are sandwiched between two flat graphite blocks to reduce warping as graphite is inert and does not attack thin films. The weight of graphite keeps the film flat and prevents wrinkling. However, sometimes it is noticed that the samples are cracked when sandwiched between graphite blocks. Use of powder bed techniques with graphite, Si_3N_4 and BN powders was tried by Janakiraman et

al. [113] but still could not avoid crack formation. It is also suggested to wrap thermally set CERASET™ in silica wool so that they could be pyrolyzed free of cracks [113] Figure 2.9 shows the surface of thin film SiCN under microscope. There were no visible cracks on the surface of the SiCN, however, small non uniformities on the surface are visible. The hard spots on the image are due to the presence of peroxide particles.

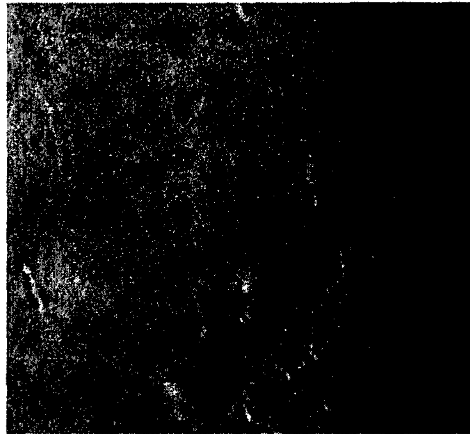

Figure 2.9: Image of the surface SiCN thin films X 100

The thickness of the SiCN specimens produced varies mostly with the rotational speed during the spin-coating process. When the CERASET™ is applied at 6000 rpm, the specimens are very thin (10-15 μm) and subsequently are also extremely fragile. Specimens made at lower speeds between 2000 rpm and 4000 rpm are thicker, whose thickness are about 30μm. Drying these films without creases or folds is much easier and results in flatter, smoother specimens. These specimens are stronger and easier to handle. SiCN thin film specimen is shown in figure 2.10.

Figure 2.10: Thin film SiCN with Canadian cent for size comparison

If the thickness of CERASET™ layer is more than 30 μm, it is possible to burn the sacrificial gelatine layer before pyrolysis process (at about 400°C – 600°C) without mechanically damaging SiCN ceramic film as in this range gelatine burns out facilitating removal of SiCN film. Thin films less than 30 μm thickness requires more attention while removing gelatine layer. This is due to the fact that removal of gelatine layer would damage the thin film SiCN.

The maximum size of uniform thin films obtained using this method is about 10 X 10 mm and the thickness is around 30 microns. Any thickness less than 30 microns poses a serious problem in handling the thin films. Surface roughness properties of thin film SiCN are studied with the optical profiler Veeko NT 1100 which has a capacity to measure three dimensional, non contact surface measurements using white light interferometry and is shown in figure 2.11.

The average surface roughness of the 100 X 100 μm area is 114.18 nano meter. The peak to peak variation is around 1.07 μm. This could be considered as fairly good surface finish. The small visible spots in figure 2.11 are caused by the tiny peroxide particles.

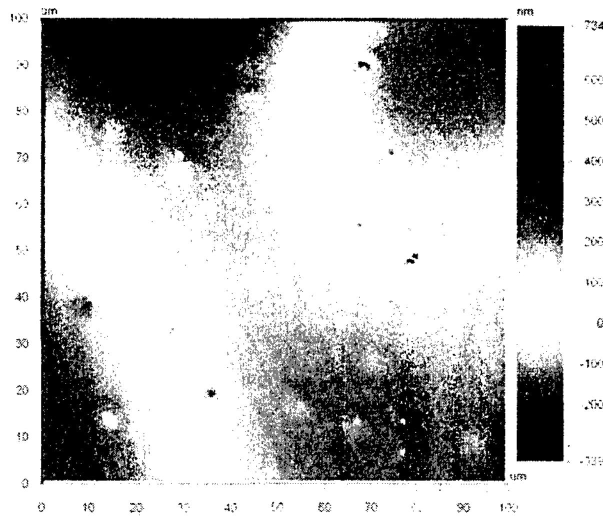

Figure 2.11: Surface roughness

Thin films that could be used as sensitive elements for the proposed sensor were fabricated in different thickness between 30 μm – 70 μm. The proposed sensor also needs SiCN as a thick form so as to form the blocking element in the range of 2 -3 mm. Unlike thin films, thick films require different type of mould as the maximum thickness is very much limited by spin coating

2.4.2 Thick film SiCN

Thick film SiCN will be used as a blocking element which requires thickness in the range of 2 – 3 mm. The desired thickness is much higher and hence it is easier to handle and cast the liquid CERASET™. Fabrication of thick SiCN films will come with large shrinkage ratio especially during pyrolysis but still shrinkage during thermo setting cannot be ignored. When thick films are pyrolyzed they result in evolution of gases at a higher rate and the chance of micro pores and cracks are also higher in thick films [113]. Using soft, flexible mould is an effective way of compensating for the shrinkage as well as to conform to the stresses developed during thermosetting of CERASET™. SiCN is

mostly fabricated as thin films and attempts to make thick films are sparsely reported in the literature. The elastomer proposed for the fabrication of mould is Polydimethylsiloaxane (PDMS) commercially named as Sylgard 184 (Dow Corning Corporation). PDMS are easily moulded, optically transparent, durable, low cost and chemically inert and provide possibility of small sized moulding and stable over wide temperature ranges [118, 119]. Even though the usability of PDMS is suggested in the range of -50°C to +200°C [120], PDMS moulds have been used to cure CERASET™ in the temperature range of 240°C while making specimens. It is mandatory to separate the solid CERASET™ after thermosetting from the PDMS mould as PDMS cannot withstand crosslinking temperature (400°C -700°C). PDMS is made by mixing two chemicals (elastomer base and elastomer curing agent) and thermosetting the mixture. The ratio of elastomer base to the curing agent is made in the range of 10:1 so as to make a mould hard enough to withstand thermosetting temperature. The time for thermosetting PDMS is temperature dependent but to ensure full curing, the thermosetting is carried out for 8 hours at 60°C. It is important to point out that thermosetting of PDMS is different from thermosetting of CERASET™. The PDMS mould made following the procedures described above is shown in figure 2.12.

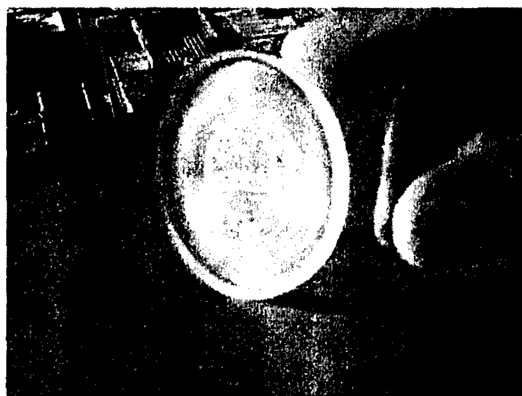

Figure 2.12: PDMS mould used to cast CERASET™

The thermally set polymer (CERASET™) can be removed either by sacrificing the mould by dissolving it in into 1.0 tetrabutylammoniumfluoride (TBAF) solution in THF [121] or by spreading aluminum as a thin sheet over the mould thereby making the mould reusable. Aluminum is used to release thermally set CERASET™ in micro level using micro forging technology [122]. The reusable mould was used to prepare specimens. Stress development and crack formation has been a major problem in the fabrication of both thin and thick films of SiCN. Attempts have been made to reduce cracks formed due to stress developed and the usage of fillers is suggested [123] and prepyrolysis of the precursor. The thermally set polymer extensively undergoes shrinking during cross linking and pyrolysis due to high temperature involved in these processes. Figure 2.13 shows the size difference between a thermally set polymer and ceramic pyrolysed at 1100°C which originated from the same disk split before pyrolysis. It is found that there is 29.83 % weight loss during transformation from thermally set polymer to SiCN ceramic and this weight loss is predominant in case of thick films than in thin films (as in thin films the maximum weight loss reported was up to 25 % during pyrolysis) [115].

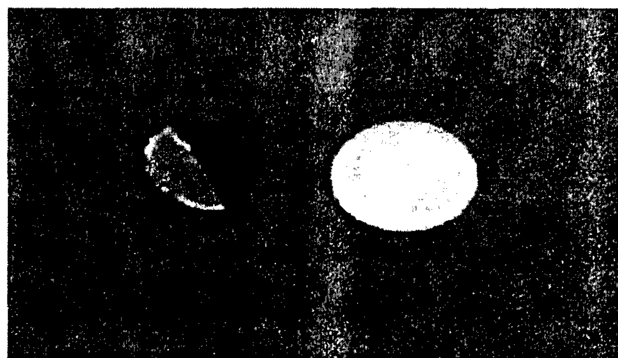

Figure 2.13: Thermally set polymer along with the ceramic

If SiCN has to be used for different applications it is highly desirable that SiCN could be fabricated with different thickness and different dimensions. Attempts have been made to make SiCN ceramics with different thickness and the results are as shown in Figure 2.14. The maximum size of the samples shown in around 6 mm^2 and the thickness is in the range of 0.5 mm to 2 mm.

Figure 2.14: SiCN chips of different thickness

2.4.2.1 Shrinkage issue and mould design

Figure 2.13 shows the SiCN in comparison with thermally set CERASET™ made of circular mould shown in figure 2.12. The dimensions of the mould are 1.85 mm deep and 21.17 mm diameter. Thermal setting of CERASET™ results in volume loss as the liquid CERASET™ solidifies due to evaporation of light isomers. It is found that there is a significant reduction of thickness in thermally set CERASET™ compared to its diameter. The thickness reduced to 1.63 mm during thermosetting without any measurable change in diameter.

The thermally set polymer is subjected to pyrolysis. The dimensions are measured after pyrolysis. The SiCN ceramic formed had a thickness of 1.08 mm and the diameter of 15.13 millimetres. Considering the initial mass of CERASET™ (before thermosetting)

is mass loss plus the final mass (after thermosetting). Below, the amount of mass lost is evaluated for one of the experiments

$$\rho_c v_c = m_t + \rho_t v_t \tag{2.1}$$

where

ρ_c is the density of CERASET™ = 1.02 g/cc [124]

v_c is the volume of CERASET™ = volume of the mould = $\frac{\pi}{4}*(2.117)^2*0.185 = 0.65118cm^3$

ρ_t is the density of thermally set CERASET™ =1.12 g/cc [124]

v_t is the volume of thermally set CERASET™ = $\frac{\pi}{4}*(2.117)^2*0.163 = 0.5737cm^3$

m_t is the mass loss due to thermosetting process

$$1.02*.65118 = m_t + (1.12*0.5737)$$

The mass loss due to evaporation during thermosetting m_t=0.0216 g.

Considering the initial mass of thermally set CERASET™ as mass loss due to cross linking and pyrolysis and the final mass (after pyrolysis).

$$\rho_t v_t = m_p + \rho_{SiCN} v_{SiCN} \tag{2.2}$$

where

ρ_t is the density of thermally set CERASET™ =1.12 g/cc [124]

v_t is the volume of thermally set CERASET™ = $\frac{\pi}{4}*(2.117)^2*0.163 = 0.5737cm^3$

ρ_{SiCN} is the density of SiCN =2.4 g/cc [124]

v_{SiCN} is the volume of SiCN = $\frac{\pi}{4}*(1.513)^2*0.108 = 0.1942cm^3$

m_p is the mass loss due to crosslinking and pyrolysis.

$$1.12 * .5737 = m_p + (2.4 * 0.1942)$$

The mass loss due crosslinking and pyrolysis m_p=0.1765 g.

The total mass loss is = $\frac{0.1765 + 0.0216}{1.02 * 0.65118} = 29.83\%$

The value coincides the ones reported in open literature

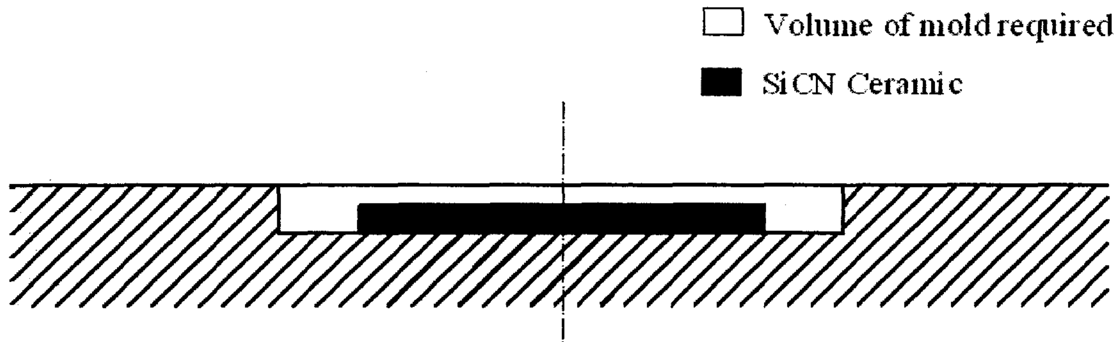

Figure 2.15: Mould design for thick SiCN

Certain applications may demand not only thin and thick SiCN films, but also SiCN in different complex shapes [125]. This could be possible if CERASET™ is made photosensitive. Photosensitivity is a property which could be inculcated by addition of certain photo-sensitive agents by which the liquid CERASET™ can be made sensitive to UV light by addition of photosensitive agents thereby enabling photolithography. Fortunately there are agents that could make CERASET™ photosensitive like 2,2 Dimethoxy-2-phenyl-acetophenone (DMPA). CERASET™ was added with photo sensitive agent and patterned SiCN was fabricated which is described as follows.

2.4.3 Patterned SiCN

CERASET™ when added with a sensitizing agent becomes photo sensitive. The sensitizing agent in this case is 2,2 Dimethoxy-2-phenyl-acetophenone (DMPA) which is added with the CERASET™ to be suitable for photo lithography. The UV light has a wave length of 370 nm which corresponds to the excitation frequency of the radical

(radicals are species with a single, unpaired electron) bond in photo initiator molecules [98]. When UV light with specific frequency hits the bond in DMPA molecule, the bond breaks down into a radical bond. This turns DMPA molecule into a radical monomer, which attacks the vinyl group (CH_2=CH-) to initiate the polymerization reaction in CERASET™ [98]. The mixtures of liquid CERASET™ with DMPA acts like a negative photo resist and cures on exposed areas.

The substrate used is glass on which a thin layer of gelatine is spin coated in order to prepare the surface for easy detachment of thermally set CERASET™ from the substrates. The speed of rotation that is used for applying the gelatine is kept relatively low at 1000 rpm for 30 seconds (as gelatine is less viscous in comparison with CERASET™) in order to ensure that the wafer is well-coated. The sole objective of gelatine is only to enable easy detachment of patterned SiCN as gelatine dissolves in hot water.

After gelatine is dried on the glass substrate, CERASET™ is mixed with Dimethoxy-2-phenyl-acetophenone (DMPA) (10% by weight), is spin-coated and treated with the UV (using EFOS Lite UV curing system). Optimum UV treatment time is 900 seconds based on trial and error (this exposure time was established after experimenting with several CERASET™ substrates starting with 100 seconds treatment up to 1000 seconds, with 50 seconds increments). The washing agent is ethanol which perfectly removes the uncured CERASET™ leaving behind a clean surface of UV cured CERASET™. The cleaning should be done after 24 hour drying in air at normal atmospheric conditions.

The only problem in the CERASET™ patterning is to be able to create a sufficiently thick CERASET™ layer in order to be able to convert it into a ceramic chip after high

temperature treatment. Shrinkage of CERASET™ after heat treatment requires a pre-treated substrate to be more than 100 micro meters thick in order to be able to obtain a chip that is thick enough to be handled after final heat treatment. Since the spin-coating provides only around 30 micro meters thickness, the obvious solution is to create a multi-layer structure of CERASET™, after drying each layer either by means of UV or heat treatment. The method above enables fabrication of SiCN layers. However the main issue is to combine these layers with very minimal thermal expansion characteristics.

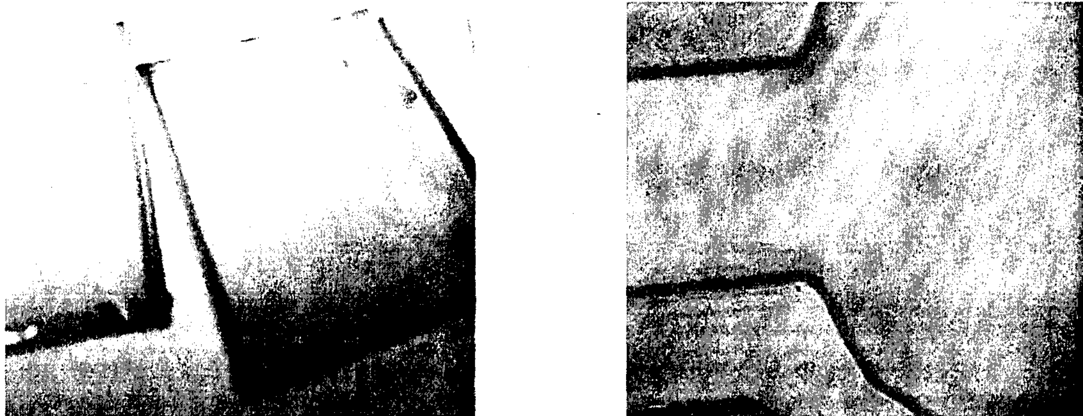

Figure 2.16: Patterned CERASET™ on the glass substrate

Figure 2.16 shows the glass substrate and a zoomed in view of the patterned CERASET™. The proposed sensor does not necessarily require patterned SiCN and hence this aspect is not elaborately discussed. Regardless of the type of structure – thick, thin or patterned SiCN, the fabrication process from thermosetting to pyrolysis follow the same protocol with small differences in temperature and pressure sequences. As a general note, the processes are not performed in a clean room as required by photolithography, and hence it is expected to have structural imperfections in the patterned specimen.

2.4.4 Machinability of SiCN

SiCN could be made into any shape using the patterning process discussed before. In addition the thermally set CERASET™ is easy to machine and could be made into any shape by machining at this stage. SiCN has serious issues in terms of machining as SiCN after pyrolysis becomes very hard and brittle which makes it very difficult to machine by conventional machining processes. Attempts have been made to ablate SiCN ceramic using femtosecond laser.

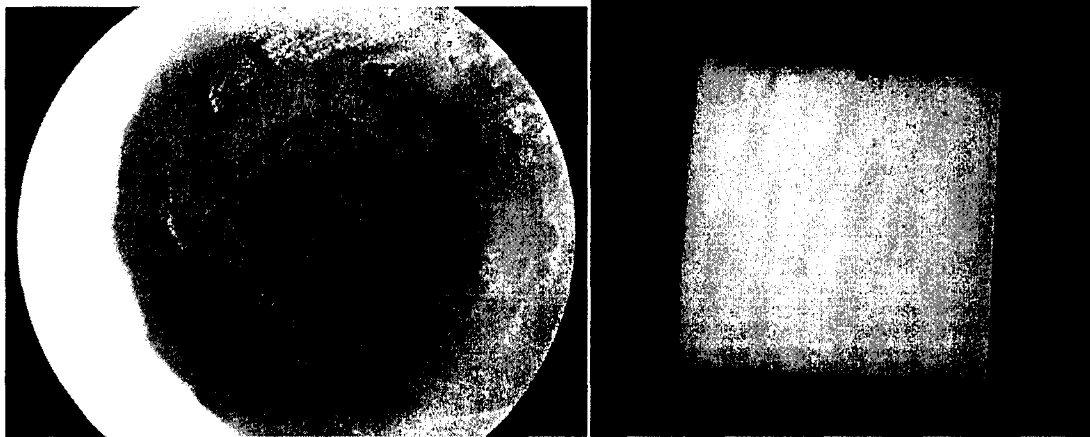

Figure 2.17: Laser ablation in SiCN ceramic using femtosecond laser

The specifications of the Ti-Sapphire femtosecond laser (Hurricane Spectra Physics Lasers) are that it emits 120 fs FWHM (Full width at half maximum), has a wavelength of 800 nm and maximum energy of 1 mJ/pulse with a pulse repetition rate of 1 kHz. In femto-second laser machining ablation occurs in vapour phase. The absorbed laser energy is converted into the thermal energy and is transferred to the lattice in a pico second time scale [126]. Thermal diffusion into the material is minimal, leading to an insignificant amount of liquid phase, absence of which allows better control of machining process [127].

In the illustrations shown in figure 2.17 a) there is a circle ablated by Femtosecond laser. Due to the very fragile nature of ceramics the thickness of the ablated line is a much larger than optimal (10-100μ compared to the optimal line thickness of 5μ). Any type of opening is possible to create in SiCN ceramic and local heat generated by laser ablation could be resisted by SiCN due to its ability to withstand high temperature. Figure 2.17 b) shows a square hole on the SiCN ceramic.

The ablation rate depends strongly on the properties of ceramic, the power and the beam spacing / width. For a given beam width a higher beam power would cause deeper cuts and based on the overlapping of the beam the surface would be rougher [128]. Figure 2.17 b) shows the laser ablated surface and the surface irregularities in left and top side of the ablated square hole. Higher power produced more distinct and deep grooves than that with lower power. When the distance between two beam spots is equal to the machined width there is neither beam overlapping nor bridges (refers to the non machined regions between the beam lines). This produces a finer texture on the cutting lines.

The property of the SiCN ceramic is defined by the constituents of the ceramic. As a preliminary attempt elementary analysis was done on a SiCN ceramic to know the constituents.

2.5. Elementary chemical analysis of SiCN

Elementary Chemical Analysis shows different content of C, N, and H (for specimens treated at different temperature) in these compounds. They were measured with Fisons Instruments SPA, (model EA1108 available at university de Montreal, Department of Chemistry). Elementary analysis could only provide the content of

Carbon, Nitrogen and Hydrogen in percentage of weight and not the content of silicon. In this analysis the content of silicon and other substances (which is available only in very minute quantity) is assumed to represent the balance.

Table 2-1: Composition of SiCN ceramics (4^{0}C/min heating rate)

Pyrolysis temp	C (wt.%)	N (wt.%)	H (wt%)
1000° C	22.19±0.13	20.54±0.18	0.67±0.01
1050° C	21.80±0.81	15.68±0.56	0.27±0.13
1100° C	20.89±0.56	16.56±0.81	0.26±0.03
1150° C	19.94±3.4	16.45±0.97	0
1200° C	20.06±6.6	12.20±4.5	0

These specimens were obtained with a rather high heating rate (4°C/min). It is found that the specimen if annealed or pyrolysed above 1100°C results in the elimination of H atoms. It is also observed that there is no significant change in constituents of ceramic formed by pyrolysis and annealing.

Table 2-2: Composition of SiCN ceramics (heating rate 1^{0}C/min) with different pyrolysis and annealing conditions

Pyrolysis	Annealing	C (wt %)	N (wt %)	H (wt%)
1000°C	-	21.45±0.20	18.99±2.00	0.62±0.12
1000°C	1100°C	21.98±0.25	19.82±0.41	0.32±0.01
1100°C	-	21.69±0.50	20.07±0.39	0.27±0.18

Table 2.2 shows the comparison between two specimens that varies only in the maximum pyrolysis temperature. First specimen pyrolysed at 1000°C and annealed to 1100°C and another specimen pyrolysed till 1100° C. The result shows that the

composition remains more homogeneous if the specimen is pyrolysed or annealed and the composition is more dependent on the temperature of pyrolysis or annealing. The carbon content has been related to the hardness of the ceramic such that more carbon is associated with higher hardness.

2.6. Influence of thermosetting temperature

Thermosetting is an irreversible process in which the liquid CERASET™ is converted to solid polymer in the presence of heat. The vinyl group bonded to Si is important for thermosetting as these vinyl group react with hydrosilyl group to form solid polymer at the end of thermosetting process. The thermosetting is carried out at temperatures in the range of 90-150°C if the CERASET™ is mixed with catalyst or in the range of 200-240°C for pure CERASET™ in the presence of nitrogen atmosphere.

The influence of thermosetting temperature on the mechanical properties of the specimen is studied for two specimens.

Specimen 1 – Pure CERASET™ (without catalyst) thermally set at 240°C

Specimen 2 – Pure CERASET™ (without catalyst) thermally set at 200°C

The specimens differ only in the thermo setting temperature (200°C and 240°C) with temperature rate being 6°C / minute and a dwell period of 90 minutes, the solid polymer is treated under the same conditions of temperature and pressure during cross linking and pyrolysis.

The crosslinking is performed at 400°C with a dwell period of 90 minutes and a pressure of 1800 psi. The cross linked specimen is heated to 1100°C with a temperature rate of 0.5°C / min at a much lower pressure of 200 psi.

The hardness test reveals that specimen 2 is softer than the specimen 1. The specimen 1 is tested for hardness with MST (CSEM) micro-scratch tester using the standard indentation method of the Vickers type diamond stylus.

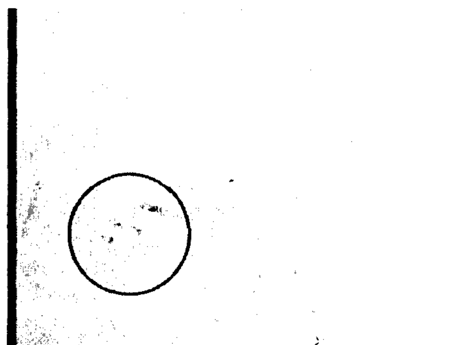

Figure 2.18: Hardness test performed using MST (CSEM) micro scratch tester

Indentation force was limited to 1 N since an excessive cracking and even specimen rupture was noticed at higher (2N) load. The hardness of specimen 1 is evaluated to be 23 GPa. Figure 2.18 shows the field view of the indentation done at 1 N force.

The hardness test on the specimen 2 is done with Hysitron Nanoindentator Berkovich tip. Figure 2.19 shows the indentation created by the Berkovich tip at two different forces for specimen 2. The test is repeated at several locations of the specimen 2 with two different loads and the average value for indentation forces of 2500μN and 4000 μN is documented in Table 2.3

Table 2-3: Hardness of SiCN without catalyst (specimen 2) at different forces

	2500 μN	**4000 μN**
Reduced Young's Modulus E_r (GPa)	62.3	68.6
Hardness (GPa)	7.38	7.71
Contact Depth (nm)	90.7	135.2
Contact stiffness (μN / nm)	40.3	61.8

Max force (μN)	2427.2	3908.6
Max Depth (nm)	136.2	194.9
Contact Area (nm^2)	$3.288e^5$	$6.371e^5$

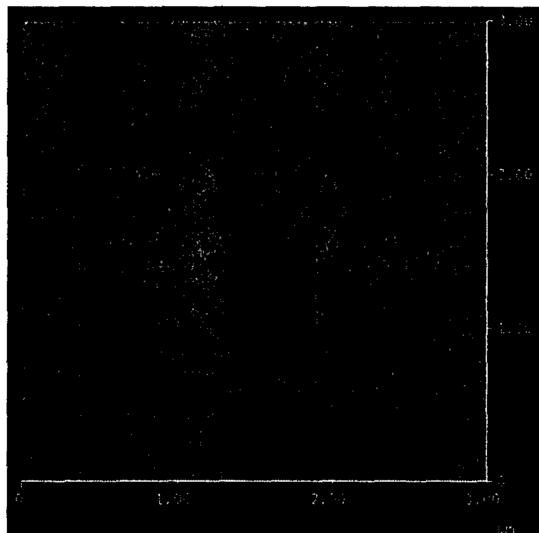

Figure 2.19: Image of Indentation marks on SiCN using Hysitron Nanoindentator

The indentation marks caused by 4000 μN and 2500 μN are easily recognizable in figure 2.19. The average hardness value obtained is 7.5 GPa. Sufficient space between the indentations is given to record the data, as very close indentation marks may cause errors in the data obtained during the second / later indentation.

The thermally set CERASET™ at 200°C (specimen 2) has a much lower hardness compared with the specimen 1. Specimen 2 was still soft (flexible solid) after thermosetting, as 200°C is not sufficient for CERASET™ in pure form (without catalyst) to completely set into a solid polymer. This is the reason for a relatively low hardness 7.5 GPa as compared to 23 GPa of specimen 1. This proves that thermosetting temperature must be sufficiently high (240°C) in case if ceramic of reasonably higher hardness has to

be fabricated. It also emphasizes the importance of addition of a catalyst that would drastically reduce the thermosetting temperature to 120°C.

It is observed that the thermosetting temperature has a major influence on the hardness of the SiCN made from pure CERASET™.

2.7. Influence of catalyst

The addition of catalyst is directly related to reduction in thermosetting temperature and hence it is worthwhile to study the influence of the catalyst on the properties of the material as well. Dicumyl peroxide is used as a catalyst and is a strong free radical source, which is used as a polymerization initiator, catalyst and vulcanizing agent. [129]

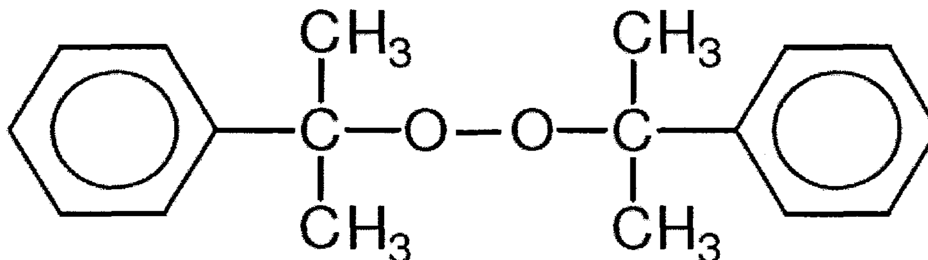

Figure 2.20: Chemical structure of Dicumyl peroxide [129]

Figure 2.20 shows the chemical structure of dicumyl peroxide [129], which shows peroxy group (-O-O-), chainlike structure containing two oxygen atoms, each of which is bonded to each other and to a radical or some element. The most valuable property of hydrogen peroxide is that it breaks down into water and oxygen and therefore does not form any persistent, toxic residual compounds. Organic peroxides are powerful oxidizing agents releasing oxygen and are widely used as initiators, catalysts and cross linking agents for polymerization process.[130] For this study, CERASET™ is added with 1%

by weight of dicumyl peroxide, which is a free radical initiator that will act as a catalyst. The thermo setting temperature goes down to 120^{0}C. The specimens were crosslinked and pyrolysed with the same temperature and pressure as in figure 2.5.

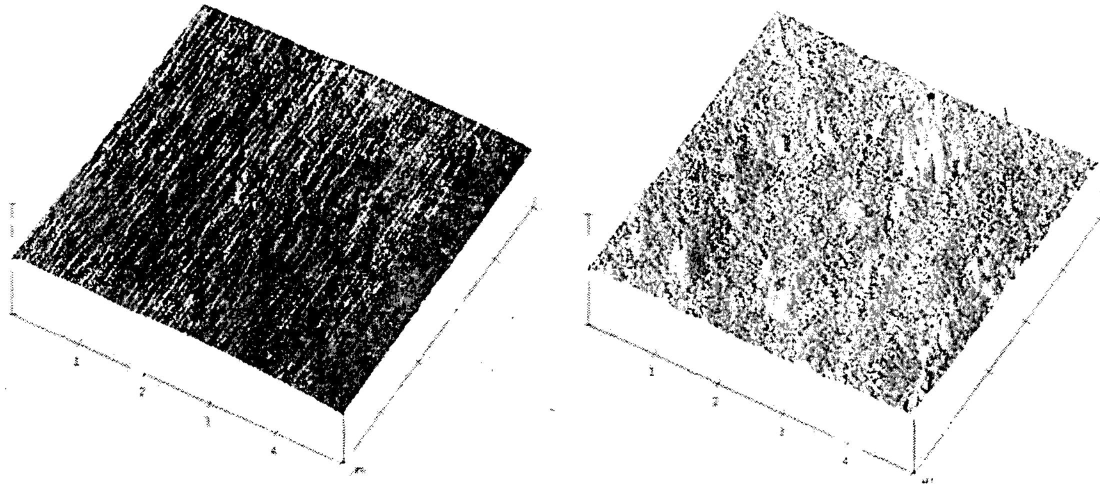

Figure 2.21: Surface topology between SiCN without and with catalyst

Dicumyl peroxide is in crystal form that melts at 39^{0}C - 41^{0}C [130]. Prior to the thermosetting process dicumyl peroxide crystals are powdered manually and mixed with liquid CERASET™. These crystals get deposited in the SiCN ceramic at micro level to form surface irregularities. Atomic force microscopic (AFM) studies were done on the surface to check for the homogeneity of the surface. The results indicate the deposition of the catalyst on the surfaces.

Figure 2.22: Dicumyl peroxide on the (5 X 5 μm) surface of SiCN ceramic

The 3-Dimensional topography of an area (5 X 5 μm^2) of the SiCN with and without the catalyst shows the peroxide crystals on the surface (as shown in figures 2.21 and 2.22). The phase diagram generated by the AFM that is operated in tapping mode clearly indicated the dispersion of the peroxide on the surface of the ceramic. The scan size (area of observation) is 5 X 5 μm^2 with the scanning frequency of 1 Hz with a resolution of 256 lines per image.

The comparison of the nano indentation results done with two specimens with and without catalyst proves to be very interesting. The addition of catalyst provided hard thermally set polymer at a lower temperature (from 200^0C to 120^0C). The hardness of the specimens varies because of the addition of catalyst (and also the thermosetting temperature). All other conditions of fabrication (crosslinking and pyrolysis) are the same. The nano indentation results are documented as in table 2.4 for a force of 2500 μN. The results point out that the value of the hardness and reduced Young's modulus is improved at the expense of surface homogeneity and surface roughness.

Table 2-4: Comparison of properties of SiCN with and without catalyst at 2500 μN force

	SiCN (with catalyst)	SiCN (without catalyst)
	120^0C	200^0C
Reduced Young's Modulus E_r (GPa)	76.3	62.3
Hardness (GPa)	9.18	7.38
Contact depth (nm)	79.8	90.7
Contact stiffness (μN / nm)	44.6	40.3
Max force (μN)	2461.7	2427.2
Max depth (nm)	121.7	136.2
Contact area (nm^2)	$2.681e^5$	$3.288e^5$

The role of the catalyst is essential in establishing the structure of the ceramic material when lower temperature is used for thermosetting.

2.8. Influence of annealing temperature

CERASET™ thermally set in a condition similar to specimen 1 is crosslinked with higher isostatic pressure (2000 psi) and pyrolysed and annealed at higher temperature of 1200° C. This resulted in a higher hardness 28 GPa as in Fig.3.23. This is the motivation for the study of the influence of the annealing temperature on the properties of SiCN.

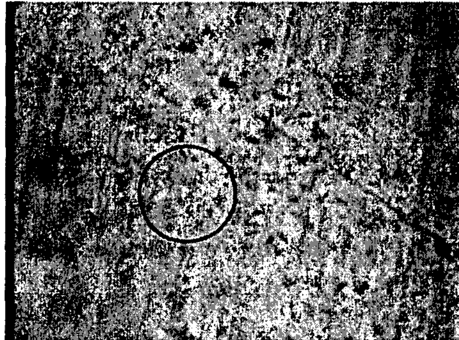

Figure 2.23: Image of hardness test mark for the specimen with highest hardness. H = 28 GPa

SiCN forms a hard solid ceramic when pyrolysed at a temperature of 1000°C. After pyrolysis the resulting SiCN is amorphous. It is highly desirable to anneal the SiCN at a higher temperature to obtain good crystal structure, higher hardness improves mechanical properties [131] and to inculcate some electrical properties [132].

2.9. X-ray powder diffractograms of SiCN ceramics

The SIEMENS diffractometer, model D5000 (UQaM, Department of Earth and Atmosphere Science) and Rigaku D/MAX 2400 12kW rotating anode diffractometer

were used for performing x-ray diffraction testing. Common scheme of the X-ray diffractometer is shown below.

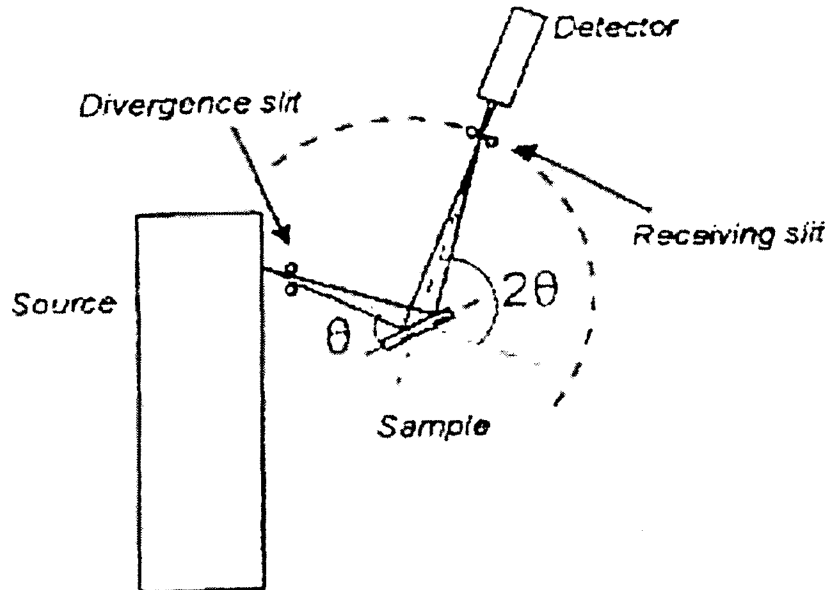

Figure 2.24: XRD principle of operation

For the powder which represents many small crystallites with random orientation, X-ray pattern is averaged over all crystallite orientations and measures the scattered intensity as a function of the angle of diffraction.

Information can be obtained from:

1) Peak position
    a) Crystal system
    b) Unit cell size.

2) Peak intensity
    a) Unit cell contents
    b) Quantitative phase determinations.

If the pattern consists of many sharp peaks, the specimen has crystalline structure

The X-ray powder diffractograms show amorphous state of SiCN ceramics for pyrolysis temperature of 1000°, 1100°, and 1200°C.

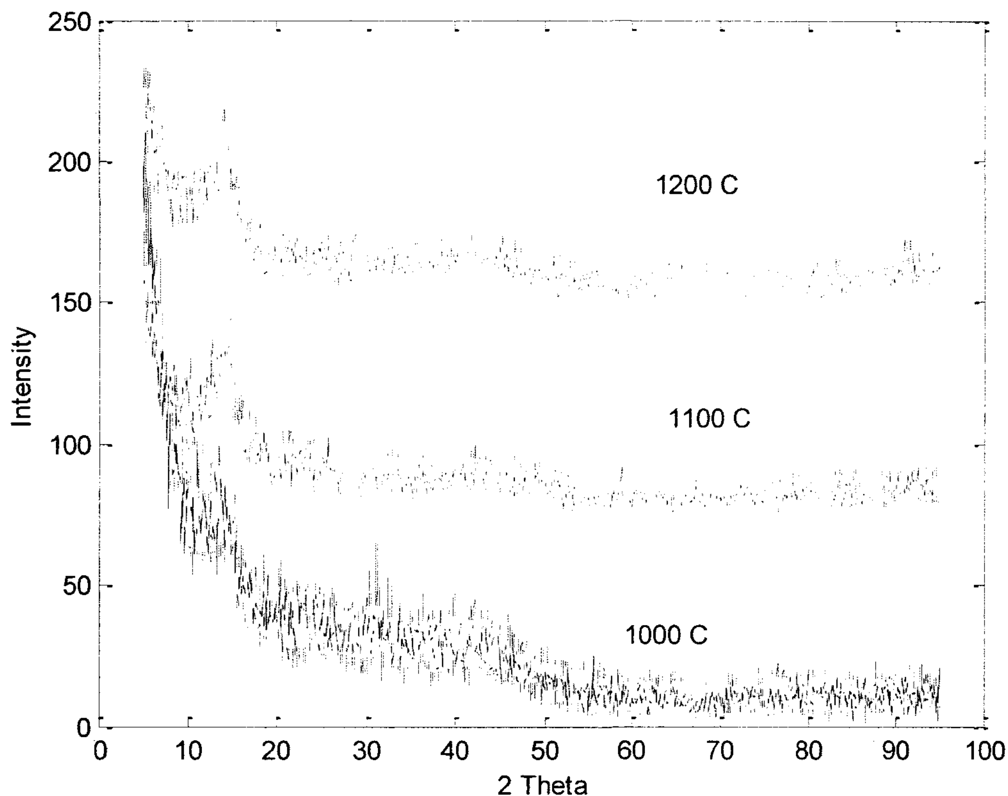

Figure 2.25: XRD peaks for a SICN at different temperatures

SiCN specimens annealed at temperatures of 1000°C, 1100°C, and 1200°C does not show visible peaks confirming the amorphous status at those higher temperatures. Further investigation on SiCN revealed that it is predominantly amorphous at temperature below 1400°C [133] X-Ray diffraction testing was carried out on SiCN which are thermally set at 120° C with temperature rate of 4°C / minute for 90 minutes, cross linked at 400°C at a pressure of 2000 psi with a temperature rate of 1° C/minute and pyrolysed till 1100°C with a temperature rate of 0.5°C and annealed to 1500°C.

For studying the influence of annealing temperature two specimens were considered

Specimen 3 – CERASET™ (with catalyst) annealed to 1500°C

Specimen 4 – CERASET™ (with catalyst) annealed to 1200°C

X-Ray diffraction testing is performed on specimen 3 and specimen 4 which are thermally set at 120°C with temperature rate of 4°C / minute for 90 minutes, cross linked at 400°C at a pressure of 1800 psi with a temperature rate of 1°C/minute and pyrolysed till 1100°C with a temperature rate of 0.5°C. The only difference between specimen 3 and specimen 4 is the annealing temperature.

XRD tests on specimen 4 could not provide visible peaks as SiCN did not crystallize in specimen 4. The results from the XRD testing for specimen 3 are shown in figure 2.26. Analysis of the peaks revealed that the Silicon is available in the form of SiC and β-Si_3N_4 and the crystallization occurs at a temperature higher than 1400°C. This corresponds to X-ray patterns of SiCN ceramics, pyrolysed at 1450°C, and ascribed to β-Si_3N_4 with hexagonal structure [134].

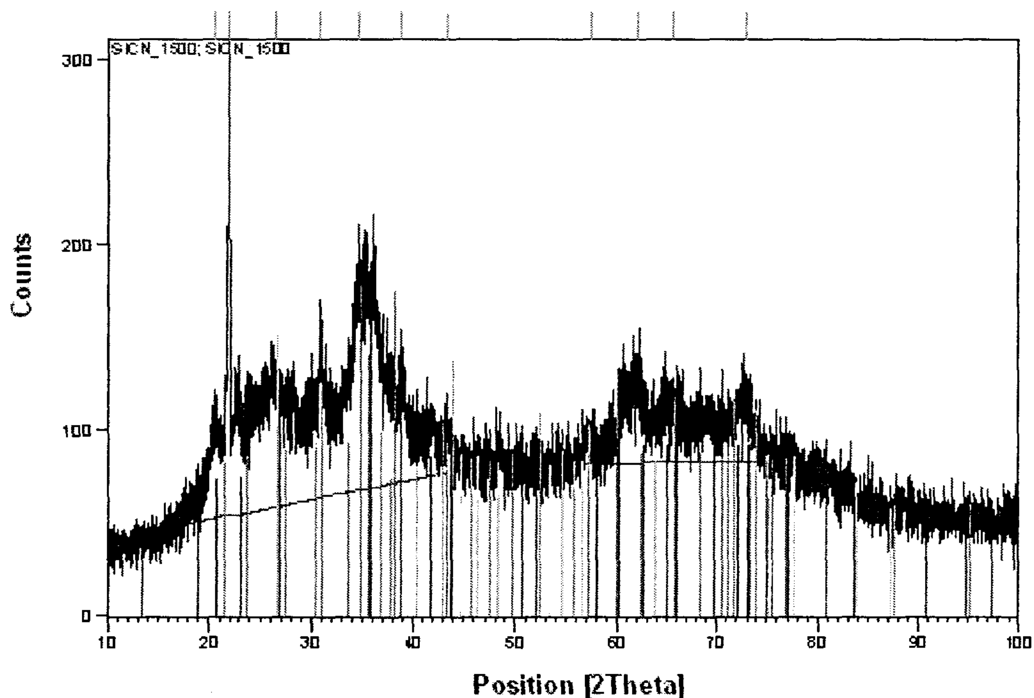

Figure 2.26: XRD peaks for a SICN annealed to a temperature of 1500°C

For the specimens pyrolyzed at 1700°C, Li et al. [135] found the existence of only three peaks near $2\theta = 35°$. They ascribed these peaks to SiC crystallites. It implies that for the specimens pyrolysed here, if annealed above 1600°C the crystallization of SiC would occur completely, as this phase exists in our specimens, pyrolyzed at 1500°C to lesser extent, than Si_3N_4 crystallites. It is interesting, that no peaks definitely corresponding to crystalline graphite were found in our specimens as graphite was used as a base to hold the specimens during cross linking pyrolysis and annealing.

The width of X-ray diffraction peaks can be used for determination of the size of SiCN crystallites. The larger the width of X-ray diffraction peak, the smaller is the size of the crystallite. The simultaneous analysis of XRD peaks at $2\theta = 21°$, 26°, 31°, 35°, 36°, 38°, 42°, 63°, 65° and 73° gives the average size of 40 ± 5 nm for Si_3N_4 crystallites in our SiCN specimens pyrolysed at 1500°C. It is to be noted that formation of $Si_3(N_{1-x}C_x)_4$ crystallites is quite possible , where a part of N ions replaced by C ions with almost the same structure as Si_3N_4.

The overall grain size of SiCN is dependent on annealing temperature. The SEM tests were conducted on specimen 3 and 4. Specimen 4 does not show clear grains. The results reinforced the XRD results at 1200°C the SiCN is still amorphous and there is no clear evidence of grain structures or boundaries. On the other hand grain structure in the range of 40-50 nm is found in specimen 3. The SEM image of specimen 3 is shown in figure 2.27.

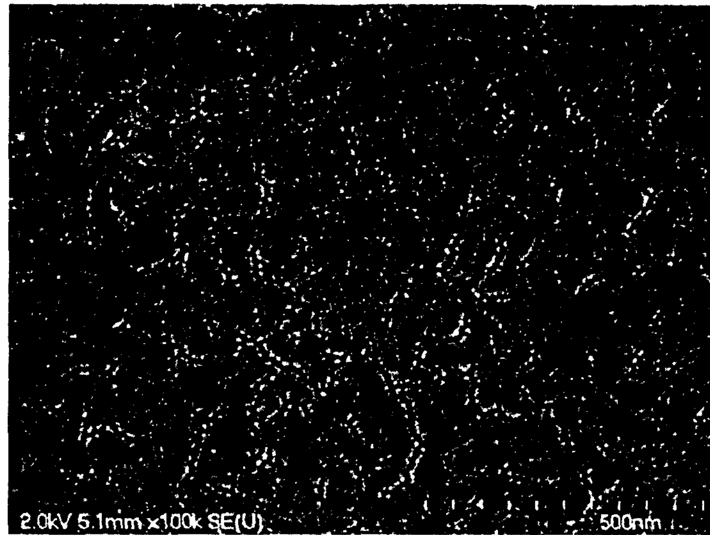

Figure 2.27: SEM image of SiCN ceramics annealed at 1500°C

The results obtained from XRD patterns and SEM patterns support each other and give an estimation of the grain size of SiCN ceramics annealed at 1500°C to be 40 -50 nm. The estimations of grain size of SiCN ceramics, obtained by Fainer et al. [95], also support our results on grain size of SiCN ceramics annealed at 1500°C.

2.10. Summary

This chapter focused on the fabrication aspect of the sensor to perform at high temperature. The suggested material for the body of the sensor is Silicon Carbon Nitride SiCN. SiCN is a polymer derived ceramic and could be made from liquid or powder precursor.

A brief introduction on the structural details and properties of SiCN is provided. The fabrication consists of thermosetting, cross liking and pyrolysis. Different shape and size of SiCN demands different type of moulds. All the three processes require high

temperature and it poses problems such as shrinkage, warping, gas formation and micro pores / cracks. It is also discussed to minimize / eliminate these high temperature issues.

Mould design is discussed for thin, thick and pattern-able SiCN along with machinability issues of these ceramics. Hydrogen peroxide is used as catalyst so as to reduce the thermosetting temperature and the influence of these peroxides on surface roughness is analysed.

In order to be used for high temperature application it is desirable to study mechanical and structural properties along with the constituents. Study of mechanical and structural properties revealed the dependency of these properties on fabrication temperature to a large extent. SiCN is pyrolysed and heated to temperature as high as 1200°C and is annealed up to 1500°C. X-ray diffraction and scanning electron microscopy are used analyse the constituents and the grain size, respectively.

Fabrication of thin and thick films of SiCN is possible in the rectangular and circular shapes. The possibility of sensor configuration has to be addressed. The following chapter address the configuration of the sensitive element.

Chapter 3 : Static and Dynamic Pressure Measurement Using Diaphragms

3.1. Introduction

Instruments measure a parameter by converting the measurand into a readable form. This transduction is done by a sensing element. The measurand in an instrument makes its first contact with the primary sensing element. This Primary sensing element produces sufficiently large strain or displacement from pressure signal. Different varieties of configurations of primary sensing element, which is usually a mechanical structure such as bellows, bourdon tube or diaphragm, are available for different measurands. The deflection created by the primary sensing element has to be converted to an equivalent electrical or other type of useful signal. The following section presents and discusses different possible ways of measuring pressure by transduction of deflection / strain.

3.2. Pressure sensing by electrical transduction

Measurement of strain could be performed by measuring change in resistance and change in capacitance. Resistance gauges measure strain by measuring the change in resistance. When used in high temperature environments, these resistance gauges require thermal compensation as temperature also influences the change in resistance. This temperature compensation is carried out on the range of temperature for which the sensor is designed to operate. Even with thermal compensation resistance strain gauges are restricted to 675°C and in case of prolonged use the upper limit should be limited to 315°C [136]. Most of strain gauges are made up of alloys of platinum, gold or chromium

which when exposed to higher temperature has to face problems such as variation of resistance with temperature and scale formation at higher temperatures. Metallurgical stability and oxidation are prominent and critical issues in resistance gauges and hence the use of this type of gauges is strictly not recommended at high temperature environment [136].

Capacitance strain gauge measures strain by accurate detection of the distance between gauge points which is mechanically related to the spacing or area between two plates. Capacitance type of strain measurement is more capable of dealing with high temperature upto 593°C and if equipped with water cooling system it could operate up to 1093°C [137]. The advantage of using capacitance strain measurement consists of the fact that the device is more stable at higher temperatures than resistance strain gauges, however, capacitance based measurement is not completely immune to the influence of temperature [138]. Capacitive pressure sensors measure capacitance in the range of 0.1 - 30 pf with a resolution in the order of 1 fF [139]. Small capacitance changes are more difficult to measure than small resistance changes, as small capacitance measurement requires the use of charge amplifier [136] and or special circuitry [140]. Further the small capacitance value cannot accommodate any transmission loss due to the stray capacitance in the wires. Hence the associated circuitry for small capacitance measurement should be close to the sensor to avoid unnecessary loss. Proximity of associated circuitry to sensor implies exposure to high temperature for certain applications which would impede the use of these sensors.

Microwave based sensors have been suggested by Woike et al. to measure tip clearance as they can operate at high temperature [141]. Microwaves used in tip clearance

measurement systems are phase based as in few radar systems [142]. In phase based system a high frequency electromagnetic wave is generated by a source that is reflected off a target and the echo is collected back by the receiver. The reflected signal is compared with an internal reference signal and change in phase corresponds to the change in displacement of the target. Microwave-based sensors are designed to operate in temperatures up to 900°C with a resolution of about 5 μm and bandwidth up to 25 MHz. However, there is a need for associated electronics capable of operating at high temperatures. The sensor can effectively operate in dirty environments and has the ability to "see" through oil, combustion products, and other common contaminants [143]. The same type of sensing scheme could be also used to measure deflection caused by pressure.

3.3. Pressure sensing by optical transduction

Pressure measurement is also performed by optical means using pressure sensitive paints (PSP). PSP technique has gained attention from the aerospace community and is also used to measure instantaneous pressure field of models in wind tunnel [144]. The principle used is that oxygen in the air flow around the surface quenches the luminescence from an oxygen sensitive dye in the paint, and by imaging the illuminated surface with a CCD camera, the oxygen concentration profile and hence the static pressure profile is mapped [145]. The oxygen sensitive dyes used in PSPs are sensitive to temperature as well. This temperature dependency arises from both the temperature sensitivity of dye luminescence and the oxygen diffusivity of the binder [146]. Pressure measurement in an environment with temperature requires compensation. Comparison of

acquired intensity with calibrated intensity patterns for known temperature and pressure conditions could provide pressure details but this needs the measurement of temperature. Temperature compensation of PSP uses binary paints that utilize two components where one would be sensitive to temperature and pressure while the other would be insensitive to pressure but would nullify the temperature insensitivity of the other component. However, these binary paints could only minimize the impact of temperature over a very small range between 5^0C to 45^0C [147]. PSPs are widely tested in the range of -3^0C to 24^0C due to higher sensitivity at higher temperature [148]. Even temperature sensitive paints are used in the range of -196^0C to 200^0C with an accuracy of 0.2^0C to 0.8^0C [149]

Even though PSP have an advantage in terms of producing static pressure patterns without using pressure probes it poses problem in terms of temperature sensitivity and inability to measure pressure at temperatures even at around 100^0C. In addition PSPs cannot be used to measure dynamic pressure or pressure variation with time as it gives instantaneous pressure. PSPs provide visual output that cannot be reproduced or used as an input for control purposes.

There are methods to measure strain using optical technique. Optical method gained importance due to issues associated with electrical strain gauges such as i) limited temperature range, ii) susceptibility to electromagnetic interference iii) long term durability. Fibre optic sensors provide improvements in terms of electromagnetic interference and it has been demonstrated in labs for high temperature operation and long term durability [150]. Fibre optic based sensors are also used for structural monitoring by measuring the strain using an embedded fibre optic cable [151,152,153]. Normally embedding a fibre optic cable creates fabrication complexity at the micro scale level as

photolithography is the core fabrication process of making micro sensor. Both packaging and signal modulation raise significant problems that rarely make the optical detection as the method of choice for strain measurement.

On the contrary, measurement of pressure through deflection seems to be a convincing idea as sapphire based fibre optic cables and microwave sensors can measure deflection at high temperatures in the range of 900°C. Furthermore deflection measurement unlike strain measurement by resistance is not affected by temperature and hence it would be a better method to quantify pressure. Using fibre optic sensors, even though is a good approach to measure deflection and / or strain, has some other issues associated with the availability of optical interface in Full Authority Digital Engine Controller (FADEC) which is the only decision making block with regards to today's gas turbine engine[154].

3.4. Sensitive element configurations

While the primary transduction results in deflection proportional to pressure the next task would be to choose the configuration of the primary detection element.

Pressure sensing element is exposed to contaminants when expected to function in gas/air flow path. The air intake in the compressor is prone to dust particles and the incomplete combustion of aviation fuel in engine forms carbon deposits on the walls [155]. The dust particles would cause erosion and forced random vibration by collision of dust / suspended particles on the sensitive element if proper protective measures to isolate sensitive element are not taken. Furthermore carbon deposits would change the geometric and structural properties of the sensitive element. In addition use of optical sensing

requires a reflecting surface and carbon deposits impede reflection. High temperature corrosive attack of ash constituent is in a different category than pure deposits [156]. Smoking and carbon deposits could be reduced by the use of additives like barium, manganese, iron or copper [155]. These carbon deposits along with the high temperature and flow conditions prevailing in the gas flow path demands design of new sensors rugged enough to withstand these difficult conditions over an extended period of time [157].

3.4.1 Micro bellows / bourdon tube as sensitive element configuration

Micro bellows and micro bourdon tubes are not popular for use in pressure sensors as it is more difficult to make such a micro devices with high resolution using 2D based micro fabrication processes [158]. Micro bellows are seen more as successful actuators than as sensing elements due to its large achievable deflection and they do not require moving parts [159]. Bourdon tube behaves in a geometrically non linear manner and hence it is difficult to solve the non linear model. Only approximate mathematical models have been developed for bourdon tubes that use circular and elliptical cross sections [159]. Micro bellows also require rims of additional materials at the joints of two layers to resist stress concentration and this adds up the intricacy of fabrication [160]. Hysteresis effects and non linear deflection are more prominent in bellows and bourdon tube configuration due to the fact that the deflection caused by pressure is higher in these configurations. Hysteresis study on macro steel bellows indicated strain hardening of the bellows on prolonged use and it is also reported that there is a variation in axial spring rate in the range of 2000 N/mm to 3000 N/mm [161].

3.4.2 Diaphragm as sensitive element configuration

Micro pressure sensors use diaphragm or cantilever configuration as they are easy to fabricate and readily compatible with micro fabrication technologies. Diaphragms and cantilever configurations are desired for sensing applications due to the following reasons

- High design flexibility and ease of micro fabrication
- No special arrangement needed to compensate for stress concentration as in the case of micro bellows
- More suitable for prolonged use
- Accurately defined mathematical model for linear deflection.

Diaphragm is the most popular configuration for pressure sensing due to the advantages in fabrication and by its simple configuration. Deflection of diaphragm is the measure of pressure and this dependency is desired to be linear. Diaphragm allows measuring pressure by either accommodating pressure to be measured on one side and vacuum or a reference pressure or vented to atmosphere on another side.

The pressure diaphragm is mostly circular or rectangular in shape. Pressure sensors fabricated with bulk micromachining methods that use anisotropic etching are normally rectangular / square in shape. Circular diaphragms have advantages over square or rectangular diaphragms due to the absence of stress concentration at the corners [162]. Figure 3.1 shows the loading scheme most commonly experienced by the diaphragm based pressure sensor. The pressure to be measured is placed on one face and other face is vented to the atmosphere or kept in atmospheric pressure or a known reference pressure conditions.

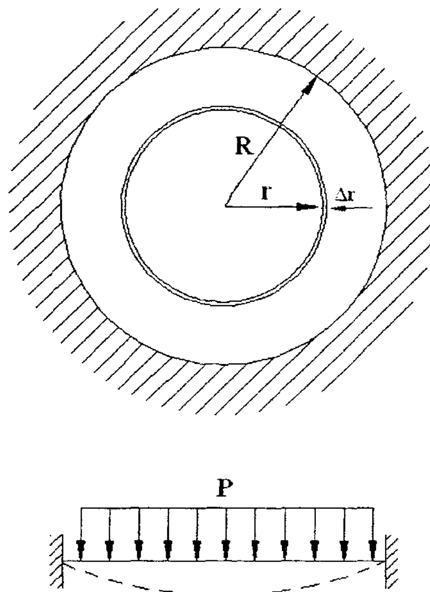

Figure 3.1: Uniform pressure loading model on a fixed diaphragm

3.5. Static and dynamic analysis of diaphragm subjected to pressure loading

The analysis below will focus mostly on diaphragm deflection under static and dynamic pressure. Static analysis is performed to evaluate deflection sensitivity and dynamic analysis provides frequency response, these are the most important parameters that have to be considered.

Deflection sensitivity is the ratio of deflection to load. It gives the displacement of the diaphragm produced by unit load. The overall sensitivity of a sensor would be determined by deflection sensitivity, and the resolution of the deflection measurement technique. The high sensitivity of a sensitive element will hint towards a limited measurement range but with a higher resolution.

Frequency response is the response of the transducer to a sine wave of different frequencies applied to it. Most of the instrumentation systems are subjected to a time

varying signal of a complex nature, where these complex waveforms could be composed using different sinusoidal signals of different amplitudes and frequencies. High frequency response is highly desirable when measurement has to be done on a rapidly varying input. In case of low frequency response the transducer can no longer respond as rapidly as its input if it changes very rapidly (which is defined by the application). This would result in loss of information.

The sensing element in the form of circular plate is found in many applications including the sensing application. Therefore it is interesting to study the bending of circular plate.

The governing differential equation for deflection of circular plate, subjected to a static pressure P, in polar co-ordinates is given by

$$\nabla^4 y = \left(\frac{\partial^2}{\partial r^2} + \frac{1}{r}\frac{\partial}{\partial r} + \frac{1}{r^2}\frac{\partial^2}{\partial \theta^2}\right)\left(\frac{\partial^2 y}{\partial r^2} + \frac{1}{r}\frac{\partial y}{\partial r} + \frac{1}{r^2}\frac{\partial^2 y}{\partial \theta^2}\right) = \frac{P}{D} \quad (3.1)$$

D – Flexural rigidity

The deformation is independent of the angular co-ordinates only when the boundary conditions, material properties, and loading are also axisymmetric. Considering axisymmetric bending wherein the deflection of the plate will depend upon radial position r only, the differential equation of the surface deflection reduces to

$$\nabla^4 y = \left(\frac{\partial^2}{\partial r^2} + \frac{1}{r}\frac{\partial}{\partial r}\right)\left(\frac{\partial^2 y}{\partial r^2} + \frac{1}{r}\frac{\partial y}{\partial r}\right) = \frac{P}{D} \quad (3.2)$$

The complete solution of equation 3.2 for the solid circular plate subjected to an axisymmetric distributed load is given by $y = C_3 r^2 + C_4 + \frac{wr^4}{64D}$

Applying boundary conditions for clamped edges, the linear deflection of the diaphragm loaded by transverse pressure P is given by [163].

$$Y_r = \frac{3P(1-\mu^2)}{16Eh^3}\left(R^2 - r^2\right)^2 \tag{3.3}$$

The tangential and radial stress involved is discussed in the forth-coming section.

In equation 3.3, Y_r is the deflection of the diaphragm at radial distance (m)

P is the pressure (Pa)

μ is the Poisson ratio = 0.17 for SiCN

E is the Young's modulus = 158 GPa for SiCN

h is the thickness (m)

R is the radius of diaphragm (m)

r is the radial distance from the center (m)

Most of the sensor applications target the maximum deflection of the diaphragm, which occurs at the center. The maximum deflection of the diaphragm at the center is given by

$$Y_{Center} = \frac{3P(1-\mu^2)R^4}{16Eh^3} \tag{3.4}$$

The restrictive assumptions made to deduce equation 3.3 include

- The diaphragm is flat and is of uniform thickness
- The material is isotropic and homogenous
- Maximum deflection is not more than 30 % of the thickness
- All forces, pressures and loads are applied normal to the plane of the diaphragm
- The diaphragm is operated within elastic limit
- The diaphragm is not too thick, (thickness $\leq$ 20% of the diameter)
- The deflection is mostly due to bending

The deflection pattern for a circular diaphragm clamped along the contour is illustrated in figure 3.2

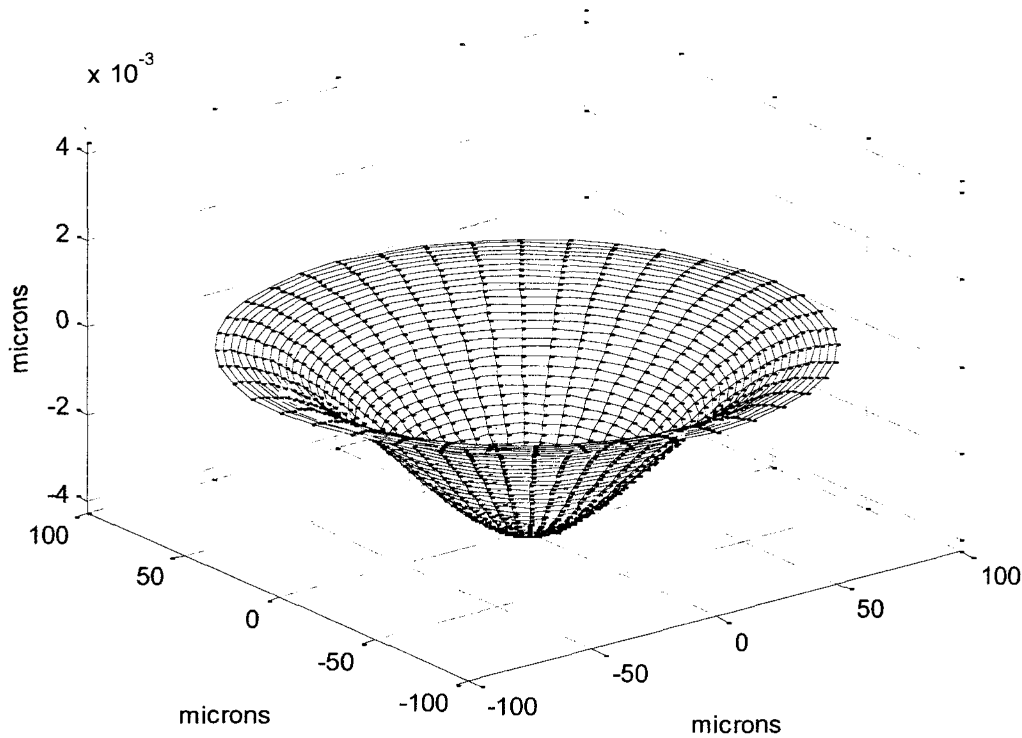

Figure 3.2: Deflection curve of a diaphragm under pressure

Deflection curve under pressure is given by

$$Y_r = \frac{3P(1-\mu^2)}{16Eh^3} R^4 \left[1-\left(\frac{r}{R}\right)^2\right]^2 = Y_{Center}\left[1-\left(\frac{r}{R}\right)^2\right]^2 \quad (3.5)$$

The above equations are based on restrictive assumption that the maximum deflection is no more than 30 % of the thickness of the diaphragm [163], i.e. $Y_{Center} \leq 0.3 * thickness$.

The diameter of the diaphragm is defined by the application and the size that enables the installation within the packaging space. Now with the knowledge of the diaphragm's diameter, the thickness could be expressed (using equation 3.4) as

$$h = R\left[\frac{3P(1-\mu^2)}{4.8 * E}\right]^{1/4} \quad (3.6)$$

Equation 3.6 expresses the correlation between the thickness and the maximum pressure to ensure a safe deflection of the membrane. The deflection is limited not to exceed 30 % of thickness to avoid non linearity. Figure 3.3 shows the relationship between thickness of a diaphragm and radius with respect to pressure and could be used to choose the required thickness based pressure to be measured and the diaphragm radius.

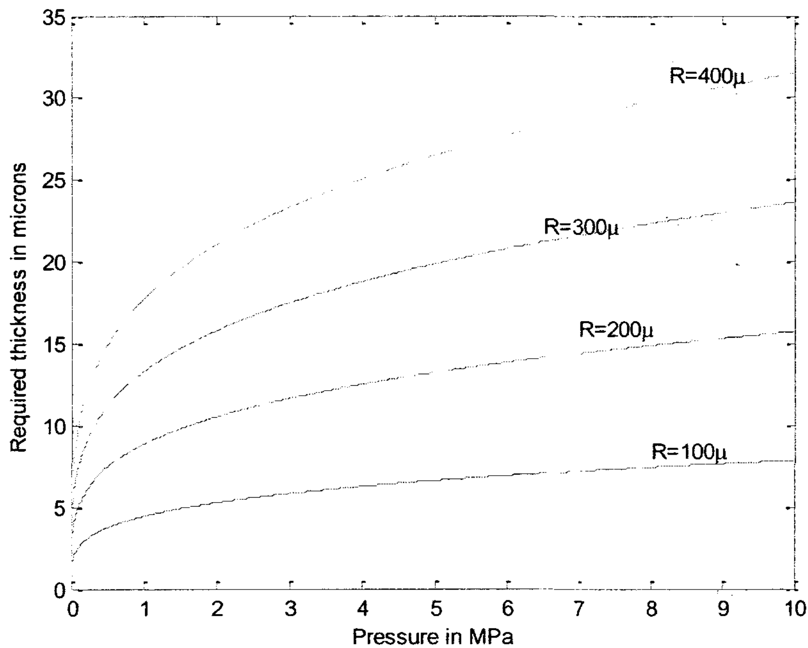

Figure 3.3: Thickness vs pressure for specific radius for SiCN diaphragm

Diaphragms capable of linear deflection are needed in many pressure sensors. In order to obtain high sensitivity the thickness of the diaphragm should be as small as possible to maximize the load – deflection responses. But at the same time thin diaphragms subjected to normalised high pressure may yield large deflections and non linear deflection might result in plastic deformation. The relationship between pressure sensitivity based on the deflection at the center of the diaphragm and the thickness for different radius is as shown in figure 3.4.

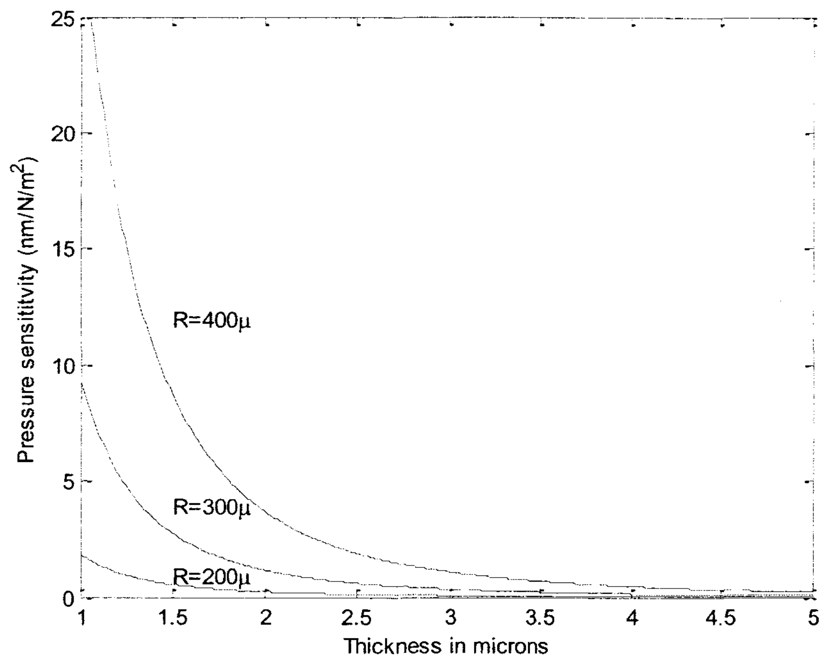

Figure 3.4: Theoretical sensitivity for different radius for SICN diaphragm

3.6. Stress analysis

Diaphragms experience stresses due to the bending that increases linearly over the thickness of the diaphragm to the outer surface where they reach their maximum values. At small deflections there are no stresses in the mid plane of the diaphragm, however the stresses increase linearly over the thickness of the diaphragm to the outer surfaces where they reach their maximum value. The diaphragm when exposed to pressure is bent in the shape of a double curve and the stress analysis should take into account the radial and tangential stresses. The maximum value for radial stress is at the edge of the diaphragm and the maximum value of tangential stress is at the center of the diaphragm whose value is equal to the radial stress at that point [163]. The variation of tangential and radial stress along the radius of the diaphragm for an applied pressure of 10 MPa is depicted in figure 3.5

The radial stress σ_r at any distance r from the center may be obtained as [163]

$$\sigma_r = \pm \frac{E*z}{(1-\mu^2)} \left[\frac{d^2y}{dr^2} + \frac{\mu}{r}\frac{dy}{dr} \right] \tag{3.7}$$

where z is the distance from neutral axis considering $z = \frac{h}{2}$. Using equation 3.3

$$\sigma_r = \pm \frac{3PR^2}{8*h^2} \left[(3+\mu)\frac{r^2}{R^2} - (1+\mu) \right] \tag{3.8}$$

The maximum radial stress is at the edge of the diaphragm

$$\sigma_r = \pm \frac{3PR^2}{4*h^2} \tag{3.9}$$

The tangential stress σ_t at any radial distance r may be calculated from the expression

$$\sigma_t = \pm \frac{E*z}{(1-\mu^2)} \left[\frac{1}{r}\frac{dy}{dr} + \mu \frac{d^2y}{d^2r} \right] \tag{3.10}$$

where z – distance from neutral axis considering $z = \frac{h}{2}$. Using equation 3.3

$$\sigma_t = \pm \frac{3PR^2}{8*h^2} \left[(3\mu+1)\frac{r^2}{R^2} - (1+\mu) \right] \tag{3.11}$$

The maximum tangential stress $\sigma_{t\max}$ is at the center where r=0

$$\sigma_t = \pm \frac{3PR^2}{8*h^2} \left[(1+\mu) \right] \tag{3.12}$$

In order to operate within linear range, the pressure must be limited to (from equation 3.6)

$$P = \frac{16*0.3Eh^4}{3*R^4\left[(1-\mu^2) \right]} \tag{3.13}$$

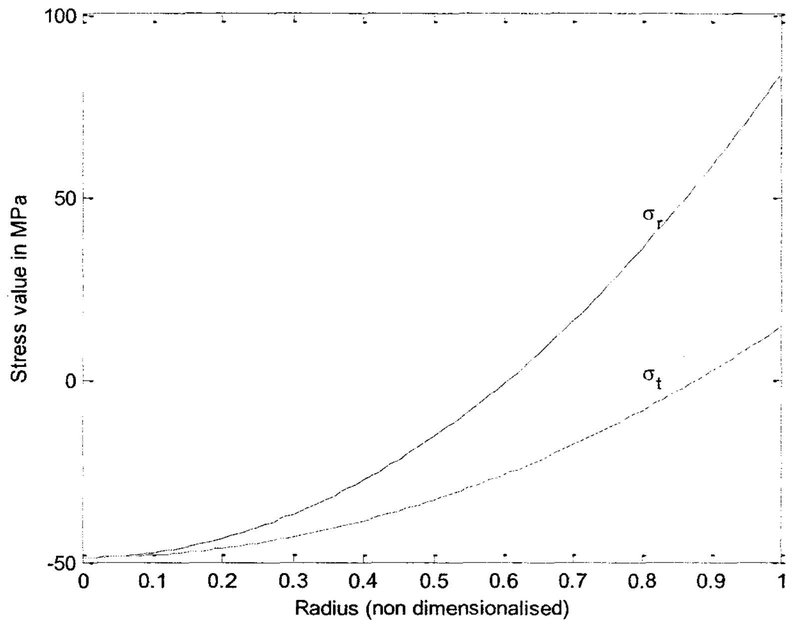

Figure 3.5: Radial and tangential stresses for SiCN diaphragm

Since the maximum pressure would be known, the stress at the linear limit could be calculated by using the pressure at linear limit and is given by

$$\sigma_t = \pm\frac{16*0.3Eh^2}{8*R^2*(1-\mu^2)}\left[(3\mu+1)\frac{r^2}{R^2}-(1+\mu)\right] \quad (3.14)$$

$$\sigma_r = \pm\frac{16*0.3Eh^2}{8*R^2*(1-\mu^2)}\left[(3+\mu)\frac{r^2}{R^2}-(1+\mu)\right] \quad (3.15)$$

3.7. Frequency response

For the purpose of dynamic pressure measurement, resonant frequency is also an important parameter. It is therefore important to characterize the relationships among diaphragm thickness, diameter, and resonant frequency in order to establish design guidelines for diaphragm based dynamic pressure sensor [69].

Frequency response and high frequency cut-off are the two specifications that describe the response of a transducer to a variable frequency sine wave input applied to it. At low frequencies a sine wave input yields a sine wave output. As the frequency of the sine wave input increases, the transducer is expected to respond faster and faster. Beyond a particular frequency the transducer can no longer respond as rapidly as its varying sinusoidal input. This creates a phase shift between input and output and the output of the transducer falls. This roll off of amplitude with an increase in input frequency describes the frequency response. The cut off frequency indicates the lowest or highest frequency of stimulus that the sensor can process. The upper cut-off frequency shows how fast the sensor reacts. The lower cut off frequency shows how slow the sensor can process changing stimuli. At lower frequency the concern is not only response but also noise which could be considerably higher than the signal.

However frequency response is provided by two different parameters in a pressure sensor. First parameter is the dynamic response due to inertia of the moving mass that could be evaluated on a lumped mass model. The second parameter which reduces the frequency response is the fluid flow itself.

Considering a diaphragm of uniform thickness fixed at its periphery and considering the deflection is symmetric about the center the maximum potential energy and maximum kinetic energy of the diaphragm are [69]

$$U = \pi D \int_0^R \left(\frac{\partial^2 Z}{\partial r^2} + \frac{1}{r} \frac{\partial Z}{\partial r} \right)^2 r dr \qquad (3.16)$$

$$T = \pi \rho h \omega^2 \int_0^R Z^2 r dr \qquad (3.17)$$

Considering a deflection function Z in terms of r (as deflection is symmetric no θ term is involved) that would satisfy the boundary conditions for a diaphragm fixed at the periphery. Taking deflection function as a series (Rayleigh Ritz method),

$$Z = a_1\left(1-\frac{r^2}{R^2}\right)^2 + a_2\left(1-\frac{r^2}{R^2}\right)^3 \tag{3.18}$$

and applying this in the Rayleigh Ritz method, with $T_{max} = \omega^2 T_{max}^{\ *}$ we get

$$\frac{\partial U_{max}}{\partial a_i} - \omega^2 \frac{\partial T_{max}^{\ *}}{\partial a_i} = 0 \tag{3.19}$$

$$\frac{\partial}{\partial a_i}\int_0^R \left\{\left(\frac{\partial^2 Z}{\partial r^2} + \frac{1}{r}\frac{\partial Z}{\partial r}\right)^2 - \frac{\rho h \omega^2}{D} Z^2\right\} r dr = 0 \tag{3.20}$$

Substituting equation 3.18 in equation 3.20, we get

$$\omega_n = \frac{\alpha}{R^2}\left[\left(\frac{g * D}{h * w}\right)\right]^{1/2} \tag{3.21}$$

where

α is the constant related to vibrating modes of diaphragm α = 10.21 first mode

ω is the frequency

g is the gravitational constant

D is the flexural rigidity $= \dfrac{E * h^3}{12(1-\mu^2)}$

E is the Young's modulus

h is the thickness

R is the radius of diaphragm

w is the specific weight of the material

Natural frequency is an important characteristic that evaluates the performance of the sensor under dynamic conditions. In order to faithfully respond to the dynamic pressures, the natural frequency of the sensor should be kept well above the highest frequency to be measured.

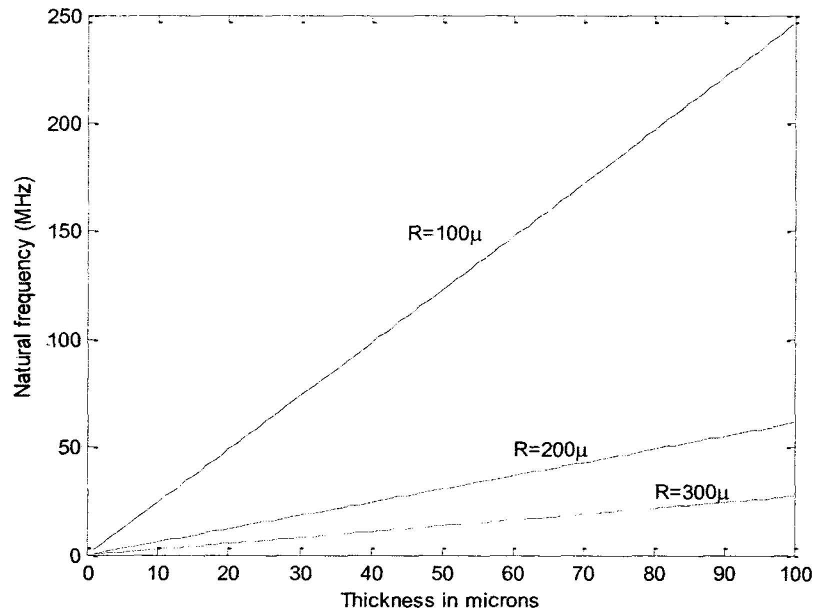

Figure 3.6: Theoretical natural frequency for SiCN diaphragm

Generally the operating frequency range of these sensors should be kept less than 60 % of the natural frequency of the sensing element [164]. Figure 3.6 shows the variation of the natural frequency of the membrane only, in relation with the thickness for different radii. Smaller the radius higher will be the natural frequency.

Diaphragm is normally used to measure static pressure due to the fact that measurement of static pressure requires pressure on both sides of the diaphragm. The pressure on one side is the reference and the other side is the measured pressure. Sealed diaphragm provides this feature by virtue of its configuration.

In the case of dynamic pressure sensing, annular diaphragms is one of the options as it allows the flow of fluid through the annulus. Sensitivity comes as a major issue for this type of sensors.

3.8. Annular diaphragms for pressure measurement

Flat circular diaphragms exhibit lower sensitivity at low pressure application. At low pressure sensitivity has to be increased either by increasing the radius or by decreasing the thickness. However both these approaches would enable non linearity creep in if the maximum deflection exceeds 0.3 times the thickness of the diaphragm. In order to improve sensitivity and linearity simultaneously particular geometries in diaphragm such as diaphragms with rigid center or boss are introduced in sensing applications [165,166].

Sensitivity issue was the motivation for the use of bossed diaphragm for low differential pressure. Higher sensitivity could be achieved at no compromise in the capability of the structure to undertake load. Annular diaphragm with center boss supported by quadruple beams to measure low dynamic pressure in the range of 500-2000 Pa with a resolution of 0.01 Pa is proposed by Tilmans et.al [167]. Pre-stressed annular plate with a rigid boss is used as an approach to deal with excessive deflection [168]. Pre-tension tends to stiffen the plate and thereby plays an important role in determining deflection. Large pre-tension increases the plate stiffness which yields in increase of the load bearing capability, but this ability comes by trading off the sensitivity. The natural frequency of the annular diaphragm can be designed based on the

above specified requirement but the response would be greatly diminished by the interaction of the fluid flow.

Annular diaphragm for use in a down hole pressure transducer for oilfield application is reported in oil wells [169]. The frequency of pressure wave pulses for such applications that the sensor is exposed to is in the range of 0.1 Hz to 30 Hz and the transducer only needs to sense dynamic pressure changes of relatively small amplitude [169]. The natural response of the annular diaphragm is a key parameter in case it has to be used for high frequency pressure change applications.

Aerospace applications mostly require dynamic pressure measurement at very high frequency. If the dynamic pressure has to be measured on the clearance between blade and the shroud, the frequency will be approximately 17.6 kHz for a compressor with 23 blades rotating at 46,000 rpm. Even though it is possible to design an annular diaphragm to a natural frequency higher than 17.6 kHz, the response of the sensor is limited by the natural response of the system in conjunction with air flow. This is the reason that the annular diaphragm based sensor reported by Atkinson et.al [169] is suggested for an application that requires a very low frequency response of 0.1 to 30 Hz. The frequency response of an annular diaphragm in conjunction with air flow could be significantly improved by increasing the diameter of the annulus in the diaphragm. But this could be achieved at the cost of significant reduction in sensitivity.

The frequency response is given by the membrane as well as the inertia of the gas flow through the annulus in the diaphragm from high to low pressure. The annular diaphragm with different pressures on either side could be considered as a pressurized tank that discharges through a flow restriction which has the behaviour of a fluid

resistance. This system could be modelled through analogy as electrical system where the pressurized tank is the charged capacitor that is discharging through a resistor.

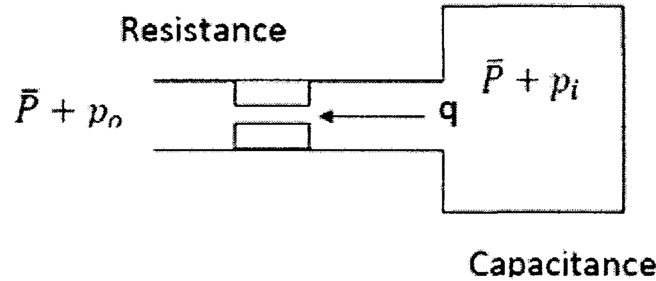

Figure 3.7: Electrical analogy with capacitance and resistance

Consider the pressure system as shown in figure 3.7, where the gas flow through the restrictor is a function of pressure difference P_i-P_o. Considering the temperature being constant and the absolute pressure $\overline{P}$ is high compared to P_i and P_o such a system could be characterized in terms of resistance and capacitance.

The fluid flow resistance is defined as the ratio of change in gas pressure difference to the change in fluid flow rate. Considering small values of pressure difference, the resistance may be assumed as constant [170]

$$R_p = \frac{P_i - P_o}{q} \tag{3.22}$$

When a specific mass of gas is stored in a vessel there is a well established relationship between the volume of the gas, pressure and temperature of the fluid. If the tangent to pressure versus volume curve is drawn at some point, then the reciprocal of the slope is defined to be the hydraulic capacitance [170].

$$\text{Fluid capacitance} = \frac{dv}{dp} \tag{3.23}$$

The gas removed from the chamber during an infinitesimal time dt is equal to infinitesimal variation of pressure dp times the capacitance.

$$C * dp_0 = q * dt \text{ or } C\frac{dp_0}{dt} = \frac{P_i - P_o}{R_p} \tag{3.24}$$

where q - is the flow .

Equation 3.24 can be written as

$$R_p C\frac{dp_o}{dt} + P_o = P_i \tag{3.25}$$

Considering P_i and P_o as input and output respectively then the transfer function of the system is

$$H(s) = \frac{P_o(s)}{P_i(s)} = \frac{1}{1 + R_p Cs} \tag{3.26}$$

The inertial effect of the travelling fluid due to the reduced amount of flow is ignored making this a first order system. Comparing equation 3.26 with the standard equation for first order system, $\frac{\Delta P_0(s)}{\Delta P_i(s)} = \frac{1}{1+s\tau}$ where the time constant τ, which is a measure of system's speed of response is the product of fluidic resistance and capacitance.

3.9. Pneumatic capacitance

The compressibility of air makes the analysis far more complex than its hydraulic counterparts. The essential difference between the pneumatic system and hydraulic system is that gases possess high compressibility and hence change in small volume of gas results in change in pressure without any change in the volume of the chamber. The

capacitance can be defined as the change in mass of air in the vessel required to make a unit change in pressure.

$$C = \frac{dm}{dP} = V\frac{d\rho}{dP} \quad (3.27)$$

where m is the mass of air (Kg)

V is the volume of chamber (m^3)

P is the absolute pressure of air (N/m^2)

ρ is the mass density of gas (Kg / m^3)

If the expansion process is expressed as polytropic process then

$$\frac{P}{\rho^n} = P\rho^{-n} \text{ constant} \quad (3.28)$$

From equation 3.28 $\frac{d\rho}{dP} = \frac{\rho}{nP}$ (3.29)

where n is the polytropic index n=1 to 1.2

Pneumatic capacitance $C = \frac{\rho * V}{n * P} = \frac{V}{n * P/\rho} = \frac{V}{n * R_{air} * T}$ (3.30)

3.9.1 Pneumatic resistance

As the fluid flows through a pipe, a valve or an orifice, there is a drop in the pressure of the fluid. The change in pressure associated with flowing fluid results from the dissipation of energy and obeys a non linear relationship between the flow rate q and the pressure difference Δp. Hydraulic resistance which was modeled as a linear resistance becomes non linear with a compressible gas flowing through it [171].

$$q = k\sqrt{\Delta p} \quad (3.31)$$

where k is the conductance factor.

Considering a steady flow of perfect gas through an orifice as shown in figure 3.8, the cross section 1 is the upstream of the flow, the cross section 2 is at the "vena contracta" where the jet area is minimum. The cross sectional area of "vena contracta" is smaller than the cross sectional area of the orifice. The ratio of $A_2/A_o = C_c$, where C_c - coefficient of contraction.

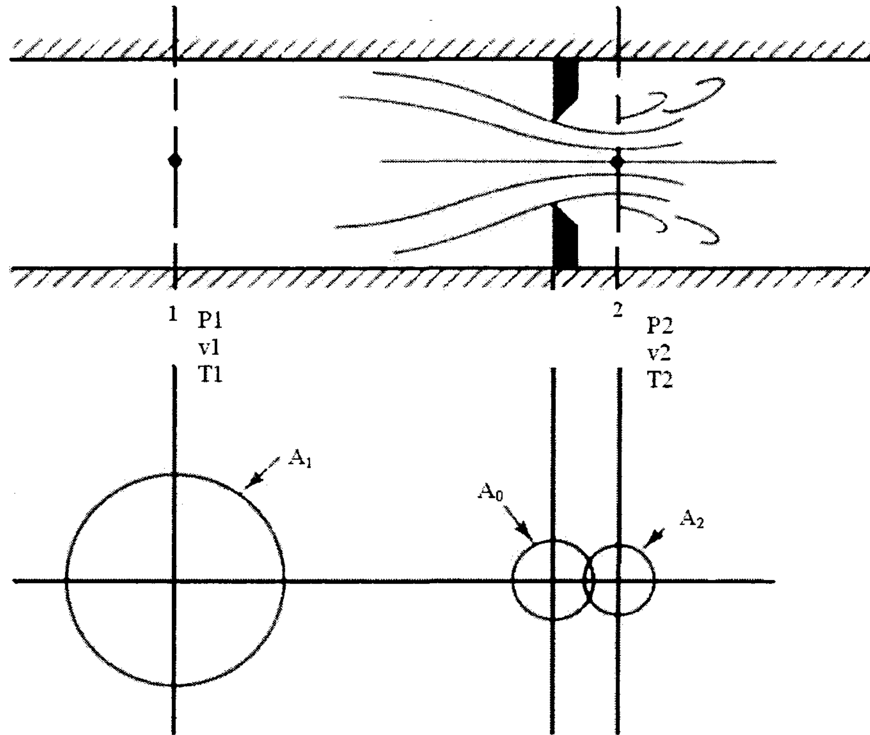

Figure 3.8: Flow through an orifice [172]

Let P_1, v_1, T_1 and P_2, v_2, T_2 be the pressure, velocity and temperature at section 1 and section 2, respectively. Considering the flow to be isentropic and it could be written $P_1 w_1^{\gamma} = P_2 w_2^{\gamma} =$ constant where γ is adiabatic index w_1 and w_2 are specific volume and which can be expressed as $w = \frac{1}{\rho}$.

$$P_1 = \rho_1^{\gamma} P_2 \rho_2^{-\gamma} \tag{3.32}$$

The equation of motion for steady flow considering constant temperature, single phase, steady and frictionless flow is

$$v dv + \frac{dP}{\rho} + g dz = 0 \tag{3.33}$$

Neglecting elevation change equation 3.33 becomes

$$v dv + \frac{dP}{\rho} = 0 \tag{3.34}$$

Differentiating equation 3.32 with respect to ρ_1 and noting that $P_2 \rho_2^{-\gamma}$ = constant, results in

$$dP_1 = \gamma \rho_1^{\gamma-1} d\rho_1 P_2 \rho_2^{-\gamma} \tag{3.35}$$

Substituting equation 3.35 in $\left(v_1 dv_1 + \frac{dP_1}{\rho_1} = 0 \right)$

$$v_1 dv_1 + \gamma \rho_1^{\gamma-2} P_2 \rho_2^{-\gamma} d\rho_1 = 0 \tag{3.36}$$

Integrating equation 3.36 and considering $P_2 \rho_2^{-\gamma} = P_1 \rho_1^{-\gamma}$ constant

$$\frac{v_1^2}{2} + \frac{\gamma}{\gamma-1} \frac{P_1}{\rho_1} = \frac{v_2^2}{2} + \frac{\gamma}{\gamma-1} \frac{P_2}{\rho_2} = \text{constant} \tag{3.37}$$

From continuity equation $\rho_1 A_1 v_1 = \rho_2 A_2 v_2$ which implies

$$v_1 = \frac{\rho_2 A_2 v_2}{\rho_1 A_1} = \left(\frac{P_2}{P_1} \right)^{1/\gamma} \left(\frac{A_2}{A_1} \right) v_2 \tag{3.38}$$

Substituting equation 3.38 in equation 3.37

$$\frac{v_2^2}{2} = \frac{\frac{\gamma}{\gamma-1} \left(\frac{P_1}{\rho_1} - \frac{P_2}{\rho_2} \right)}{1 - \left(\frac{P_2}{P_1} \right)^{2/\gamma} \left(\frac{A_2}{A_1} \right)^2} \tag{3.39}$$

From the figure 3.8 area A_2 is sufficiently smaller than A_1 and $P_2/P_1 < 1$ therefore

$$1-\left(\frac{P_2}{P_1}\right)^{2/\gamma}\left(\frac{A_2}{A_1}\right)^2 \approx 1 \tag{3.40}$$

So equation 3.39 becomes

$$\frac{v_2^2}{2}=\frac{\gamma}{\gamma-1}\left(\frac{P_1}{\rho_1}-\frac{P_2}{\rho_2}\right) \tag{3.41}$$

Substitution of $\rho_2=(P_2/P_1)^{1/\gamma}\rho_1$ in equation 3.41 yields

$$v_2=\sqrt{\frac{2\gamma}{\gamma-1}\frac{P_1}{\rho_1}\left[1-\left(\frac{P_2}{P_1}\right)^{\frac{\gamma-1}{\gamma}}\right]} \tag{3.42}$$

Mass flow rate q= $\rho_2 A_2 v_2$

$$q=\rho_2 A_2\sqrt{\frac{2\gamma}{\gamma-1}\frac{P_1}{\rho_1}\left[1-\left(\frac{P_2}{P_1}\right)^{\frac{\gamma-1}{\gamma}}\right]} \tag{3.43}$$

Substituting $\rho_2=(P_2/P_1)^{1/\gamma}\rho_1$ and $A_2=C_c A_o$

$$q=C_c A_o\sqrt{\frac{2\gamma}{\gamma-1}P_1\rho_1\left[\left(\frac{P_2}{P_1}\right)^{\frac{2}{\gamma}}-\left(\frac{P_2}{P_1}\right)^{\frac{\gamma+1}{\gamma}}\right]} \tag{3.44}$$

Considering coefficient of discharge C_d that would include frictional effect and contraction coefficient C_c and knowing that $\rho_1=\frac{P_1}{RT_1}$ equation 3.44 modifies to

$$q=C_d A_o\sqrt{\frac{2\gamma}{\gamma-1}\frac{P_1^2}{RT_1}\left[\left(\frac{P_2}{P_1}\right)^{\frac{2}{\gamma}}-\left(\frac{P_2}{P_1}\right)^{\frac{\gamma+1}{\gamma}}\right]} \tag{3.45}$$

Multiplying 3.45 by $\sqrt{\frac{P_2(P_1-P_2)}{P_2(P_1-P_2)}}$

$$q = C_d A_o \sqrt{\frac{2\gamma}{\gamma-1} \frac{P_1^2}{RT_1} \frac{P_2(P_1-P_2)}{P_2(P_1-P_2)} \left[\left(\frac{P_2}{P_1}\right)^{\frac{2}{\gamma}} - \left(\frac{P_2}{P_1}\right)^{\frac{\gamma+1}{\gamma}}\right]} \tag{3.46}$$

Considering expansion factor $\xi = \sqrt{\frac{\gamma}{\gamma-1} \frac{P_1^2}{P_2(P_1-P_2)} \left[\left(\frac{P_2}{P_1}\right)^{\frac{2}{\gamma}} - \left(\frac{P_2}{P_1}\right)^{\frac{\gamma+1}{\gamma}}\right]}$ [172] the modified mass flow rate becomes

$$q = C_d A_o \xi \sqrt{\frac{2}{RT_1} P_2 (P_1 - P_2)} \tag{3.47}$$

Referring to figure 3.7 $P_1 = \overline{P} + P_i$ and $P_2 = \overline{P} + P_o$ we have mass flow rate

$$q = C_d A_o \xi \sqrt{\frac{2}{RT_1} (\overline{P} + P_o)(P_i - P_o)} = C_d A_o \xi \sqrt{\frac{2\overline{P}}{RT_1} \left(1 + \frac{P_o}{\overline{P}}\right)(P_i - P_o)} \tag{3.48}$$

As P_o is sufficiently smaller than $\overline{P}$ by approximating $\sqrt{1 + \frac{P_0}{\overline{P}}} \approx 1$. Hence

$$q = C_d A_o \xi \sqrt{\frac{2\overline{P}}{RT_1} (P_i - P_o)} \tag{3.49}$$

Comparing equation 3.49 with the general form $q = k\sqrt{P_i - P_o}$

$$k = C_d A_o \xi \sqrt{\frac{2\overline{P}}{RT_1}} \tag{3.50}$$

Pneumatic resistance can be defined as the change in differential pressure between the upstream and downstream of a flow restricting device required to make a unit change in mass flow rate

$$R_p = \frac{d\Delta P}{dq} \quad (3.51)$$

The mass flow rate is proportional to the square root of the pressure difference. The curve that would relate the flow rate and the pressure difference is depicted in figure 3.9.

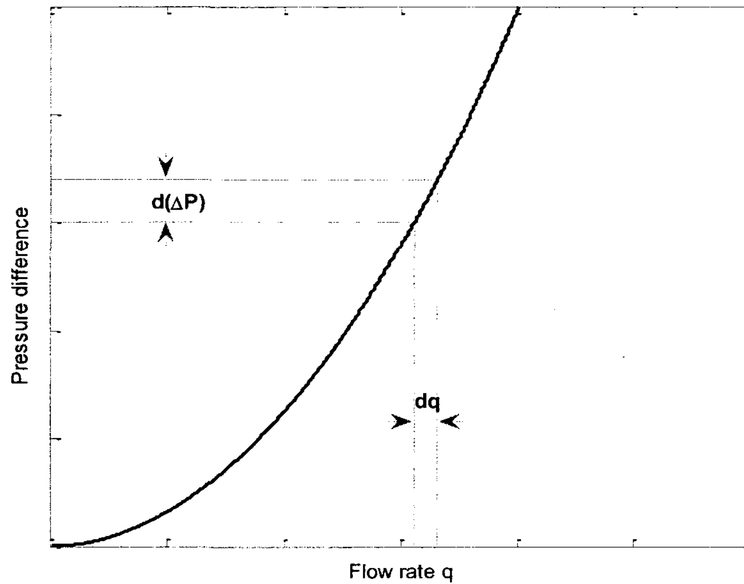

Figure 3.9: Resistance as a slope of pressure difference and mass flow rate

The slope of this curve at an operating point gives the value of pneumatic resistance provided by the orifice. Normally pneumatic resistance offered at an operating point is calculated using a similar graph experimentally obtained.

3.10. Response of the system

Since the main application in the present work is measurement of dynamic pressure in gas turbine engine, a case study is selected that is associated with gas turbine engine. Two types of compressors are used in today's gas turbine engine. They are the axial compressor and the centrifugal compressor. The axial compressor is used primarily in medium and high horsepower applications, while the centrifugal compressor is utilized

in low horsepower applications [4]. Axial compressors used for aerospace applications has a pressure ratio of 1.15 – 1.6 per stage [4].

For calculation purpose, an axial compressor that has a pressure ratio of 1.25 per stage is considered. Considering the inlet pressure to be 14 psi and the required exit pressure is approximately 130 psi. So approximately in 8th stage the pressure difference would be around 16.75 psi. Considering this pressure difference in the model illustrate in figure 3.6, the resistance provided by diaphragms in three different openings is as shown in figure 3.10.

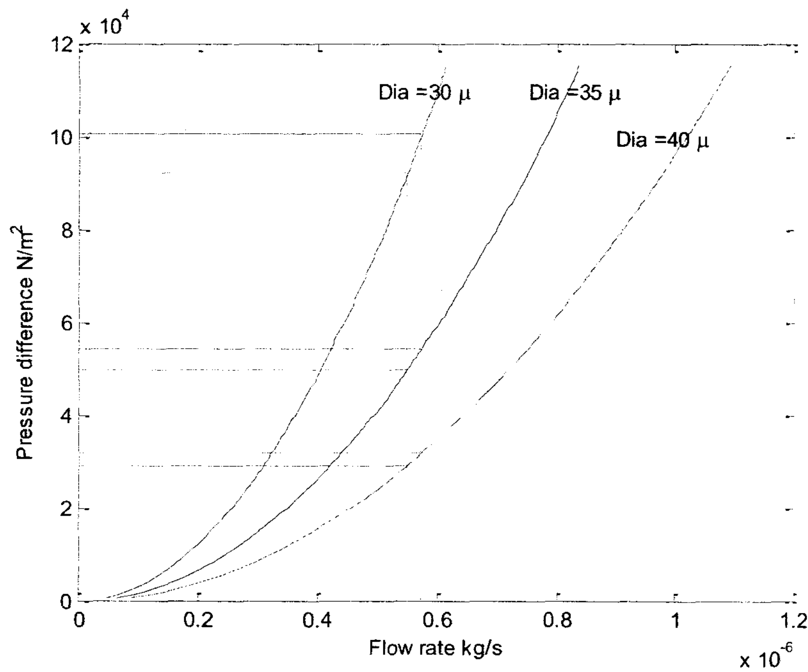

Figure 3.10: Resistance provided by orifices of different diameters

From figure 3.10 it is clear that the pneumatic resistance is higher with decrease in orifice diameter. The resistance values for the orifices with diameters 30 microns, 35 microns and 40 microns are 3.4214 X10^{11} N-s / Kg – m^2, 1.8468 X10^{11} N-s / Kg – m^2 and 1.0825 X10^{11} N-s / Kg – m^2.

Considering the sensor is based on an annular diaphragm configuration, the high pressure compressed air has to flow through the orifice in the diaphragm, also causes deflection of the annular diaphragm. The natural frequency of the structure will be higher at a higher diameter of the orifice on the annular diaphragm for same diameter and thickness of the diaphragm. However, higher diameter of perforation reduces the sensitivity of the diaphragm which cannot be traded off as less sensitivity would engulf valuable pressure data.

Consider an annular diaphragm of diameter 2000 microns with a perforation of 30 microns. The pneumatic resistance offered by the perforation of 30 microns is $3.4214X10^{11}$ N-s / Kg – m^2. A diaphragm of 2000 microns with a finite volume (volume is formed by the wall of the shroud as the sensing element will be housed within the shroud) at its back, considering a gap of 1 mm, the total volume formed by the diaphragm will be $\pi*\left(1X10^{-3}\right)^2*1X10^{-3}=3.14X10^{-09}m^3$. When the blade crosses above the sensing unit, the sensing unit is loaded and the volume behind the sensing unit is filled with compressed air. This causes a deflection of the diaphragm and it tends to regain its flat position by attaining equilibrium. It is mandatory that pressure equilibrium is attained before the increase of pressure caused by the passing of the next blade. It is impossible to allow all the flow in the clearance to pass through the orifice in the annular diaphragm, also a situation like this (a vibrating diaphragm with a back volume) requires a large back volume for better sensitivity [173]. Considering the volume if $3.14X10^{-09}$ m^3, the pneumatic capacitance by substituting $R_{air}=287$ N-m / Kg K, and considering temperature 273 K and n =1 equation 3.30 yields

$$C = \frac{3.14X10^{-9}}{1*287*273} = 4.0076X10^{-14}\text{kg-m}^2/\text{N} \quad (3.52)$$

Considering the resistance value 3.4214X10^{11} N-s / Kg – m^2 the time constant is 0.0137 seconds, which corresponds to a frequency of 72.9 Hz. In actual case the frequency would be little higher as the volume that actually participates in the fluid exchange will be a fraction of the total volume. Taking the inverse Laplace transforms of equation 3.26 the pressure

$$\frac{P_o(t)}{P_i(t)} = L^{-1}\left(\frac{1}{s+\frac{1}{\tau}}\right) = e^{-t/\tau} \quad (3.53)$$

The resulting graph would be an exponentially decaying graph. With the knowledge of the pneumatic capacitance and resistance, time constant can be found, which would give the response of the system. If the discharge characteristic curve is found experimentally, the time constant can be found out from the time taken by the response to fall approximately 63% of the initial value.

By calculating the slope at a point where the response becomes one third of the initial pressure, we get the time response of the system to be 0.013707 seconds. In case of an annular diaphragm being used for dynamic pressure sensor the frequency response of the system is the lowest frequency between the natural frequency of the annular diaphragm and the frequency corresponding to the time constant of the first order system that is generated by the flow of air through the orifice. The natural frequency of the diaphragm could be made much higher than the frequency corresponding to the response of the diaphragm with fluid interaction (reciprocal of time constant).The response of the system is determined by lowest of the two frequencies.

As the response of a pressure sensor obeys the coupling between fluid flow and mechanical response, the configurational arrangement of the sensor is essential in obtaining the best dynamic performance of the sensing system. Hence an attempt to build a dynamic pressure sensor based on annular diaphragm would result in sensor system that could be used only for a low frequency application. Further suspended particles in the input flow would form a layer of deposition on the diaphragm and also these particles might produce random vibration by colliding on the diaphragm and add mass to the membrane. There is a serious need to protect the sensitive element from the invading particles.

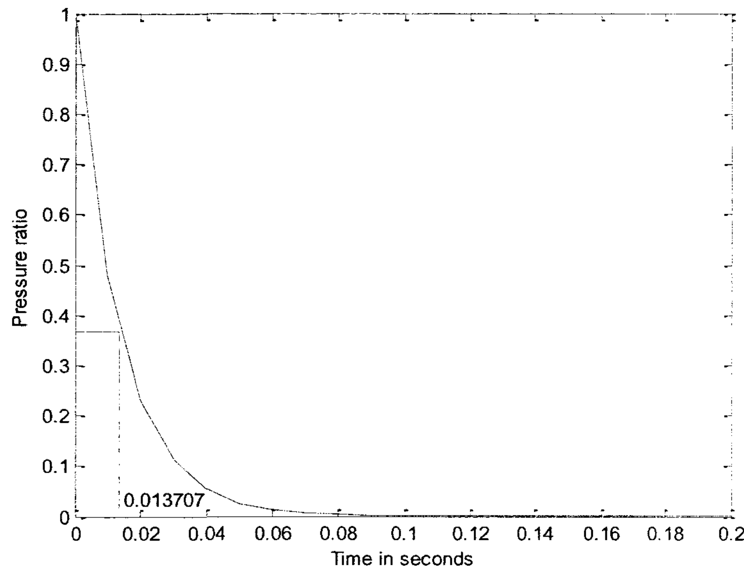

Figure 3.11: Time response of first order system of annular membrane

To protect the sensing element from the invading particles, it is mandatory to make sure that those particles do not reach the sensing element. Most of the pressure sensing applications connects the sensing element (diaphragm) to the pressure source by tubing [163]. These narrow access tubes, even though could reduce the invading particles are out of discussion for certain applications with space restriction as this would

evade the usage of access tubes. Further these tubes would reduce the natural frequency of the system and to prevent this degradation the tubing diameter should be as high as possible while its length should be at its minimum as practicable [163].

3.11. Summary

In this chapter pressure measurement is discussed with different types of signal transductions. Emphasis is on electrical and optical system as they are suitable for high frequency application. The frequency response of a transducer is dependent on configuration, size and gas-structure coupling. The importance on the configuration of sensitive elements is emphasized along with the design considerations for diaphragm based sensitive element which is a major configuration in pressure sensor design. It is also illustrated that the diaphragm based configuration mostly is used for static pressure measurement and for dynamic pressure measurement annular diaphragms are used.

Annular diaphragm used for dynamic pressure measurement is used for only low frequency application. An annular diaphragm based system is formulated based on electrical analogy and the resulting system is a first order system whose time constant reveals that annular diaphragm based system cannot be used to measure dynamic pressure of high frequency.

As the annular diaphragm configuration that is used to measure dynamic pressure in oil wells cannot be used for high frequency application, the possibility of using aeroelastic phenomena for sensing application is analyzed in chapter 4. Aeroelastic phenomenon use lift, drag or shear force generated by moving fluid on a surface as the working principle.

Chapter 4 : Different Configurations of Sensitive Element

4.1. Introduction

Microsensors use different configurations depending on the application. The most common configurations are the cantilevers and diaphragms. Annular diaphragm is used as sensing element configuration for low frequency, low temperature applications as described in chapter 3. This chapter will deal with the different configurations for GTE application with high temperature and high frequency environment. Since it is necessary to measure the fluctuating pressure also the possibility of using diaphragms with multiple holes is studied in this chapter. Multiple holes in a diaphragm will enhance its response when the sensitive element interacts with the flowing fluid.

Cantilever configuration is mostly used in aeroelastic based sensors which have flow parallel to the sensitive element as in lift based sensors or flow perpendicular to the sensitive element as in drag based sensors.

Cantilever configuration in lift based sensors is generally used for very low velocities as this configuration has problems of flutter which become significantly high at higher flow conditions [174,175]. To accommodate higher sensitivity and higher loading conditions special arrangements to the cantilever sensitive element is made as shown in figure 4.1.

Drag based sensors that use cantilever beam as sensing element has serious overloading issues due to the direct exposure of the sensitive element perpendicular to the flow.

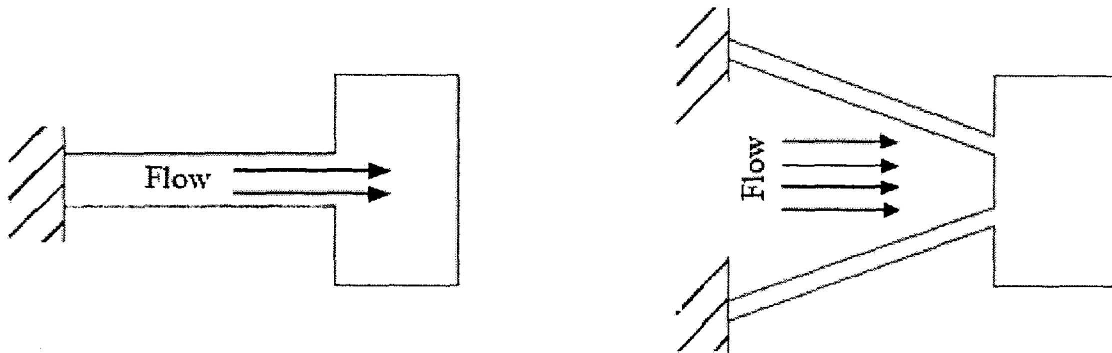

Figure 4.1: Top view of sensitive elements for lift force based sensing [174,175]

Diaphragms are also used for shear force based sensing as it has a larger surface area, but the stiffness is being reduced by special arrangements. Square diaphragms with 120 X 120 μm surface area is used as sensing element for a sensing scheme that uses flow induced displacement caused by shear force [176].

Diaphragm based flow induced shear stress measurement devices are stiffer than their cantilever counterparts and hence special arrangements to reduce the stiffness is required to make them more sensitive [177].

Circular diaphragms could be made less stiff by adding perforations to them. However, perforations also reduce the mass. Perforations closer to the clamped edge at the periphery of the circular diaphragm will have significant effect on the stiffness. The following study will focus on the change in natural frequency of the disks with the position of the perforations.

4.2. Analytical formulation using Bessel's function

Consider a homogenous and perfectly flexible circular plate that is assumed to move only in a direction perpendicular to the plane of the plate. With the origin of the polar coordinates fixed at the center of the circular plate, its displacement w(r, θ, t) is

assumed to be very small when compared to the dimensions of the membrane. The equation of motion for the free transverse vibration of the plate is

$$D\nabla^4 w + \rho h \frac{\partial^2 w}{\partial t^2} = 0 \tag{4.1}$$

$$\nabla^4 \mathrm{w} = \nabla^2(\nabla^2(\mathrm{w})) \tag{4.2}$$

where

$$\nabla^2\left(w(r,\theta,t)\right) = \frac{\partial^2 w(r,\theta,t)}{\partial r^2} + \frac{1}{r}\left(\frac{\partial w(r,\theta,t)}{\partial r}\right) + \frac{1}{r^2}\left(\frac{\partial^2 w(r,\theta,t)}{\partial \theta^2}\right) \tag{4.3}$$

and D is the flexural rigidity, ρ is the density, h is the thickness, and ∇^2 is the Laplacian operator.

Then equation 4.1 becomes

$$\left(\nabla^4 - \beta^4\right) w = 0 \tag{4.4}$$

where $\beta^4 = \frac{\rho h \omega^2}{D}$. Equation 4.4 could be written as

$$\left(\nabla^2 + \beta^2\right)\left(\nabla^2 - \beta^2\right) w = 0 \tag{4.5}$$

whose solution can be obtained as the superposition of the solutions of the two linear differential equations

$$\left(\nabla^2 - \beta^2\right) w_1 = 0 \tag{4.6}$$

$$\left(\nabla^2 + \beta^2\right) w_2 = 0 \tag{4.7}$$

Let w_1 and w_2 be corresponding solutions of equations 4.6 and 4.7. Superposition of these solutions will give original solution $w=w_1+w_2$ of equation 4.5.

The solution for equation 4.6 can be expressed as $w(r,\theta,t) = R(r)\Theta(\theta)T(t)$.

Method of variable separation yields the following equations

$$\frac{\partial^2 T}{\partial t^2} + c^2\beta^2 T = 0 \tag{4.8}$$

$$\frac{\partial^2 R(r)}{\partial r^2} + \frac{1}{r}\frac{\partial R(r)}{\partial r} + \left(\beta^2 - \frac{\alpha^2}{r^2}\right)R(r) = 0 \tag{4.9}$$

$$\frac{\partial^2 \Theta}{\partial t^2} + \alpha^2\Theta = 0 \tag{4.10}$$

where α^2 is a constant that must yield displacement as a periodic function of θ with a period of 2π such that α must be an integer, i.e., considering α=m and m=0, 1, 2…

The solutions of equations 4.8 and 4.10 could be expressed as

$$T(t) = L_1 \cos\beta t + Q_1 \sin\beta t \tag{4.11}$$

$$\Theta(\theta) = G_1 \cos m\theta + H_1 \sin m\theta \tag{4.12}$$

Equation 4.9 can be written as

$$r^2\frac{d^2R(r)}{dr^2} + r\frac{dR(r)}{dr} + \left(r^2\beta^2 - m^2\right)R = 0 \tag{4.13}$$

Equation 4.13 can be identified as Bessel's equation of order m with parameter β. The solution of equation 4.13 could be expressed as

$$R(r) = AJ_m(\beta r) + BY_m(\beta r) \tag{4.14}$$

where $\tilde{A}$ and $\tilde{B}$ are constants that could be determined from the boundary conditions and J_m and Y_m are Bessel functions of first and second kind, respectively.

The solution can be expressed as

$$w_1(r,\theta,t) = W_1(r,\theta)\left(L_1 \cos\beta t + Q_1 \sin\beta t\right) \tag{4.15}$$

where $W_1(r,\theta) = \left(AJ_m(\beta r) + BY_m(\beta r)\right)\left(G_1 \cos m\theta + H_1 \sin m\theta\right)$. Similarly

$$w_2(r,\theta,t) = W_2(r,\theta)\left(L_2 \cos\beta t + Q_2 \sin\beta t\right) \tag{4.16}$$

where $W_2(r,\theta) = \left(CI_m(\beta r) + DK_m(\beta r)\right)\left(G_2 \cos m\theta + H_2 \sin m\theta\right)$.

Combining $W_1(r, \theta)$ and $W_2(r, \theta)$, the complete solution is obtained as

$$w_m(r,\theta) = \left[\tilde{A}_m J_m(\beta r) + \tilde{B}_m Y_m(\beta r) + \tilde{C}_m I_m(\beta r) + \tilde{D}_m K_m(\beta r)\right](\cos m\theta) + \left[\tilde{A}_m^* J_m(\beta r) + \tilde{B}_m^* Y_m(\beta r) + \tilde{C}_m^* I_m(\beta r) + \tilde{D}_m^* K_m(\beta r)\right](\sin m\theta) \tag{4.17}$$

where $\tilde{A}_m, \tilde{A}_m^*, \tilde{B}_m, \tilde{B}_m^*$, $\tilde{C}_m, \tilde{C}_m^*$, $\tilde{D}_m$ and $\tilde{D}_m^*$ are constants and J_m , I_m and Y_m , K_m are Bessel functions of first kind, modified first kind, second kind and modified second kind, respectively.

4.2.1 Circular plate

Consider a circular plate of radius 'a'. Let the origin of the polar co-ordinate system be at the center of the circular plate. For a circular plate $w(r,\theta,t) = R(r)\Theta(\theta)T(t)$ must be finite. Since Y_m (βr) and K_m (βr) approach infinity, the constants B_n, D_n, B_n^*, and D_n^*must be zero. If the boundary conditions possess symmetry with respect to one or more diameters of the circular plate, it is possible to discard sin mθ term. Therefore equation 4.17 reduces to

$$w_n(r,\theta) = \left[\tilde{A}_n J_n(\beta r) + \tilde{C}_n I_n(\beta r)\right](\cos n\theta) \tag{4.18}$$

where the subscript n will denote nodal diameters, the coefficient $\tilde{A}_n$ and $\tilde{C}_n$ determine mode shapes and could be solved from the boundary conditions.

4.2.1.1 Circular plate with clamped boundary condition

Consider a circular plate with outer radius 'a' with the edge of the plate axisymetrically clamped, such that the deflection and slope are zero at the clamped edge.

$$W(r,\theta)\Big|_{r=a}=0 \tag{4.19}$$

$$\left.\frac{\partial W(r,\theta)}{\partial r}\right|_{r=a}=0 \tag{4.20}$$

Substituting the boundary conditions in equation 4.18, one has

$$\tilde{A}_n J_n(\beta a)+\tilde{C}_n I_n(\beta a)=0 \tag{4.21}$$

$$\tilde{A}_n \frac{dJ_n(\beta a)}{dr}+\tilde{C}_n \frac{dI_n(\beta a)}{dr}=0 \tag{4.22}$$

Writing equations 4.21 and 4.22 in matrix form

$$\begin{pmatrix} J_n(\beta a) & I_n(\beta a) \\ \dfrac{dJ_n(\beta a)}{dr} & \dfrac{dI_n(\beta a)}{dr} \end{pmatrix} \begin{Bmatrix} \tilde{A}_n \\ \tilde{C}_n \end{Bmatrix} = \begin{Bmatrix} 0 \\ 0 \end{Bmatrix} \tag{4.23}$$

$\begin{Bmatrix} \tilde{A}_n \\ \tilde{C}_n \end{Bmatrix} \neq 0$, and hence for a non trivial case, the characteristic determinant must be zero.

Accordingly

$$\begin{vmatrix} J_n(\beta a) & I_n(\beta a) \\ \dfrac{dJ_n(\beta a)}{dr} & \dfrac{dI_n(\beta a)}{dr} \end{vmatrix} = 0 \tag{4.24}$$

The frequency equation is given by

$$J_n(\beta a)\frac{dI_n(\beta a)}{dr}-\frac{dJ_n(\beta a)}{dr}I_n(\beta a)=0 \tag{4.25}$$

Using recurrence relation, Bessel function of higher order can be converted to Bessel function of lower order as

$$\frac{dJ_n(\beta a)}{dr} = \frac{n}{\beta a} J_n(\beta a) - J_{n+1}(\beta a) \quad (4.26)$$

$$\frac{dI_n(\beta a)}{dr} = \frac{n}{\beta a} I_n(\beta a) + I_{n+1}(\beta a) \quad (4.27)$$

Substituting in equation 4.25, the frequency equation is given by

$$J_n(\beta a) I_{n+1}(\beta a) + I_n(\beta a) J_{n+1}(\beta a) = 0 \quad (4.28)$$

where the eigen value is the frequency parameter and is given by

$$\beta^2 a^2 = a^2 \omega \sqrt{\frac{\rho h}{D}} \Rightarrow \omega = \beta^2 \sqrt{\frac{D}{\rho h}} \quad (4.29)$$

4.2.1.2 Annular plate with outer edge clamped and inner edge free

Consider a annular plate with an outer radius 'a' and with an inner radius 'b'. There will be additional boundary conditions at the inner boundary. The deflection corresponding to this case will become

$$w_n(r,\theta) = \left[\tilde{A}_n J_n(\beta r) + \tilde{B}_n Y_n(\beta r) + \tilde{C}_n I_n(\beta r) + \tilde{D}_n K_n(\beta r)\right](\cos n\theta) \quad (4.30)$$

The boundary conditions corresponding to outer edge clamped and inner edge free will be

$$W(r,\theta)\Big|_{r=a} = \frac{\partial W(r,\theta)}{\partial r}\Bigg|_{r=a} = 0 \quad (4.31)$$

$$M_r(r,\theta)\Big|_{r=b} = V_r(r,\theta)\Big|_{r=b} = 0 \quad (4.32)$$

Based on boundary conditions when r =a, equation 4.30 will become

$$\tilde{A}_n J_n(\beta a) + \tilde{B}_n Y_n(\beta a) + \tilde{C}_n I_n(\beta a) + \tilde{D}_n K_n(\beta a) = 0 \quad (4.33)$$

$$\tilde{A}_n \frac{dJ_n(\beta a)}{dr} + \tilde{B}_n \frac{dY_n(\beta a)}{dr} + \tilde{C}_n \frac{dI_n(\beta a)}{dr} + \tilde{D}_n \frac{dK_n(\beta a)}{dr} = 0 \tag{4.34}$$

Considering bending moment $M_r(b) = -D\left[\frac{d^2 w}{dr^2} + \frac{\mu}{r}\frac{dw}{dr}\right]\bigg|_{r=b} = 0$, equation 4.30 becomes

$$\tilde{A}_n \left\{ \frac{d^2 J_n(\beta b)}{dr^2} + \frac{\mu}{\beta b}\frac{dJ_n(\beta b)}{dr} \right\} + \tilde{B}_n \left\{ \frac{d^2 Y_n(\beta b)}{dr^2} + \frac{\mu}{\beta b}\frac{dY_n(\beta b)}{dr} \right\} + \tag{4.35}$$
$$\tilde{C}_n \left\{ \frac{d^2 I_n(\beta b)}{dr^2} + \frac{\mu}{\beta b}\frac{dI_n(\beta b)}{dr} \right\} + \tilde{D}_n \left\{ \frac{d^2 K_n(\beta b)}{dr^2} + \frac{\mu}{\beta b}\frac{dK_n(\beta b)}{dr} \right\} = 0$$

Considering shear force $V_r(b) = -D\frac{\partial}{\partial r}\left[\nabla^2 w\right]\Big|_{r=b} = \frac{\partial}{\partial r}\left(\frac{d^2 w}{dr^2} + \frac{1}{r}\frac{dw}{dr}\right)\bigg|_{r=b} = 0$

$$\tilde{A}_n \left\{ \frac{d^3 J_n(\beta b)}{dr^2} + \frac{1}{\beta b}\frac{d^2 J_n(\beta b)}{dr^2} - \frac{1}{\beta^2 b^2}\frac{dJ_n(\beta b)}{dr} \right\} + \tag{4.36}$$
$$\tilde{B}_n \left\{ \frac{d^3 Y_n(\beta b)}{dr^2} + \frac{1}{\beta b}\frac{d^2 Y_n(\beta b)}{dr^2} - \frac{1}{\beta^2 b^2}\frac{dY_n(\beta b)}{dr} \right\} +$$
$$\tilde{C}_n \left\{ \frac{d^3 I_n(\beta b)}{dr^2} + \frac{1}{\beta b}\frac{d^2 I_n(\beta b)}{dr^2} - \frac{1}{\beta^2 b^2}\frac{dI_n(\beta b)}{dr} \right\} +$$
$$\tilde{D}_n \left\{ \frac{d^3 K_n(\beta b)}{dr^2} + \frac{1}{\beta b}\frac{d^2 K_n(\beta b)}{dr^2} - \frac{1}{\beta^2 b^2}\frac{dK_n(\beta b)}{dr} \right\} = 0$$

Equations 4.33 to 4.36 are four homogenous equations in four unknowns $\tilde{A}_m$, $\tilde{B}_m$, $\tilde{C}_m$, and $\tilde{D}_m$. For a non trivial solution, the determinant of coefficients will be zero. The frequency determinant will have higher order Bessel functions and these are reduced to first and zeroeth order by using identity relations of Bessel functions.

The frequency determinant for an axisymmetric case (n=0) with a clamped outer edge and a free inner edge is [178]

$$\begin{vmatrix} J_0(\beta a) & Y_0(\beta a) & I_0(\beta a) & K_0(\beta a) \\ J_1(\beta a) & Y_1(\beta a) & -I_1(\beta a) & K_1(\beta a) \\ J_0(\beta b) & Y_0(\beta b) & -I_0(\beta b)+QI_1(\beta b) & -K_0(\beta b)-QK_1(\beta b) \\ J_1(\beta b) & Y_1(\beta b) & I_1(\beta b) & -K_1(\beta b) \end{vmatrix} = 0 \tag{4.37}$$

where $Q = \dfrac{2(1-\mu)}{\beta b}$

4.3. Analytical formulation using the Rayleigh Ritz method

The Rayleigh Ritz method is used to obtain the approximate natural frequencies and the natural modes of a structure. In this method an approximate expression for the deflection of the structure is assumed that satisfies at least the geometrical boundary conditions. This approximate deflection is used to obtain the maximum values of the potential and kinetic energies. In a conservative system the maximum potential energy must be equal to the maximum kinetic energy

The maximum strain energy of the deformed circular plate is given by

$$U_{\max} = \frac{D}{2}\int_A \left(\begin{array}{l} \left(\dfrac{\partial^2 W}{\partial r^2} + \dfrac{1}{r}\dfrac{\partial W}{\partial r} + \dfrac{1}{r^2}\dfrac{\partial^2 W}{\partial \theta^2}\right)^2 - 2(1-\mu)\dfrac{\partial^2 W}{\partial r^2}\left(\dfrac{1}{r}\dfrac{\partial W}{\partial r} + \dfrac{1}{r^2}\dfrac{\partial^2 W}{\partial \theta^2}\right) \\ +2(1-\mu)\left(\dfrac{\partial}{\partial r}\left(\dfrac{1}{r}\dfrac{\partial W}{\partial \theta}\right)\right)^2 \end{array} \right) dA \tag{4.38}$$

where W is the deflection of the plate, $D = \dfrac{Eh^3}{12(1-\mu^2)}$ is the flexural rigidity , E is the Young's modulus, h is the thickness of the plate and μ is the Poisson's ratio.

The maximum kinetic energy is given by

$$T_{\max} = \frac{1}{2}\rho h \omega^2 \int_A W^2 dA \tag{4.39}$$

where, ρ is the mass density per unit volume and ω is the natural frequency of the plate.

Substituting the deflection function as $W(r,\theta)=\sum_{m=1}\phi_m(r)\sum_{n=0}\left(A_{mn}\cos n\theta+B_{mn}\sin n\theta\right)$ into the above expressions for maximum kinetic and potential energies will result in:

$$T_{\max}=\frac{1}{2}\rho h\omega^2\int_A\left(\sum_{i=1}\sum_{j=0}\phi_i(r)\left(A_{ij}\cos j\theta+B_{ij}\sin j\theta\right)\right)\left(\sum_{m=1}\sum_{n=0}\phi_m(r)\left(A_{mn}\cos n\theta+B_{mn}\sin n\theta\right)\right)dA \tag{4.40}$$

$$\begin{aligned}U_{\max}=\frac{D}{2}\int_A\Bigg[&\left(\sum_{i=1}\sum_{j=0}V_{ij}^1\left(A_{ij}\cos j\theta+B_{ij}\sin j\theta\right)\right)\left(\sum_{m=1}\sum_{n=0}V_{mn}^1\left(A_{mn}\cos n\theta+B_{mn}\sin n\theta\right)\right)\\
&-(1-\mu)\left(\sum_{i=1}\sum_{j=0}\phi_i''(r)\left(A_{ij}\cos j\theta+B_{ij}\sin j\theta\right)\right)\left(\sum_{m=1}\sum_{n=0}V_{mn}^2\left(A_{mn}\cos n\theta+B_{mn}\sin n\theta\right)\right)\\
&-(1-\mu)\left(\left(\sum_{i=1}\sum_{j=0}V_{ij}^2\left(A_{ij}\cos j\theta+B_{ij}\sin j\theta\right)\right)\left(\sum_{m=1}\sum_{n=0}\phi_m''(r)\left(A_{mn}\cos n\theta+B_{mn}\sin n\theta\right)\right)\right)\\
&+2(1-\mu)\left(\left(\sum_{i=1}\sum_{j=0}V_{ij}^3\left(-A_{ij}\sin j\theta+B_{ij}\cos j\theta\right)\right)\left(\sum_{m=1}\sum_{n=0}V_{mn}^3\left(-A_{mn}\sin n\theta+B_{mn}\cos n\theta\right)\right)\right)\Bigg]dA\end{aligned} \tag{4.41}$$

where

$$\begin{aligned}V_{mn}^1&=\phi_m''(r)+\frac{1}{r}\phi_m'(r)-\frac{n^2}{r^2}\phi_m(r)=\frac{r^2\phi_m''(r)+r\phi_m'(r)-n^2\phi_m(r)}{r^2}\\
V_{mn}^2&=\frac{1}{r}\phi_m'(r)-\frac{n^2}{r^2}\phi_m(r)=\frac{r\phi_m'(r)-n^2\phi_m(r)}{r^2}\\
V_{mn}^3&=\frac{n}{r}\phi_m'(r)-\frac{n}{r^2}\phi_m(r)=\frac{nr\phi_m'(r)-n\phi_m(r)}{r^2}\end{aligned} \tag{4.42}$$

The Rayleigh quotient is given by

$$\omega^2=\frac{U_{\max}}{T_{\max}^{*}} \tag{4.43}$$

where $T_{\max}=\omega^2T_{\max}^{*}$

Applying the condition of stationarity of the natural frequencies with respect to the arbitrary constants A_{ij} and B_{ij}, one has $\frac{\partial\omega^2}{\partial A_{ij}}=0 \, and \, \frac{\partial\omega^2}{\partial B_{ij}}=0$

These equations yields in an eigen value problem as follows

$$[K]\begin{Bmatrix} A_{ij} \\ \hline B_{ij} \end{Bmatrix} = \omega^2 [M]\begin{Bmatrix} A_{ij} \\ \hline B_{ij} \end{Bmatrix} \tag{4.44}$$

where the elements of matrices [K] and [M] are given by

$$[K] = \begin{bmatrix} \partial U_{\max} \big/ \partial A_{ij} \\ \hline \partial U_{\max} \big/ \partial B_{ij} \end{bmatrix} and [M] = \begin{bmatrix} \partial T_{\max}^{*} \big/ \partial A_{ij} \\ \hline \partial T_{\max}^{*} \big/ \partial B_{ij} \end{bmatrix} \tag{4.45}$$

The terms in the mass and stiffness matrices are

$$\frac{\partial T}{\partial A_{ij}} = \int_A \phi_i(r) \cos j\theta \left(\sum_{m=1} \sum_{n=0} \phi_m(r) \left(A_{mn} \cos n\theta + B_{mn} \sin n\theta \right) \right) dA \tag{4.46}$$

$$\frac{\partial T}{\partial B_{ij}} = \int_A \phi_i(r) \sin j\theta \left(\sum_{m=1} \sum_{n=0} \phi_m(r) \left(A_{mn} \cos n\theta + B_{mn} \sin n\theta \right) \right) dA \tag{4.47}$$

$$\begin{aligned} \frac{\partial U}{\partial A_{ij}} = \int_A \Bigg[& V_{ij}^1 \cos j\theta \left(\sum_{m=1} \sum_{n=0} V_{mn}^1 \left(A_{mn} \cos n\theta + B_{mn} \sin n\theta \right) \right) \\ & - (1-\mu) \left(\phi_i''(r) \cos j\theta \left(\sum_{m=1} \sum_{n=0} V_{mn}^2 \left(A_{mn} \cos n\theta + B_{mn} \sin n\theta \right) \right) \right) \\ & - (1-\mu) \left(V_{ij}^2 \cos j\theta \left(\sum_{m=1} \sum_{n=0} \phi_m''(r) \left(A_{mn} \cos n\theta + B_{mn} \sin n\theta \right) \right) \right) \\ & + 2(1-\mu) \left(V_{ij}^3 \sin j\theta \left(\sum_{m=1} \sum_{n=0} V_{mn}^3 \left(A_{mn} \sin n\theta - B_{mn} \cos n\theta \right) \right) \right) \Bigg] dA \end{aligned} \tag{4.48}$$

$$\begin{aligned} \frac{\partial U}{\partial B_{ij}} = \int_A \Bigg[& V_{ij}^1 \sin j\theta \left(\sum_{m=1} \sum_{n=0} V_{mn}^1 \left(A_{mn} \cos n\theta + B_{mn} \sin n\theta \right) \right) \\ & - (1-\mu) \left(\phi_i''(r) \sin j\theta \left(\sum_{m=1} \sum_{n=0} V_{mn}^2 \left(A_{mn} \cos n\theta + B_{mn} \sin n\theta \right) \right) \right) \\ & - (1-\mu) \left(V_{ij}^2 \sin j\theta \left(\sum_{m=1} \sum_{n=0} \phi_m''(r) \left(A_{mn} \cos n\theta + B_{mn} \sin n\theta \right) \right) \right) \\ & + 2(1-\mu) \left(V_{ij}^3 \cos j\theta \left(\sum_{m=1} \sum_{n=0} V_{mn}^3 \left(-A_{mn} \sin n\theta + B_{mn} \cos n\theta \right) \right) \right) \Bigg] dA \end{aligned} \tag{4.49}$$

With 'a' as the outer radius of the plate, the following dimensionless values are defined in order to help us to compare the results with the available literature.

$$\lambda^4 = \Omega^2 = \frac{\rho h a^4 \omega^2}{D} \qquad (4.50)$$

4.3.1 Generation of boundary characteristic orthogonal polynomials

The deflection functions $\emptyset(r)$ are assumed in the form of a set of boundary characteristic orthogonal polynomials [178]. The first member of the boundary characteristic orthogonal polynomial set is constructed to satisfy the boundary conditions of the plate. For plate with clamped conditions given by $\phi(R) = \phi'(R) = 0$, the first member may be constructed as

$$\phi_1(r) = d_1(r^2 - R^2)^2 \qquad (4.51)$$

such that the displacement and the slope vanish at the outer edge of the plate. The Gram-Schmidt process [178] has been used to generate the higher order members of the boundary characteristic orthogonal polynomial set.

$$\phi_2(r) = d_2(r - b_1)\phi_1(r) \qquad (4.52)$$

$$\phi_m(r) = d_m\left[(r - b_{m-1})\phi_{m-1}(r) - c_{m-1}\phi_{m-2}(r)\right] \quad \forall m \geq 3 \qquad (4.53)$$

where

$$b_{m-1} = \int_{R_i}^{R} r^2 \phi_{m-1}^2(r)dr \qquad (4.54)$$

$$c_{m-1} = \int_{R_i}^{R} r^2 \phi_{m-1}(r)\phi_{m-2}(r)dr \qquad (4.55)$$

The set of boundary characteristic orthogonal polynomials is normalized such that in equations 4.50 -4.52 the constant d_m can be identified by using the following equation.

$$\int_{R_i}^{R} \phi_m^2(r) r dr = 1 \qquad (4.56)$$

resulting in ortho-normal functions. It should be mentioned that R_i refers to the inner radius of the plate and in the case there is no hole at the center, it is equal to zero.

4.3.2 Coordinates of perforations in plates

When there are eccentric perforations over the plate, first the potential and kinetic energies are estimated for a plate without any perforations. Then, the amounts of energies corresponding to the holes are calculated and subtracted from the total energy. Referring to figure 4.2, kinetic and potential energies of a circle off the center are calculated in this region $r_1(\theta) \leq r \leq r_2(\theta)$ and $\theta_0 - \alpha \leq \theta \leq \theta_0 + \alpha$. It should be noted that:

$$\sin\alpha = \frac{a}{e} \tag{4.57}$$

$$r_1(\theta) = e\cos\theta - \sqrt{a^2 - e^2\sin^2\theta} \tag{4.58}$$

$$r_2(\theta) = e\cos\theta + \sqrt{a^2 - e^2\sin^2\theta} \tag{4.59}$$

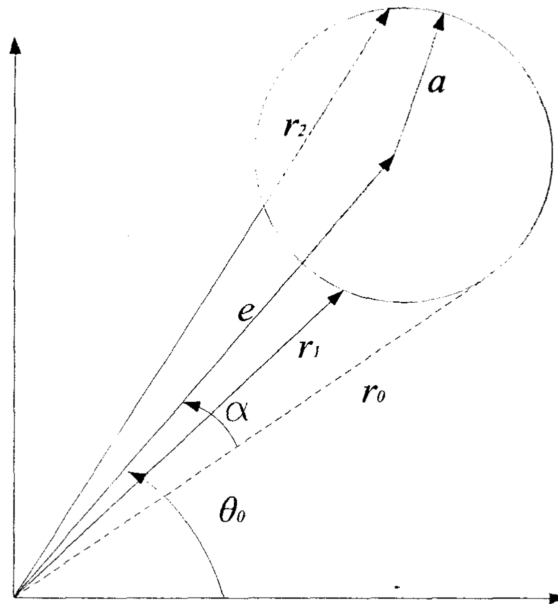

Figure 4.2: Coordinates of the perforation

4.4. Experimental Investigation

Exact solution using Bessel functions is not possible for disks with multiple perforations located at different distances from the center. Approximate solutions are obtained using the Rayleigh Ritz method. In order to validate these approximate results experimental investigations on perforated disks are performed.

The setup consists of a disk assembly, shaker (Model S062), signal conditioner and accelerometer. The shaker is excited from frequency 10 Hz to 1000 Hz. The disk assembly consists of a thick base plate, two rings and the disk. The rings sandwich the disks and are used to clamp the disks using nut and bolt assembly.

The vibration is picked up by B & K Accelerometer, amplified and fed to the signal analyser. The FFT analysis of the amplified signal shows the peak corresponding to the natural frequency.

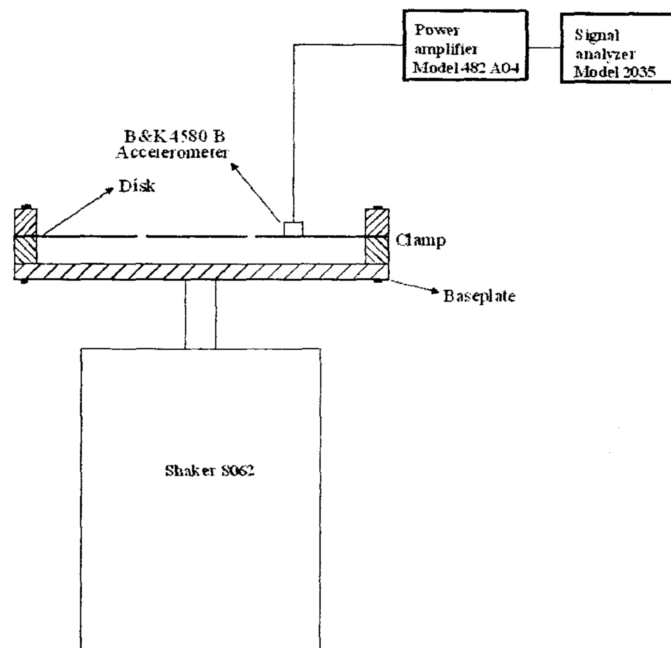

Figure 4.3: Schematic layout of experimental setup

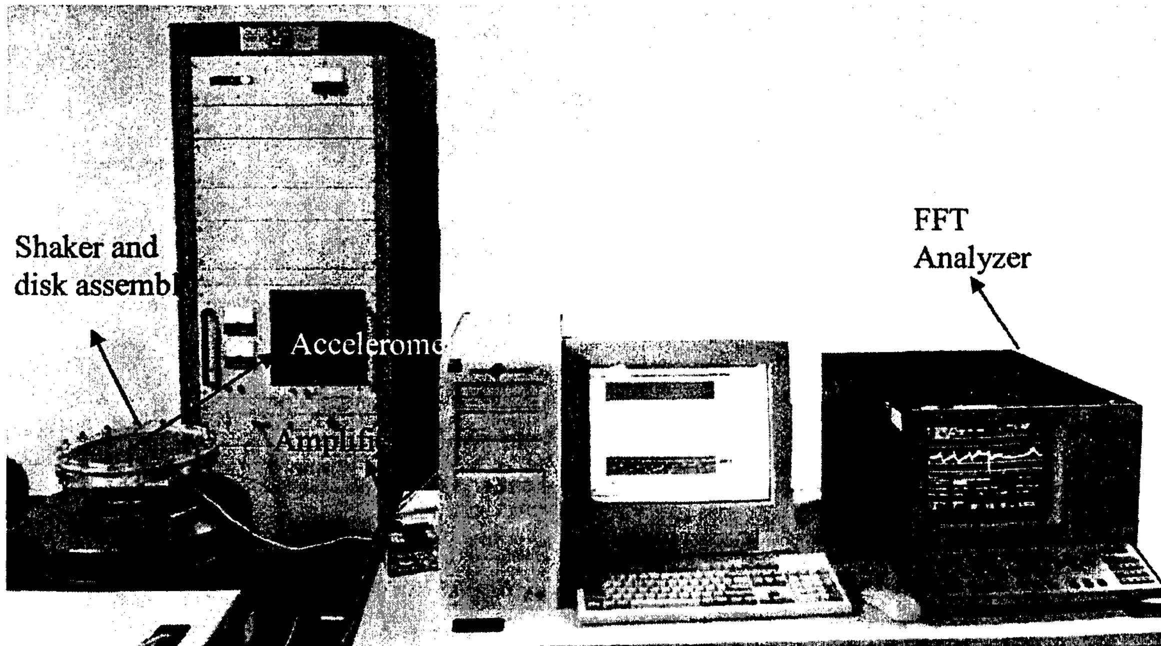

Figure 4.4: Experimental setup

The experimental setup is shown in figure 4.3 and figure 4.4. An accelerometer is placed on the shaker and disk assembly, and the signal is amplified through amplifier (Model 482-A04) and fed to the signal conditioner (FFT Analyzer K&B model 2305). The accelerometer 4580 B 001 can be used for measurements between 10 Hz to 8 kHz. The position of the accelerometer is very crucial when searching for higher modes as care must be taken to avoid positioning the accelerometer on a nodal circle. The experiments are repeated by placing the accelerometer at different positions for confirmation. The experimental investigations are performed on 4 different disks made of the aluminum sheet metal of same thickness, the outer radius of the disks are 150 mm. All the holes made in the disks have the same radius of 12.7 mm. The disks are clamped at the periphery and the holes have free boundary conditions.

4.5. Test cases

Four cases are considered for experimental investigations in order to validate the results from analytical methods.

Case 1. Full circular plate

Case 2. Plate with a perforation positioned at its center (annular plate)

Case 3. Plate with 1 perforation at its center and 8 perforations closer to the center (at a distance of 50 mm from the center)

Case 4. Plate with 1 perforation at its center and 8 perforations closer to the outer edge (at a distance of 100 mm from the center)

Case 5. Plate with 1 perforation at its center and 8 perforations at a distance of 50 mm from the center and 16 perforations at a distance of 100 mm from the center.

In the cases from 2 to 5 the ratio of perforation radius to the plate radius (b/a) is taken to be 12.7/150 = 0.085 based on the limitation offered on the maximum possible perforation radius by the in house machining facility. Only first 5 frequencies are considered in the experiment due to the limitation of maximum excitation frequency in the shaker.

4.5.1 Case 1 and 2 Full circular Plate and annular plate

Case 1 and 2 could be considered as a standard, as it is possible to validate both the experiment and Rayleigh Ritz's method with analytical approach using Bessel's function. Table 4.1 and 4.2 describes the comparison of the Rayleigh Ritz method and experiment with Bessel function approach for full circular plate and annular plate with clamped periphery and the results are in good agreement except for the first and fourth mode.

Table 4-1: Comparison of the dimensionless natural frequencies Ω of a circular plate with clamped boundary using M=10 orthogonal polynomials with Bessel function

n → / number of radial nodes ↓	0			1			2			3		
	Bessel function	Rayleigh Ritz method	Experiment	Bessel function	Rayleigh Ritz method	Experiment	Bessel function	Rayleigh Ritz method	Experiment	Bessel function	Rayleigh Ritz method	Experiment
0	10.2128	10.2158	7.9407	21.2544	21.2603	21.0114	34.8838	34.8768	34.0726	51.0338	51.0298	51.3613
1	39.7751	39.7711	41.8967	60.8283	60.8289	N/A	84.5894	84.5829	N/A	111.0231	111.0221	N/A
2	89.0900	89.1041	N/A	120.0832	120.0790	N/A	153.8282	153.8160	N/A	190.2951	190.3286	N/A
3	158.1746	158.1852	N/A	199.0427	199.0929	N/A	242.7286	242.9415	N/A	289.1615	289.4017	N/A

Table 4-2: Comparison of the natural frequencies Ω of a circular annular plate (b /a =0.085*) in clamped free BC using M=10 orthogonal polynomials with experiment and Bessel function

n → / number of radial nodes ↓	0			1			2			3		
	Bessel function	Rayleigh Ritz method	Experiment	Bessel function	Rayleigh Ritz method	Experiment	Bessel function	Rayleigh Ritz method	Experiment	Bessel function	Rayleigh Ritz method	Experiment
0	10.1649	10.1645	9.3384	21.22	21.2243	20.9483	34.8661	34.6235	34.4512	51.0332	51.0039	51.7399
1	39.4164	39.4255	42.4014	60.3846	60.3993	N/A	84.5342	83.7496	N/A	111.0231	110.892	N/A
2	89.4585	89.4669	N/A	118.1841	118.2072	N/A	153.4564	151.9598	N/A	190.2537	189.8584	N/A
3	161.398	161.3979	N/A	194.2888	194.3155	N/A	241.2353	239.3481	N/A	289.0085	288.1837	N/A

* The value of b/a = 0.085 is chosen on the basis of limitation offered by the experimental facility.

Table 4.1 compares the values with the exact solution using Bessel function with the Rayleigh Ritz method and the experiment for a full circular plate. The Rayleigh Ritz method is in good agreement with the exact solution. There are some errors between the experimental investigations as compared with the Bessel function approach, which could be attributed to the fact that perfect clamping condition is not possible in experimental setup.

The disk is sandwiched between two rings made of plexiglass. The entire setup is clamped to the base plate using 16 equally spaced clamps. The distance between these clamps is approximately 62.5 mm. The restriction offered by the clamping condition is not perfect as in the analytical model. However, the clamping makes the plate stiffer than simply supported condition. It should be noted that the fundamental frequency parameter for simply supported condition is 4.977 and the same for a perfect clamped condition is 10.2158 [178]. The experimental result for the fundamental frequency is 7.9407. This error is because of the lack of perfect clamping.

It is interesting to note that the lack of perfect clamping condition in experiments do not provide a closer result to that of the perfectly clamped boundary as in the analytical solution, for the first and fourth modes, which are axisymmetric. However, in antisymmetric modes i.e. second, third and fifth modes, experimental results match with the analytical solution. From the experimental results it could be inferred that the non compliance to perfect clamping condition has affected the axisymmetric modes to a greater extent than the antisymmetric mode shapes.

4.5.2 Case 3: Disk with 1 perforation at its center and 8 perforations closer to the center (at a distance of 50 mm from the center)

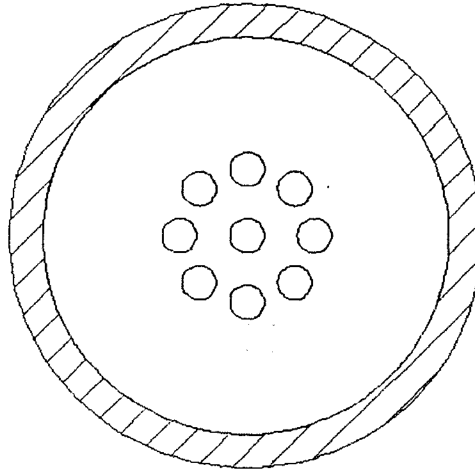

Figure 4.5: Circular plate with 9 perforations close to center in clamped free boundary condition

Case 3 has 9 perforations as shown in figure 4.5. The perforations are close to the center of the plate, and hence there is an effective reduction in mass. There is a noticeable difference in the frequencies when the results (in table 4.2 and table 4.3) are compared.

Table 4-3: Comparison of the natural frequencies Ω of a circular plate with perforations case 3 (b /a =0.085*) in clamped free BC with experiment

Ω	Distance =50 mm Figure 4.5	
	Rayleigh Ritz method	Experiment
1	10.5847	12.6195
2	21.1379	22.3996
3	34.4872	34.8298
4	38.7089	43.8527
5	49.9968	49.9100
6	60.4258	N/A
7	68.2305	N/A
8	84.8114	N/A
9	86.7696	N/A
10	89.5255	N/A

4.5.3 Case 4: Disk with 1 perforation at center and 8 perforations closer to the outer edge (at a distance of 100 mm from the center)

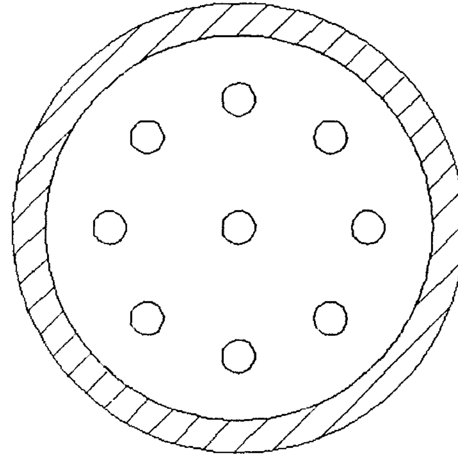

Figure 4.6: Circular plate with 9 perforations in clamped free boundary condition

Case 4 has 9 perforations as shown in figure 4.6. Case 4 differs from case 3 only in the positioning of the perforations. The perforations are close to the outer edge, causing an effective reduction in the stiffness as compared to the case 3. Comparing the tables 4.3 and 4.4 the frequencies for this case are lower than those of case 3. Hence positioning of the perforations is quite important in controlling the natural frequencies.

Table 4-4: Comparison of the natural frequencies Ω of a circular plate with perforations case 4 (b /a =0.085*) in clamped free BC with experiment

Ω	Distance e =100 mm Figure 4.6	
	Rayleigh Ritz method	Experiment
1	10.1648	10.4742
2	21.5376	21.2007
3	34.9697	34.7036
4	39.9376	41.0133
5	51.7232	51.8861
6	60.8489	N/A
7	69.2284	N/A
8	73.1309	N/A
9	84.014	N/A
10	89.4748	N/A

4.5.4 Case 5: Disk with 1 perforation at center and 8 perforations at a distance of 50 mm from the center and 16 perforations at a distance of 100 mm from the center.

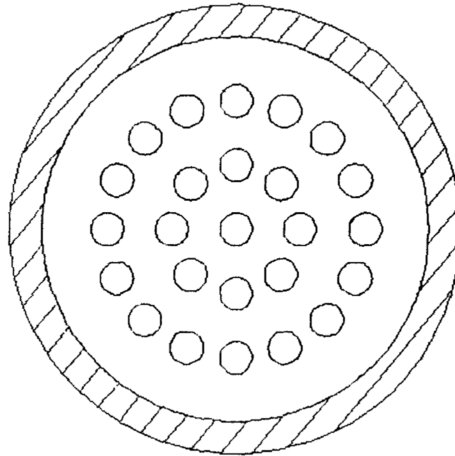

Figure 4.7: Circular plate with 25 perforations in clamped free boundary condition

Case 5 corresponds to superposition of case 3 and case 4 with additional 8 holes distributed evenly at a distance of 100mm that would contribute for both mass and stiffness loss. There is a change in mass as well as stiffness, and the reduction in mass increases the natural frequency whereas the presence of additional holes close to the clamped edge reduces the frequency.

Table 4-5: Comparison of the natural frequencies Ω of a circular plate with perforations case 5 (b /a =0.085*) in clamped free BC with experiment

Ω	Rayleigh Ritz method	Experiment
1	10.5243	11.8623
2	21.8869	21.4531
3	35.5827	33.8202
4	39.8545	40.8871
5	51.7732	49.4684
6	61.1589	N/A
7	71.1655	N/A
8	85.5563	N/A
9	86.75	N/A
10	93.9313	N/A

4.5.5 Discussion

Considering the four cases there is a possibility of using diaphragms for sensing application. Case 3 and case 4 clearly depict the change in stiffness for the same mass reduction evidenced by change in natural frequencies. The position of perforations will influence the sensitivity of the sensitive element and proper positioning could be considered as an option to improve sensitivity on shear sensing.

The diaphragm based shear sensing concept is a potential candidate for dynamic pressure application. Diaphragms with multiple perforations when used as a sensitive element will respond faster to the pressure changes than its annular counterpart. However if the sensitivity of the sensing element has to be improved, the diameter of the diaphragm has to be increased. Smaller diameter diaphragms are stiffer and less sensitive to the input pressure change. Sensitive element with large diameters cannot be accommodated by the proposed application due to its space restrictions. Furthermore, high temperature sensing applications may pose some problems related to thermal expansion of the sensitive element [179]. The following section analyses the influence of temperature on sensitive element configurations such as diaphragms and cantilever beams.

4.6. Influence of temperature on sensitivity

The configuration of the sensitive element even though plays a role in making the structure resistant to high temperature, high temperature regime still demands the need for materials that would effectively withstand high temperatures. The influence of

temperature in sensor systems is defined by two parameters i) Thermal coefficient of modulus of elasticity ii) Coefficient of thermal expansion.

The following study is a comparison between the sensitivity of a diaphragm and cantilever beam at higher temperatures

4.6.1 Diaphragm

The maximum deflection of diaphragm under uniform load pressure would be

$$Y_{Center} = \frac{3P(1-\mu^2)R^4}{16Eh^3} \quad \text{or} \tag{4.60}$$

$$Y_{Center} = K_1 \frac{PR^4}{Eh^3} \tag{4.61}$$

where Y_r is the deflection of the diaphragm at radial distance r (m)

P is the pressure (Pa)

μ is the Poisson ratio

E is the Young's modulus

h is the thickness (m)

R is the radius of diaphragm (m)

K_1 is a constant $K_1 = \frac{3(1-\mu^2)}{16}$

Expressing thickness h in terms of radius, $h = \in R_0$ in equation 4.61, sensitivity at room temperature t_0 could be expressed as

$$\left(\frac{Y}{P}\right)_{t_o} = \frac{K_1 R_o^{\ 4}}{E_o \varepsilon^3 R_o^{\ 3}} \tag{4.62}$$

Sensitivity due to temperature change from t_0 to t (Δt)

$$\left(\frac{Y}{P}\right)_t = \frac{K_1\left[R_o\left(1+\alpha*\Delta t\right)\right]^4}{E_o\left(1+C_e*\Delta t\right)\left[\varepsilon R_o\left(1+\alpha*\Delta t\right)\right]^3} \tag{4.63}$$

where C_e is the thermal coefficient of modulus of elasticity per degree change in temperature,

α is the coefficient of thermal expansion per degree change in temperature

Change in sensitivity due to temperature change Δt may be expressed by the ratio of sensitivities at t_o and t as

$$\frac{\left(\frac{Y}{P}\right)_t}{\left(\frac{Y}{P}\right)_{t_o}} = \frac{\left(1+\alpha*\Delta t\right)}{\left(1+C_e*\Delta t\right)} \tag{4.64}$$

which becomes

$$\left(\frac{Y}{P}\right)_t = \frac{\left(1+\alpha*\Delta t\right)}{\left(1+C_e*\Delta t\right)}\left(\frac{Y}{P}\right)_{t_o} \tag{4.65}$$

4.6.2 Cantilever beam

Considering the deflection of the cantilever beam due to an uniformly distributed load with W as total load on the cantilever beam, we have

$$Y_{tip} = \frac{Wl^3}{8*E*\frac{bh^3}{12}} \tag{4.66}$$

$$Y_{tip} = \frac{K_2Wl^3}{E*bh^3} \tag{4.67}$$

Expressing thickness h and width b in terms of length (multiplied by constant), equation 4.67 could be expressed as sensitivity at room temperature t_0

$$\left(\frac{Y_{tip}}{W}\right)_{t_o} = \frac{K_2 l_o^3}{E_o * \varepsilon_1 l_o \varepsilon_2^3 l_o^3} \tag{4.68}$$

Sensitivity due to temperature change from t_0 to t (Δt)

$$\left(\frac{Y}{W}\right)_t = \frac{K_2\left[l_o(1+\alpha*\Delta t)\right]^3}{E_o(1+C_e*\Delta t)\varepsilon_1 l_o(1+\alpha*\Delta t)\left[\varepsilon_2 l_o(1+\alpha*\Delta t)\right]^3} \tag{4.69}$$

Change in sensitivity due to temperature change Δt may be expressed by the ratio of sensitivities at t_o and t

$$\frac{\left(\frac{Y}{W}\right)_t}{\left(\frac{Y}{W}\right)_{t_o}} = \frac{1}{(1+\alpha*\Delta t)(1+C_e*\Delta t)} \tag{4.70}$$

which becomes

$$\left(\frac{Y}{W}\right)_t = \frac{1}{(1+\alpha*\Delta t)(1+C_e*\Delta t)}\left(\frac{Y}{W}\right)_{t_o} \tag{4.71}$$

Figure 4.8 depicts the dependency of sensitivity ratio which is the sensitivity at a given high temperature to the sensitivity at reference (room) temperature. The coefficient of thermal expansion and thermal coefficient of modulus of elasticity are taken for titanium alloy (6-Al-4-V) as C_e = $-31e^{-5}$ psi/psi-^{0}C and α = 5.7 μm/μm-^{0}C for the temperature range of -50^{0}C to 150^{0}C [163] limiting the graph to -50^{0}C to 150^{0}C range in the x-axis. The thermal coefficient of modulus of elasticity C_e is negative for almost all materials as Young's modulus decreases with increase in temperature. Also it should be

noted that coefficient of thermal expansion is positive for all encountered cases.

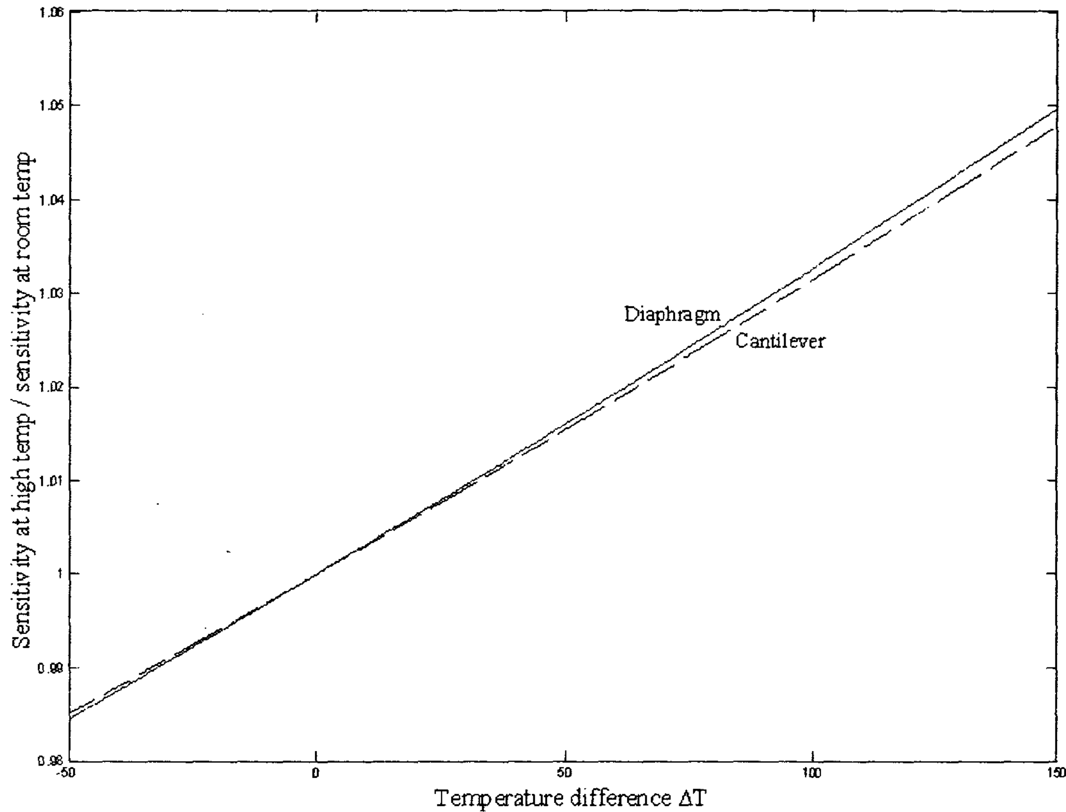

Figure 4.8: Temperature sensitivity of cantilever and diaphragm configurations fabricated using same material

It should be noted from the graph that the sensitivity ratio for the cantilever beam is less than that of the diaphragm configuration. Diaphragm has also another problem in terms of buckling as it is restricted in all sides and there is no means to ease the strain as in case of cantilever beam. This major drawback of thermal buckling and sensitivity discouraged the use of the diaphragm based shear sensor.

4.7. Drag based sensors

Drag based sensors utilize the drag force generated by a moving fluid on a stationary body. Most of the sensors that work based on drag force have cantilever beam

configuration as the choice of sensing element by virtue of its sensitivity and moreover, cantilever configuration is also insensitive to static pressure. However drag based cantilever beam sensor has limitation in terms of inability to be used in large flow applications [174]. Applications with high dynamic pressure come with a need to protect the sensitive element from overloading in order to prevent large deflection. The protection becomes inevitable if the high pressure flow is accompanied by suspended particles (in the case of gas turbine engine application) as it is mandatory to provide a protection for the sensitive element from the solid particles in order to withstand the rugged conditions experienced in gas turbine engine.

4.7.1 Cantilever beam as sensing element for dynamic pressure

In a high temperature environment, diaphragm based sensors might abruptly fail because of the buckling of the membrane due to thermal expansion. Various membrane or micro plate based sensors use optical sensors to measure deflection of the sensitive element and they are mostly designed for room temperature [180,181]. Further in case the sensors have to be used in high temperature environment it is better to trade off this advantage of higher natural frequency due to its high sensitivity to thermal expansion and choose cantilever beam based sensor.

Drag based sensors are mostly based on cantilever geometry. The major advantage of this type of sensor is that it gives the magnitude and direction of velocity. The disadvantage is the presence of moving parts which may require frequent maintenance and replacement. Cantilever based micro sensors are very popular for flow as it is easier and faster to etch a cantilever beam rather than a diaphragm. Cantilever based drag force sensor draws its inspiration from nature in the form of fish lateral line

sensors [182] that is used to monitor surrounding flow and flow sensitive mechano-sensors of crickets [183]. The measure of deflection by optical means [184] or the strain at the bottom of cantilever [185] gives a measure of the velocity.

Drag based sensor made out of high aspect ratio (700 μm tall and 80 μm diameter) silicon cantilever beam with high aspect ratio performs well for measurement of velocity both in steady and oscillating flow with a detection limit of below 1 mm/s for oscillatory flow [186]. Grobe et al. [187] reported a novel micro optomechanical system based on a flexible micro pillar that utilizes a cantilever cylindrical micro pillar that could provide a reliable detection of forces in the range of about 5 -10 nN. MEMS based double beam cantilever flow sensor reported by Pang et al. [188] considers the influence of temperature in the sensing of velocity as temperature coefficient of resistance will gain importance with variation in temperature. They have suggested a correction equation including temperature compensation based on temperature in the range of 0 to 40 ^{0}C [188].

Most of the drag based sensors use cantilever beams or rods as sensitive elements. These sensors could be custom designed for range, sensitivity and maximum deflection based on the application for which the sensor is intended to be used. Deflection measurement is either done by optical means or by measuring the strain of the cantilever sensitive element. In high temperature domain piezoresistive strain gage cannot be used as means to measure the effect of flow on cantilever based drag sensor due to the cross sensitivity of resistance with temperature. However optical means of deflection measurement could be used as they are immune to temperature effects.

Even though cantilever based configurations is better than diaphragms in resisting buckling caused by thermal expansion at high temperature, there are other issues related to using cantilever configuration in terms exposing the sensitive element to unprecedented loading. Overloading of the sensitive element is an important aspect under these circumstances. Generally speaking drag force mode micro sensors are more suitable for small flow rates (ex. below 10 μl/min) [189]. This limitation is mainly due to excessive deflection that would be caused in case of high flow rate. This in turn would cause the deformation to enter into plastic deformation stage. Other disadvantage to this type of sensors is sensitivity to the particles in the flow [190].

The aerospace application is high frequency high flow situation where suspended particles are likely to be in the flow. These particles would contribute in the creation of instability in the sensitive element. These reasons strongly discourage the direct exposure of the sensitive element. This limitation resulted in a new type of sensing scheme that uses the pressure reduction formed by a bluff body to protect the thin sensitive element. This sensing scheme has two elements namely, a blocking element and a sensing element. The blocking element is thick and has a cantilever configuration and the primary objective of the blocking element is to act as a bluff body to produce a pressure drop behind it and the secondary objective is to protect the thin sensitive element from direct impingement of high dynamic pressure.

4.8. Summary

In this chapter different aeroelastic phenomena are described and the possibility of using these phenomena for sensing application for high temperature high flow application is discussed. Cantilever based sensitive element is an attractive choice for the lift force/drag force based sensors, however, shear force based sensors make use of diaphragms. Cantilever configuration is used mostly for low flow application due to problems of flutter and over loading issues. Diaphragm based shear force sensors even though could be used for high flow applications, need some special design to reduce the stiffness and make them more sensitive.

The GTE application considered in this thesis is a high flow high temperature application. Diaphragm based sensors cannot handle high temperature due to issues like buckling where as cantilever based sensors cannot deal with high flow due to overloading issues. This calls for a new sensing scheme that would provide overload protection along with the possibility of handling high temperature.

The new sensing scheme which uses indirect drag effect is the proposed sensor configuration discussed in the forth coming chapter. This scheme has protection in the form of a blocking element, which would protect the sensing element from the possible impingement from suspension particles and over loading.

Chapter 5 : Analysis of Proposed Drag Based Sensor for Dynamic Pressure Measurement

5.1. Introduction

MEMS technology and micro machining techniques have made possible the miniaturization of sensors. MEMS sensors have advantages in terms of small size, high natural frequency, low power consumption and are non intrusive. One of the most used configurations of the sensing element in micro sensors is the cantilever beam mainly due to the ease of fabrication [191]. Micro machined cantilevers were first introduced as force sensors in atomic force microscopy [192] where the cantilever beam is used to detect and amplify surface asperities. Cantilevers are the choice of sensing elements for micro resonators [193], chemical reaction detectors [194], humidity sensors [195] and for measuring protein aggregation [196] for bio medical applications because of better sensitivity.

Drag force measurement is based on the principle that drag force causes a displacement of the sensing element, which induces a corresponding change in output of the piezo resistors or strain gauges [197,198]. In drag based sensors the flow is perpendicular to the sensitive element and the drag force is the cause of deflection.

Aircraft engines especially for military application are exposed to foreign object damage (FOD) due to ingestion of sand, or dust. Aircrafts operated in harsh environments in mid 60s had an average operating life of about 300 hours; however engine protection systems such as inlet particle separators, erosion resistant coatings could push the limits of operation [199]. Desert operations in Middle East where sand erosion was prominent in detrition of GTE parts used in helicopters and tanks and forced engine removal in as

little as 100 hours [199]. Even civilian aviation has faced problems due to volcanic ash hazard. Tests in university of Cincinatti showed that volcanic ash is four times more erosive than quartz sand [200]. These situations explained above emphasize the need for protecting the sensing element from the direct exposure of suspended particles.

5.2. Sensor configuration

If a sensor has to work in high temperature environment with high level of foreign body ingestion it must be protected properly for effective functioning. This yields to a novel sensing scheme based on two elements, sensitive element covered by the blocking element. The blocking element is kept between the flow and the sensitive element. The pressure drop caused by the blocking element which is proportional to the input dynamic pressure and created because of the obstruction of flow produces the deflection of the sensitive element. Both the sensitive and blocking element of the proposed sensor are in the form of cantilever beams as they have superior capabilities in terms of performing under high temperature conditions.

Figure 5.1 shows the proposed configuration of the sensor in macro scale. The flow causes the tip of the sensitive element to bend towards the blocking element (upwards) if the gap between them is maintained appropriately [201]. However in this type of sensing it should be understood that there is a grave need for calibration as the flow is modified by the presence of the blocking element.

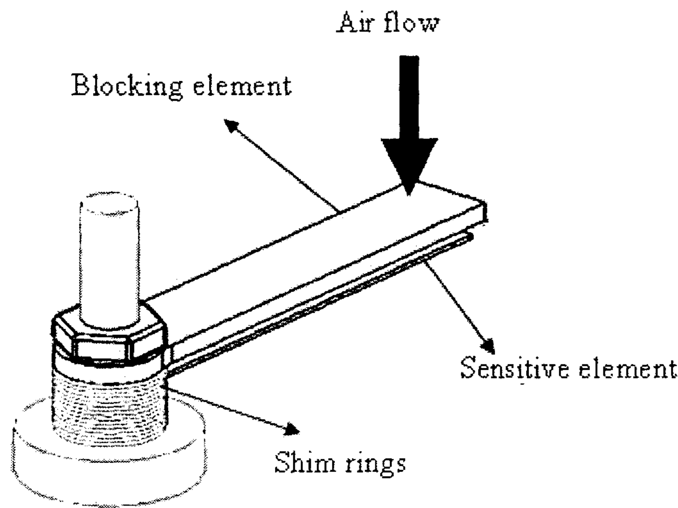

Figure 5.1: Experimental configuration of sensor setup

The function of the blocking element is to protect sensitive element against direct contact with the flow thereby preventing the sensitive element from particle impingement and also to produce a pressure drop proportional to the incoming dynamic pressure that would cause the sensitive element to deflect towards the blocking element.

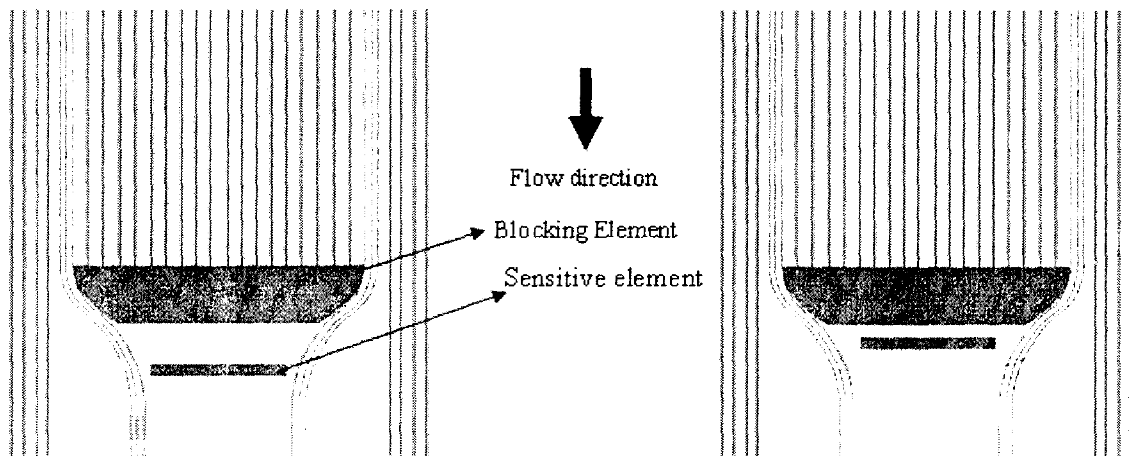

Figure 5.2: Front view of the tip of sensitive element before and after deflection

Figure 5.2 illustrates the deflection of the tip of the sensitive element before and after deflection. One of the major advantages of this type of sensor with blocking element and sensitive element is the limitation offered by the blocking element for higher

deflection. Blocking element restricts the maximum deflection of the sensitive element to the gap between them, thus eliminating a common problem faced by most of the drag based sensors. In addition to functionality the blocking element could also provide convenient packaging. Hence it is mandatory that the blocking element is significantly thicker than the sensitive element. Thicker blocking element would resist the high drag force produced by the impinging flow and will provide adequate support to the sensitive element in case of overloading.

5.3. Experimental investigation

Preliminary investigation of the phenomenon of the drag effect on which the proposed sensor is based is demonstrated by an experiment using a scaled up model with sensitive element made from aluminum strip and the blocking element made from steel. The configuration of both the blocking and sensitive elements is taken to be cantilever shape as cantilever configuration is easy to fabricate at micro scale.

The influence of the input pressure and the gap (between the sensing element and the blocking element), on the performance of the sensor is experimentally studied on a scaled up model. The deflection of the sensitive element is caused by the pressure drop created by the blocking element that is proportional to the dynamic pressure that is impinging on the blocking element. The measurement of deflection to quantify dynamic pressure requires a complete understanding on the configuration of the blocking element sensitive element assembly most importantly the gap between them. The blocking element used in the experiments had rectangular cross section with the width of the blocking element being 33% higher than that of sensitive element for better performance.

This choice is made by trial and error to minimize the disturbances on the sensitive element caused by the flow. The sensitive element is very thin in the order of 30 microns, with rectangular cross section for maximum sensitivity.

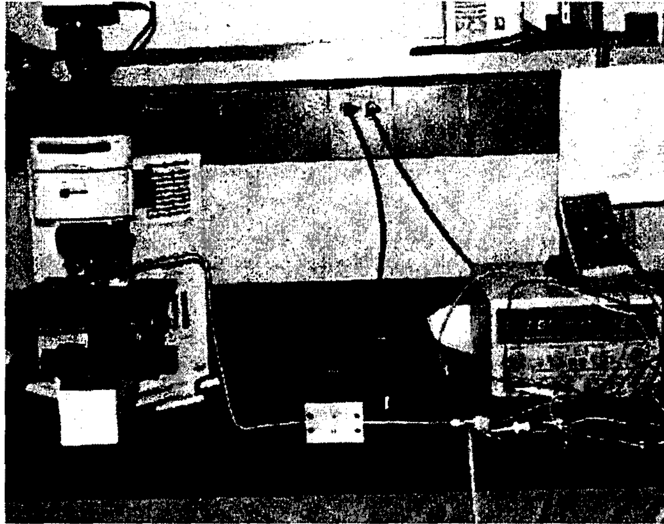

Figure 5.3: Experimental setup

This preliminary experiment is performed in a confined environment under the microscope and the static line pressure is related to the deflection of the sensitive element under steady condition. However, a more detailed investigation using jets has been carried out and presented at the later part of this chapter that relates the pressure drop caused by the dynamic pressure and the deflection of the sensitive element.

The experimental setup consists of blocking element, sensitive element, and spacing shim rings packed together in stud, optical breadboard for accurate positioning of the stud, microscope, image acquisition camera and mirror for optical measurements, static pressure sensor (to measure the line pressure) with a range of 1 - 5 psi (6.89 – 34.5 kPa), XYZ positioner for fine tuning, air source and air tubing. The compressed air is directed through a valve (at the desired pressure using a regulator) through the copper tubing.

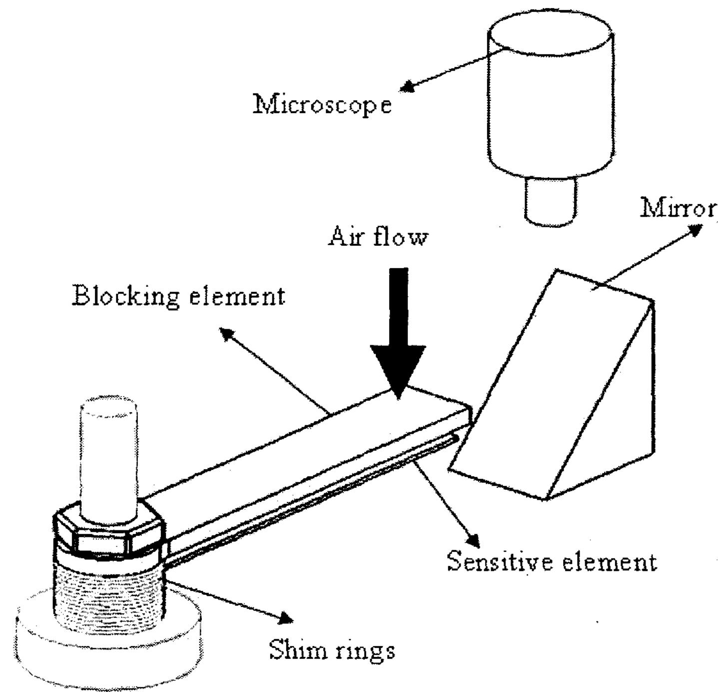

Figure 5.4: Experimental setup – schematic layout

Figure 5.4 shows the schematic diagram of the experimental set up in macro scale using aluminum sensitive element and steel blocking element that were used to demonstrate the sensing phenomenon at room temperature condition [201]. The air flow past the blocking element creates a pressure drop behind the blocking element. With the increase in the velocity of the air the pressure drop increases to a level wherein the sensitive element deflects towards the blocking element if the gap between them is appropriately set. The deflection of the thin sensitive element which is a thin flat aluminum strip will be focused by the microscope through the mirror as shown in figure 5.4. The image of the tip of the cantilever sensitive element is reflected through the mirror and deflection is measured using a microscope with graduated eye piece. The gap between the blocking element and the sensitive element is maintained using a shim ring of thicknesses in the range of 300 microns to 500 microns. This deflection could be correlated to the air flow velocity or in turn, to the dynamic pressure. Figure 5.5 shows

the side view of the cantilever sensitive element (not the tip) that shows the deflection through the microscope.

Figure 5.5: Side view of the cantilever sensitive element as zoomed in the microscope

The major positioning is performed by the adjustment knob of the microscope and the XYZ positioner is used for fine tuning of distance between the end of the copper tube and the block.

Figure 5.4 shows the experimental setup with the blocking and sensitive element. The sensitive element is made from aluminum strip with E =170 Gpa which is 27 mm long, 6 mm wide with thickness of 38 microns. The air is blown above the blocking element exactly perpendicular to the tip of the sensitive element.

The deflection is influenced by the following parameters

- Geometry of the sensing element including thickness, width, length of the sensitive element, distance to the clamping point, cross section of the sensitive element. The flow past the blocking element produces a difference in pressure on the sensitive element. The sensitive element is basically a cantilever beam subjected to load caused by the flow. Hence the tip deflection is directly

proportional to the load, length and inversely proportional to the width, thickness and Young's modulus.

- Gap between the air source and the blocking element

The air flow is through an orifice on the copper tube, and the vertical distance between the blocking element and the air duct is 1143 microns. The distance 1143 microns is calculated using the lead of the screw of the XYZ positioner. XYZ positioner has 3 screws on X, Y and Z directions with the lead of the screw to be $1/1000^{th}$ of an inch. The distance was based on trial and error for maximum sensitivity for a specific diameter of the perforation. The diameter of the hole is 3572 microns.

- Gap between the blocking element and the sensitive element

The influence of the gap is unknown and hence the experiment was done with three different spaces between the blocking element and sensitive element of 1500 microns, 900 microns and 600 microns. Above 1800 microns and below 600 microns the gap does not create significant deflection due to the fact that the sensitive element is too close or too far from the blocking element and there is no significantly higher pressure drop between the blocking and sensitive element.

Hence the sensor has more geometric features as listed above enabling to tailor the design to suit a specific application. The entire pack of sensitive element, shim rings and the mirror is placed on an optical bread board which would rest on the microscope base. An optical bread board of 6 x 6 inch was used. The side of the sensitive element is focused through the mirror to the microscope that shows the deflection of the sensitive element towards the blocking element in the upward direction.

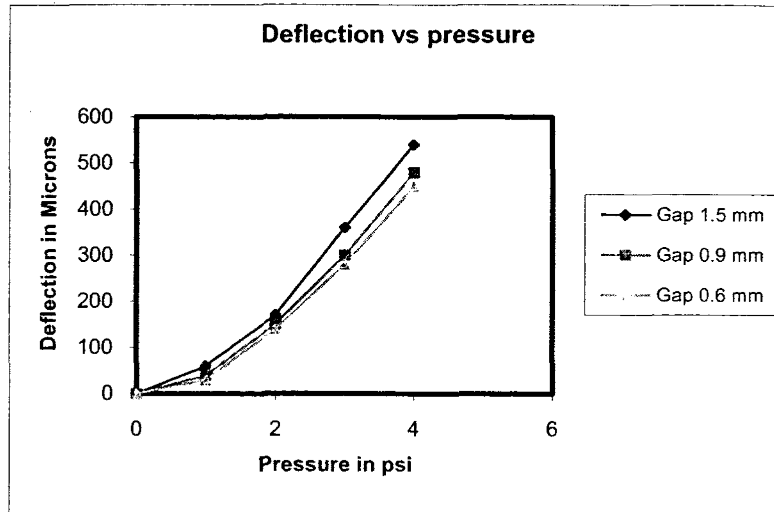

Figure 5.6: Graph (obtained experimentally) depicting deflection versus pressure

The deflection of the sensitive element is due to the dynamic pressure imposed on the blocking element even though the flow that causes the dynamic pressure is steady flow. The temperature and gas density were corresponding to the room temperature

The pressure which is used as a reference in figure 5.6 is the line pressure in the copper tubing. It is varied from 1 to 4 psi (6.89 –27.6 kPa). The reason for low line pressure is due to the fact that higher pressures make the sensitive element to stick to the blocking element. This is a case of overloading which sensors are supposed to overcome.

In order to be used in a dynamic pressure environment the deflection has to be correlated with dynamic pressure and not with the static line pressure as in the previous case. This requires a modification in experimental setup that would create flow with different velocities. This called for the need of an experimental set up using jets that would create a flow whose velocity would decay with the increase in distance from the tip of the nozzle. This is an easy way to generate flow of air with different velocities. As a first step the jet has to be characterized so as to have some knowledge on the velocity pattern.

5.3.1 Jets – introduction

The turbulent jets have been a basic element of study of free shear flow and it dates back to 1850s. Jets are classified into many types based on the conditions that influence the jet in downstream. If the air jet is not influenced by any obstructions then the jet is called free jet. On the contrary if the air jet performance is influenced by reverse flow, created by the same jet entraining ambient air then it is confined jet. Mixed jet has more than one type of jet mixing to form a new stronger jet. When considering the temperature difference between the supply air and room ambient air, the air jets can be divided into isothermal jets and non isothermal jets.

To generate different velocities a free axisymmetric isothermal jet is considered and a pressure regulator is used to regulate the line pressure that supplies pressure to the nozzle.

In ASHRAE literature, jet is divided into four zones based on the centerline velocity decay [202].

Zone 1, a conical zone where centerline velocity is equal to outlet velocity

Zone 2, a transition zone where the velocity starts to decrease, often approximated as proportional to x $^{-0.5}$, where x is the axial distance

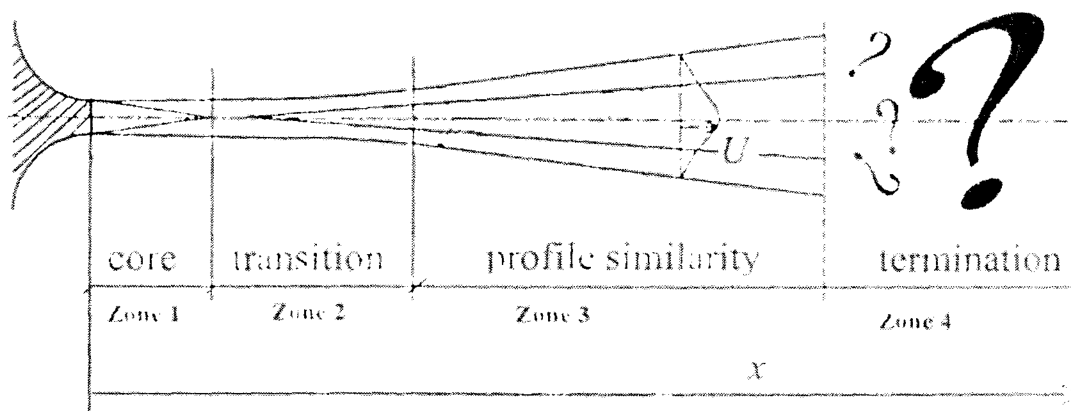

Figure 5.7: Jet expansion zones [202]

Zone 3, where transverse velocity profiles are similar at the different value of x and velocity decay is assumed proportional to x^{-1}.

Zone 4, the jet terminal zone where the centerline velocity rapidly decreases.

For an axial jet, the first two zones are strongly influenced by the diffuser, the third zone is the developed jet, and the fourth zone represents the jet termination. In the first three zones room air is entrained into the jet and mixed with supply air. In the fourth zone the jet collapses inward from the boundaries and the supply air is distributed to the room air as the jet disintegrates.

The characterisation of jet is mostly approached experimentally as the analytical solution for a problem with an open boundary cannot be obtained by wholly analytical means [203]. Experimental methods using pitot tube was mostly used to characterize compressible jet as early as 1954 by Walter [204] followed by Donaldson et.al, Jones and Birch et.al [205,206,207]. Recent computational power and advancement in numerical simulation tools also could simulate and predict the jet characteristics [208,209].

There are accurate models in commercial CFD codes that would accurately predict the dynamic pressure distribution and velocity decays in jets, however, an experiment would yield a more realistic dynamic pressure distribution and hence on the characterization on the proposed sensor.

5.3.2 Jet characterization

Jet characterization enables to generate different dynamic pressures that would act as input to the proposed pressure sensor. The experimental setup consists of a compressor

connected to storage tank. Figure 5.8 shows the experimental layout for jet characterization where, a feedback compressor maintains a constant pressure in the storage tank. The compressor and storage tank are connected by a feedback system that would ensure the storage tank pressure to be 100 psi (~ 690 kPa). The exit of the storage tank has a flow control valve that is used to maintain constant flow rate. The line pressure has to be maintained constant as this defines the nozzle exit velocity and eventually the velocity decay. A pressure regulator would follow the storage tank that would maintain constant pressure at the outlet while maintaining a constant flow rate. These aspects ensure repeatability.

The pressure at the exit of the regulator could be set by connecting a dial indicator between the regulator and the nozzle. The diameter of the nozzle is $1/8^{th}$ of an inch and it is held in position by means of XYZ positioner. The XYZ positioner has a maximum displacement of 1 inch on x, y and z axes with a resolution of $1/1000^{th}$ of an inch. The XYZ positioner is required to accurately position the tip of the nozzle on top of the optical breadboard on which the set up is mounted on.

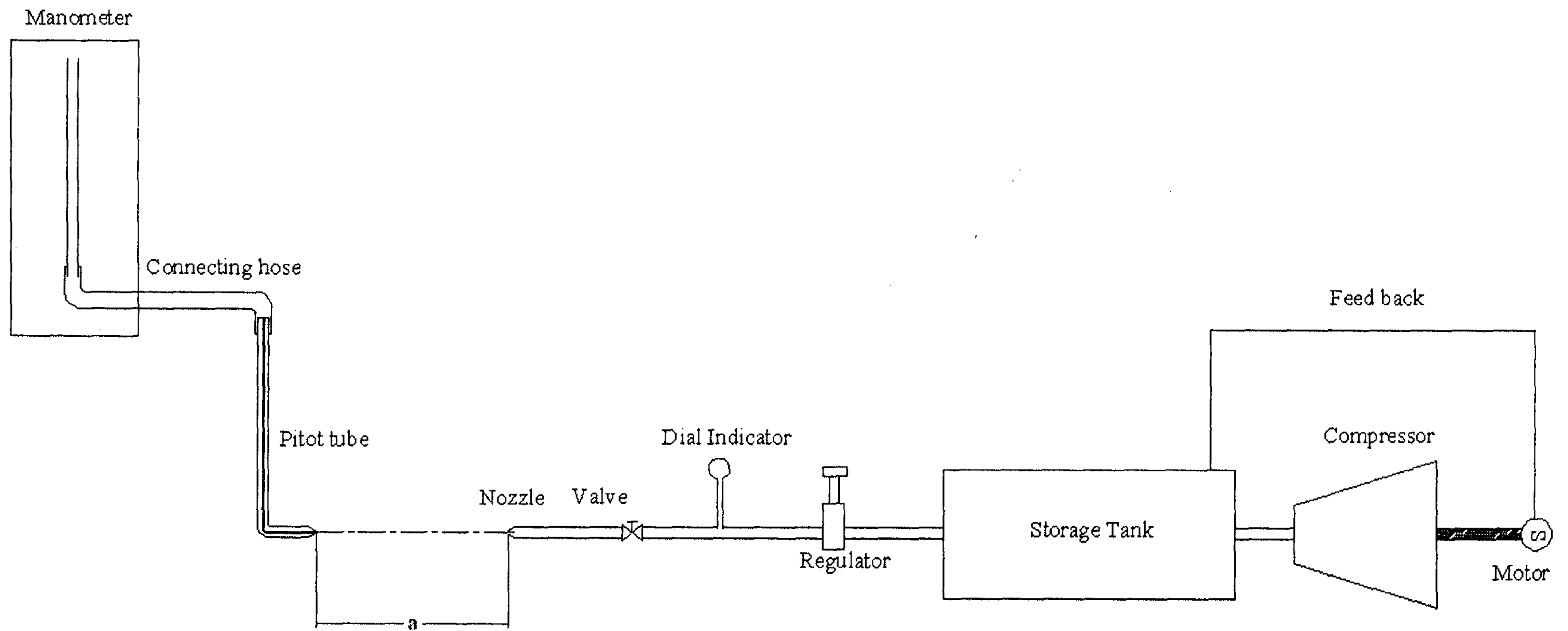

Figure 5.8: Experimental layout for jet characterization

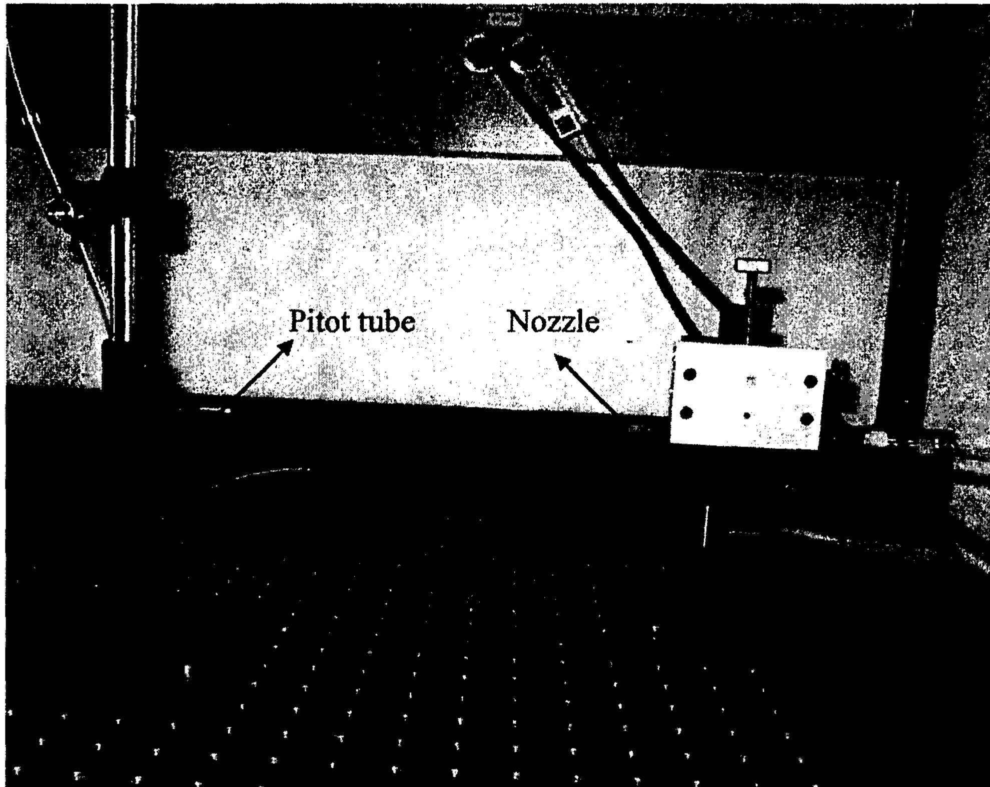

Figure 5.9: Nozzle and pitot tube arrangement

The entire set up of the nozzle arrangement is mounted on an optical breadboard with 1/4"-20 tapped holes with a spacing of 1 inch (25.4 mm) between the centers of two adjacent holes. The optical bread board with center to center distance of 1 inch (25.4 mm) provides an opportunity to measure the velocity at different points. The space between these points depends on the resolution of the optical bread board. This limits the distance between the nozzle and the pitot tube in terms of 1 inch (25.4 mm) resolution. Pitot tube is used to measure the point velocity followed by velocity sensor TSI VELOCICALC to confirm repeatability.

Based on the characterization of the jet, experiments were carried out to demonstrate the drag based phenomenon which is the operating principle of the proposed sensor.

Figure 5.10 shows the variation of velocity with respect to the distance. This graph shows the possibility of generating any velocity between 0 -120 m/s by positioning the sensor arrangement at different distances. The graph shows four points along the same distance which is along the x axis, where these points correspond to four different line pressures 60, 70, 80 and 90 psi (413.7, 482.6, 551.6, 620.53 kPa).

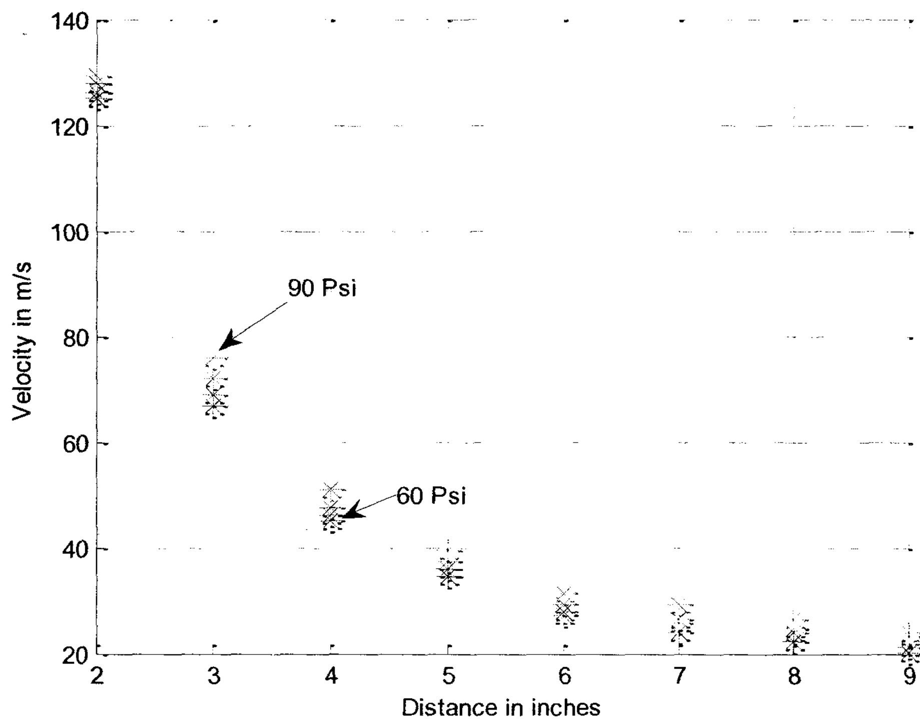

Figure 5.10: Jet velocity decay with distance

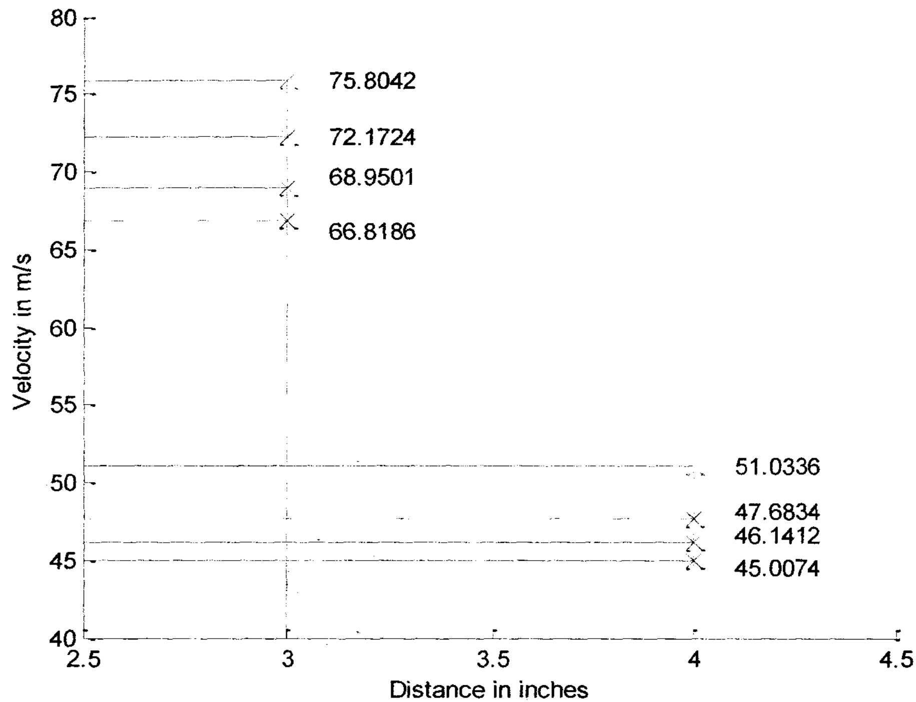

Figure 5.11: Zoomed in view of figure 5.10 within the area of interest

Figure 5.11 depicts the velocity decay graph for four different line pressures. The velocities at two different distances of 3 and 4 inches (76.2 mm and 101.6 mm), respectively, from the nozzle are marked in the graph. These velocities at the blocking element cause a pressure drop proportional to the input velocity which is experienced by the sensitive element. The sensitive element deflects towards the blocking element, and the measure of this deflection is indirectly a measure of the input velocity.

5.3.3 Tip deflection measurement

The blocking and sensing element units are kept under the microscope to measure the tip deflection. The experimental setup is shown in figure 5.12. The nozzle feeds in the air at desired velocity. The regulator controls the line pressure and flow rate is maintained constant so as to reproduce the velocity exactly. The tip deflection is measured under the microscope. The scaled up model is used instead of a micro level model using SiCN as it

is easy to measure deflection in a scaled up model as compared with its micro counterpart.

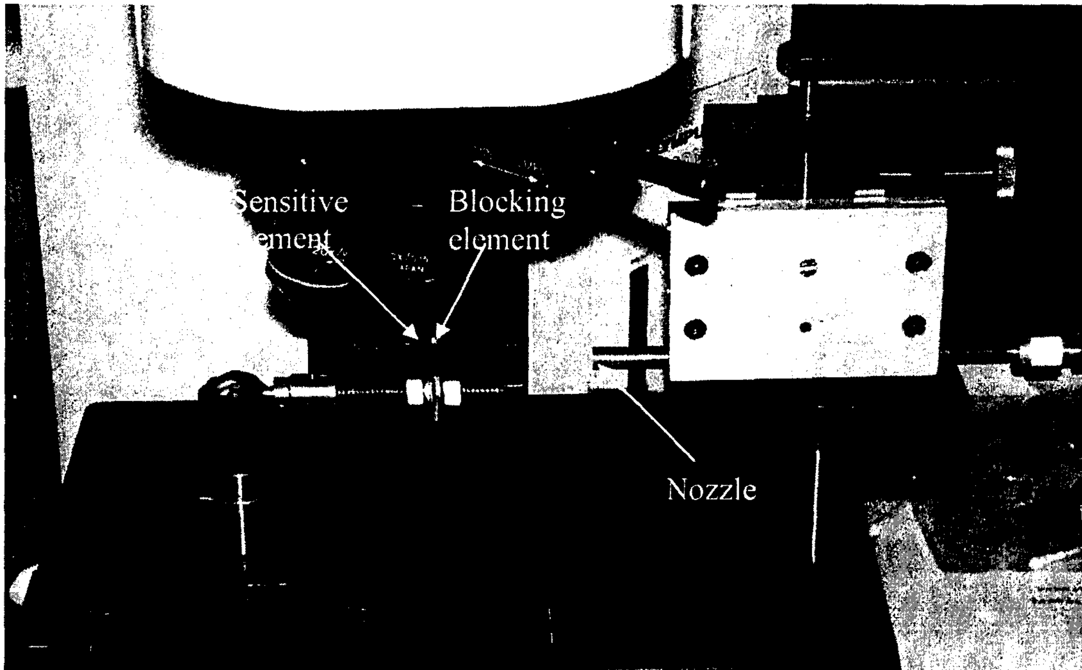

Figure 5.12: Deflection measurement set up

The deflection of the tip of the cantilever beam is measured using the microscope and the trend is as shown in the figure 5.13. The deflection varies in a non linear fashion but is proportional to velocity and the gap between the blocking element and sensitive element. The blocking element is steel plate with thickness 3 mm and length 1.3 inch (33.02 mm). The sensitive element is a thin aluminum strip of 30 microns thickness with a length of 1 inch (25.4 mm) and width of 4 mm. The gap is maintained by combining shim rings of standard thicknesses of 300 microns and 500 microns. The distance between the nozzle and the blocking element was fine tuned using the XYZ positioner. The same setup explained in figure 5.8 is used to generate dynamic pressure except the pitot tube setup is replaced by the microscopic arrangement to measure deflection.

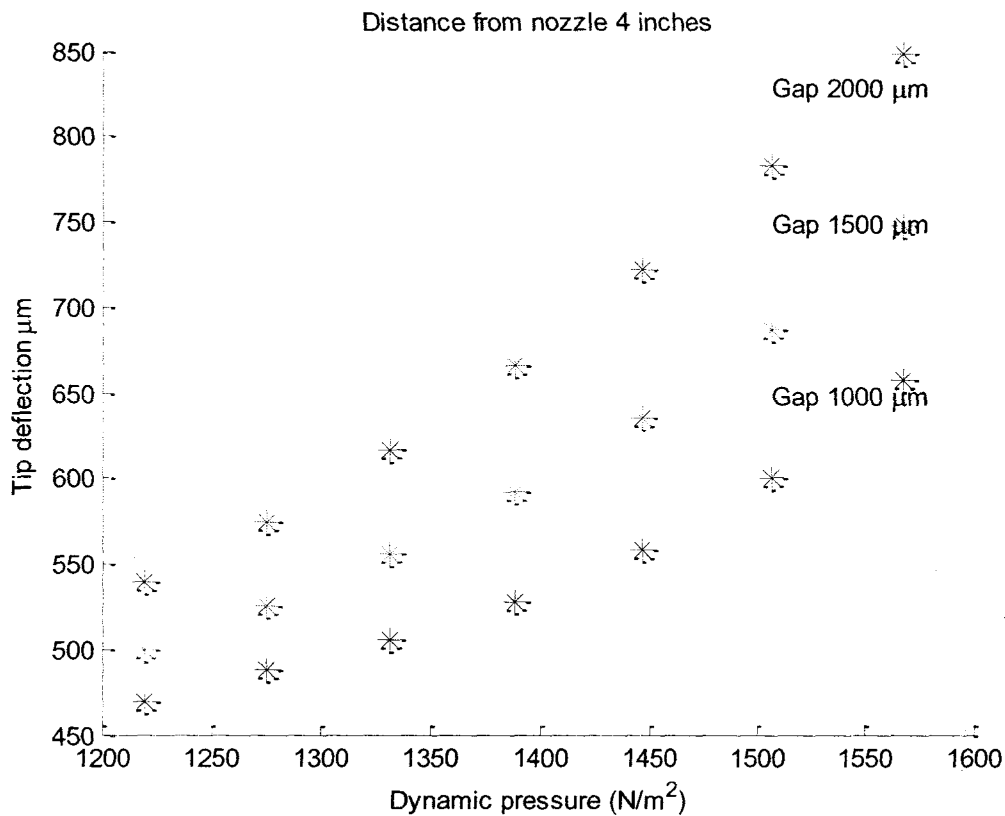

Figure 5.13: Tip deflection at different velocities as measured from figure 5.12

The experimental results show the dependency of the deflection of the sensitive element with dynamic pressure imposed on the blocking element. The blocking element arrangement provides a pressure reduction on the sensitive element. This enables such type of sensor to be suitable for high dynamic pressure conditions without actually exposing the sensitive element to the flow. This reduction in pressure provided by the blocking element is also dependent on the gap between the blocking element and the sensitive element. Figure 5.13 illustrates the dependency of the tip deflection on the distance between the blocking and sensitive element depicted as gap. The initial experiments carried out which is illustrated in figure 5.7, also emphasizes the dependency of the gap on the tip deflection.

5.3.4 Stress analysis

Stress analysis for any structure is integral part of design. Cantilevers are extensively used micro structure in MEMS [210]. Micro cantilevers are used to measure surface stress changes [211] and for atomic force microscopy [212] require detailed study of stress distribution. Further the design of sensing element in a sensor has to be conceived not only for normal purposes but also for conditions of uncertainties like over loading. During normal operation the deflection of the cantilever beam can be correlated to the stress developed in the beam.

$$\sigma_{\max} = \frac{Mz}{I} \tag{5.1}$$

where

M is the bending moment

z is the distance from neutral axis to outer surface where maximum stress occurs

I is the moment of inertia I_{zz}.

Equation 5.1 corresponds to the linear domain as the tip experiences small deflection and it does not enter non linear domain until a contact with the blocking element is established. The maximum stress is found near the fixed end. The loading profile is assumed to be uniformly varying load with maximum intensity at the tip. The cantilever beam has a length of 1 inch (25.4 mm) with its width being 4mm and thickness is 30 microns. The material of the beam is aluminum. The stress value is found based on the load calculated from the deflection assuming uniformly varying load. The maximum stress is near the fixed end and is plotted for various velocities as shown in figure 5.14. The yield stress for aluminum material used is 215 MPa and the maximum stress for flow velocity of 51 m/s corresponding to a gap of 2000 microns is around 5.03 MPa.

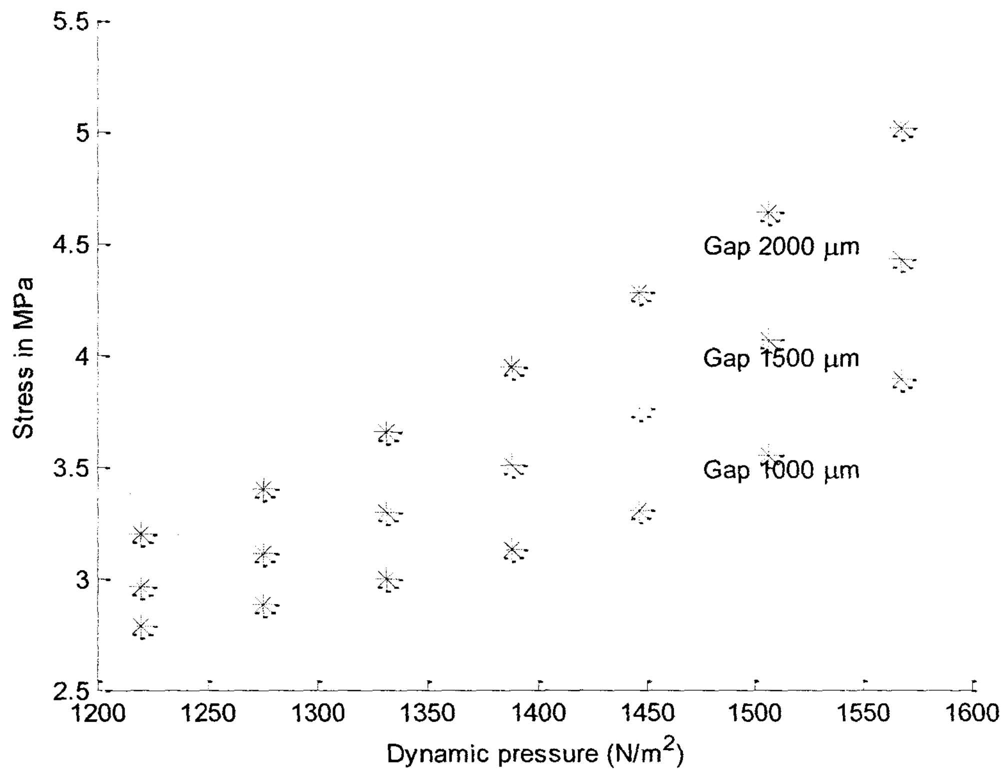

Figure 5.14: Stress at fixed end for different velocities

It was observed during the experiments that at higher velocities the sensitive element deflection is so high that it is snaps with the blocking element. This overloading issue should be addressed as this would increase the stress on the sensitive element.

5.4. Overloading of the sensitive element

In developing the sensor it is most important to design a proper sensing mechanism that would convert the given input to required output accurately. The sensing accuracy which is one of the most important requirements of the sensing mechanism depends on the stiffness of the sensing element. Hence it is important to make the sensing structure more sensitive. A sensitive structure implies that it is incapable to withstand unexpected forces. For example the sensitive element for a pressure sensor with

maximum pressure of 5 bar is not designed to withstand higher pressure by increasing the thickness of the sensitive element because increasing the thickness decreases (the deflection per unit load) sensitivity. Hence sensitive element has to be designed to withstand higher load without compromising sensitivity. This calls for overload protection.

Sensor design should consider overload bearing capacity in case of unprecedented input variations caused by the uncertainties in application. Pressure sensor is no exception and mostly sensor designers build the sensor system with overload protection. The most common overloading protection is done using external overload protection stop that prevents the sensitive element from being loaded beyond their limit [213]. Some applications that may not allow implementation of stops for overload protection, requires stiff sensitive element (sensitive element that are prestressed). Also linearity degrades with higher deflection and this would be compensated by reducing the dimensions (length and width) of the sensor thereby increasing the stiffness. But this dimension change is limited by resolution, handling capacity and space for assembly [214].

All strategies for overload protection use mechanical stoppers like pins but these methods require external parts for protection [215]. One interesting overload protection without any additional parts was realized using H shaped slots along the thickness of the cantilever beam type sensitive element [215].

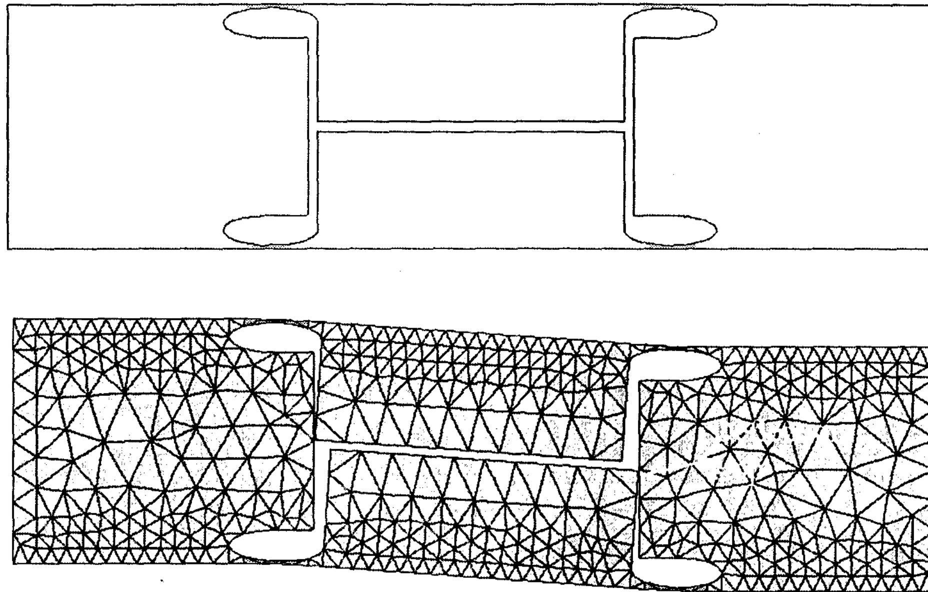

Figure 5.15: Overloading protection strategy H slot along the thickness [215]

The H-slot structure cannot deform more than a certain limit since the slot structure locks further deflection as depicted in figure 5.15. This kind of special design comes with the design flexibility on the stoppers acting point by changing breadth of the notches, beam length, thickness etc. This special design has a negative aspect in terms of stress concentration due to slot formation.

Overloading issue is sometimes unavoidable in industrial applications, for example, as in tank level sensors for liquid [216]. If there is a fault in the valve that supplies the liquid to the tank or in the bypass valve that maintains the pressure , the hydrostatic pressure experienced by the sensor increases beyond the normal routine. Capacitive differential pressure sensor with a range of 100 kPa and overloading capacity of 25 MPa is used to measure tank level [217] This is a typical application where the sensor is exposed to high hydrostatic pressure and should survive high overpressure range due to uncertainties in the working conditions eg: failure of valve.

Overload protection issue is also prominent in beam based sensors. While many beam arrangements are possible, most designs have used either a cantilever or a doubly fixed beam configuration [218]. The cantilever beam configuration is more sensitive than doubly fixed configuration due to the fact that the maximum deflection of a cantilever beam is higher than the maximum deflection of the doubly fixed beam under same loading and geometric conditions. This advantage offers the potential for batch fabrication because cantilever design of a given sensitivity can be fabricated in a smaller area [217]. However basic cantilever design is less resistant to overloading than double fixed beam design by virtue of its reduced stiffness. Under overload conditions a cantilever design continues to bend in the same way as it bends under normal conditions. In bending mode, stress is concentrated along one surface of the beam and the beam breaks. In contrast a doubly clamped design under overload can go into linear tension as well as bending stress distributing the overload throughout the thickness of the beam and hence supporting a greater overload than a cantilever design of equal sensitivity [217].

Cantilever beam arrangement needs more over range protection features than double fixed beam. In the proposed sensor configuration the blocking element also acts as an overload protection stop for the sensitive element as the deflection is towards the blocking element. The maximum tip deflection of the cantilever beam is limited by the gap between the blocking element and sensitive element.

5.4.1 Deflection regime

Excessive loading conditions could make the sensitive element to touch the blocking element and there will be a serious stress formation on the thin cantilever

sensitive element. Sensor design should accommodate this unprecedented loading and it is mandatory to study the stress values at this over range pressures.

There are two types of deflection regime as shown in figure 5.16

Case 1: Deflection that is caused by the load when the sensitive element does not touch the blocking element.

Case 2: Deflection results in the sensitive element touching the blocking element and being supported by it, which happens only under excessive loading conditions.

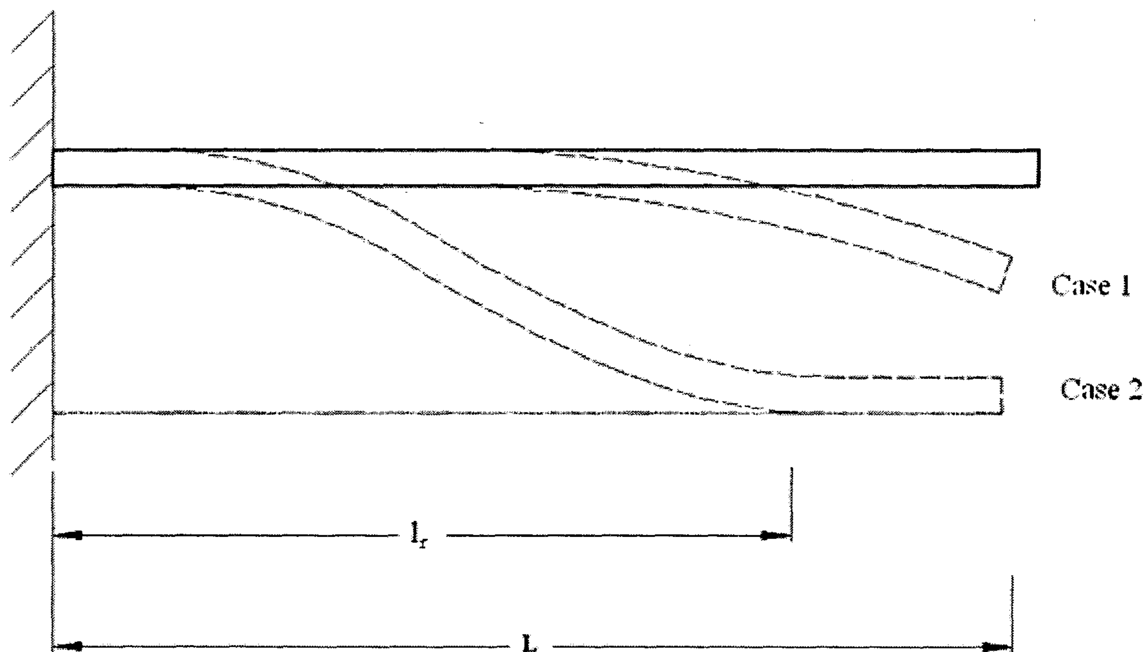

Figure 5.16: Deflection regimes of sensitive element

Overload protection measure as in case 2 type deflection in figure 5.16 is also used as way to increase the range of the force sensor by restricting the deflection of a silicon diaphragm using a spring whose stiffness can be varied [218]. The spring part is associated with the fine measurement of the measurand that defines the resolution.

Let δ be the gap between the blocking element and sensitive element which would be the maximum deflection that the sensitive element could attain as any deflection

higher than δ will be restricted by the blocking element. The limiting load will be the load that causes the tip of the sensitive element to deflect by δ thereby touching blocking element.

Any load higher than the limiting load will cause the sensitive element to deflect till δ and then will be supported by the blocking element. Assuming the supported part remains straight which in this case is true as blocking element is made thicker than the sensitive element and there is no bending moment acting on the flat portion of the beam and the load is balanced by distributed reaction. However, at the part C as shown in figure 5.17 there will be a concentrated reaction that is unbalanced and that causes a slope at the tip C [219].

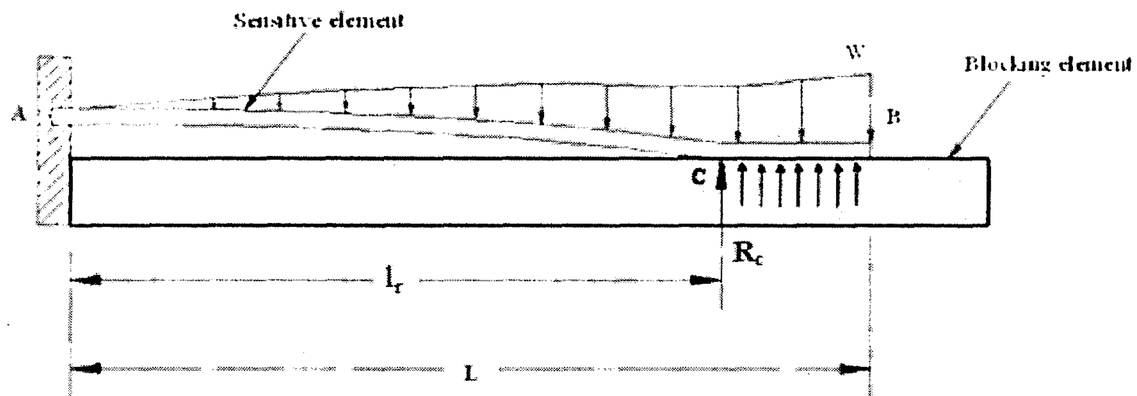

Figure 5.17: Sensor scheme at over loading conditions

Let w be the load / length which is more than the limiting load that causes the sensitive element to touch the blocking element. Now the sensitive element could be considered as a cantilever beam with uniformly varying load w with a length "l_r" less than L and a tip reaction R_c as shown in figure 5.17. To find out the tip reaction the slope and deflection at point C are considered. Uniformly varying loading profile is considered to match the experiment. Air flow from the nozzle with diameter of 1/8th of an inch impinges on the tip of the sensitive element that is 1 inch length. The jet when diffuses

had maximum velocity at the center and was progressively decreased to a very low value towards the periphery. The slope at the point C caused due to uniformly varying load will be equal to the slope caused by the reaction R_c at the point C.

$$\frac{wl_r^3}{8EI} = \frac{R_c l_r^2}{2EI} \tag{5.2}$$

From which (5.3)

$$R_c = \frac{wl_r}{4}$$

At point C the deflection in the gap will be δ, which is the tip deflection caused by the uniformly varying load against the tip deflection caused by reaction force at C.

$$\frac{11wl_r^4}{120EI} - \frac{R_c l_r^3}{3EI} = \delta \tag{5.4}$$

Substituting $R_c = \frac{wl_r}{4}$ yields

$$\frac{11wl_r^4}{120EI} - \frac{\left(\frac{wl_r}{4}\right)l_r^3}{3EI} = \delta \tag{5.5}$$

The reduced length of the cantilever beam could be derived as

$$l_r = \sqrt[4]{\frac{120EI\delta}{w}} \tag{5.6}$$

And the reaction force on the tip of the cantilever beam will be

$$R_c = \sqrt[4]{\frac{15EIw^3\delta}{32}} \tag{5.7}$$

5.4.2 Stress involved in overloading

During the experiments it was noticed that under excessive flow conditions sensitive element was overloaded and supported by the blocking element. This restriction

offered by the blocking element created a non linear deflection of the sensitive element. Even though the restriction acts as a deflection stop which is a major advantage provided by this type of sensor, excessive loading even with a deflection stop would result in the excessive stress development when the contact distance becomes larger.

Contact problems occur frequently in engineering stress analysis, even though some problems could be solved using the known solutions [218] most of the configurations encountered in practice are too complex to be solved via classical methods [221]. To resolve these issues finite element analysis (FEA) is a natural tool [221] as FEA could provide point to surface or surface to surface contacts. ANSYS model using contact elements (CONTAC 52) were used to model this overloading situation.

The blocking and sensitive elements are cantilever beams that are taken to be of same dimensions in terms of the length and thickness except for the width as there is more interest in the contact area. The width of the blocking element is made the same as that of the sensitive element. This would spare unwanted computational time and complexity in the model. The material of blocking and sensitive element is aluminum with Young's modulus of 70 GPa. The dimensions of the elements are length 25.4 mm. width 4 mm and thickness 30 microns. The gap between the blocking element and the sensitive element is 2mm.The blocking and sensitive elements were modeled using solid45 elements and the gap between them is modelled using CONTAC 52.

CONTAC 52 is a surface to surface contact element that represents the space between two surfaces which may maintain or break physical contact and may slide relative to each other. The capability of the CONTAC 52 element to deal with the surfaces that make and break contacts and the possibility of introducing zero stiffness

between the contact surfaces as the resistance offered to the deflection by the air available in the gap between blocking and sensitive element is infinitesimally small. The contact element gets into action only when contact is established i.e. when deflection exceeds the gap.

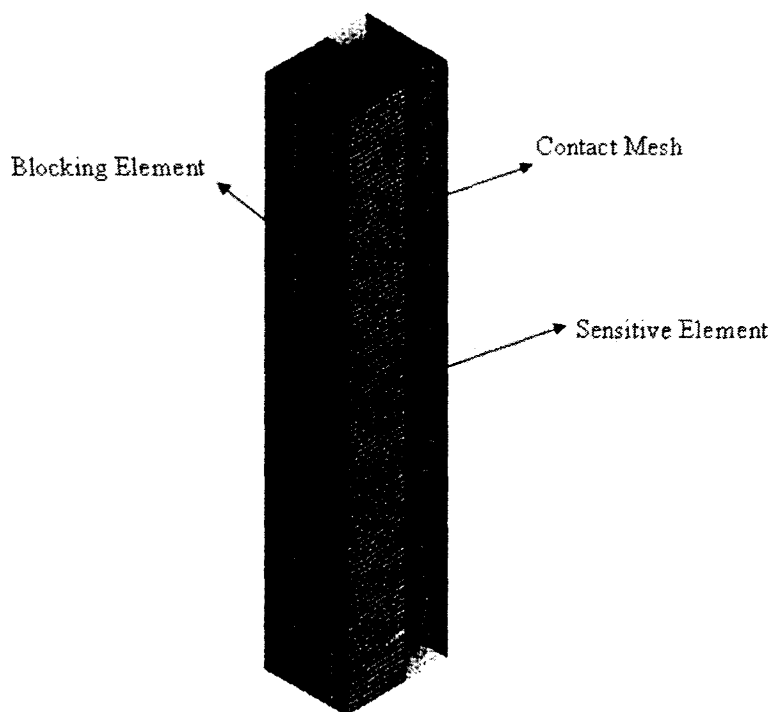

Figure 5.18: ANSYS contact model

During the experiment as the nozzle is pointed towards the tip of the sensitive element the velocity would be maximum near the tip and it would progressively drop down towards the fixed end. To match with this situation, the assumed load profile is triangular load with maximum intensity of load on the tip and zero intensity on the fixed end.

The tip deflection before actual contact with the blocking element matches with the tip deflection of a cantilever beam of length l, Young's modulus E and moment of inertia I, with a uniformly varying load with the maximum intensity of load w_1 at the tip.

The figure 5.19 illustrates a uniformly varying applied pressure on the sensitive element with varying magnitude as shown by the color code.

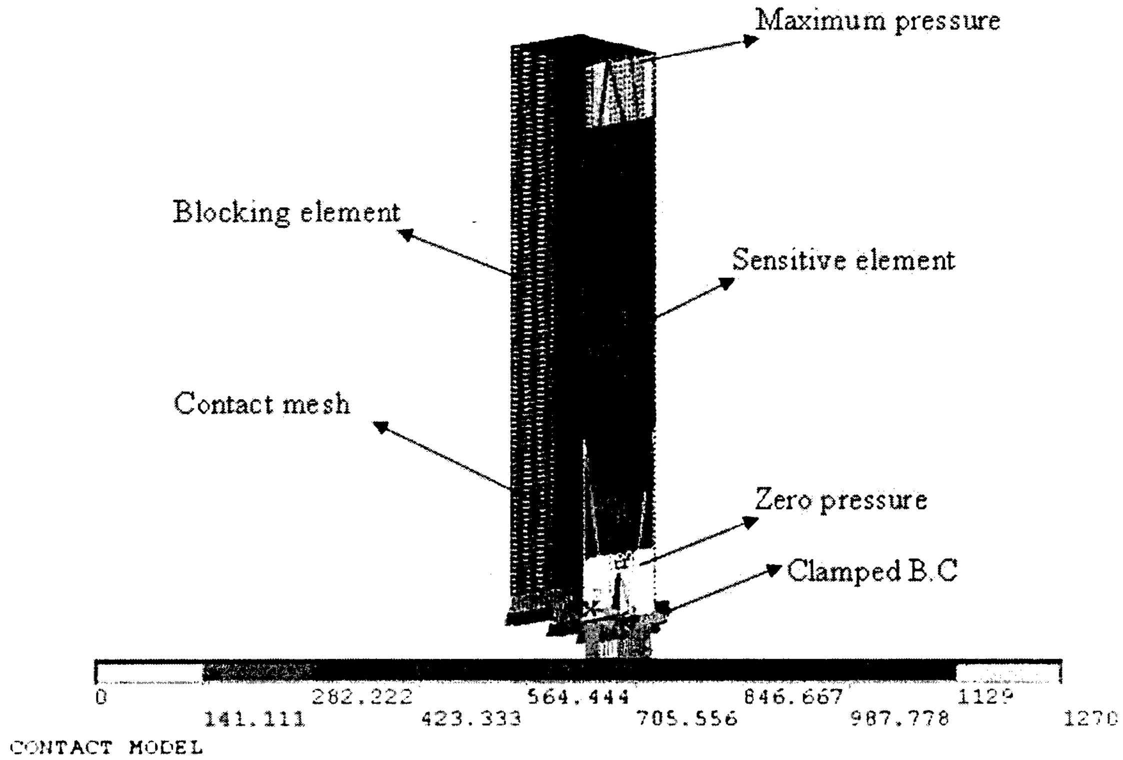

Figure 5.19: Sensitive element with applied pressure

Uniformly varying profile is used as the loading profile, since the flow velocity is maximum at the tip of the sensitive element and minimum at the fixed end. The gap between the blocking element and the sensitive element is maintained at 2 mm. The gap between the blocking and sensitive element is modelled using contact element CONTAC 52 which is a solid - solid contact element.

The maximum pressure intensity is at the tip of the cantilever sensitive element. The value 1270 N/m^2 corresponds to the pressure per meter length of 50,000 N/ m^2, i.e. for a length of the 1 meter the intensity of pressure varies from 0 to 50,000 N/ m^2 and hence for a length of 25.4e-3 m, which is the length of sensitive element the pressure

intensity value is 1270 N/m^2. The value is chosen so that the deflection would be in case 2 regime of deflection in figure 5.17. Reduced length is the length that is calculated after subtracting the contact distance from the total length.

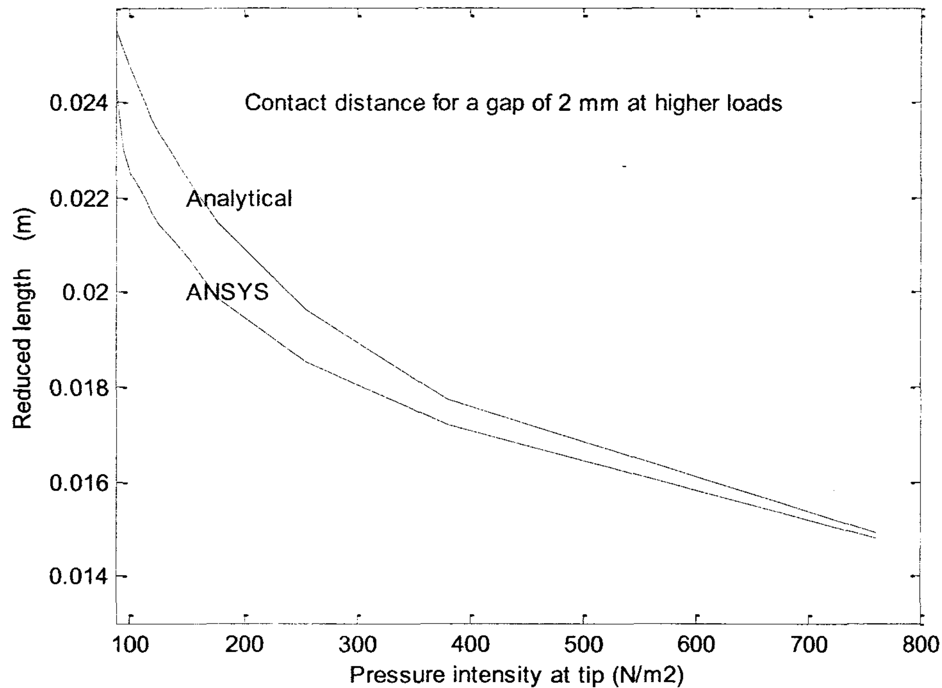

Figure 5.20: Unsupported length of the sensitive element

Contact distance obtained from ANSYS is plotted against the analytical calculation for the length of the unsupported sensitive element as defined by equation 5.6 as shown in figure 5.20. The maximum error between ANSYS and analytical calculation is 8 %. The ANSYS model matches with the value of deflection obtained analytically during the case 1 deflection regimes in figure 5.17. Also the contact distance which is calculated by detecting unsupported length of sensitive element from the total length matches with the analytical model once the contact is established in case 2 regime of deflection as shown in figure 5.21.

Based on the fact that the ANSYS model is valid for both pre and post contact deflection regime, the stress values obtained for post contact deflection regime that are higher than the pre contact regime from the ANSYS model are listed in table 5.1.

Table 5-1: Contact stress and distance

Pressure intensity @ tip per meter length (Pa / m)	Pressure intensity @ tip for a length of 25.4e-3 m	Maximum Stress near the fixed end N/m^2	Contact Distance mm
3500	88.9	$32.3e^6$	1.1
3750	95.25	$33.8e^6$	2.381
4000	101.6	$34.8e^6$	2.91
4250	107.95	$35.7e^6$	3.175
4500	114.3	$36.5e^6$	3.44
4750	120.65	$37.2e^6$	3.704
5000	127	$38.0e^6$	3.969
6000	152.4	$40.7e^6$	4.7
7000	177.8	$43.2e^6$	5.556
10000	254	$49.8e^6$	6.879
15000	381	$58.4e^6$	8.2
30000	762	$76.5e^6$	10.58
50000	1270	$93.2e^6$	11.9

Table 5.1 provides details on the stress developed at the fixed end and the contact distance due to sensor overloading after establishing contact. The results show that the stress values for the overloading conditions due to the presence of overloading pressure are well below the yield stress. Moreover the contact distance could also be used to

measure the pressure which opens new concept of sensing of pressure based on contact distance.

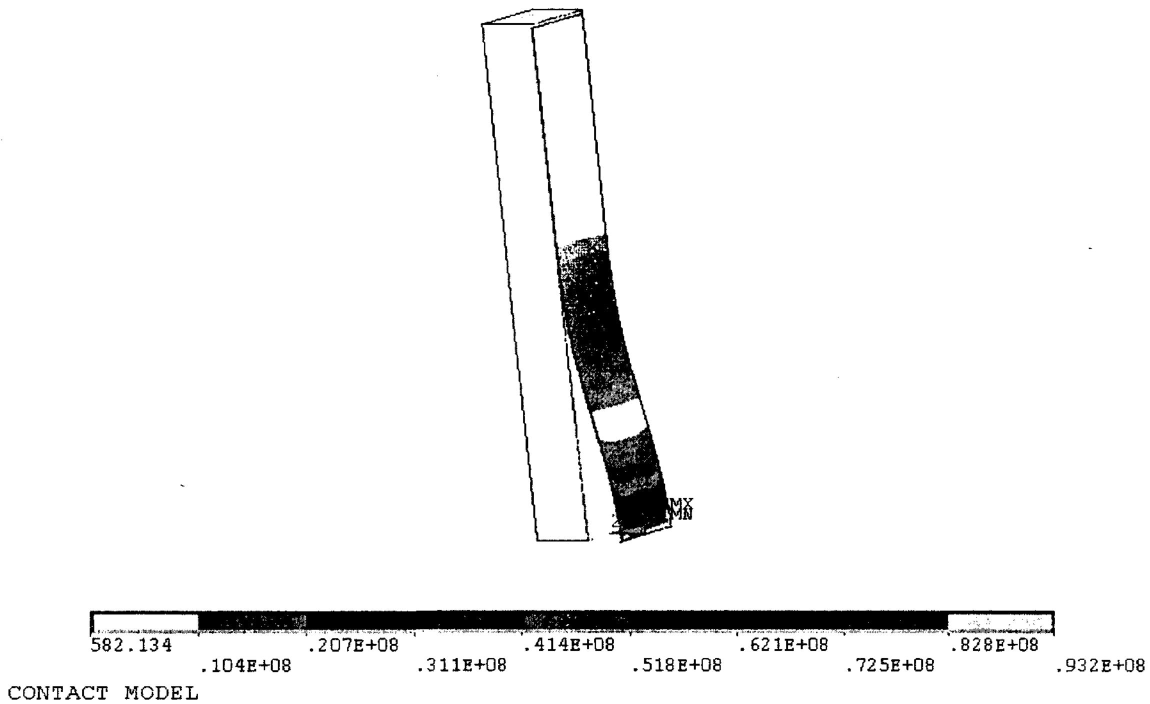

Figure 5.21: Stress distribution along the sensitive element N/m^2

Figure 5.21 represents the stress developed for the loading scheme shown in figure 5.19, when the contact distance is 11.9 mm which is well in the range of case 2 deflection regime in figure 5.17. The maximum stress at the fixed end is 93.2 MPa, and a contact distance of 11.9 mm for a pressure intensity of 1270 N/m^2 at the tip. The yield stress for aluminum is 215 MPa and the maximum stress involved is 93.2 MPa which is still lower than yield stress and hence the sensor works in safe operating domain. Hence the overloading due to exceptional situation could be handled by the deflection stop provided by the blocking element.

5.5. Numerical study on the phenomenon

The phenomenon that causes the deflection of the sensitive element due to the pressure drop created by the blocking element is not reported in literature. Challenges are also due to the condition under which debris may enter between the blocking and sensing element. In such situations the sensor would operate improperly and packaging should be conceived to avoid such situation. These issues have not been reported in the open literature. There is no analytical model found in the literature for this physical phenomenon. Numerical analysis using CFD is performed to understand the physics behind the phenomenon.

The deflection of the sensitive element towards the blocking element initiated the interest to study the flow pattern behind the sensitive element. Attempts were made to gather particle image velocimetry (PIV) data to learn the velocity profile which posed serious problems in terms of seeding. Seeding is the addition of oil/water particles to the stream of air so that the illuminating laser is reflected by these particles. This reflection is captured by the camera which is processed to acquire velocity profile. High velocity air required more seeding so as to capture an image with reasonable particle density. High steam seeding caused water particle deposition or oil mist deposition. This is not possible due to open flow conditions. Seeding within a closed duct made of transparent plexiglass resulted in oil mist deposition or condensation of steam on the walls of the duct making capturing of the image difficult.PIV was attempted during the duration of the research program and due to the above said problem numerical analysis using ANSYS CFD is used to model the same.

5.5.1 Problem definition

Figure 5.23 shows the computational domain for 2-D flow analysis using ANSYS. The inlet for the domain is defined as velocity inlet and the flow domain in the outlet is pressure outlet. Wall boundary condition is used for defining the boundaries of the blocking element and the sensitive element which is not visible in figure 5.22 but could be seen in figure 5.23.

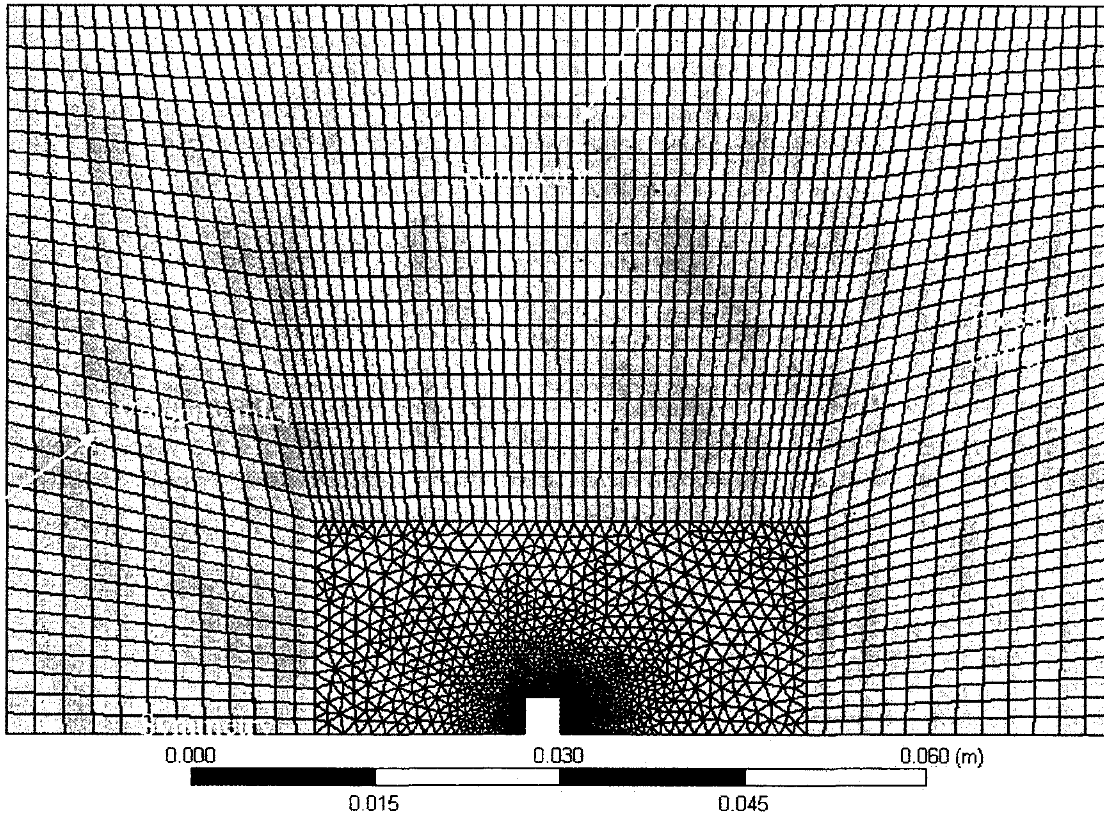

Figure 5.22: Computational domain with boundary conditions (Sensitive element is not visible)

The symmetry option reduces the required computational effort by enabling the modelling of half of the flow domain and mirrors the results once they are computed. The shown computational domain is equivalent to the top view of the actual flow domain. The Y coordinate of the blocking element and sensitive element in computational domain in figure 5.22 represents the half width of the blocking and the sensitive element.

The K-epsilon model is free-shear layer flows with relatively small pressure gradients. Similarly, for wall-bounded and internal flows, the model gives good results only in cases where mean pressure gradients are small.

The flow model used is K-epsilon model, however is suited for the model the best suited model will be Large Eddy Simulation (LES) which is possible only with 3-dimensional model which involves CPU intensive computations.

5.5.2 Meshing

Meshing is an integral part of the numerical analysis, and robust meshing is instrumental to accurate finite element analysis. The computational domain uses three kinds of mesh, hexahedral, tetrahedral and inflation mesh. This kind of meshing with multiple types of mesh in single computational domain is known as hybrid mesh. Hybrid mesh capabilities are required to optimize computational time without compromising with the accuracy of validating physical model [222].

The internal computational domains around the blocking and sensitive element are meshed with hexahedral mesh as complex meshing area could be easily meshed with hexahedral which offers the possibility of getting better mesh density. Also hexahedral mesh is best suited for parameterized design as it has better mesh adaptability [223]. Mesh adaptability is the capability of the mesh to adapt with the change in dimensions of the blocking and sensitive element and gap between them within the computational domain. This mesh adaptation is very important as severely distorted elements can cause inaccurate results, yield slow convergence, and premature analysis termination [223]. The outer computational domain has tetrahedral mesh and the mesh density is less in light of the reduced importance of those areas of computational domain.

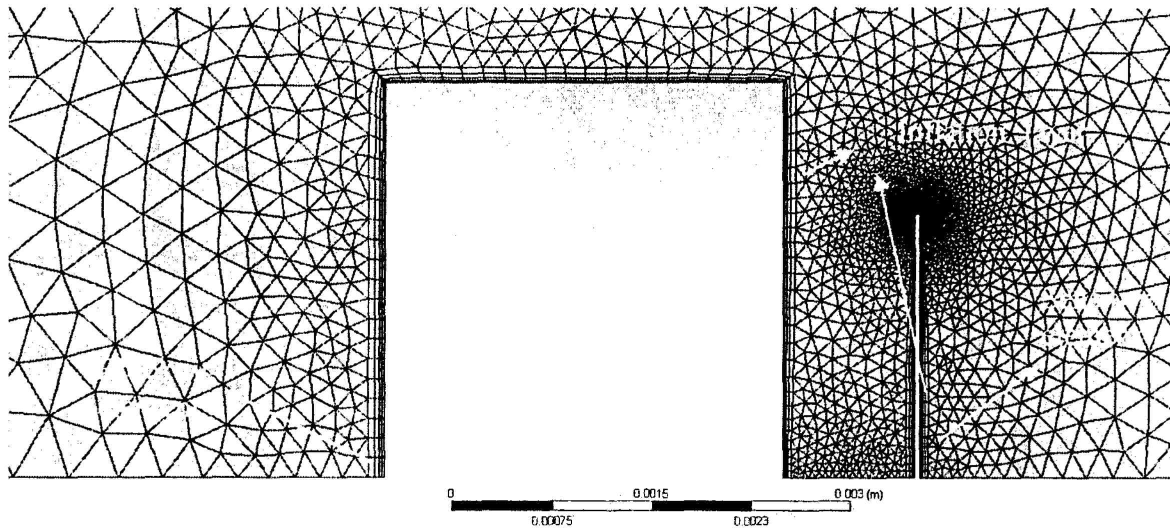

Figure 5.23: Zoomedin view of computational domain close to blocking / sensitive element

Figure 5.23 shows the zoomed-in view of the blocking element and sensitive element, and the mesh also has inflation near the solid boundaries of the mesh. Inflation can be added to the hex-meshing methods to capture boundary layers. Inflation meshes are particularly useful in handling large changes in mesh size, or to handle an interface between different physics. For example, when modeling a fluid structure interaction (FSI) problem, the solid and fluid regions share common interfaces and there is a huge difference in velocity. In this case there are 4 inflation meshes with a growth rate of 1.5 between adjacent meshes.

5.5.3 Results and discussion

The inlet flow was chosen to be 50 m/s based on the experimental values of velocity at a distance of 4 inches (101.6 mm) from the nozzle. The velocity stream line is as shown in figure 5.24. The velocity is the major consideration as this is what defines the dynamic pressure. The temperature is considered to be room temperature due to the fact that the experiments were carried out at room temperature.

Figure 5.24 shows the velocity streamline which clearly depicts the formation of vortex behind the sensitive element. Figure 5.25 shows the velocity vectors in the zone of interest that shows the formation of vortex behind the sensitive element.

It must be noted from the figure 5.25, that the stream after passing through the blocking element tends to rejoin after passing the sensitive element. This rejoining disturbs the sensitive element and hence the width of the sensitive element must be reduced to 0.8 times and the thickness of blocking element for the input velocity and dimensions are defined by the experimental setup.

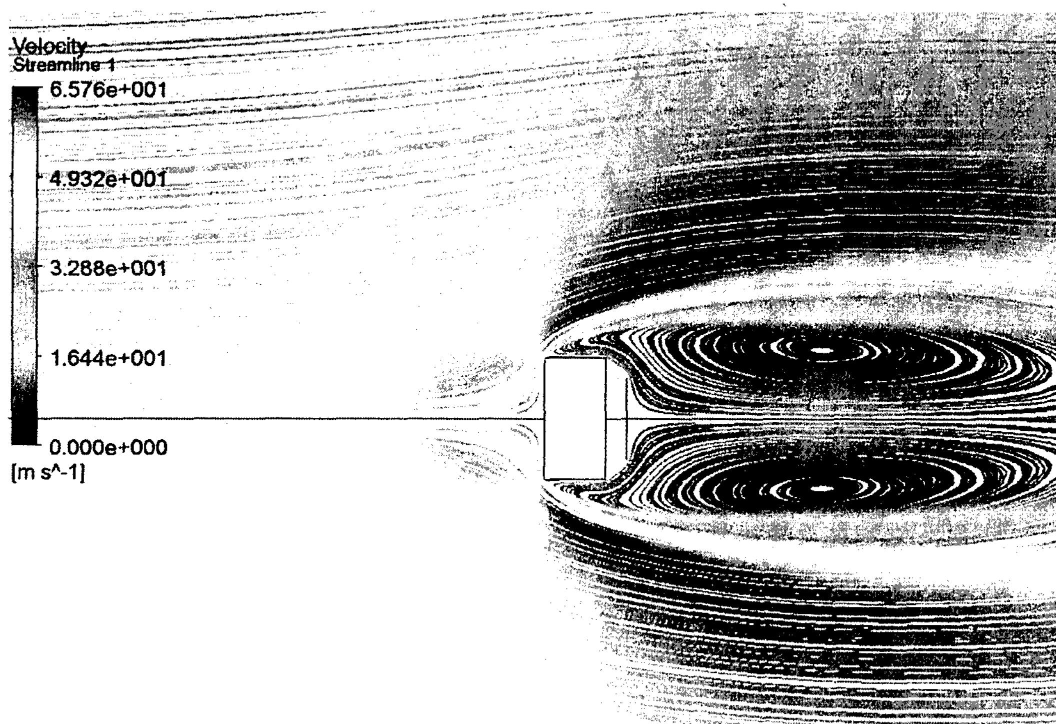

Figure 5.24: Velocity stream line with vortex formation behind the sensitive element

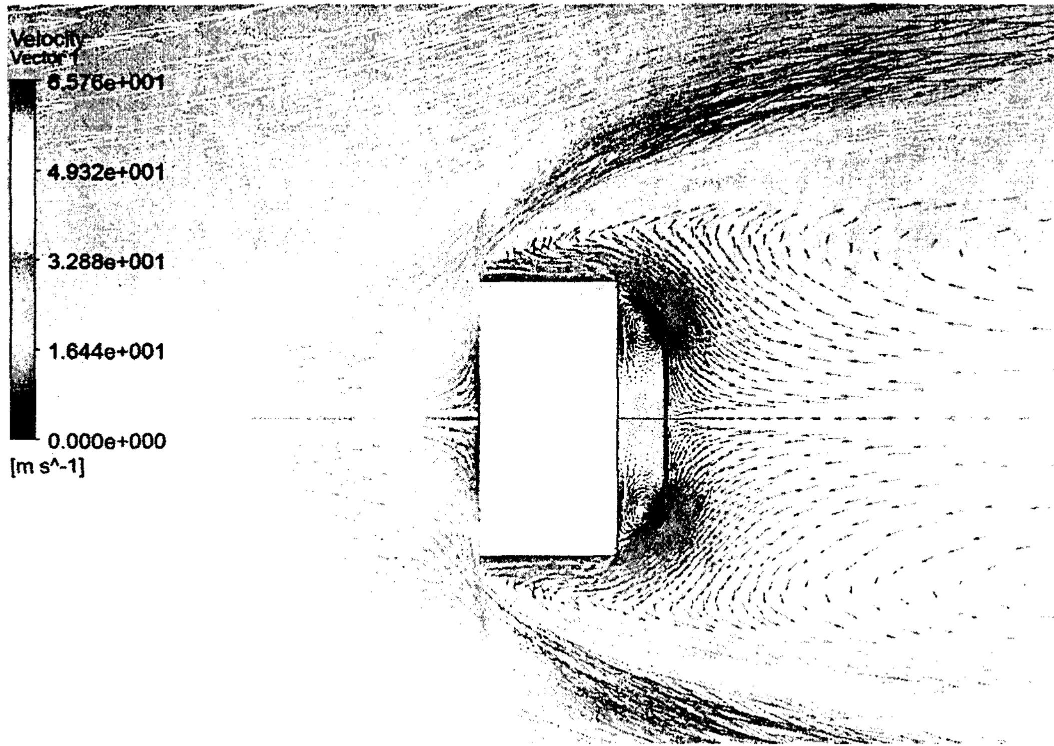

Figure 5.25: Velocity vectors close to the blocking / sensitive element

Numerical simulation gives some idea of the phenomenon in which the velocity pattern is similar to bluff body based Karman vortex flow meters. A Karman vortex is a term used in fluid dynamics for a repeating pattern of swirling vortices caused by the unsteady separation of flow of a fluid over bluff bodies.

Karman vortex has a long history but still there has been no analytical modelling to predict the drag or vortex formation and most of the work relies on experimental data for comprehensive understanding of the phenomenon due to its exceptional complexity [224].

Vortices are two dimensional phenomena that affect the velocity and pressure behind a bluff body. There are different methods of investigation and each method provides only partial information concerning the phenomenon [224]. One such

investigation for vortex formation by Gerrard, Bentley et.al [225,226] distinguishes three streams in the process of generating vortices as shown in figure 5.26

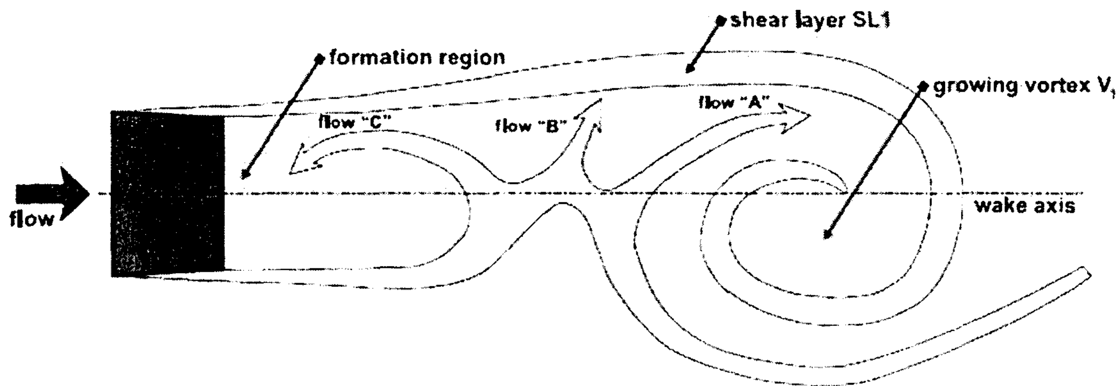

Figure 5.26: Streams in flow during vortex formation [225,226]

Stream A – entrained into the growing vertex generated from the opposite shear layer.

Stream B – entrained by turbulent shear layer SL1.

Stream C – directed back into the formation region and generating new vortex.

This hypothesis of 3 streams proposed by [225,226] concludes that from the point of view of the strength of vortices stream C should be maximized, stream A should be minimized and stream B should be sufficiently high for the vortex to detach. However there is no analytical or experimental proof offered to quantify the strength of the streams.

This phenomenon of pressure drop behind a bluff body is used to measure mass flow rate [227]. The concept behind vortex flow meter is with the knowledge of frequency of vortex shedding and the average pressure drop between the upstream and downstream the mass flow rate could be calculated:

$$f = \frac{St}{d} v \quad (5.9)$$

where *St* is the Strouhal number

v is the flow velocity

d is the maximum width of the bluff body

f is the frequency of vortex shedding

Vortex meters are mostly targeted towards measurement of velocity. The major advantage of these vortex meters based on vortex shedding phenomenon is that the vortex shedding is not sensitive to physical properties of fluid like viscosity and density [224]. This insensitivity is used to measure the velocity of molten steel by Iguchi et.al [228]. This set up has a probe that measures the shedding frequency of molten steel by measuring the strain on the probe and there by measuring velocity.

The problems with these vortex meters are the accurate mathematical modelling of the physical phenomenon occurring in vortex meters are not available and only optimization based on the laboratory investigation is feasible [229]. Experimental based investigations are used as a design and performance index for various bluff body based flow meters [230].

During the experiments it is observed that the tip of the sensitive element has some disturbance of small magnitude super imposed on the deflection. This is due to the formation of vortex that produces a disturbance on the deflection of sensitive element

5.6. Summary

Chapter 5 presents with the use of cantilever based configuration that has been used for various measuring applications. The configuration of using a blocking element and sensitive element and the phenomenon that causes the deflection of sensitive element is studied experimentally. A jet was created using the compressed air that has been properly regulated to ensure repeatability and this was used to generate velocity as required.

Further, overloading issue has been addressed as sensors are designed for overload protection. This sensor configuration also has a feature of overload protection because in case of overloading the blocking element acts as a deflection stopper. Stress involved during overloading and contact distance for a particular load is studied.

Further, as the phenomenon has not been studied earlier and attempts were made to study the phenomenon. Numerical analysis is carried out to learn the flow pattern around the sensitive element and behind the sensitive element. From the flow patterns it is interesting to note that the formation of vortex and the streams that form the vortex also produces disturbance of small magnitude superimposed on the sensitive element deflection.

Pressure measurement based on deflection at high temperature requires information on temperature as well so as to quantify the influence of temperature on deflection.

Chapter 6 provides a brief discussion on integrated measurements and describes a novel method to perform integrated measurements of temperature and pressure using acoustics.

Chapter 6 : Integrated Dynamic Pressure and Temperature Measurement at High Temperature

6.1. Introduction

Current sensor development efforts focus mainly on MEMS (Micro Electro Mechanical Systems) and smart sensing. Only MEMS technology made it possible to mass produce sensors cost effectively while improving their functionality and miniaturizing them. Smart sensor development is aimed at improving reliability and durability of these sensors and to make them more easily adaptable to new functions and conditions during the operating phase. Smart sensors should be able to communicate more than simply providing with a basic feedback signal.

Sensors have progressed through a number of identifiable generations. First generation devices had little electronics associated with them, while second generation devices were part of pure analog systems. Most of the sensor systems that are available today are third generation systems with the first stage amplification in the sensor module itself [231]. After first step of amplification, the data is fed to remote electronics or a micro computer. Many automotive sensing units belong to this category [231] as most of the signals are amplified and transmitted to the electronic control unit (ECU). Digital and analog electronics on the same chip with two way communication between the sensor and the host computer is the fourth generation sensors and some pressure sensors represent fourth generation components [232].

The prospective fifth generation sensors would accomplish signal conditioning on the chip so that the bidirectional communication with the host computer / controller will be in digital mode. These devices will be digitally compensated using field

programmable read only memories (PROMS) to achieve accuracy and compensation over a dynamic range [231]. They are expected to have self diagnostics (failure prevention and detection), self adaptation (compensation of secondary parameters), self calibration (automatic calibration for external influence caused by secondary parameters like temperature) and various computationally intensive operations [231]. The low cost of the field programmable gate array offer a perfect solution of implementation of the intelligent sensors in multiple applications with little effort.

6.2. Need for integrated smart sensors

It is very important that a pressure sensor capable of operating at high temperature needs input that would characterize the influence of temperature on the pressure measurement. This cross sensitivity issue calls for

- self diagnostic feature to detect the cause of a problem in measurement
- self adaptive and self calibration feature to take control measures for reliable measurement.

These control schemes require the use of another sensor to measure temperature as the major influencing factor in most of the pressure measurement cases [233]. Thus there is a need for integrated sensors that would measure two parameters, where one parameter would be the actual measurand while the other parameter is the source of uncertainty. Integrated sensor takes advantage of integrated measurement to more closely track the changes in the measurand and compensates for the effect of the environmental factor that creates discrepancy in the reading [234]. Integrated smart sensor should perform the following functions

- ❖ Sensing – one or more parameters
- ❖ Interfacing – signal conditioning, A/D conversion
- ❖ Self calibration and self diagnostics

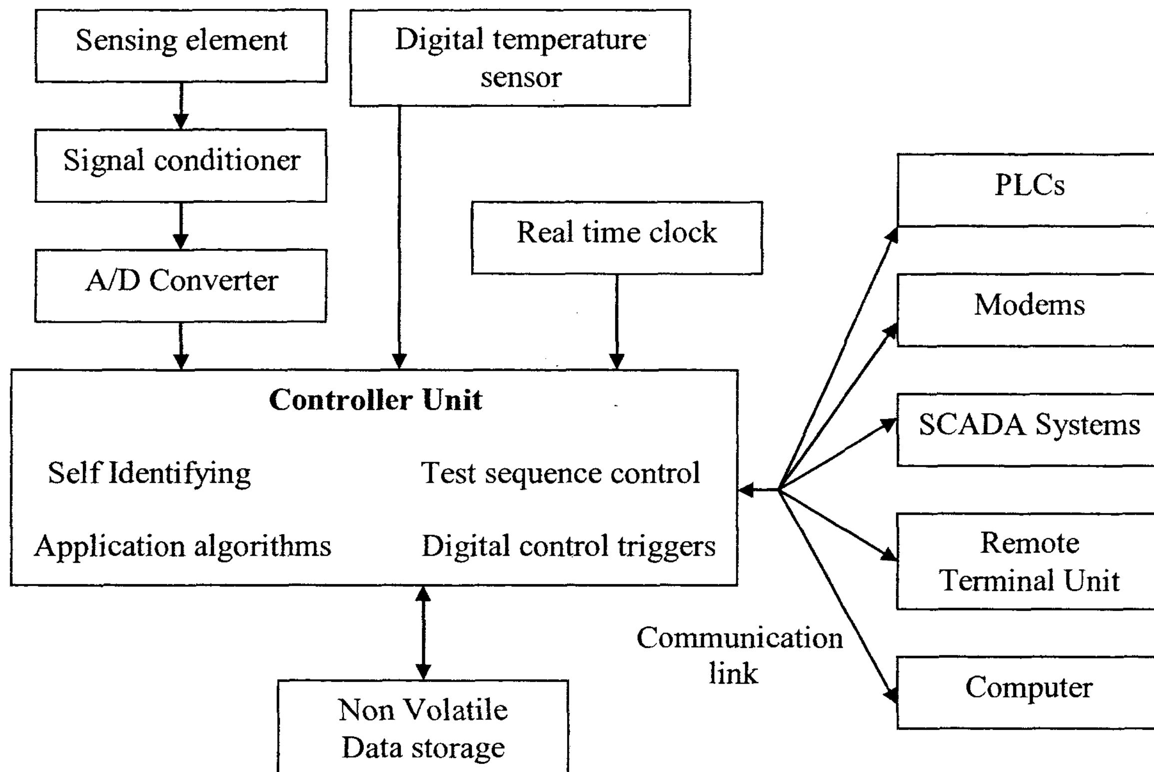

Figure 6.1 : Smart sensor block diagram

High temperature sensors based on Silicon on Insulator or Silicon Carbide (SiC) technology can withstand 300°C and 500 °C, respectively [235]. The limitation that is imposed on these sensors is not due to the incapability of the material to withstand high temperatures but because of the packaging [236] and electronics [235].

Smart sensors at high temperatures are out of discussion as the associated electronics needs further refinement to withstand more than 200°C. Silicon Carbide (SiC), gallium arsenide and other large band gap materials could be possibly extended to high temperature application, but they are still in development phase and are not yet cost

effective for high volume production [237]. Materials that can withstand high temperatures along with the high temperature electronics are of no use if there is no proper packaging [237].

The major issues of high temperature sensing in terms of packaging are [236]

- Mitigation of thermal stress caused by thermal expansion mismatch
- Thermal shock
- High level of heat dissipation to keep temperature in operable limit

Wire bonds are also a major impediment in high temperature packaging. The major issues related to high temperature electronics and wire bonds are [235].

- Thermal diffusion (temperatures > 300°C allows lateral diffusion)
- Interdiffusion – decreases bond strength and increases contact resistance
- Intermetallic formation – causes brittle phase and weakens the bond
- Melting

Also wiring these sensors will be a real challenge as it needs special wires that would resist extreme temperature conditions. Ni-30% Cr-16%Si alloy is used as material of construction of these wires that with insulation could work at 815°C [33] but the wires themselves are bulky and in this case would be significantly larger than the size of sensor itself.

Packaging and high temperature electronics even though has to be addressed before realizing high temperature sensors are out of scope of this research and hence it is not elaborately discussed. However, a general discussion on the potential candidates and technologies for pressure sensors to operate at high temperature is provided in chapters 1 and 3.

6.3. Integrated temperature and pressure measurements

Temperature and pressure are the most desirable parameters in different engineering applications. Temperature and pressure sensors hold first and second position in the world market based on highest market volume [238]. Pressure and temperature measurements underlie on different principles. Temperature measurement is carried using simple thermal expansion (thermal switches) to colour change caused by high temperature (pyrometer) while pressure measurement is mostly done by secondary or tertiary transduction of the pressure in the form of displacement and strain, respectively.

Most of the application demands simultaneous measurement of temperature and pressure at certain locations that often may have extreme conditions. Sensors that would measure temperature and pressure are available by integrating a temperature and pressure sensor in the same chip/module for commercial applications as offered by Kulite semiconductors [239]. These sensors operate within a temperature range of -55°C to +175°C and a pressure range for different applications starting with 25 bar to 250 bar. This is a combined sensor based on thin film resistance temperature detector (RTD) for temperature and a standard silicon diaphragm with four piezo resistive elements for pressure measurement. Laser interferometry based sensor for measurement of temperature and pressure are available with the primary measurand as temperature with an accuracy of 0.42% and a pressure as secondary measurand with an accuracy of 5.4 % [240]. Pressure and temperature measurement targeted for fluid power application, uses silicon diaphragm for static pressure measurement, (range 0 to 6MPa) silicon dioxide diaphragm for differential pressure measurement (range 0 to 35 kPa) and thermistor based temperature sensor (range 0 to 51°C). Differential pressure sensor might require

thinner diaphragm for higher sensitivity and thickness control of silicon diaphragm for very high sensitivity is difficult to achieve [241]. Some integrated sensors compromise sensitivity or accuracy of one of the measurand for attaining multiple measurements [242] and in case of higher sensitivity requirement the range is compromised to 80 kPa for a static pressure sensor. Furthermore, all integrated temperature and pressure sensors work on traditional methods of temperature and pressure measurement combined one way or another and is used in a lower temperature regime <175 °C [239].

6.3.1 Pressure sensing and cross sensitivity issues

In industrial application, instrumentation often encounters temperature cross sensitivity issues. Temperature compensation techniques are often based upon placing a compensating element exposed to the same temperature conditions as the sensing element in order to reduce the temperature effects [243]. These compensation issues are only for small differences in temperature and at higher temperature difference cross sensitivity effects are still observed even in the perfectly manufactured sensors with exactly equal sensing and compensating parts [244]. When there is a large extent of temperature variation, temperature compensation would be practically impossible [244] hence only way to deal with this is to measure the temperature and induce a self calibrating scheme that would produce an accurate result for dynamic pressure based on temperature variation. This clearly explains the need for integrating a temperature measurement scheme (as a secondary measurand) in a pressure sensor.

6.3.2 Discussion on the integrated sensing scheme

Young's modulus decreases with increase in temperature and hence the deflection due to loading is sensitive to temperature. The choice of material has to be in such a way that the change in Young's modulus with temperature is small. This is an additional factor that affects the accuracy. However the deflection due to thermal expansion is not too significant when compared with the influence of Young's modulus on deflection [245].

The data acquisition (digital resolution of the deflection measurement) interval is another important parameter in determining the sensitivity of the sensor. The sensing scheme requires continuous monitoring of data at a frequency of at least 10 times the frequency of dynamic pressure which is 17.6 * 10 =176 kHz in a compressor with 23 blades rotating at 46000 rpm. The number of sampling points depends on the type of signal. However there are high speed multi channel data acquisition systems capable of measuring high frequency data up to 200 kHz [246].

Deflection could be measured in many ways, Fibre optics and microwave seems to withstand higher temperatures till 700 °C [52, 53], however, microwave sensors require high temperature electronics for data processing [65].

Deflection measured by any of the possible means that can handle elevated temperature requires electrical signal that has to be processed to provide desired output. The transmission of electrical signal poses a problem due to the limitations posed by electronics with increase in temperature.

Even though with fibre optic sensors signal processing is facilitated as it could be placed away from the measurement zone, access to the measurement zone is mandatory

through the fibre optic cables that would withstand higher temperatures. Some application demands measurement to be done with minimum or no intervention to the measurement zone. In gas turbine engines Full authority digital engine controller (FADEC) is not equipped with optical interface and research and development activities are active to demonstrate and evaluate optical technologies in next generation military and commercial aircrafts [32]. This restricts the use of fibre optic cables or any other probes to measure pressure on the present configuration of the engine controller.

Acoustic waves could be used to measure dynamic pressure as it can travel through metals, although there is loss of intensity of the sound wave with distance. An innovative method to measure dynamic pressure and temperature is proposed in the forth coming section.

6.4. Acoustic sensor for dynamic pressure and temperature measurements

The proposed sensing scheme is aimed at measuring both temperature and dynamic pressure that utilizes a resonant cavity. Such a method is intended for measuring temperature and dynamic pressure in extreme environment such as very high temperature, corrosive gases etc. The resonant cavity is formed by either drilling a specified hole or attaching a small tube of desired length. SiCN could be used for that purpose on the measurement zone. The resonant cavity will be a one-end closed tube, the closed side having the wall followed by a microphone positioned after a small gap to capture the acoustic signal that is transmitted through the wall.

The dynamic pressure signal will be characterized by amplitude and frequency, the amplitude of the acoustic signal that passes through the wall that encloses the measurement zone, is picked up by the microphone. The captured signal has some loss in signal strength due to dissipation that is proportional to the thickness and material of the wall. However, extreme wall thickness will make the acoustic signal feeble and difficult to handle. The amplitude of time signal could be related to the amplitude of pressure if the enclosure of the measurement zone is calibrated for its acoustic signal loss.

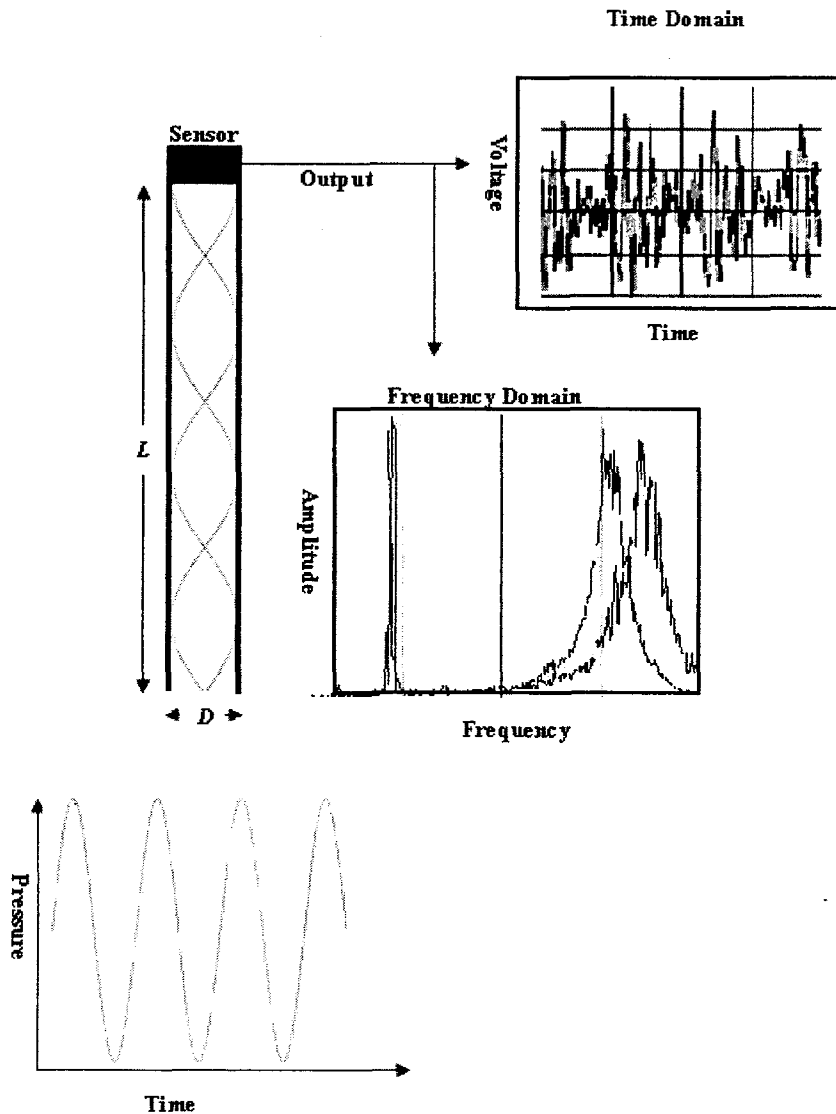

Figure 6.2: Pressure and temperature measurement scheme used in the experiments

Temperature and frequency of dynamic pressure signal can be interpreted from the acoustic signal by time to frequency conversion from the FFT analysis. The output of FFT analyser will have an amplitude value along y axis and frequency along x-axis. The amplitude will be higher when the frequency corresponding to the frequency of the dynamic pressure and also at resonant frequencies of the tube.

A peak in amplitude can also be appearing due to a steady noise; however such noise signal could be identified and filtered out. It is observed that there is a shift in the frequency peak when the input dynamic pressure is caused by hot air. This shift in frequency peak is corresponding to the difference in temperature.

An experimental investigation is performed to measure the frequency of dynamic pressure and the temperature. The pressure and temperature detection mechanisms and the signal processing and data analysis approach employed in the experiments are shown in figure 6.2.

6.4.1 Experimental setup

The source of dynamic pressure is a fan in the experiments described below. Figure 6.3 depicts the fan connected to regulated power supply along with the resonance tube and microphone arrangement. The resonance tube which is made up of plexiglass is 24.5 cm long and has a diameter of 7 mm. The bottom end of the tube is attached to the perforated fan casing over the blades, while the top end is closed-off with the microphone as shown in figure 6.3, thereby exposing the microphone to the acoustic vibration of air caused by passage of the blade. The resonant tube in this situation is open – closed pipe. The microphone on the top of the fan picks up the signal when each blade passes by. The

fan is powered by a regulated power supply that allows the variation of the rotational speed.

The resonance tube along with the microphone acts as a closed tube whose resonant frequency is given by

$$f^{(L,T)} = \frac{v_{air}^{T}}{4 * L_{eff}} \tag{6.1}$$

where $f^{(L,T)}$ is the standing wave frequency and it is both a function of temperature T and effective length L_{eff} of the resonance tube. The diameter D of the tube also contributes to the standing wave frequency, so that a correction for tube end effects has been added to the length of the tube [247],

$$L_{eff} = L + 0.3D \tag{6.2}$$

The velocity of sound in air at a given temperature is given by the relationship [248]

$$v_{air}^{(T)} = 331.13 * \left(1 + \left(\frac{T_m}{273.15}\right)\right)^{0.5} \tag{6.3}$$

where $v_{air}^{(T)}$ is the velocity of sound in air at a given temperature T, T_m is the measured temperature in ^{0}C, and 331.13 (m/s) is the speed of sound in air at 0^0C.

The effective length of the resonant tube is $245 + 0.3*(7) = 247.1$ mm. The velocity of sound in air at 20^0C is 343.2 m/s and the resonant frequency of the tube is 347.2 Hz.

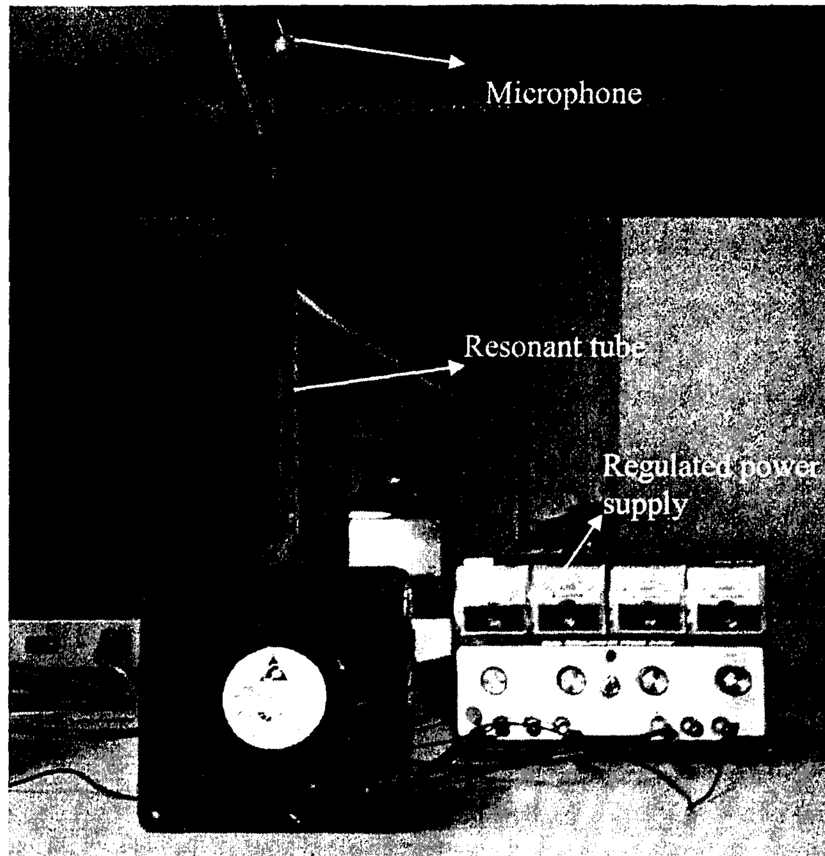

Figure 6.3: Experimental setup for dynamic pressure measurement

The length of the resonant tube and rotational speed of the fan are so chosen as to ensure that the resonant frequency of the tube and the blade passing frequency do not overlap. The speed of the fan is 1500 rpm, which is measured using non contact type tachometer while the fan has 11 blades. The frequency response signal gives a peak at around 275 Hz which is the frequency of the passing of the blade.

$$\text{Frequency} = \frac{rpm * n_b}{60} = \frac{1500 * 11}{60} = 275$$

where n is the number of blades, with n_b=11 in this case

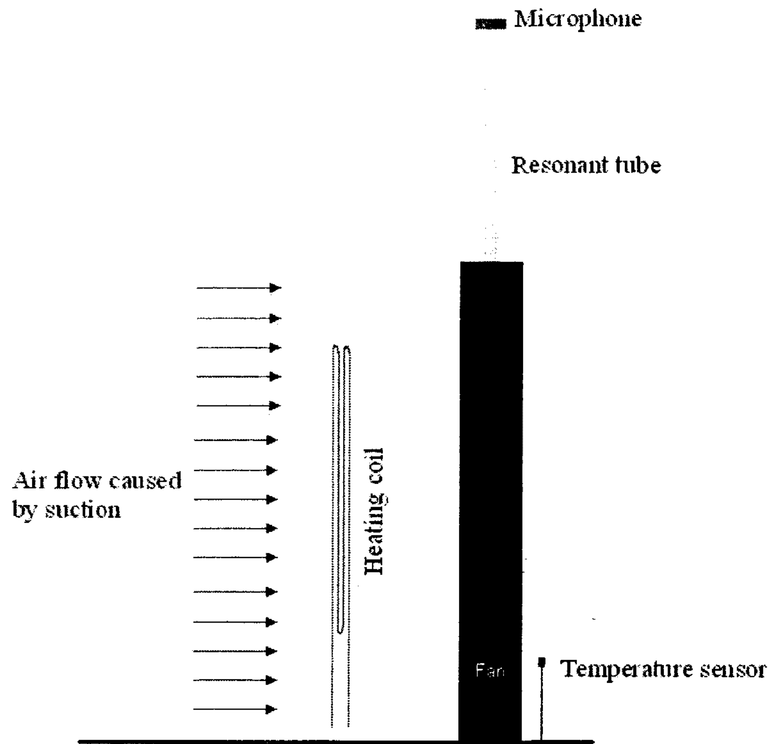

Figure 6.4: Schematic diagram with heating coil to heat the suction side of the fan (not to scale)

The suction side of the fan is heated using a heating coil, the schematic diagram is as shown in figure 6.4. The temperature is measured using TSI VELOCICALC which is an integrated temperature and velocity sensor.

The suction side of the air is heated till the temperature in the temperature sensors reached 30^0C. The velocity of sound in air at 30^0C is 349 m/s so that the resonant frequency of the tube is 353.1 Hz. The shift due to this temperature change was 354 Hz as seen is figure 6.5. The difference in frequency due to temperature of 10^0C is around 6.8 Hz.

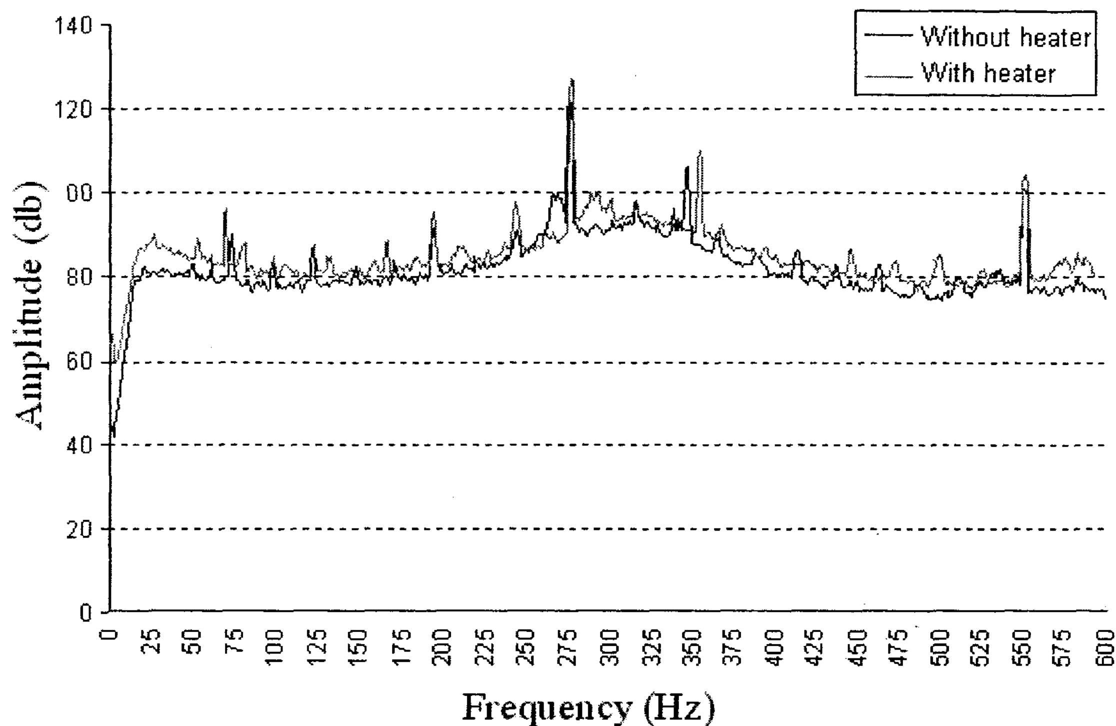

Figure 6.5: FFT analysis showing peak shift corresponding to temperature

Figure 6.5 shows the output of FFT analyzer (Bruel & Kjaer 2035). The peaks at 275 Hz and 550 Hz correspond to the frequency of blade passing. The graph also depicts the shift in the peak value when air in the suction side is heated using a heating coil. The temperature peaks correspond to 347 and 354 Hz at two different temperatures 20^0C and 30^0C.

6.4.2 Time signal analysis

The amplitude of the dynamic pressure signal has to be related with the amplitude of the time domain signal. A preliminary study of the time signal with the resonant tube is as shown in figure 6.6. The dependency of the intensity of time signal with revolution is observed during the experiment.

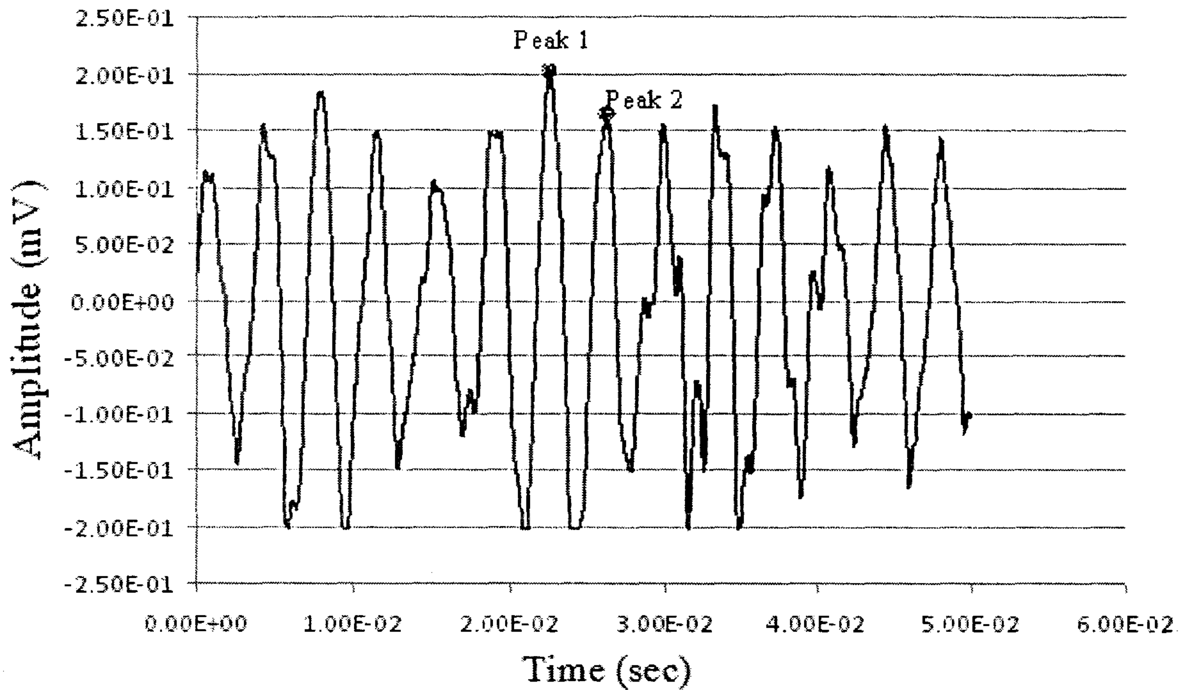

Figure 6.6: Time signal for an rpm of 275

Figure 6.6 shows the time signal with two peaks that correspond to the blade crossing. Peak 1 and peak 2 correspond to time of 2.28e-2 and 2.64e-2, respectively. This corresponds to frequency of 277 Hz while the actual rpm of the blade crossing was 1500 rpm that corresponds to 275 Hz. The above experiment validates the concept of temperature and dynamic pressure of gas measurement the above discussed principle.

6.5. Sensing scheme as applied to GTE application

Extending this sensing scheme to GTE application, the acoustical signal is transmitted through the enclosure (shroud). The intensity of acoustic signal depends on the thickness and material of the wall.

Figure 6.7 shows the measurement zone of interest for GTE application. The concept of temperature and dynamic pressure sensing when used within a closed chamber requires some modification.

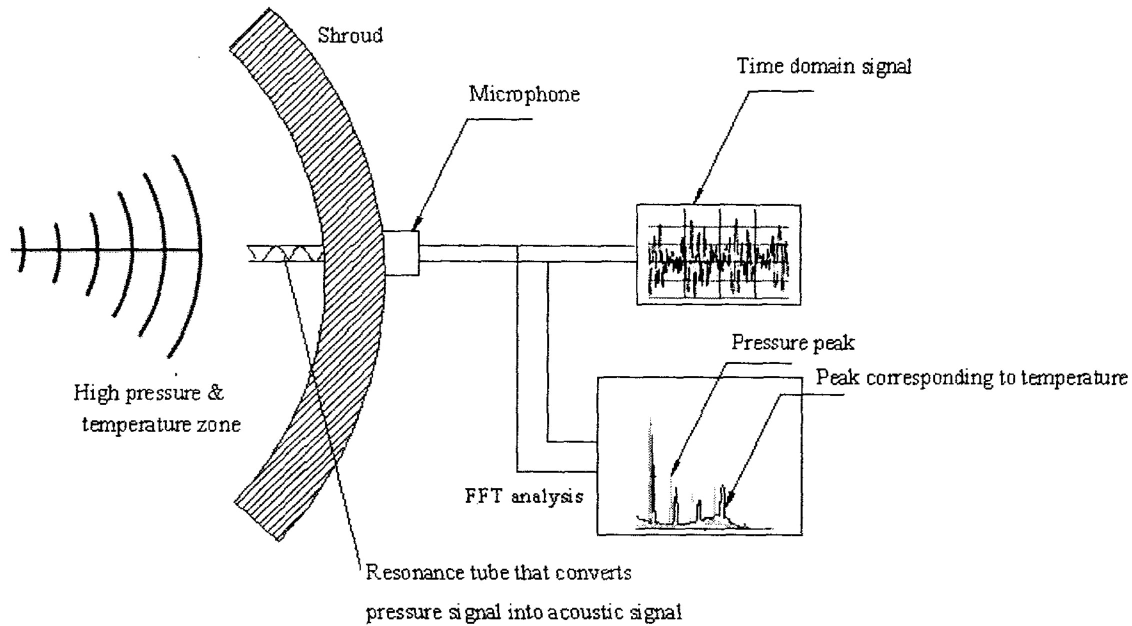

Figure 6.7: Schematic diagram of implementation of acoustic sensing

The casing of the enclosed chamber could be of any material of finite thickness. A resonant tube of desired dimension that is formed either by attaching a tube that can withstand high temperatures or by making a blind hole in the wall of the casing. The signal is captured by a microphone from the exterior of the chamber. This way the acoustic signal proportional to dynamic pressure and temperature can be picked up without any wires/cables passing through the shroud. The high temperature zone remains undisturbed and completely enclosed.

The noise spectrum in the application is a limiting factor for acoustic sensing scheme. All components involved in moving, burning and propelling air generate noise and GTE is no exception. Compressor and turbine produces blading noise, burning process produces noise of low order and jet of hot gas propelled through the nozzle to mix with the atmosphere produces the most powerful form of random noise [249]. The frequency range of noise could be from 60 Hz to 20 kHz [249]. This large frequency

range of the ambient noise generated by the GTE would be a challenge in successfully implementing the acoustic sensing scheme.

Assumptions

Wall has finite thickness that allows acoustic signals to pass through

Steady thermal conditions prevail around the resonant tube

Static pressure is known

The temperature across the wall of the shroud is constant

The velocity of sound through the wall is known. It has to be noted that the velocity of sound depends on the temperature distribution and material of the wall.

6.5.1 Temperature measurement

As shown earlier by the experiments the frequency of acoustic signal will have a shift in peak due to increase in temperature. This shift in peak is attributed to the temperature change as the excitation frequency remains unchanged.

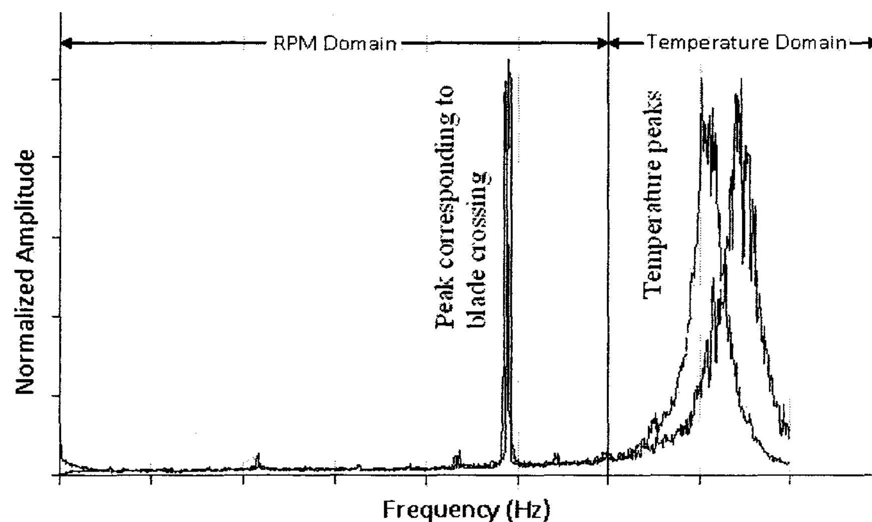

Figure 6.8: Temperature and rpm frequency domain

The key factor in temperature measurement is choosing the resonant frequency of the tube. It should be chosen in such a way that it does not overlap with the frequency of the dynamic pressure, blade passing frequency or any such noise which might disturb the sound collected by the microphone within the range of the temperature measurement. Figure 6.8 shows the need for avoidance of the overlapping of the frequencies. It is better to have a higher resonant frequency of the tube than the maximum frequency of dynamic pressure to avoid frequency overlapping.

The range of variation in the frequency of dynamic pressure should be known earlier in order to customize the sensor for specific application. The dimensions of the resonant tube could be designed based upon the overlap avoidance requirement. In gas turbine engines the frequency requirement for dynamic pressure is in the range of a few kHz which demands a resonant tube in micro scale.

Higher the frequency of dynamic pressure higher will be the range of temperature measurement as the difference of frequency between two harmonics is higher. Also the range could be altered based upon the dimensions of the tube. This shows the possibility of tailoring the range of the sensor based on the application.

6.5.2 Frequency and amplitude measurement

The frequency and amplitude of the dynamic pressure could be measured by measuring the time signal that passes through the wall of the enclosing chamber. Consider a source of dynamic pressure that has a frequency of ω. The signal will suffer a significant phase shift of $\omega t-(K_1 * X_1)-(K_2 * th)$ while they pass through a wall however, the frequency will be the same, where

X_1 is the distance travelled by the acoustic wave in air

h is the thickness of the wall

K_1 and K_2 are the wave numbers in air and in the material of the wall, respectively.

The amplitude of the signal can be found by measuring the acoustic signal that passes through the wall. The study on the amplitude loss of the acoustic signal through the wall would enable to quantify the amplitude of the dynamic pressure within the chamber.

Considering a dynamic pressure source that produces an acoustic pressure waves, along x axis only, we have

$$\frac{\partial^2 p}{\partial x^2} = \frac{1}{c^2}\frac{\partial^2 p}{\partial t^2} \tag{6.4}$$

Solution of this equation describes the pressure evolution of one dimensional plane sound wave propagating in air. Two initial conditions and two boundary conditions are required for a fully defined solution of equation 6.4.

Considering the waves that only move in the x-direction, the solution for a mono frequency sound wave could be represented as

$$P(x,t) = P_m e^{i(\omega t - Kx)} \tag{6.5}$$

where P_m is the peak amplitude of the sound pressure,

K is the wave number $K=\frac{\omega}{C}$.

When the acoustic pressure reaches the wall of the chamber, the waves would have travelled a small distance x that would have reduced the amplitude of the wave by

$p(x) = p_m e^{-\alpha x}$,

where p(x) is the amplitude after the wave has propagated a distance x through the medium

α is the attenuation coefficient of air that is frequency dependent.

However this amplitude loss will be significantly lower.

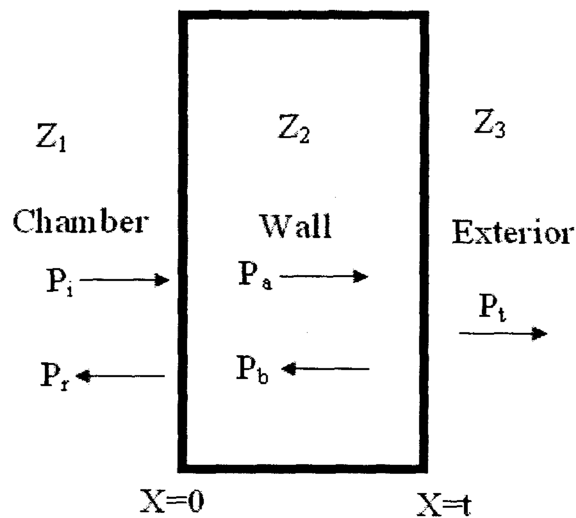

Figure 6.9: Reflection and transmission of a plane wave normally incident on a wall

Let Z_1, Z_2, and Z_3 be the characteristic acoustic impedances of the fluid in chamber, wall and the fluid in the exterior, respectively. When the incident signal in fluid 1 arrives at the boundary between the fluid and the wall, some of the incident wave P_i is reflected as P_r and some will be transmitted into the wall as P_a. The transmitted wave will pass through the wall and some will be reflected P_b and some will pass through the wall to the exterior P_t. The wave when travels through different media will suffer a phase shift.

Assuming the incident wave train as a mono harmonic frequency carrier and the wall has a uniform thickness, the incident wave would be $P_i = P_i e^{i(\omega t - K_1 x)}$ and the wave that is reflected back into the chamber is $P_r = P_r e^{i(\omega t + K_1 x)}$. The transmitted and reflected waves in the wall are $P_a = Ae^{i(\omega t - K_2 x)}$ and $P_b = Be^{i(\omega t + K_2 x)}$. The wave transmitted to the fluid in the exterior would be $P_t = P_t e^{i(\omega t - K_3 x)}$

The acoustic impedance at any point would be $Z = \dfrac{p_i + p_t}{U_i + U_t}$. Considering the continuity of normal specific impedance at X=0 and X=L in figure 6.9 we have

$$Z_1 \frac{p_i + p_r}{P_i - P_r} = Z_2 \left(\frac{A+B}{A-B} \right) \tag{6.6}$$

$$Z_2 \frac{Ae^{-iK2L} + Be^{iK2L}}{Ae^{-iK2L} - Be^{iK2L}} = Z_3 \tag{6.7}$$

Algebraic manipulation would yield the pressure reflection coefficient $\frac{p_r}{p_i}$ as [250]

$$R = \frac{\left(1 - \frac{z_1}{z_3}\right)\cos(K_2 L) + i\left(\frac{z_2}{z_3} - \frac{z_1}{z_2}\right)\sin(K_2 L)}{\left(1 + \frac{z_1}{z_3}\right)\cos(K_2 L) + i\left(\frac{z_2}{z_3} + \frac{z_1}{z_2}\right)\sin(K_2 L)} \tag{6.8}$$

The intensity transmission coefficient that describes the amplitude or the intensity of a transmitted wave relative to an incident wave is found as [250]

$$T_I = \frac{4}{2 + \left(\frac{z_3}{z_1} + \frac{z_1}{z_3}\right)\cos^2(K_2 L) + i\left(\frac{z_2^{\,2}}{z_1 z_3} + \frac{z_1 z_3}{z_2^{\,2}}\right)\sin^2(K_2 L)} \tag{6.9}$$

This procedure allows picking up acoustic signal proportional to velocity and dynamic pressure without any wires/cables. The high temperature zone remains undisturbed and is completely enclosed.

Consider an unknown source of dynamic pressure that generates pressure wave of certain frequency and amplitude. Consider the density of the air within the chamber to be 1.205 kg /m^3 and the chamber is made of steel of density 7800 kg /m^3. The output of a Simulink model formed by varying the thickness of the wall of the chamber, and the acoustic signal output are plotted in figure 6.10.

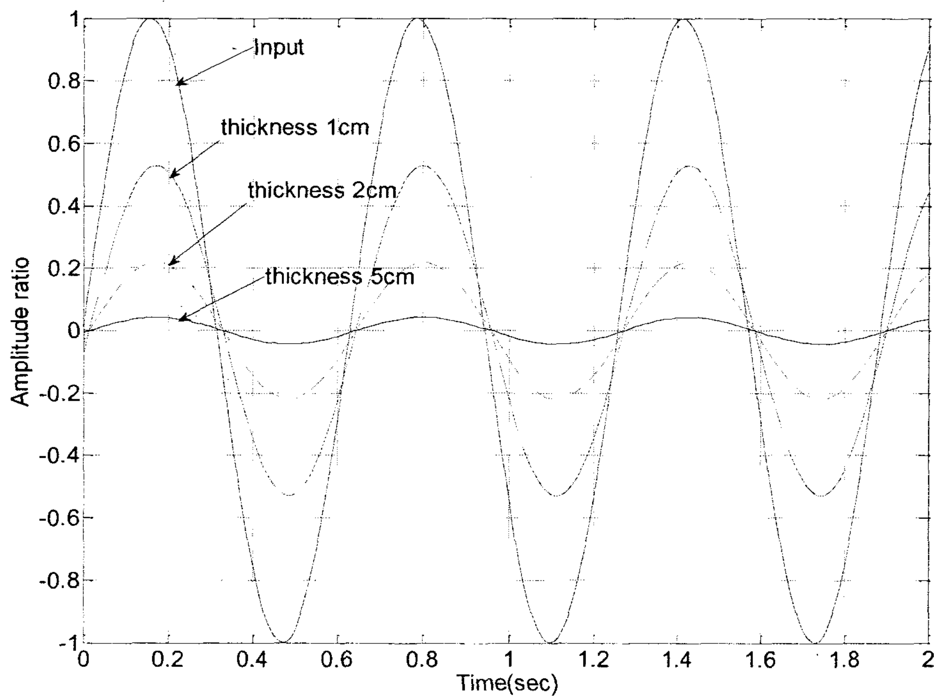

Figure 6.10: Non dimensionalized acoustic output obtained through walls of different thicknesses

The conditions inside the chamber are considered to be atmospheric, and the velocity of sound is considered at 20^{0}C. Figure 6.10 depicts the output obtained from the model for different thicknesses.

It is observed that the frequency of the wave form is the same as that of the source signal but there is a phase shift. The phase shift is dependent on the thickness of the wall.

The amplitude of the signal decreases with the increase in thickness governed by the equation 6.9.

6.6. Discussion on acoustic sensing scheme

The major advantage with acoustic sensing is the wireless transmission of data, which ensures non – invasive measurement. Acoustic signals are absorbed by the enclosure and hence very high thickness of walls would produce a weak signal that demands signal amplification. In an application like gas turbine engine, there will be noise signals and signal amplification and filtering requirements. Signal conditioning becomes very crucial as this has a major impact on the interpretation of the measurand.

Static pressure or density of the medium should also be known for this sensing scheme to be successful as temperature measurement is performed by knowing the velocity of sound in the medium, and velocity of sound is also dependent on density of the medium.

Acoustic sensing scheme when extended to GTE applications has to filtering requirements due to wide noise spectrum associated with GTEs . Gas turbine engine noise can be divided into two types, internally generated noise associated with the rotating components and externally generated noise or jet noise. Basically all parts of GTE contributes to engine noise, the relative magnitude of different noise source can vary not only with make and model of engine but also with operating conditions. These variations poses problems associated with noise filtration.

6.7. Summary

Chapter 6 discusses the integration of temperature and dynamic pressure measurement. A novel sensing scheme for dynamic pressure and temperature based on acoustic signals is proposed and discussed. Temperature could be measured by inserting a resonant tube in the chamber and the shift in resonant frequency of the tube is proportional to the velocity of sound. The frequency and amplitude of the dynamic pressure signal could be found out from the FFT analysis and time signal analysis.

Acoustic measurement can be used to measure temperature and also could be used as a confirmation for the dynamic pressure signal measured. Filtering of noise and design of filters would be a major task as gas turbine engine comes with high intensity noise of different frequencies. Material of resonant tube could be made from SiCN which is not thermally affected up to 900^0C. The fabrication details of SiCN are available in chapter 2.

The following chapter discusses the issues related to implementation and also addresses the requirement of data acquisition systems as required by the application. Sapphire based fiber optic cable for data acquisition is suggested in chapter 7 in view of the capability of sapphire based cables to withstand temperatures in the range of 900^0C – 1000^0C.

Chapter 7 : Implementation Issues

7.1. Introduction

Pressure measurements in aerospace applications, especially in the gas turbines have to be carried out at very high frequencies due to the high speed of the pressure variation in compressor/turbine so as to enable gas turbine engine to handle large amount of air. In today's large gas turbine engine the exit temperature of the compressor is as high as 650 - 760 °C [1]. Dynamic pressure sensors for real time sensing and control are required at different parts of the gas turbine engine. Dynamic pressure measurements in the compressor have a direct role in the detection of compressor stall events. The need for accurate dynamic pressure measurements at high temperatures is an integral step towards implementing active control system for performance enhancement of gas turbine engines.

For an example, if the dynamic pressure has to be measured within the compressor, considering the data available in table 7.1, the frequency of operation will be in kHz. The design of the sensitive element should avoid the natural frequency, so as to prevent resonance which demands that the natural frequency of the sensor be higher than that of the dynamic pressure by about one order of magnitude.

The frequency of loading on the sensing element for the GTE depends on the type of engine. Table 7.1 gives some typical frequency ranges for some of the compressor and turbine test cases [251]. Based on the frequency of operation the sensor has to be custom designed by choosing the dimensions of the sensitive element.

Table 7-1: Typical compressor stage frequency ranges in GTE

Platform	No of stages	No of blades	Rotation speed in rpm	Tip clearance (mm)	Frequency (kHz)
NASA Rotor 37	Rotor alone	36	17,190	0.356	10.31
NASA Rotor 67	Rotor alone	21	16,043	Data not available	5.61
E/CO-3 Subsonic compressor stage	Single	41 (R) 73 (S)	9,262.5	0.1125	6.32
E/CO-4 transonic Compressor	Single	28 (R) 60 (S)	20,260	0.3 (running)	9.454
E/CO-5 Low speed compressor	Two	R1 (44) S1 (44) R2 (44) S2 (44)	650	4.1656	0.476
E/TU-3 Subsonic Turbine	Single	20 (S) 31 (R)	7,800	0.25	4.03
Generic Case	Single	23	46,000	Data not available	17.6

The variation in the frequency of operation indicates the need for customization of sensor design based on the platform that is addressed.

7.2. Sensor design and material

As described in chapter 2, the material of consideration is SiCN with the following properties.

Table 7-2: Properties of SiCN

Properties	**SiCN**
Young's Modulus (GPA)	158
Density (Kg/m^3)	2250
Coefficient Thermal Expansion (m / mK)	$0.5X10^{-6}$
Poisson ratio	0.17

With the knowledge of frequency of operation [251], and the material to be SiCN, the dimensions of the beam could be chosen in such a way that the natural frequency is significantly higher than the operating frequency. Considering the thickness of the SiCN cantilever beam that is used as sensitive element to be 30 microns, which is the minimum thickness of the thin film SiCN that was achieved from liquid precursor as part of this work, the length could be designed based on the frequency requirement. For a SiCN cantilever beam with length of 450 microns, thickness of 30 microns and width of 70 microns, the natural frequency is about 200 kHz.

Figure 7.1 shows the frequency of a micro cantilever beam obtained using finite element method using MATLAB. The response of the cantilever sensitive element with the above dimensions is described in section 7.3.

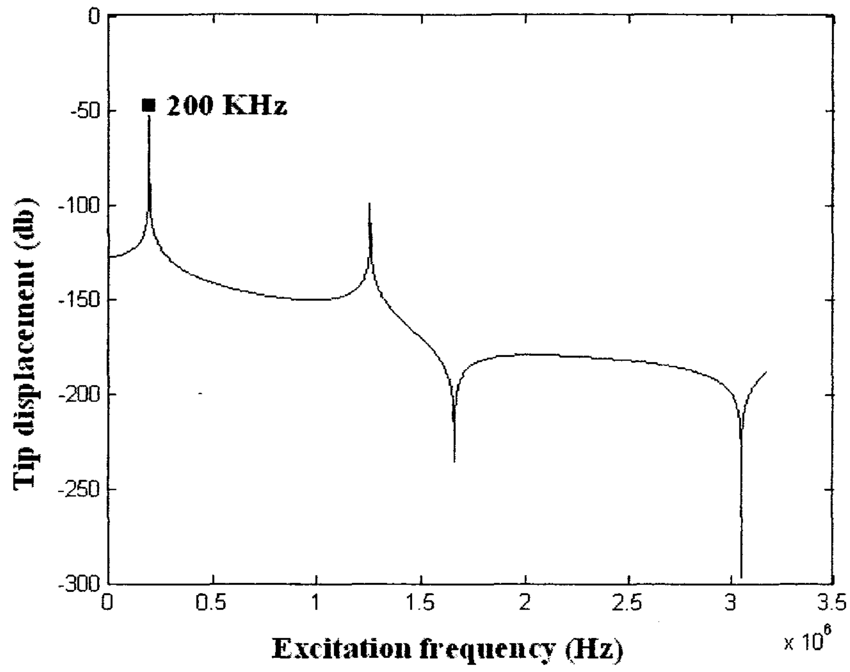

Figure 7.1: Frequency Vs displacement for SiCN sensitive element

7.3. Forced vibration solution for sensitive element

The sensitive element of the proposed sensor experiences load whenever the blade passes the sensor. The loading profile on the sensitive element is sinusoidal as shown in figure 7.2.

Micro phone

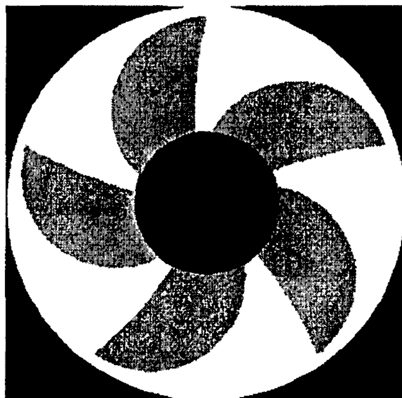

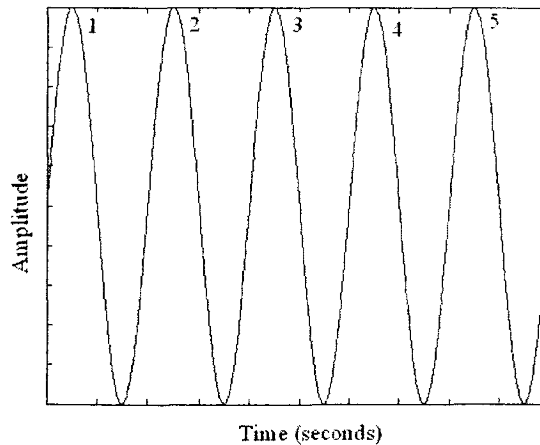

Time (seconds)

Figure 7.2: Loading scheme for 5 blade fan (Generalized)

A simple fan and a microphone arrangement that is connected to an oscilloscope are used to obtain the time domain signal which is in the form of sinusoidal profile. Figure 7.2 shows the fan microphone arrangement that provides a sinusoidal loading on the sensitive element.

The maximum amplitude V_{max} at the sensitive element depends on the speed with which the blade passes the sensor and the reduction offered by the blocking element. The time period T depends on the rpm of the blade passing as

$$f(t) = V_{max} \sin\left(\frac{2\pi t}{T}\right) \quad (7.1)$$

Consider a GTE with a compressor having 46 blades that rotates at 23,000 rpm. The blade passing frequency is 17.6 kHz. As the blade passes by the sensor it would provide a load on the sensitive element. The load on the sensitive element will be attenuated due to the presence of the blocking element. The load would have a maximum value each time the blade passes and loading scheme would be as shown in figure 7.2. An arbitrary time dependent load on the sensitive element is applied as uniformly distributed load across the length of the beam. The loading profile is considered as uniformly distributed load since the width of the blade is larger than that of the sensor. The uniformly distributed load corresponds to drag force experienced by the sensitive element. The magnitude of the time varying drag force on the sensitive element is assumed to vary from 0 to a maximum value of $10X10^{-3}$ N/m in a harmonic with a frequency of 17.6 kHz. The response of a cantilever sensitive element is obtained as follows.

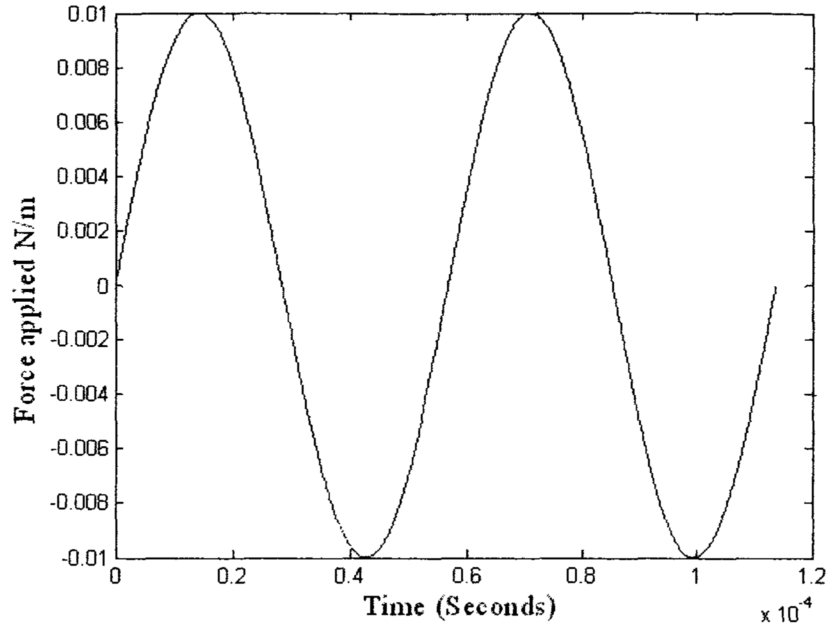

Figure 7.3: Loading scheme on the sensitive element

The forced vibration solution of a beam can be determined using the mode superposition principle. The deflection of the beam is assumed in the form of a linear combination of the normal mode responses as

$$y(x,t)=\sum_{n=1}^{\infty} y_n(x)q_n(t) \tag{7. 2}$$

where y_n is the nth normal mode or characteristic function satisfying equation 7.3, given by

$$EI\frac{d^4y_n(x)}{dx^4}-\omega_n^{\ 2}\rho Ay_n(x)=0 \tag{7.3}$$

where q_n is the generalized co-ordinate of the nth mode.

Substituting the deflection function in homogenous form of the equation

$$EI\sum_{n=1}^{\infty}\frac{d^4y_n(x)}{dx^4}q_n(t)+\rho A\sum_{n=1}^{\infty}\frac{d^2q_n(t)}{dt^2}y_n(x)=f(x,t) \tag{7.4}$$

Using equation 7.3, in equation 7.4

$$\sum_{n=1}^{\infty} \omega_n^2 y_n(x) q_n(t) + \sum_{n=1}^{\infty} \frac{d^2 q_n(t)}{dt^2} y_n(x) = \frac{1}{\rho A} f(x,t) \tag{7.5}$$

By multiplying equation 7.5 through out by $\int_0^l y_m(x)$ and using orthogonality condition

$$\int_0^l y_n(x) y_m(x) = 0$$

$$\frac{d^2 q_n(t)}{dt^2} + \omega_n^2 q_n(t) = \frac{1}{\rho A \int_0^l y_n^2(x)} \int_0^l y_n(x) f(x,t) \tag{7.6}$$

Equation 7.6 could be written as

$$\frac{d^2 q_n(t)}{dt^2} + \omega_n^2 q_n(t) = \frac{1}{\rho A e} Q_n(t) \tag{7.7}$$

where $Q_n(t) = \int_0^l y_n(x) f(x,t) dx$ is the generalized force along $q_n(t)$ and $e = \int_0^l y_n^2(x) dx$ is a constant.

Solution for equation 7.7 could be expressed using Duhamel integral as

$$q_n(t) = A_n \cos \omega_n t + B_n \sin \omega_n t + \frac{1}{\rho A e \omega_n} \int_0^t Q_n(\tau) \sin \omega_n (t - \tau) d\tau \tag{7.8}$$

The first two terms of equation 7.8 on the right hand side represent transient or free vibration resulting from initial conditions and the third term denotes the steady state vibration resulting from forcing function.

As the sensitive element is a cantilever beam the continuous system frequency equation is

$$\cosh \beta_n l + \cos \beta_n l = -1 \tag{7.9}$$

and the normal mode function would be

$$y_n(x) = C_n\left[\sin\beta_n x - \sinh\beta_n x - \alpha_n\left(\cos\beta_n x - \cosh\beta_n x\right)\right] \quad (7.10)$$

where $\alpha_n = \left(\dfrac{\sin\beta_n l + \sinh\beta_n l}{\cos\beta_n l + \cosh\beta_n l}\right)$ and the first five values of the eigen values $\beta_n l$ are given

as

$$\beta_1 l = 1.875104$$
$$\beta_2 l = 4.694091$$
$$\beta_3 l = 7.854757$$
$$\beta_4 l = 10.995541$$

The generalized forcing function is given by

$$Q_n(t) = \int_0^l y_n(x) f(x,t)\,dx \quad (7.11)$$
$$= \int_0^l \left[\sin\beta_n x - \sinh\beta_n x - \alpha_n\left(\cos\beta_n x - \cosh\beta_n x\right)\right] * V_{\max}\sin\left(\frac{2*\pi*t}{T}\right)$$

The steady state response of the sensitive element is given by

$$q_n(t) = \frac{1}{\rho A e \omega_n}\int_0^t Q_n(\tau)\sin\omega_n(t-\tau)\,d\tau \quad (7.12)$$
$$= \frac{1}{\rho A e \omega_n}\int_0^t \left[\begin{array}{l}\int_0^l \left[\sin\beta_n x - \sinh\beta_n x - \alpha_n\left(\cos\beta_n x - \cosh\beta_n x\right)\right] * \\ V_{\max}\sin\left(\frac{2*\pi*t}{T}\right)\end{array}\right]\sin\omega_n(t-\tau)\,d\tau$$

Thus the response of the sensitive element would be

$$y(x,t) = \sum_{n=1}^{\infty} y_n(x)\,q_n(t) \quad (7.13)$$

The forced response for a peak load of $1X10^{-3}$ N is shown in figure 7.3. It follows the same form of the input sinusoidal load. The response as shown in figure 7.4 is in the

same form of the forcing function figure 7.3 with a small phase shift between the input loading and the response of the sensitive element.

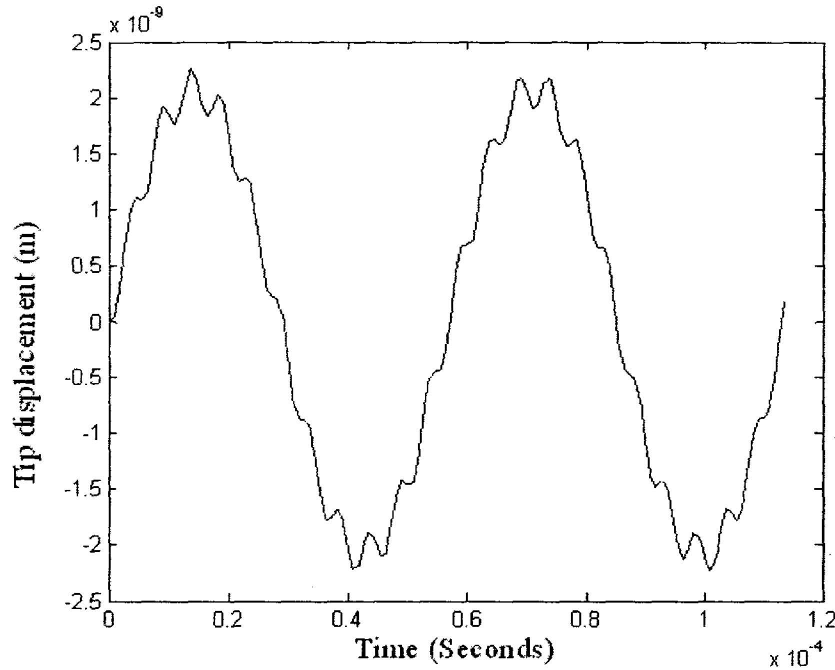

Figure 7.4: Forced response for a sinusoidal load

7.4. Material consideration for gas turbine engines

Material development program is the key to increase the performance of the gas turbine engines. Estimates predict about 50% of the performance improvement will come from improved materials and processes [252].

Present day GTEs are made of Ni and Co based alloys enabled with thermal barriers coatings (TBC) [253]. Co-based alloys have superior thermal fatigue and hot corrosion resistance over Ni based alloys and Ni alloys are stronger at low and intermediate temperatures and have better oxidation resistance when Al is added as alloying element [252]. TBCs have oxidation resistant bond coat and a thermal insulating top coat and these coatings could reduce the maximum metal temperature by 20% and

thermally induced radial expansion by 34% [254]. Clearance control coating in compressors of GTE and better thermal barrier coating in turbine blades could improve stage efficiency by 3% and overall efficiency by about 1% [255]. Metallurgical development if exploited to a level that cooling air quantity could be minimized, will result in performance enhancement as Rolls Royce engines used only 5 % of compressor air to cool its row of high pressure turbine blades [256].

GE has reported [253] engine performance improvement needs revolutionary materials such as

- Metal matrix composites (MMC)
- Ceramic matrix composites (CMC)
- Light weight, high temperature intermetallic
- Polymer matrix composites (PMC) for low temperature usage (370^0C) in casings and static structures
- TiAl composite blades, ceramic bearings and dry lubricants.

7.5. Fiber optics for data acquisition

Measurement of deflection could be performed by many schemes such as strain gauges, capacitance, piezoelectric or optical ways. When exposed to high temperature metallurgical stability and oxidation are the prominent critical issues [136]. Resistance strain gauges at high temperatures are affected by temperature co-efficient of resistance. Capacitive scheme when used for micro application has to measure small values of capacitance and these require charge amplifiers and/or special circuitry which are extremely sensitive and vulnerable to high temperature [140]. There are possibilities of

inducing piezoelectricity in SiCN by doping iridium and inculcate magnetic properties in SiCN by doping manganese [108], but these potential solutions are still in research phase.

The fibre optic means of deflection measurement is the choice for most of the high temperature applications due to the availability of high temperature fibre optic cables made up of sapphire and quartz [256,257]. Fibre optic sensing is advantageous over conventional instrumentation particularly under harsh conditions [258]. However there are other components of fibre optic sensing that have limitations in terms of high temperature withstanding capability. Fibre optic couplers can operate at a maximum limit of 200^0C, while some experimental devices operate at 300^0C. Light sources such as laser diodes and modulators, are limited to 100^0C [259]. Also detectors can be made to operate at temperatures close to 200^0C [259]. Because of these reasons the nearest term approach to encounter high temperature environment is to locate these components in a relatively cool area and expose only the fibre transducers to higher temperatures. Fibre optic sensor gained importance because the transmission path is immune to electromagnetic interference, they are very light in weight and are chemically and physically compatible with wide range of host materials [260] and they do not rely on any electronic related material property like conductivity or piezoelectric effect [179]

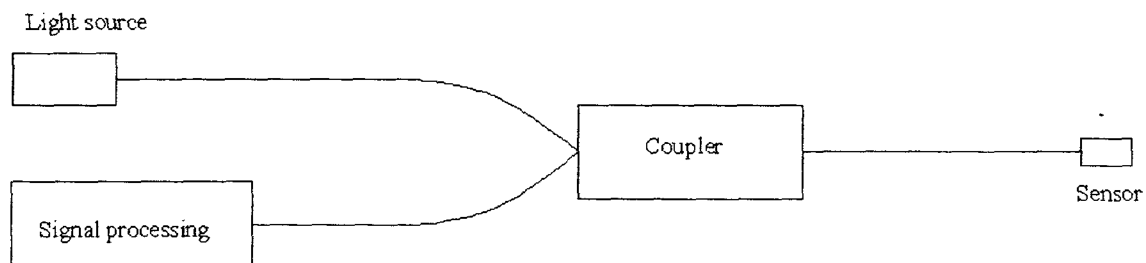

Figure 7.5: Fibre optic sensing scheme

Fibre optic sensors work by detecting intensity, phase, or wavelength. All detection techniques are influenced by temperature but interferometry based sensors could be used in gas turbine engine application / high temperature applications due to the existence of compensation schemes to overcome these problems [260,261,262].

7.5.1 Sapphire as material for optical fibre

Fibre optic sensors at high temperatures experience a serious drop in performance as the optical fibre is the only component exposed to high temperature. High temperature sensing above 500^0C is possible only with sapphire or quartz based fibre optic cables. [263]. Although quartz and sapphire can withstand high temperatures, fibre sizes of diameter 5 microns that would be minimally invasive could be made only from sapphire. The fabrication includes a significant infrastructure which may be quite expensive [264].

Sapphire is preferred at high temperature application for the following features [263,264]

- It is an excellent optical material with high internal reflection from 150 nm to 6000 nm wavelength – from far UV to middle infra red.
- It is chemically inert
- High index of refraction (1.77) at visible wavelength (390 -750 nm)
- High thermal conductivity, (46 W/mK) facilitating fast heat dissipation.
- Maintains its structural integrity up to 1600^0C to 1700^0C after which it becomes increasingly plastic and melts at just above 2000^0C.

The problem with sapphire based fibre is cladding. Cladding is required to keep the light inside the fibre and also used to increase the fibre strength. Fibre optic cables at high temperature encounter cladding issues due to thermal expansion coefficient mismatch and cooling issues. The essence of cladding problem is that cladding material should have

index of refraction less than that of sapphire, with matching coefficient of thermal expansion and temperature bearing capability. Cladding using polycrystalline alumina, although seems adequate, is not cost effective, even platinum based cladding still yields problems [263].

One solution for cladding problem is to leave the fibre unclad which also solves cooling issues as loose fibres are easily cooled but the strength of the fibre comes as a drawback. In order to compensate for that, sapphire cables are made larger in diameter, at 40 – 120 microns. Most of the sapphire based cables are used without cladding (air is the cladding material) [265,266].

Small diameter fibres result in strict axial thermal gradients and hence thermal stresses are negligible in radial direction and high thermal conductivity equalizes temperature across fibre and facilitates cooling. However, high coefficient of thermal expansion is a disadvantage in case of sapphire ($7.7X10^{-6}/^{0}C$ @ $500^{0}C$). It also should be noted that refractive index of sapphire is dependent on temperature and wavelength of the light. Temperature dependency of refractive index for sapphire cables has been studied with reasonable accuracy in ranges from room temperature close to the melting temperature [267]. The refractive index increases linearly from 1.77 at room temperature to 1.8 at $2000^{0}C$ for light with a wavelength of 0.5145 microns. These studies are useful to support the use of sapphire cables for diverse applications involving high temperatures.

Sapphire fibre optics is used in conjunction with GRIN lenses that would provide a collimated light beam with a divergent angle of less than 0.05^{0} [268]. GRIN has to be glued to the fibre and this would limit the capability to handle higher temperature.

Hence the parameters that must be considered include type of light source, dimension of the sapphire fibre which is limited to 40 microns because any smaller dimensions make the fibre extremely fragile, maximum deflection of the sensitive element and positioning of the sapphire fibre relative to the tip of the sensitive element.

7.5.2 Installation of the fiber

Sapphire based optical fibres face another problem of integration as these sensor systems are highly delicate without cladding. The entire sapphire fibre is considered to be the core with the surrounding air with lower refractive index as fibre cladding. These fibres should have a considerable length as required by the application and have to be integrated to an application, in most of the cases have to be bent at certain radii. These integration issues are to be addressed in case if this has to be extended to the next level.

For a fibre of core radius a, refractive index of core n_{co}, refractive index of cladding n_{cl}, and a bend radius R, the ratio of output power p_{out} to input power p_{in} is given by Marcuse [269], as

$$\frac{P_{out}}{P_{in}} = \exp(\alpha l_b) \tag{7.16}$$

where l_b is the length of the bend and α is pure bend loss coefficient.

$$\alpha = \frac{1}{2}\left(\frac{\pi}{\gamma^3 R}\right)\frac{\kappa^2}{V^2 K_1(\gamma a)}\exp\left(\frac{-2\gamma^3 R}{3\beta^2}\right) \tag{7.17}$$

where $k = \frac{2\pi}{\lambda}, \kappa = \left(k^2 n_{co}^2 - \beta^2\right)^{\frac{1}{2}}, V = ak\left(n_{co}^2 - n_{cl}^2\right)^{\frac{1}{2}}, \gamma = \left(\beta^2 - k^2 n_{co}^2\right)^{\frac{1}{2}}$ and β propagation constant

Sapphire fibres with different radii of bend are tested for high temperature measurements. Sapphire fibres are usually protected by inserting them to a titanium tube

(melting point 1660 ± 10^0C). The sapphire and tube are bent together and the bend loss as a function of effective refractive index and bend radius (from 1 cm to 2.4cm) for different wavelengths are studied [258]. High purity alumina ceramic paste is used to fix the fibre inside the titanium tube. Alumina ceramic paste is also suggested as an applicable product for both titanium and sapphire [270]. This high temperature alumina ceramic paste and titanium offers a very robust package [258].

Figure 7.6 shows the integration of sapphire based fibre for GTE application. The bending of optical fibre and the radius of curvature will pose significant problem.

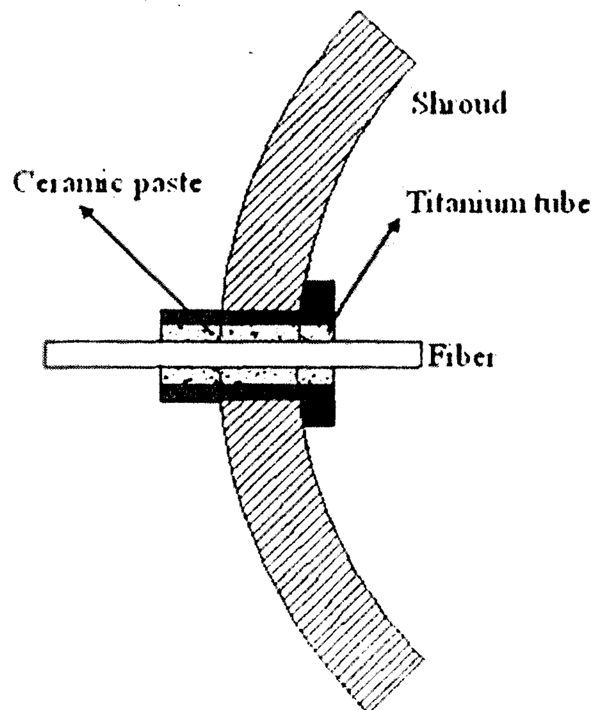

Figure 7.6: Integration of sapphire fibre on the shroud

The same combination could also be used to provide leak proof joint at the shroud, wherein the fibre has to be supported and taken out to the sheltered domain where signal processing is performed.

7.5.3 Positioning of the sensor

The positioning of the sensor is very important so as to produce a reliable measurement. The maximum size of the sensor is limited by the space available for its installation. The proposed sensor is intended to measure dynamic pressure in the clearance space between the blade and the shroud in gas turbine engine. This clearance management is a challenging problem by itself since the development of gas turbine engine. This is because the clearance between the blade tip and the shroud tend to vary due to changes in thermal and mechanical loads on rotating and stationary structures.

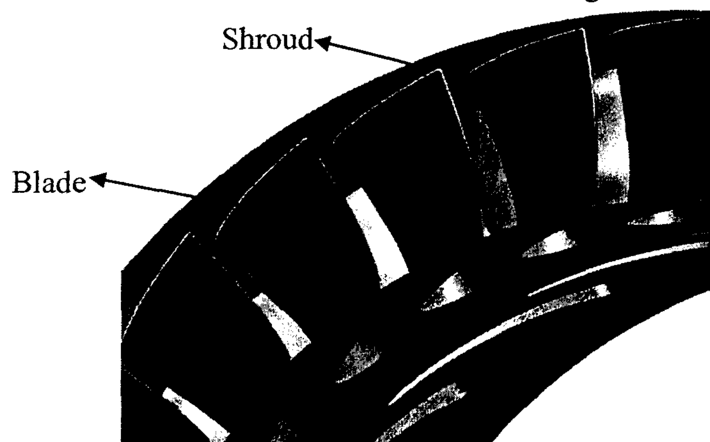

Figure 7.7: Typical axial compressor stage: rotor with the tip clearance

A typical axial compressor stage is shown in the Figure 7.7 illustrating the tip clearance. As engine is started from a cold condition there is a clearance depending on the make and model of engine that exists between the blade and shroud. This clearance is rapidly diminished, when the speed of the engine increases for takeoff due to centrifugal loading on the rotor as well as the rapid heating of the blades causing rotating components to grow radially outwards. This produces a minimum gap or pinch point as the shroud expands at a much lower rate and there is no centrifugal load on the shroud [271]. Eventually with time the shroud expands due to heating thereby increasing the

clearance. During cruise conditions of the engine the clearance remains constant as the speed is constant and thermal equilibrium is attained.

During deceleration, the clearance is rapidly increased due to mechanical unloading of the rotor but it takes time to cool down and regain its original clearance. Centrifugal and thermal loads are responsible for largest radial variation in tip clearance [271]. The axisymmetric clearance change is caused by expansion and contraction of the rotor during changes in engine acceleration. Thermal loads produces axisymmetric clearance changes due to thermal expansion and contraction of stationary and rotating parts and how uniformly these parts are heated or cooled. Figure 7.8 shows the various parameters affecting the clearance.

There are two other uncommon events in gas turbine engine operation that would affect the clearance. An aborted landing mission which would result in spooling up of the engine after being in decelerated condition so as to make the air craft climb or make an evasive manoeuvre. There are some events such as when the engine stalls in the air or when the aircraft is tested for acceptance [271] for in flight shut down followed by a restart. This would also affect the clearance due to sudden change in centrifugal load with thermal loads being the same as it takes time for the engine to cool down. Aircraft acceptance testing includes shutting down of the engine at an altitude followed by a dwell time during which the engine continues to rotate due to air craft's forward momentum and is finally restarted and accelerated back to power. In this case the engine is not only just decelerated (as the centrifugal load is less than normal) but is also cooled down due to flow of air through the casing and the rotor.

Tip sealing is more challenging in aero engines than in land based power gas turbine engines due to the frequency of changes in operating points, inertia forces due to manoeuvres and aerodynamic loads during flights [271, 272]. The major contributors for tip clearance variations are engine loads and flight loads which are further classified as shown in figure 7.8. The sensor has to be positioned to measure dynamic pressure in a highly varying clearance and sometimes under unexpected conditions the rotor rubs with the shroud, hence the sensor cannot be housed in the clearance and has to be housed within the shroud in small slots. Meanwhile the variable clearance would induce sudden local variation of pressure which could be interpreted as variation due to flow through compressor.

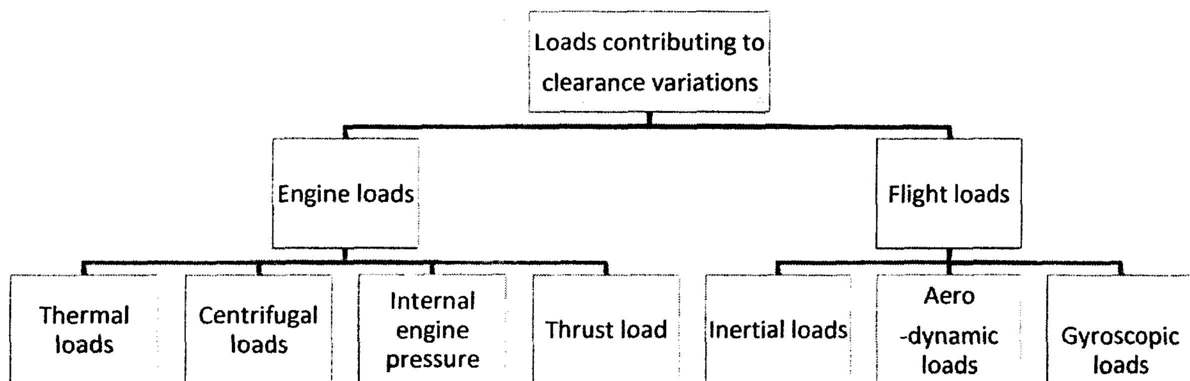

Figure 7.8: Classification of loads contributing to clearance variation

Table 7-3: Details of axial gaps between stator and rotor blades in GTE

Type	No of stages	No of blades	Chord length of stator blades mm	Tip clearance (mm)	Gap between Stator blades (mm)	Axial gap (between rotor and stator blades)
E/CO-3 Subsonic	Single	41 (R) 73 (S)	29.41 (mid chord)	0.1125	20.59	9.03 mm (@ tip)

compressor stage						
E/CO-4 transonic Compressor	Single	28 (R) 60 (S)	29.364 (mid chord)	0.45 (static) 0.3 (running)	11.67	26 mm (@ tip)
E/CO-5 Low speed compressor	Two	R1 (44) S1 (44) R2 (44) S2 (44)	101.6 (mid chord)	4.1656	105.664	43.6372 mm(@ tip)
E/TU-3 Subsonic Turbine	Single	20 (S) 31 (R)	95.5 (mid chord)	0.25	Data not Available	54 mm (@mid span)

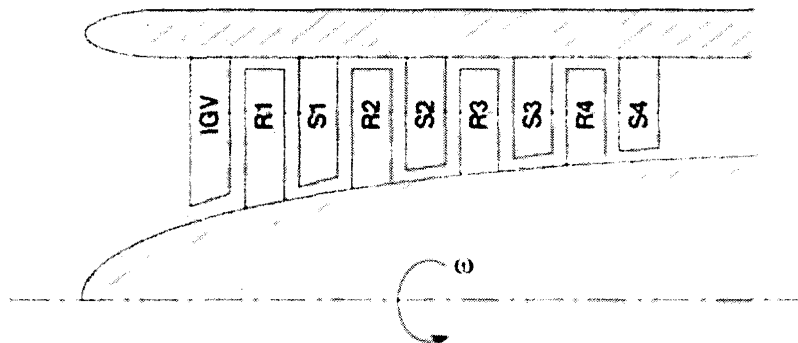

Figure 7.9: Schematic representation of an axial flow compressor (with axial gaps)

Positioning of the sensor in the gap between blades and shroud is not possible due to uncertainty in the gap as explained above. This positioning issue could be successfully alleviated by placing the sensor in the axial gap between the rotor and stator or between the stator blades. However, placing the sensor in those places will pose a problem with maintenance of the sensor as accessibility to the sensor requires disassembly of the engine.

Additional information on the streamlines is required to justify the position of the sensor in terms of minimizing vortices and boundary layers. However a flow analysis will

be required to study the formation of vortices and boundary layers in between the blades. Also study on influence of positioning on the pressure pattern experienced by the sensitive element will be required before finalizing the location. Axial gaps for some axial compressor and turbine test cases available are given in table 7.3 and the schematic representation of an axial flow compressor in Figure 7.9. The axial gap is sufficient and the sensor could be fixed on the casing, so as to ensure the safety of the sensor.

7.6. Summary

The contents of chapter 7 emphasizes on different implementation of the dynamic pressure sensor on issues associated with GTE application.

The loading on the sensitive element will be at a high frequency, of a harmonic fashion. The sensitive element has to adequately be protected and the data acquisition from the measurement zone to the optical interface needs to be addressed.

Sapphire based fibre optic sensing could be a solution due to the ability of the sapphire fibre to operate in high temperature. However, there are some cladding issues and problems in integrating them to the GTE due to limitation offered by the bending radius of the fibre. These issues are addressed in chapter 7.

Finding a suitable place to install the sensor is another issue which is discussed in chapter 7. The sensor could be placed in between the stator and rotor blades or between two stator blades due to variation in the gap between blade and the shroud. However a detailed flow analysis between the blades is highly recommended before finalizing the installation location.

Chapter 8 : Conclusions and Suggestions for Future Work

8.1. Contributions

The thesis mainly focuses on the development of a sensor that can withstand high temperature and also is more sensitive to the input dynamic pressure. High temperature sensing is very crucial and needs a lot of refinement in the existing instrumentation systems.

Through the realization of such a sensor it would be possible to perform online condition monitoring of many complex systems including gas turbine engine. As of today, GTEs being an intricate system do not have any way to perform online condition monitoring due to lack of sensors functional at high temperatures.

The thesis work concentrates on the following main aspects

I. Material – Silicon carbon nitride (SiCN)

SiCN is a polymer derived ceramic that could be fabricated from a powder or liquid based polymer. Liquid based polymer is used in the present work due to the superior qualities exhibited by SiCN produced from liquid CERASET™. SiCN fabrication process includes thermosetting, crosslinking and pyrolysis.

II. Fabrication of SiCN

SiCN has to form the body of the sensor and hence it has to be fabricated in different shapes and thicknesses. SiCN is made as a thin film with thickness of around 30 microns using gelatine based mould. Thick films of SiCN with thickness in the range of 2 -3 mm required special reusable mould based on Poly dimethyl Siloxane (PDMS). Also patterned SiCN is made by mixing CERASET™ with Dimethoxy-2-phenyl-

acetophenone (DMPA). The addition of DMPA makes the liquid CERASET™ to be photosensitive and therefore patternable in batch process. Fabrication of patterned SiCN can lead to mass fabrication and possibility of cost effective sensor fabrication is addressed. SiCN samples have been fabricated from 30 micron thickness to 3 mm thickness with different surface areas from 100 X 100 microns 5 X 5 mm of with surface finish of peak to peak 114.18 nanometers.

III. Characterization of SiCN

The influence of the process parameters like thermosetting temperature, annealing temperature etc. is discussed. The hardness is greatly influenced by the thermosetting and annealing temperature. Samples were made with hardness values ranging from 7.5 GPa to 23 GPa by controlling thermosetting and annealing temperature. Also X- ray diffraction testing of the samples revealed recrystallization occurs after 1400^0C and existence of SiC and Si_3N_4 crystallites. Detailed investigations on the properties on SiCN prove their suitability for high temperature application up to 1500°C.

IV. Analysis of annular diaphragm or diaphragm with multiple perforations as possible configuration of sensitive element

Dynamic pressure sensor uses annular diaphragms as sensitive element. Annular diaphragm based diaphragms are used for low frequency applications, GTE being high frequency application annular diaphragms will not be a solution due to the restriction offered by the interaction of the flow with the sensitive element. Diaphragm with multiple perforations is equally good candidate for dynamic pressure application. However, the space restriction in GTEs and high temperature associated with that are the obstacles in the use of such sensitive elements.

V. Sensing scheme based on indirect drag phenomena

Analysis of cantilevers and diaphragms as suitable configuration for high temperature sensing revealed that cantilever beam is a better configuration based on their resistance to thermal expansion effects. In order to protect the sensitive element from undue damage caused by the incoming flow a novel sensing scheme based on indirect drag effect is introduced.

VI. Experimental characterization of the sensing scheme

Indirect drag effect consists of two elements, namely a blocking element and a sensitive element. The measurement of deflection of the sensitive element based on the pressure drop caused by the flow past the blocking element provides the input dynamic pressure. Macro level testing is done using aluminum sensitive element of 30 microns thickness. Testing done up to 1550 N/m^2 dynamic pressure at room temperature resulted in a maximum deflection is 850 microns for a gap of 2 mm between the blocking and the sensitive element. The blocking element provides shelter for the sensitive element against suspended particles and also acts as an overload protection thereby making it suitable for high dynamic pressure applications. The overload protection scheme is analysed using ANSYS contact element scheme.

VII. Integrated temperature and pressure detection scheme

A novel sensing scheme to detect the pressure and temperature with wireless pickup using acoustic signals is discussed. This sensing scheme could be extended to chemical reactors or GTEs. The sensing scheme uses a resonant tube whose frequency depends on the velocity of sound in the medium which in turn depends on the temperature. Dynamic pressure could be measured by the amplitude of pressure wave

measured by the microphone after being absorbed by the wall. The sensing scheme is validated using an experiment. Temperature could be measured with < 1°C resolution. Testing is done in the temperature range of 20°C to 30°C. The resonant tube can be fabricated by SiCN and the dimensions of the tube could be tailored according to the requirement. Sensing scheme is experimentally and a Matlab/Simulink model for the absorption of acoustic signals through the enclosure is developed.

8.2. Conclusions

SiCN proves to be an excellent candidate for high temperature sensing application. Possibility of batch fabrication of SiCN was tested (photolithography of CERASET) and the results provide the possibility of cost reduction per unit by mass production. The sensing schemes even though very successful in the lab environment will require customized packaging and high frequency data acquisition system for implementation.

Active control in high temperature environment is implementable only if the gap between the existing sensing system and the advanced sensing requirement is minimized. More work is required on the sensor side as it is the weakest link in a high temperature instrumentation and control. SiCN based high temperature sensor may be still far from practical usage in the near future but the research work presented is a proof towards the interest in implementation of SiCN for such applications. Also the thesis work has significant output in terms of versatile sensing schemes that could enhance the possibility of active control that is functional in harsh environment in aero engines.

Acoustic sensing scheme needs careful attention in terms of filtering out the noise signals. GTEs have a wide noise spectrum and the success of the acoustic sensing scheme needs extensive study.

Further implementation and air worthiness certification are some of the issues that have to be addressed. Additional investigations are required to implement these technologies in engine rig and finally to the produce engines without compromising engine air worthiness, safety, reliability and durability requirements.

The conclusions that could be drawn from the thesis work are as follows

(i) High temperature sensing above 500°C requires new materials like SiCN as existing materials like Si, SoI and SiC cannot perform satisfactorily at those temperatures.

(ii) SiCN is a polymer derived ceramic and it has been fabricated in different forms (30 micron thickness to 3 mm thickness) and tested in temperatures up to 1500 °C, which implies that the material could be used as the body of the pressure sensor.

(iii) Developed a fabrication scheme to enable thin, thick and patterned film fabrication, characterized the film SiCN and validated possibility to machine the material.

(iv) Indirect drag effect phenomenon has been demonstrated experimentally and it is found that this phenomenon could be used for places with high particle ingestion, and it is also insensitive to static pressure.

(v) The sensitive element and blocking element configuration provides overload protection to the sensitive element. Over-load protection is a major

requirement for high flow applications as it protects the sensitive element from unprecedented loads.

(vi) Acoustic sensing could be another possibility of extracting data from high temperature zone. Acoustic sensing offers the possibility of measuring temperature and dynamic pressure.

8.3. Suggestions for future work

The following investigations would extend the scope of the present study.

8.3.1 Modeling of the Indirect Drag effect

The indirect drag effect that is based on the pressure drop created by the blocking element is difficult to model analytically as no analytical modelling of Karman vortex (similar phenomenon) exists in the open literature. Sensors that work on this phenomenon are mostly addressed experimentally. However numerical modelling using ANSYS 12 handles the fluid structure interaction more robustly and is possible to model it using latest version of ANSYS. Analytical modelling of the phenomenon remains unexplored and it is not addressed in the open literature.

8.3.2 Testing at high temperature – Indirect drag effect sensing scheme

The testing of the sensors at high temperature environment could be addressed as SiCN samples for these applications are already fabricated. Generation of high temperature environment and possibility of performing measurement and data acquisition is a challenge by itself. Even though testing at high temperatures in the range of 400°C - 500°C is not possible, a test setup that could generate 50°C - 100°C could be developed in

the lab with appropriate handling and ventilation of hot air. Simulating similar flow conditions like in GTE is practically impossible in the laboratory.

Optical means of deflection measurement / data acquisition is possible and standard sensors that can withstand 50°C can be used for calibration purpose.

8.3.3 Optical measurement at high temperature

Optical measurement scheme could be tested to measure the deflection of the sensitive element. Sapphire based cables which are commercially available could be used in conjunction with the sensor made from SiCN.

The effect of temperature on the performance of the optical sensing scheme could be measured.

8.3.4 Testing at high temperature – Acoustic sensing scheme

Acoustic sensing even though is performed at low temperatures could be extended to higher temperatures of around 100 °C.

Acoustic sensing scheme should be tested to measure temperature and dynamic pressure inside a closed chamber in a sound proof environment. The acoustic signals will be partly absorbed by the wall and the reduction in amplitude of acoustic signal is proportional to the thickness of the wall.

References

1. **Cullinane, W. F., Strange, R. R.,** *"Gas turbine engine validation instrumentation: measurements, sensors and needs"*, Proceedings of SPIE Conference on Harsh Environment Sensors, Vol. 3852, Boston, Massachusetts, 1999, pp. 2 -13.

2. **Andronenko, S., Stiharu, I., Packirisamy, M.,** *"The use of microelectromechanical system for surge detection in gas turbine engines"*, International Conference on MEMS,NANO and Smart Systems, Banff, Alberta, 2005, pp. 355-358.

3. **Rolls-Royce .,** *"The jet engine"*, Rolls-Royce Publications, 1996, ISBN: 0902121235.

4. **Boyce, M.P.,** *"Gas turbine engineering handbook"*, Gulf Professional Publishing, 2002, ISBN: 0884157326.

5. **French, P. J., Muro, H., Shinohara, T., Nojiri, H., Kaneko, H.,** *"SOI pressure sensor"*, IEEE International Conference on Solid-State Sensors and Actuators, San Francisco, 1991, pp. 181-184.

6. **Mehregany, M., Zorman, C. A.,** *"Micromachining techniques for advanced SiC MEMS"*, Material Research Society, Vol. 640, 2001, pp. H 4.3.1 – H 4.3.6.

7. **Liew, A. L., Zhang, W., An, L., Shah, S., Luo, R., Liu, Y., Cross, T Dunn, M L., Bright, V., Daily, J. W., Raj, R., Anseth, K.,.** *"Ceramic MEMS new materials, innovative processing and future applications"*, American Ceramic Society Bulletin, Vol. 80, Westerville, 2001, pp. 25-30.

8. **Sreenivasan, K. R., Raghu, S.,** *"The control of combustion instability:A perspective"*, IAS Current Science, Vol. 79, 2000, pp. 867 – 883.

9. **Horn, W., Hiller, S. J., Pfoertner, H., Schadow, K., Rosenfeld, T., Garg, S.,** *"Actively controlled components"*, NATO Technical Report, RTO-TR-AVT-128, 2009, pp. 2-12 -2-40.

10. **Epstein, A. H.,** *"Smart engine component- A micro in every blade"*, 21st AIAA/SAE/ASME/ASEE Joint Propulsion Conference, California, 1985.

11. **Bock, S., Horn, S., Wilfert, G., Sieber, J.,** *"Active core technology within the NEWAC research program for cleaner and more efficient aero engines"*, European Air Space Conference, Munchen, 2007.

12. **Spakovszky, Z. S., Paduano, J. D., Larsonneur, R., Traxler, A., Bright, M. M.,** *"Tip clearance actuation with magnetic bearings for high speed compressor stall control"*, ASME Journal of Turbomachinery, Vol. 123, 2001, pp. 464 - 472.

13. **Simon, D. L., Garg, S., Semega, K. J.,** *"Sensor needs for control and health managment of intelligent aircraft engines"*, NASA Technical Manual, 213202, 2004.

14. **DeLaat, J. C., Breisacher, K. J., Saus, J. R., Paxson, D. E.**, *"Active combustion control for aircraft gas turbine engines"*, NASA Technical Manual, 210346, 2000.

15. **Culley, D. E., Bright, M. M., Prahst, P. S., Strazisar, A. J.,** *"Active flow seperation control of a stator vane using surface injection in a multistage compressor experiment"*, NASA Technical Manual, 212356, 2003.

16. **Hansman Jr, R. J., Kang, B. H.,** *"Preliminary definition of pressure sensing requirements for hypersonic vehicles",* AIAA/NASA/AFWAL Conference on Sensors and Measurement Techniques for Aeronautical Applications, Atlanta, Georgia,1988.

17. **Powrie, H. E. G., McNicholas, K.,** *"Gas path condition monitoring during accelerated mission testing of a demonstrator engine"*, 33rd AIAA/NASA/ASME/SAE/ASEE Joint Conference Propulsion Conference, Seattle, 1997.

18. **Litt, J. S., Simon, D. L., Garg, S., Guo, T. H., Mercer, C., Millar, R., Behbahani, A., Bajwa, A., Jensen, D. T.,** *"A survey of intelligent control and health management technologies for aircraft propulsion systems"*, Journal of Aerospace Computing Information and Communication, 2004, pp. 543-563.

19. **Stiharu, I., Rybarik, P.,** *"Sensor requirements and road maps"*, NATO Technical Manual, RTO-TR-AVT-128, 2009, pp. 6.1 – 6.46.

20. **Suder, K. L., Hathaway, M. D., Thorp, S. A., Strazisar, A. J., Bright, M.B.,** *"Compressor stability enhancment using discrete tip injection"*, ASME Journal of Turbo Machinery, Vol. 123, 2001, pp. 14-23.

21. **Weigl, H. J., Paduano, J. D., Frechette, L. G., Epstein, A. H., Greitzer, E. M., Bright, M. M., Strazisar, A. J.,** *"Active stabilization of rotating stall and surge in a transonic single stage axial compressor"*, International Gas Turbine & Aeroengine Congress & Exposition, Orlando, 1997, pp.625-636.

22. **Przybylko.,** *"MEMS for aircraft engines"*, DARPA ELTO Workshop on MEMS for Harsh Enviornments, 1998.

23. **Crook, A. J., Greitzer, E. M., Tan, C. S., Adamczyk, J. J.,** *"Numerical simulation of compressor endwall and casing treatment flow phenomena"*, ASME Journal of Turbomachinery, Vol. 115, 1993, pp. 501-512.

24. **Saha, L S., Kurkawa, J., Matsui, J., Imamura, H.**, *"Passive control of rotating stall in a parallel-wall vaned diffuser by J-grooves"*, ASME Journal of Fluids Engineering, Vol. 123, 2001, pp. 507 - 515.

25. **Paduano, J. D., Epstein, A. H., Valavani, L., Longley, J. P., Greitzer, E. M., Guenette, G. R.**, *"Active control of rotating stall in a low speed axial compressor"*, ASME Journal of Turbomachinery, Vol. 115, 1993, pp. 48 – 56.

26. **Kurtz, A. D, Ned, A. A., Epstein, A H.**, *"Ultrahigh temperature,minature,SOI sensors for extreme enviornments"*, International High Impact Technology Exchange Conference, Santa Fe, New Mexico, May, 2004, pp.1-11.

27. **Kurtz, A. D., Kane, A., Godman, S., Landmann, W., Geras, L., Ned, A.A.**, *"High accuracy piezoresistive internal combustion engine transducers"*, Kulite Semiconductor Products Inc, Automotive Testing Expo, Stuttgart, Germany, 2004.

28. **Jong, P. C. D., Meijer, G. C. M.**, *"A smart accurate pressure-transducer for high-temperature applications"*, IEEE Instrumentation and Measurement Technology Conference, Venizia, Italy, 1999, pp. 309-314.

29. **Raymond, L. S., Nelson, L. N., Hamilton, D. J., Kerwin, W. J.**, *"Fabrication of passive components for high-temperature instrumentation"*, IEEE Transactions on Components, Hybrid and Manufacturing Technology, Vol. 4, 1979, pp. 395 – 398.

30. **Garg, S., Kumar, A., Mathews, K. H., Rosenfeld, T., Rybarik, P., Viassolo, D. E.**, *"Intelligent control and health monitoring"*, NATO Technical Report, RTO-TR-AVT-128, 2009, pp. 3.1 – 3.16.

31. **Osiander, R., Darrin, M. A. G., Champion, J. L.**, *"MEMS and microstructures in aerospace applications"*, CRC Press, 2006, ISBN: 0824726375.

32. **Pinnock, R. A.**, *"Optical pressure and temperature sensors for aerospace applications"*, Sensor Review, Vol. 18, 1998, pp. 32-38.

33. **Rai, A. K., Nagarajan, V., Nguyen, C., Mehta, K., Smith, G., McMahon, R., Orsagh, R.**, *"Development of high temperature wiring for hotter section of turbine engines"*, 9th Joint FAA/DoD/NASA Aging Aircraft Conference, Atlanta, 2006.

34. **Suster, M., Young, D. J., Ko, W. H.**, *"Micro-power wireless transmitter for high-temperature MEMS sensing and communication application"*, 15th IEEE International Conference on MEMS, Las Vegas, USA, 2002.

35. **Sberveglieri, G.**, *"Recent developments in semiconducting thin-film gas sensors"*, Sensors and Actuators. Vol. 23, 1995, pp. 103-119.

36. **Golego, N., Studenikin, S. A., Cocivera, M.**, *"Sensor photoresponse of thin-film oxides of zinc and titanium to oxygen gas"*, Journal of the Electrochemical Society, Vol. 147, 2000, pp. 1592 -1594.

37. **Wrbanek, J. D., Fralick, G. C., Blaha, C. A., Rachel Busfield, A., Thomas., V. D.**, *"A multilayered thin film insulator for harsh environment"*, NASA Technical Manual, 211873, 2002.

38. **Martin, C. L., Wrbanek, J. D., Fralick, G C.**, *"Thin film sensors for surface measurements"*, International Congress on Instrumentation in Aerospace Simulation Facilities, NASA Technical Manual, 211149, 2001.

39. **Lourenco, M. J., Serra, J. M., Numes, R. M., Vallera, A. M., Nietode Castro, C. A.**, *"Thin-film characterization for high-temperature applications"*, Journal of Thermophysics, Vol. 19, 1998, pp. 1253 - 1265.

40. **Wrbanek, J. D., Laster, K. L. H.**, *"Preperation and analysis of platinum thin films for high temperature sensor application"*, NASA Technical Manual, 213433, 2005.

41. **Lei, J. F., Martin, L. C., Will, H. A.**, *"Advances in thin film sensor technologies for engine application"*, NASA Technical Manual, 107418, 1997.

42. **Lei, J. F., Will, H. A.**, *"Thin-film thermocouples and strain-gauge technologies for engine application"*, Sensors and Actuators, Vol. 65, 1998, pp. 187-193.

43. **Wrbanek, J. D., Fralick, G. C., Gonzales, J. M.**, *"Developing multilayer thin film strain sensors with high thermal stability"*, NASA Technical Manual, 214389, 2006.

44. **Martin, L. C., Fralick, G. C., Taylor, K. F.**, *"Advances in thin film thermocouple durabilty under high temperature and pressure testing conditions"*, NASA Technical Manual, 208812, 1999.

45. **Rajanna, K., Mohan, S., Nayak, M. M., Gunashekaran, N., Muthunayagam, A. E.**, *"Pressure transducer with Au-Ni thin-film strain gauges"*, IEEE Transactions on Electron Devices, Vol. 40, 1993, pp. 521 - 524.

46. **Chung, G. S.**, *"Micromachined chromium nitride thin-film pressure sensor for high temperature applications"*, Electronics Letters, Vol. 42, 2006, pp. 754-755.

47. **Wrbanek, J. D., Fralick, G. C., Farmer, S. C., Sayir, A., Blaha, C. A., Gonzalez, J. M.,** *"Development of thin film ceramic thermocouples for high temperature environment"*, NASA Technical Manual, 213211, 2004.

48. **Zhang, Y.,** *"Novel optical sensors for high temperature measurement in harsh enviornment"*, Ph.D Thesis, Virginia Polytechnic Institute and State University, Virginia, 2003.

49. **Xu, J., Pickrell, G., Wang, X., Peng, W., Cooper, K., Wang, A.,** *"A novel temperature-insensitive optical fiber pressure sensor for harsh enviornment"*, IEEE Photonics Technology Letter, Vol. 17, 2005, pp. 870-872.

50. **XU, J.,** *"High temperature high bandwidth fiber optic pressure sensors"*, Ph.D Thesis, Virginia Polytechnic Institute and State University, 2005.

51. **Zhu, Y., Wang, A.,** *"Miniature Fiber-Optic Pressure Sensor"*, IEEE Photonics Technology Letters, Vol. 17, 2005, pp. 447 – 449.

52. **Pulliam, W., Russler, P.,** *"High-temperature, high bandwidth, fiber-optic, MEMS pressure sensor technology for turbine engine component testing"*, Proceedings of SPIE Fibre Optic Sensor Technology and Applications, Vol. 4578, 2002, pp. 229 -238.

53. **Berthold, J.W., Ghering, W. L., Varshneya, D.,** *"Design and characterization of a high temperature fiber-optic pressure transducer"*, Journal of Lightwave Technology, Vol. 5, 1987, pp. 870-876.

54. **Wang, A., He, S., Fang, X., Jin, X., Lin, J.,** *"Optical fiber pressure sensor based on photoelasticity and its application"*, Journal of Lightwave Technology, Vol. 10, 1992, pp. 1466 – 1472.

55. **Bock, W. J., Chen, J., Milulic, P., Eftimov, T.,** *"A novel fiber-optic tapered long-period gratingsensor for pressure mountin"*, IEEE Transaction on Instrumentation and Measurement, Vol. 56, 2007, pp. 1176 – 1180.

56. **Lekki, J. D., Adamovsky, G., Floyd, B.,** *"Demodultion system for fiber optic bragg grafting dynamic pressure sensing"*, NASA Technical Manual, 210895, 2001.

57. **Zuckerwar, A. J., Cuomo, F. W.,** *"Fiber optic sensor for measurement of pressure fluctuations at high temperatures"*, IEEE International Congress on Instrumentation in Aerospace Simulation Facilities, Gottingen, 1989, pp. 503-509.

58. **Zhu, Y., Cooper, K. L., Pickrell, G. R., Wang, A.,** *"High-temperature fiber-tip pressure sensor"*, Journal of Lightwave Technology, Vol. 24, 2006, pp. 861 -869

59. **Pulliam, W., Russler, P., Mlcak, R., Murphy, K., Kozikowski, C.,** *"Micromachined SiC fiber optic pressure sensors for high temperature aerospace applications"*, Proceedings of SPIE Industrial Sensing Systems, Vol. 4202, 2000, pp. 21- 30.

60. **Peng, W., Qi, B., Pickrell, G. R., Wang, A.,** *"Investigation on cubic zirconia-based fiber optic pressure sensor for high temperature application"*, Proceedings of IEEE Industrial Sensing Systems, Vol. 1, 2003, pp. 713-717.

61. **Wendeker, M., Kaminski, T.,** *"Development of a fiber-optic sensor for the measurement of dynamic cylinder pressure in spark ignition engine"*, The 4th IEEE Conference on Sensors, Vol. 2, 2005, pp. 885 – 892.

62. **MacPherson, W. N., Gardner, M. J., Barton, J. S., Jones, J. D. C., Owen, C. L., Watson, A. J., Allen, R. M.,** *"Blast pressure measurement with a high-bandwidth fibre optic pressure sensor"*, Measurement Science and Technology. Vol. 17, 1999, pp. 95 -102.

63. **Wang, W. J., Guo, D. G., Lin, R. M., Wang , X. W.,** *"A single-chip diaphram-type minature fabry-perot pressure sensor with improved cross-sensitivity to temperature",* Measurement Science and Technology, Vol. 15, 2004, pp. 905-910.

64. **Nyfors, E., Vainikainen, P.,** *"Industrial microwave sensors "*, IEEE Microwave Symposium Digest,1991, pp. 1009 – 1012.

65. **Nyfors, E.,** *"Industrial microwave sensors- A review"*, Subsurface Sensing Technologies and Applications, Vol. 1, 2000, pp. 23 - 43.

66. **Eaton, W. P., Smith, J. H.,** *"Micromachined pressure sensors:review and recent developments"*, Smart Materials and Structures, Vol. 6, 1997, pp. 530 -539.

67. **Chang, S. P., Allen, M. G.,** *"Demonstration for integrating capacitive pressure sensor with read-out circuitry on stainless steel substance"*, Sensors and Actuators, Vol. 116, 2004, pp. 195-204.

68. **Marco, S., Samitier, J., Ruiz, O., Morante, J. R., Esteve, J.,** *"High-performance piezoresistive pressure sensors for biomedical applications using very thin structured membranes"*, Measurement Science and Technology, Vol. 7, 1996, pp. 1195-1203.

69. **Wang, X., Li, B., Russo, O. L., Roman, H. T., Chin, K. K., Farmer, K. R.,** *"Diaphram design guidelines and an optical pressure sensor based on MEMS technique"*, Microelectronics, Vol. 37, 2006, pp. 50-56.

70. **Chou, B. C. S., Shie, J. S., Chen, Y. W.,** *"A highly sensitive pirani vaccum gauge"*, The 8th International Conference on Solid-State Sensors and Actuators, Vol. 53, 2006, pp. 167 -170.

71. **Zhao, Y. L., Zhao, L. B., Jiang, Z. D.,** *"High temperature and frequency pressure sensor based on silicon-on-insulator layer"*, Measurement Science and Technology, Vol. 17, 2005, pp. 519-523.

72. **George, T., Son, K. A., Powers, R. A., Del Castillo, L. Y., Okojie, R.,** *"Harsh enviornment microtechnologies for NASA and terrestrial applications"*, IEEE Sensors, 2005, pp. 1253 -1258.

73. **Ned, A. A., Kurtz, A. D., Beheim, G., Masheeb, F., Stefanescu, S.,** *"Improved SiC leadlesspressure sensor for high temperature, low and high pressure applications"*, 21st Transducer Workshop, Kulite Semiconductors Products Inc, Lexington, 2004.

74. **Okojie, R. S., Ned, A. A., Kurtz, A. D.,** *"Operation of α (6H)-SiC pressure sensor at 500^0 C"*, IEEE Solid State Sensors and Actuators, Vol. 2, Chicago, 1997, pp. 1407-1409.

75. **Palmour, J. W., Milligan, J. W., Henning, J., Allen, S. T., Ward, A., Parikh, P., Smith, R. P., Saxler, A., Moore, M., Wu, Y.,** *"SiC and GaN based transistor and circuit advances"*, 12th GAAS Symposium, Amsterdam, 2004, pp. 555-558.

76. **Okojie, R. S., Fralick, G. C., Saad, G. J., Blaha, C. A., Adamczyk, J. J., Feiereisen, J. M.,** *"A single crystal SiC plug-and-play high temperature drag force transducer"*, 12th International Conference on Solid-State Sensors Actuators and Microsystems, Boston, 2003.

77. **Spertz, A. L., Tobias, P., Baranzahi, A., Martensson , P., Lundstrom, I.,** *"Current status of silicon carbide based high-temperature gas sensors"*, IEEE Transactions on Electron Devices, Vol. 46, 1999, pp. 561-566.

78. **Du, J., Young, D. J., Zorman, C. A., Ko, W. H.,** *"Single crystal SiC capacitive pressure sensor at 400^{0}C"*, IEEE International Electron Devices Meeting, Washington, DC, 2003, pp. 32.6.1 – 32.6.4.

79. **Young, D. J, Du, J., Zorman, C. A., Ko, W. H.,** *"High-temperature single-crystal 3C-SiC capacitive pressure sensor"*, IEEE Journal of Sensors, Vol. 4, 2004, pp. 464-470.

80. **Wu, C. H., Zorman, C. A., Mehregany , M.,** *"Fabrication and testing of bulk micromachined silicon carbide piezoresistive pressure sensors for high temperature application"*, IEEE Journal of Sensors, Vol. 6, 2006, pp. 316-324.

81. **Okojie, R. S., Ned, A. A., Kurtz, A. D.,** *" α(6H)-SiC pressure sensors for high temperature applications"*, IEEE International Conference on Solid State Sensors and Actuators, Vol. 2, 1997, pp. 1407-1409.

82. **Beheim, G., Ned, A. A., Masheeb, F., Kurtz, A. D., Wolff, J. M.,** *"Dynamic pressure measurements using silicon carbide transducers"*, 19th IEEE International Congress on Instrumentation in Aerospace Simulation Facilities, Cleveland , 2001, pp. 240-245.

83. **Okojie, R. S., Page, S. M., Wolff, M.,** *"Performance of MEMS-DCA SiC pressure transducer under various dynamic condition",* Proceedings of the International High Temperature Electronics Conference, Santa Fe, New Mexico, May 2006, pp. 70-74.

84. **Awad, Y., El Khakani, M. A., Aktik, C., Mouine, J., Camiré, N., Lessard, M., Scarlete, M.,** *"Thermally induced interfacial interactions between various metal substrates and a-SiC thin films deposited by a polymer-source chemical vapour deposition"*, Materials Chemistry and Physics, Vol. 104, 2007, pp. 350-355.

85. **Chidambaram, N. V.,** *"A numerical and experimental study of temperature cycle wire bond failure"*, Proceedings of 41st IEEE Electronic Components and Technology Conference, Atlanta , 1991, pp. 877-882.

86. **Okojie, R. S., Nguyen, P., Nguyen, V., Savrun, E., Lucko, D., Buehler, J., McCue, T., Knudsen, S.,** *"Parametric stability and failure mechanism of silicon carbide pressure sensors"*, Proceedings of the International High Temperature Electronics Conference, Santa Fe, New Mexico, May 2006, pp. 82-86.

87. **Michaelides, S., Sitaraman , S. K.,** *"Die cracking and reliable die design for flip-chip assemblies"*, IEEE Transactions on Advanced Packaging. Vol. 22, 1999, pp. 602-613.

88. **Savrun, E., Nguyen, V., Okojie, R., Blaha, C.,** *"Accelerated stress testing of SiC MEMS-DCA pressure transducer"*, IMAPS International High Temperature Electronics Conference, Santa Fe, New Mexico, May 2004.

89. **Mehregany, M., Zorman, C. A., Rajan, N., Wu, C. H.,** *"Silicon carbide MEMS for harsh environment"*, Proceedings of the Integrated Sensors, Microactuators and Microsystems Conference, Vol. 86, 1998, pp. 1594-1609.

90. **Kleebe, H. J., Stormer, H., Trassl, S., Ziegler, G.,** *"Thermal stability of SiCN ceramics studied by spectroscopy and electron microscope"*, Applied Organometallic Chemistry, Vol. 15, 2001, pp. 858-866.

91. **Xie, E, Ma, Z., Lin, H., Zhang, Z., He, D.,** *"Preparation and characterization of SiCN films"*, Optical Materials, Vol. 23, 2003, pp. 151-156.

92. **Chen, L. C., Chen, K. H., Wei, S. L., Kichambare, P. D., Wu, J. J., Lu, T. R., Kuo, C. T.,** *"Crystalline SiCN: a hard material to cubic BN"*, Thin Solid Films, Vol. 112, 1999, pp. 355-356.

93. **Martin, J., Filipiak, S., Stephens, T., Huang, F., Aminpur, M., Mueller, J., Demircan, E., Zhao, L., Werking, J., Goldberg, C., Park, S., Sparks, T., Esber, C.,** *"Integration of SiCN as a low κ etch stop and CU passivation in a high performance CU/low κ interconnect"*, IEEE Interconnect Technology Conference, 2002, pp. 42-44.

94. **Lee, J. Y. P.,** *"Fabrication of SiCN thin film on a substrate and measurement of sheet resistivity"*, University of Colarado, Boulder, MECN 5208 Course Material.

95. **Fainer, N. I., Kosinova, M. L., Rumyantsev, Y. M., Maksimovskii, E. A., Kuznetsov, F. A., Kesler, V. G., Kirienko, V. V., Shan, H. B., Cheng, L.,** *"Synthesis and physicochemical properties of nanocrystalline silicon carbonitrid films deposited by microwave plasma from organoelement compounds"*, Proceedings of the Topical Meeting of the Eurpoean Ceramic Society Nanoparticles, Structures and Nanocomposites, Vol. 31, St. Petersburg, 2005, pp. 427 – 432.

96. **An, L., Zhang. W., Bright, B. M., Dunn, M. L., Raj, R.,** *"Development of injectable polymer derived ceramics for high temperature MEMS",* IEEE Conference on MEMS, Miyazaki, Japan, 2000, pp. 619-623.

97. **Kion Corporation.,** *"TB1 Kion Ceraset polyureasilazane and Kion ceraset polysilazane 20 – heat curable resins"*, Technical Bulletin, 2004.

98. **Bright, V.M., Raj, R., Dunn, M. L., Daily, J. W.,** *"Injectable ceramic microcast silicon carbonitride (SiCN) micromechanical sysytems for extreme temperature environments with extension : micro packages for nano devices"*, Final Technical Report, AFRL –IF-RS-TR-2004-2, Air force research laboratory, Rome, New york, 2004.

99. **Liew, L. A., Zhang, W., Bright, V. M., An, L., Dunn, M. L., Raj, R.,** *"Fabrication of SiCN ceramic MEMS using injectable polymer-precursor technique",* Sensors and Actuators, Vol. 89, 2001, pp. 64-70.

100. **Liew, L.A., Zhang, W., An, L., Shah, S., Lou, R., Liu, Y., Cross, T., Dunn, M. L., Bright, V., Daily, J.W., Raj, R., Kristi, A.,** *"New materials, innovative processing and future applications"*, Journal of American Ceramic Society, Vol. 80, 2001, pp. 25-31.

101. **Bharadwaj, L., Fan, Y., Zhang, L., Jiang, D., An, L.,** *"Oxidation behavior of a fully dense polymer derived amorphous silicon carbonitride Ceramic"*, Journal of American Ceramic Society, Vol. 87, 2004, pp. 483-486.

102. **An, L., Bharadwaj, L., Zhang, L., Fan, Y., Jiang, D., Sohn, Y.H, Desai, V. H., Kapat, J., Chow, L. C.,** *"Silicoaluminum carbonitride with anomalously high resistance to oxidation and hot corrosion"*, Advanced Engineering Materials, Vol. 6, 2004, pp. 337-340.

103. **Wang, Y., Fan, Y., Zhang, L., Zhang, W., An, L.,** *"Polymer derived SiAlCN ceramics resist oxidation at 1400°C"*, Scripta Materialia, Vol. 55, 2006, pp. 295-298.

104. **Wang, Y., An, L., Fan, Y., Zhang, L., Burton, S., Gan, Z.,** *"Oxidation of polymer derived SiAlCN ceramics"*, Journal of American Ceramic Soceity, Vol. 88, 2005, pp. 3075-3080.

105. **Wang, Y., Zhang, L., Xu, W., Jiang, T., Fan, Y., Jiang, D., An, L.,** *"Effect of thermal initiator of the electrical behavior of polymer derived amorphous silicon carbonitrides"*, Journal of American Ceramic Society, Vol. 91, 2008, pp. 3971-3975.

106. **Ramakrishnan, P. A., Wang, Y. T., Balzar, D., An, L., Haluschka, C., Riedel, R., Hermann, A. M.,** *"Silicoboron – carbonitride ceramics: A class of high temperature dopable electronic materials"*, Applied Physics Letters, Vol. 78, 2001, pp. 3076-3078.

107. **Hermann, A.M., Wang, Y.T., Ramakrishnan, P.A., Balzar, D., An, L., Haluschka, C., Riedel, R.,** *"Structure and electronic properties of Si-(B)- C-N ceramics"*, Journal of American Ceramic Society Vol. 84, 2001, pp. 2260-2264.

108. **Andronenko, S., Stiharu, I., Mishra S.K.,** *"Synthesis and characterization of polyureasilazane derived SiCN ceramics"*, Journal of Applied Physics Vol. 99, 2006, pp. 113907.1 - 113907.5.

109. **Zhang, L., Wang, Y., Wei, Y., Xu, W., Fang, D., Zhai, L., Lin, K.C., An, L.,** *"A silicon carbonitride ceramic with anomalously high piezoresistivity"*, Journal of American Ceramic Society, Vol. 91, 2008, pp. 1346-1349.

110. **Wang, Y., Zhang, L., Fan, Y., Jiang, D., An, L.,** *"Stress dependent piezoresistivity of tuneling percolation systems"*, Journal of Material Science, Vol. 44, 2009, pp. 2814 – 2819.

111. **Wan, J., Gasch, M. J., Mukherjee, A. K.,** *"Silicon carbonitride cerammics produced by pyrolysis of polymer ceramic precursor"*, Materials Research Society, Vol. 15, 2000, pp. 1657-1660.

112. **Li, Y. L, Riedel, R, Steiger J, Seggern, H. V.,** *"Novel transparent polysilazane glass: Synthesis and properties"*, Advanced Engineering Materials, Vol. 2, 2000, pp. 290 – 293.

113. **Janakiraman, N., Aldinger, F.,** *"Fabrication and characterization of fully dense Si–C–N ceramics from a poly(ureamethylvinyl)silazane precursor"*, Journal of European Ceramic Society, Vol. 29, 2009, pp. 163-173.

114. **Ziegler, G., Ritcher, I., Suttor, D.,** *"Fiber-reinforced composites with polymer-derived matrix: processing, matrix formation and properties"*, Applied Science and Manufacturing, Vol. 30, 1999, pp. 411- 417.

115. **Weinmann, M., Zern, A., Aldinger, F.,** *"Stoichiometric silicon nitride / silicon carbide composites from polymeric precursors"*, Advanced Materials, Vol. 13, 2001, pp. 1704 -1708.

116. **Saha, A., Shah, S. R., Raj, R.,** *"Amorphous Silicon Carbonitride Fibers Drawn from Alkoxide Modified Ceraset™"*, Journal of the American Ceramic Society, Vol. 86, 2003, pp. 1443 - 1445.

117. **Liu, Y., Liew, L. A., Luo, R., An, L., Bright, V. M., Dunn, M. L., Daily, J. W., Raj, R.,** *"Fabrication of SiCN MEMS structures using microforged molds"*, IEEE Conference on MEMS, Interlaken, Switzerland, 2001, pp. 119-121.

118. **Mello, A. D.,** *"Plastic fantastic"*, The Royal Society of Chemistry, Vol. 2, 2002, pp. 31N – 36N.

119. **Brehman, M., Conrad, L., Funk, L.,** *"New developments in soft lithography"*, Journal of Dispersion Science and Technology, Vol. 24, 2003, pp. 291 – 304.

120. **Chow, W. W. Y., Lei, K. F., Shi G., Li W.J., Huang, Q.,** *"Microfluidic channel fabrication by PDMS-interface bonding"*, Smart Materials and Structures, Institute of Physics, Vol. 15, 2006, pp. S112 –S116.

121. **Lee, D. H., Park, K. H., Hong, L.Y., Kim, D. P.,** *"SiCN ceramic patterns fabricated by soft lithography techniques"*, Sensors and Actuators, Vol. 135, 2007, pp. 895 – 901.

122. **Liu, Y., Liew, L. A., Luo, R., An, L., Dunn, M. L., Bright, V. M., Daily, J. W., Raj, R.,** *"Application of microforging to SiCN MEMS fabrication"*, Sensors and Actuators, Vol. 95, 2002, pp. 143-151.

123. **Lewinsohn, C. A., Colombo, P., Reimanis, I., Unal, O.,** *"Stresses occurring during joining of ceramics using preceramic polymers"*, Journal of American Ceramic Society, Vol. 84, 2001, pp. 2240 – 2244.

124. **Kion Corporation.,** *"Kion defense technologies Ceraset polysilazane 20 – heat curable ceramic precursor"*, Technical Bulletin #2, 2004.

125. **Liew, L. A., Liu, Y., Luo, R., Cross T., An, L., Bright, V. M., Dunn, M. L., Daily, J. W., Raj, R.,** *"Fabrication of SiCN MEMS structures by photopolymerization of pre ceramic polymer"*, Sensors and Actuators, Vol. 95, 2002, pp. 120 -134.

126. **Wang, X. Y., Riffe, D. M., Lee, Y. S., Downer, M. C.,** *"Time-resolved electron-temperature measurement in a highly excited gold target using femtosecond thermionic emission"*, Physical Review, Vol. 50, 1994, pp. 8016 – 8019.

127. **Momma, C., Chichkov, B. N., Nolte S., Alvensleben, F. V., Tunnermann, A., Welling, H., Wellegehausen, B.,** *"Short-pulse laser ablation of solid targets"*, Optics Communications, Vol. 129, 1996, pp. 134 -142.

128. **Huang, H., Zheng, H. Y., Lim, G. C.,** *"Femtosecond laser machining characteristics of Nitino"*, Applied Surface Science, Vol. 228, 2004, pp. 201 – 206.

129. **Ace chemical corporation.,** *"Product data sheet- Di cumyl peroxide"*, Material Safety Data Sheet, Taiwan, 2006.

130. **Chemical land Inc.,** *"Product Identification data sheet- Di cumyl peroxide"*, Material Safety Data Sheet, Seoul, Korea, 2005.

131. **Haluschka, C., Kleebe H. J., Franke, R., Riedel , R.,** *"Silicon carbonitride ceramics derived from polysilazanes Part I. Investigation of compositional and structural properties"*, Journal of European Ceramic Society, Vol. 20, 2000, pp. 1355 – 1364.

132. **Haluschka, C., Engel, C., Riedel, R.,** *"Silicon carbonitride ceramics derived from polysilazanes Part II. Investigation of electrical properties"*, Journal of European Ceramic Society, Vol. 20, 2000, pp. 1365 – 1374.

133. **An, L., Riedel, R., Konetschny, C., Kleebe, H. J., Raj, R.,** *"Newtonian Viscosity of Amorphous Silicon Carbonitride at High Temperature"*, Journal of American Ceramic Society, Vol. 81, 1998, pp. 1349 – 1352.

134. **Bahloul, D., Pereira, M., Gerardin, C.,** *"Pyrolysis chemistry of polysilazane precursors to silicon carbonitride"*, Journal of Materials Chemistry, Vol. 7, 1997, pp. 109 – 116.

135. **Li, L. Y., Kroke, E., Riedel, R., Fasel, C., Gervais, C., Babonneau, F.,** *"Thermal cross linking and pyrolytic conversion of poly(ureamethylvinyl)*

silazanes to silicon based ceramics", Applied Organometallic Chemistry, Vol. 15, 2001, pp. 820 – 832.

136. **Sharpe, W. N.,** *"Strain gages for long-term high-temperature strain measurement"*, Experimental Mechanics, Vol. 15, 1975, pp. 482- 488.

137. **Yeakley, L. M., Lindholm, U. S.,** *"Development of capacitance strain transducers for high-temperature and biaxial applications",* Experimental Mechanics, Vol. 14, 1974, pp. 331- 336

138. **Weichsel, C., Pagni, O., Van Wyk, E., Leitch, A.W.R.,** *"Temperature-dependent capacitance studies of palladium/zinc oxide Schottky diodes",* Superlattices and Microstructures, Vol. 39, 2006, pp. 1-7.

139. **Huang, S. M., Stott, L. A., Green, R. G., Beck, S. M.,** *"Electronic transducers for industrial measurement of low value capacitances",* Journal of Physics: Scientific Instruments, Vol. 21, 1998,pp. 242-250.

140. **Marioli, M., Sardini, E., Taroni, A.,** *"Measurement of small capacitance variations"* IEEE Transactions on Instrumentation and Measurement, Vol. 40, 1991, pp. 426-428.

141. **Woike, M. R., Roeder, J. W., Hughes, C. E., Bencic, T.J.,** *"Testing of a microwave blade tip clearance sensor at the NASA Glenn research center"*, 47th Aerospace Sciences Meeting sponsored by the AIAA, Orlando, Florida, 2009, pp 1-20.

142. **Wagner, M., Schulze, A., Vossick, M., Stephelbauer, C., Weigel, R., Vortmeyer, N., Heide, P.,** *"Novel microwave vibration monitoring system for industrial powergenerating turbines"*, IEEE International Microwave Symposium Digest, Vol. 3, 1998, pp. 1211-1214.

143. **Geisheimer, J. L., Billington, S. A., Burgess, D. W.,** *"A microwave blade tip clearance sensor for active clearance control applications"*, 40th AIAA/ASME/SAE/ASEE Joint Propulsion Conference and Exhibit, Florida, 2004, pp. 3720-3740.

144. **Klein , C.,** *"Application of pressure sensitive paint (PSP) for the determination of instantaneous pressure field of models in a wild tunnel"*, Aerospace Science and Technology, Vol. 4, 2000, pp. 103-109.

145. **Vollan, A., Alati, L.,** *"A new optical pressure measurement system"*, IEEE International Congress on Instrumentation in Aerospace Simulation Facilities, 1991, pp. 10-16.

146. **Hradil, J., Davis, C., Mongey, K., McDonagh, C., MacCraith, B. D.,** *"Temperature corrected pressure sensitive paint measurements using a single camera and a dual lifetime approach"*, Measurement Science and Technology, Vol. 13, 2002, pp. 1552 -1557.

147. **Goss, L., Jones, G., Crafron, J., Fonov, S., Fonov, V.,** *"Temperature compensation for lifetime-based pressure sensitive paint system"*, 21st International Congress on Instrumentation in Aerospace Simulation Facilities, Sendei, Japan, 2005, pp. 283- 292.

148. **Woodmansee, M. A., Dutton, J. C.,** *"Treating temperature-sensitivity effects of pressure-sensitive paint measurements"*, Experiments in Fluids, Vol. 24, 1998, pp. 163-174.

149. **Liu, T., Sullivan, J. P.,** *"Pressure and temperature sensitive paints"*, Springer – Verlag Berlin Heidelberg, 2005, ISBN 3540222413.

150. **Udd, E., Schulz, W., Seim, J., Haugse, E., Trego, A., Johnson, P., Bennett, T. E., Nelson, D., Makino, A.,** *"Multidimensional strain field measurements using fiber optic grating sensors"*, Proceedings of Sensors Expo, Milford, CT, 2000.

151. **Kim, J., Ren, F., Pearton, S. J.,** *"Strain measurement in 6H-Sic under external stress"*, Journal of Ceramic Processing Research, Vol. 7, 2006, pp. 239-240.

152. **Tahir, B. A., Ali, J., Rahman, R .A.,** *"Strain measurements using fiber bragg grating sensor"*, American Journal of Applied Science (spl issue), Vol. 2, 2005, pp. 40-48.

153. **Melle, S. M., Liu, K., Measures, R. M.,** *"A passive wavelength demodulation system for guided-wave Bragggrating sensors"*, IEEE Photonics Technology Letters, Vol. 4, 1992, pp. 516-518.

154. **Vachon, J., Malhotra, S.,** *"Optics in aircraft engines"*, IEEE Proceedings of the National Aerospace and Electronics Conference,Vol. 2, Dayton, OH, 1991, pp. 585-590.

155. **Maiko, P., Seregin, E. P., Lerner, M. O., Aleksandrova, L. A., Petrov, V. I., Bugai, V. T.,** *"Improvement of fuel combustion process in gas turbine engines by theuse of additives"*, Chemical, Oil and Fuel Technologies (english translation), Vol. 13, 1977, pp. 253 – 256.

156. **Lubbock, I.,** *"Combustion problems of gas turbine"* , Transaction of Institution of Engineers and Ship Builders, Vol. 67, 1951, pp. 131 -154.

157. **Docquier, N., Candel, S.,** *"Combustion control and sensors: A review",* Progress in Energy and Combustion Science, Vol. 28, 2002, pp. 107 -150.

158. **Kang, H. W., Lee, I. H., Cho, D. W.,** *"Development of a micro bellows actuator using micro stereolithography technology"*, Microelectronic Engineering, Vol. 83, 2006, pp. 1201 – 1204.

159. **Mutzenich, S, Vinay, T., Rosengarten, G.,** *"Analysis of a novel micro-hydraulic actuation for MEMS"*, Sensors and Actuators ,Vol. 116, 2004, pp. 525-529.

160. **Yang, X., Tai, Y. C., Ho, C. M.,** *"Micro bellow actuator",* IEEE International Conference on Solid State Sensors and Actuators , Vol. 1, Chicago, 1997, pp. 45-48.

161. **Sharma, D. K., Henschel, R., Krawchuk, M.,** *"Strain and fatigue testing of large expansion bellows"*, Experimental Mechanics, Vol. 18, 1978, pp. 49-55.

162. **Allen, J. J.,** *"Micro electro mechanical system design"*, CRC Press, 2005, ISBN 0824758242.

163. **Giovanni, M. D.,** *"Flat and corrugated diaphragm design handbook"*, Marcel Dekker Inc, 1982, ISBN 0824712811.

164. **Fraden, J.,** *"Handbook of modern sensors"*, AIP Press (Springer- Verlag, Inc), 2004, ISBN 0387007504.

165. **Bhat, K. N.,** *"Silicon micromachined pressure sensor",* Journal of Indian Institute of Science, Vol. 87, 2007, pp. 115-131.

166. **Xu, Y., Chiu, C. W., Jiang, F., Lin, Q., Tai, Y.,** *"Mass flow meter using a multi-sensor chip",* IEEE 13th Annual International Conference on Micro Electro Mechanical Systems, Miyazaki, Japan, 2000, pp. 541-546.

167. **Tilmans, H. A. C., Bouwstra, S.,** *"Novel design of a highly sensitive differential-pressure sensor using built-in resonant strain gauges"*, Journal of Micromechanics and Microengineering, Vol. 3, 2003, pp. 198-202.

168. **Su, Y. H., Chen, K. S., Roberts, D.C., Spearing S.M.,** *"Large deflection analysis of a pre-stressed annular plate with a rigid boss under axisymmetric loading"*, Journal of Micromechanics and Microengineering, Vol. 11, 2001, pp. 645-653.

169. **Atkinson, C., Huang , S.,** *"Analysis of a flat annular-shaped diaphragm for use in down-hole pressure transducer"*, Measurement Science and Technology, Vol. 18, 2007, pp. 1167-1174.

170. **Close, C. M., Frederick, D. K., Newell, J. C.,** *"Modelling and analysis of dynamic systems"*, John Wiley and Sons, 2001, ISBN 9780471394426.

171. **Kulakowski, B. T., Shearer J. L.,** *"Dynamic modelling and control of engineering systems"*, Cambridge University Press, 2007, ISBN 0521864356.

172. **Ogata, K.,** *"System dynamics"*, Prentice Hall, 1998, ISBN 0136757456.

173. **Kim, H. J., Lee, S. Q., Lee, J. W., Lee, S. K., Park, K. H.,** *"A miniature silicon condenser microphone improved with a flexure hinge diaphragm and a large back volume"*, Proceedings of Materials Research Society, Vol. 1052, 2008, pp. 197 – 204.

174. **Wang, Y. H., Lee, C. Y., Chiang, C. M.,** *"A mems based air flow sensor with a free standing micro cantilever structure"*, Sensors, Vol. 7, 2007, pp. 2389 – 2401.

175. **Su, Y., Evans, A. G. R., Brunnschweiler, A.,** *"Micromachined silicon cantilever paddles with piezoresistive readout for flow sensing"*, Journal of Micromechanics and Microengineering, Vol. 6, 1996, pp. 69 -72.

176. **Padmanabhan, A., Goldberg, H. D., Breuer, K. S., Schmidt, M. A.,** *"A silicon micromachined floating element shear stress sensor with optical position sensing by photodiodes"*, Digest of Technical Papers, Transducers '95, Stockholm, 1995, pp. 439 – 439.

177. **Wang, L., Beebe, D. J.,** *"A silicon based shear force sensor: development and characterization"*, Sensors and Actuators, Vol. 84, 2000, pp. 33 – 44.

178. **Chakraverty, S.,** *"Vibration of plates"*, CRC press, 2009, ISBN: 9781420053951.

179. **Palmer, M. E., Davis, M. A., Engelbrecht, G. P., Fielder, R. S., Ng, W. F., Ringshia, Song, B.,** *"High temperature, uncooled interstage turbine pressure measurement in small gas turbine engine"*, 41st AIAA/ASME/SAE/ASEE Joint Propulsion Conference and Exhibit, Tuscan, 2005.

180. **Yang, Z., Matsumoto, S., Tsaur, J., Maeda, R.,** *"Drag force flow sensor using micro laser interferometer"*, Proceedings of the 21st Sensor Symposium, Vol. 21, Tsukuba, Japan, 2004, pp. 291-294.

181. **Richter, M., Wackerle, M., Woias, P., Hillerich, B.,** *"A novel flow sensor with high time resolution based on differential pressure principle"*, Proceedings of 12th IEEE International Workshop on MEMS, Orlondo, Florida, 2000, pp. 118 – 123.

182. **Fan, Z., Chen, J., Zou, J., Bullen, D., Liu, C., Delcomyn, F.,** *"Design and fabrication of artificial lateral line flow sensors"*, Journal of Micromechanics and Microengineering, Vol. 12, 2002, pp. 655-661.

183. **Krijnen, G. J. M., Dijkstra, M., Van Baar, J. J., Shankar, S. S., Kuipers, W.J., De- Boer, R. J. H., Altpeter, D., Lammerink, T.S.J., Wiegerink, R.,** *"MEMS based hair flow-sensors as model systems for acoustic perception studies"*, Nanotechnology, Vol. 17, 2006, pp. 884-889.

184. **Lien, V., Vollmer, F.,** *"Microfluidic flow rate deflection based on integrated optical fiber cantilever"*, The Royal Society of Chemistry, Vol. 7, 2007, pp. 1352–1356.

185. **Ozaki, Y., Ohyama, T., Yashuda, T., Shimoyama, I.,** *"An air flow sensor modeled on wind receptor hairs of insects"*, The 13th Annual International Conference on Micro Electro Mechanical Systems, 2000, pp. 531-536.

186. **Chen, N., Tucker, C., Engel, J. M., Yang, Y., Pandya, S., Liu, C.,** *"Design and characterization of artificial haircell sensor flow with ultrahigh velocity and angular sensitivity"*, Journal of Micro Electro Mechanical Systems, Vol. 16, 2007, pp. 999-1014.

187. **Große, S., Schröder, W., Brücker, C.,** *"Nano-newton drag sensor based on flexible micro-pillars"*, Measurement Science and Technology, Vol. 17, 2006, pp. 2689-2697.

188. **Pang, J., Segawa, T., Ikehara, T., Yoshida, H., Kikushima, Y., Abe, H., Meada, R.,** *"Fabrication and tests of a MEMS-based double-beam cantilever flow sensor with clarifying of temperature effect"*, Smart Structures Devices, and Systems,Vol. 5649, 2005, pp. 253-264.

189. **Nishimoto, T., Shoji, S., Esashi, M.,** *"Buried piezoresistive sensors by means of MeV ion implantation"*, Sensors and Actuators, Vol. 43, 2004, pp. 249-253.

190. **Beeby, S., Ensell, G., Kraft, M., White, N.,** *"MEMS mechanical sensors"*, Artec House Inc, 2004, ISBN 1580535364.

191. **Madou, M. J.,** *"Fundamentals of micro fabrication – The science of miniaturization"*, CRC Press, 2002, ISBN 0849308267.

192. **Binnig, G., Quate, C. F.,** *"Atomic Force microscope"*, Physical Review Letters, Vol. 56, 1986, pp. 930–933.

193. **Tellier, C. R., Leblois, T. G.,** *"On the design of GaAs (hhl) resonant cantilevers study of piezoelectric excitation, of piezoresistive sensing and of micromachined structure"*, Sensors and Actuators, Vol. 132, 2006, pp. 224-235.

194. **Abedinov, N., Popov, C., Yordanov, Z., Rangelow, I. W., Kulish, W.,** *"Investigations of the sorption behaviour of amorphous nitrogen-rich carbon nitride films as sensitive layers for cantilever sensors"*, Applied Physics: Material Science and Processing, Vol. 79, 2004, pp. 531 -536

195. **Lee, C. Y., Lee, G. B.,** *"Micromachine based humidity sensors with integrated temperture sensors for signal drift compensation"*, Journal of Micromechanics and Microengineering, Vol. 13, 2003, pp. 620-627.

196. **Knowles, T. P. J., Shu, W., Huber, F., Lang, H. P., Gerber, C., Dobson, C. M., Welland, M. E.,** *"Label free detection of amyloid growth with microcantilever sensors"*, Nanotechnology, Vol. 19, 2008, pp. 384007 - 384012.

197. **Lee, C. Y., Wen, C .Y., Hou, H. H., Yang, R. J., Tsai, C. H., Fu, L. M.,** *"Design and characterization of MEMS-based flow-rate and flow-direction microsensor"*, Microfluidics and Nanofluidics, Vol. 6, 2009, pp. 363-371.

198. **Su, Y., Evans, A. G. R., Brunnschweiler, A., Ensell, G.,** *"Characterization of a highly sensitive ultra-thin piezoresistive silicon cantilever probe and its application in gas flow velocity sensing"*, Micromechanics and Microengineering, Vol. 12, 2002, pp. 780-785.

199. **Warren, J., Gordan, S., Hoff, S., Alby, F.,** *"Air,land, sea, and space fod issues"*, NATO Technical Report, RTO-TR-AVT-094, 2005, pp. B1 - B12,.

200. **Hamed, A., Tabakoff, W., and Wenglarz, R.,** *"Erosion and Deposition in Turbomachinery"*, Journal of Propulsion and Power, Vol. 22, 2006, pp. 350 -360.

201. **Leo, A., Stiharu, I., Bhat, R. B., Moustapha, H.,** *"Micro pressure sensor for high temperature applications"*, International Soceity of Air Breathing Engine", Vol. 1335, 2007, pp. 1335 – 1342.

202. **Yue, Z.,** *"Air jet velocity decay in ventillation applications"*, Bulletin of Royal Institute of Technology (KTH), 1999, Bulletin no 48, 0284-141X.

203. **Miller, D. R., Comings, E .W.,** *"Static pressure distribution in the free turbulent jet"*, Journal of Fluid Mechanics, Vol. 3, 1957, pp. 1-16.

204. **Warren, W. R.,** *"The static pressure variation in compressible free jets"*, Report of Princeton University, James Forrestal Research Center, 1954, Report No: 270, AD0057735.

205. **Donaldson, C. P., Snedeker, R. S.,** *"A study of free jet impingement Part 1. mean properties of free and impinging jets"*, Journal of Fluid Mechanics, Vol. 45, 1971, pp. 281-319.

206. **Jones, C. N.,** *"Steady incompressible jet flow – An engineer's guide"*, Proceedings of Thermofluids Conference, Hobart, Tasmania, 1976, pp. 41 – 45.

207. **Birch, A. D., Hughes, D. J., Swaffield, F.,** *"Velocity decay of high pressure jets"*, Journal of Combustion Science and Technology, Vol. 52, 1987, pp. 161 - 167.

208. **Catanase, A., Barglazan, M., Hora, C.,** *"Numerical simulation of a free jet in pelton turbine"*, Proceedings of 6th International Conference on Hydraulic Machinery Hydro Dynamics, Timisora, Romania, 2004.

209. **Shamami, K. K., Birouk, M.,** *"Three dimensional numerical simulation of an equilateral triangular turbulent free jet"*, International Journal of Numerical Methods for Heat Fluid Flow, Vol. 19, 2009, pp. 894 -912.

210. **Zhang, Y., Ren, Q., Zhao, Y. P.,** *"Modelling analysis of surface stress on a rectangular cantilever beam"*, Journal of Physics, Vol. 37, 2004, pp. 2140-2145.

211. **Sander, D., Tian, Z., Kirschner, J.,** *"Cantilever measurements of surface stress, surface reconstruction, film stress and magnetoelastic stress of monolayers"*, Sensors Journal, Vol. 8, 2008, pp. 4466-4486.

212. **Godin, M., Cossa, V. T., Grutter, P.,** *"Quantitative surface stress measurements using a micro cantilever"*, Applied Physics Letters, Vol. 79, 2001, pp. 551 – 553.

213. **Hardy, J. E.,** *"Performance of a drag transducer under simulated PWR refill/refloodflow conditions"*, IEEE Transactions on Instrumentation and Measurement, Vol. 41, 1992, pp. 611 - 615.

214. **Maeder, T., Fahrny, V., Stauss, S., Corradini, G., Ryser, P.,** *"Design and characterisation of low-cost thick-film piezoresistive force sensors for the 100 mN to 100 N range"*, XXIX International Conference of International Micro Electronics and Packing Society, Kozalin. Poland, 2005, pp. 429-434.

215. **Abe, K., Uchiyamma, M.,** *"Overload protection mechanisms for force detecting beam in a force sensor"*, Mechatronics and Automation, Harbin, China, 2007, pp. 2662-2667.

216. **Hein, S., Holzner, K., Schlichting, V., Obermeier, E., Barton, K.,** *"Capacitive differential pressure sensor with high overloadcapability using silicon/glass technology"*, IEEE Conference on Solid State Sensors and Actuators,Vol. 2, Chicago, USA, 1997.

217. **Barth, P.W., Pourahmadi, F., Mayer, R., Poydock, J., Petersen, K.,** *"A monolithic silicon accelerometer with integral air damping and overrange*

protection", IEEE Solid State Sensors and Actuator workshop, Vol. 6, California, USA, 1988, pp. 35-38.

218. **Yoshida, K. I., Tanigawa, H.,** *"Development of a force sensor for minute load measurement"*, Transactions on 6th International Symposium on Electronic Manufacturing Technology, Japan, 1989, pp. 201 – 204.

219. **Timoshenko, S.,** *"Strength of materials - Advanced theory and problems"*, Van Nostrand Company, 1940, ISBN B000ERXVSC.

220. **Johnson K. L.,** *"Mechanical variables measurement"*, Cambridge University Press, 1985, ISBN 0521347963.

221. **Sezer, S., Sinclair, G.B.,** *"An assessment of ANSYS contact elements"*, Proceedings of the 12th ANSYS Conference, Southpointe, PA, 2006.

222. **ANSYS Inc.** *"Technical report for meshing solutions - Release 12"*, 2009.

223. **Dheeravongkit, A., Shimada, K.,** *"Inverse adaptation of a hex dominant mesh for large deformation finite element analysis"*, Computer Aided Design, Vol. 39, 2007, pp. 427 -438.

224. **Pankanin, G. L.,** *"The vortex flowmeter: various methods of investigating phenomena"*, Measurement Science and Technology, Vol. 16, 2005, pp. R1-R16.

225. **Gerrard, J.H.,** *"The mechanics of the formation region of vortices behind bluff bodies",* Journal of Fluid Mechanics, Vol. 25, 1966, pp. 401-413.

226. **Bentley, J.P., Mudd, J.W.,** *"Vortex shedding mechanism in single and dual bluff bodies",* Flow Measurement and Instrumentation, Vol. 14, 2003, pp. 23 -31.

227. **Huang, Y., Zhang, H., Sun, Z.,** *"Measurement of mass flow rate using a vortex flowmeter",* Proceedings of IEEE Sensors,Vol. 1, Toronto, Canada, 2003, pp. 344-347.

228. **Iguchi, M., Kosaka, H., Hayashi, A., Terauchi, Y., Mizukami, H., Hanao, M., Kawamoto, M., Kawabata, H.,** *"Development and calibration of a karman vortex probe for measurement of molten-steel velocities"*, Metallurgical and Materials Transactions, Vol. 30B, 1999, pp. 53-59.

229. **Pankanin, P. L.,** *"Influence of vortex meter configuration of measure signalparameters"*, IEEE Conference on Instrumentation and Measurement Technology, 2003, pp. 337-340.

230. **Bentley, J. P., Nichols, A. R.,** *"Advantages of and developments in dual bluff-body vortex flowmeters"*, Transactions of the Institute of Measurement and Control, Vol. 12, pp. 209-218.

231. **Najafi, K.,** *"Smart sensors"*, Journal of Micromechanics and Microengineering, Vol. 1, 1991, pp. 86-102.

232. **Ishihara, T., Suzuki, K., Suwazono, S., Hirata, M., Tanigawa, H.,** *"CMOS integrated silicon pressure sensor"*, IEEE Journal of Solid State Circuits, Vol. 22, 1987, pp. 151 -156.

233. **Patra, J. C., Gopalkrishnan, V., Ang, E. L., Das, A.,** *"Neural network based self calibration / compensation of sensors operating in harsh environment"*, Proceedings of IEEE Sensors, Vienna, Austria, 2004, pp. 425–428.

234. **Frank, R.,** *"Understanding smart sensor"*, Artech House, 2000, ISBN 1580533981.

235. **Mccluskey, P. F., Grzybowski, R., Podlesak, T. P.,** *"High temperature electronics"*, CRC Press, 1997, ISBN 0849396239.

236. **Savren, E.,** *"Packaging considerations for very high temperature microsystems"*, Proceedings of IEEE sensors, Vol. 2, Orlando, FL, USA, 2002, pp. 1139-1143.

237. **Swenson, G, M.,** *"High temperature electronics and transducers"*, HITEN Magazine Article, 1995.

238. **Schroder, N.,** *"Sensor markets 2008"*, Press Report Intechno Consulting Group, 1999.

239. **Kurtz, A. D., Kane, A., Goodman, S., Geras, L.,** *"Miniature combination pressure / temperature sensors with redundant capability"*, Technical Report of Kulite Semi Conductor Products Inc, 2004, pp. 1- 8.

240. **Stevens, R., Ewart, P.,** *"Single shot measurement of temperature and pressure using laser induced thermal gratings with a long probe pulse"*, Applied Physics – Laser and Optics, Vol. 78, 2004, pp. 111-117.

241. **Groepper, C. W., Cui, T., Li, P. Y., Stelson, K. A.,** *"Fabrication of integrated pressure flow temperature sensor for hydraulic systems"*, ASME International Mechanical Engineering Congress and Exposistion, Chicago, USA, 2006.

242. **Pramanik, C., Saha, H., Gangopadhyay, U.,** *"An integrated pressure and temperature sensor based on nanocrystalline porous silicon"*, Journal of Micromechanics and Microengineering, Vol. 16, 2006, pp. 1340-1348.

243. **Bock, W. J., Nawrocka, M. S., Urbanczyk, W.,** *"Highly sensitive fiber optic sensor for dynamic pressure measurements"*, IEEE Transactions on Instrumentation and Measurement, Vol. 50, 2001, pp. 1085-1088.

244. **Bock, W. J., Urbanczyk, W., Buczynski, R., Domanski, A.W.,** *"Cross sensitivity effect in temperature compensated sensors based on birefringent fibers"*, Journal of Applied Optics, Vol. 33, 1994, pp. 6078-6083.

245. **Boley, B. A., Weimer, J. H.,** *"Theory of thermal stresses"*, John Wiley and Sons Inc, 1960, ISBN 0486695794.

246. **Malley, D., Brown, B., Kennedy, E., Meredith, R., Stanic, S.,** *"A high speed multi channel data acquisisiton system"*, Proceedings of High Frequency Ocean Acoustics Conference, Vol. 728, La Jolla, California, 2004, pp. 438-446.

247. **Vasilev, L. S., Zaripov, R. G., Magsumova, T., Salyanov, R.,** *"Experimental investigation of the outer wave field at the open end of the pipe"*, Translated from Innzhenerno- Fizicheskie Zhurnal, Vol. 61, 1991, pp. 714-716.

248. **Sen, S. N.,** *"Acoustics waves and oscillations"*, John Wiley and Sons, 1990, ISBN 8122402666.

249. **Smith, M. J. T.,** *"A look into the aero engine noise problem"*, Journal of Physics Eduction, Vol. 6, 1971, pp. 193-271.

250. **Kinsler, L. E., Frey, A. R., Coppens, A. B., Sandres, J. V.,** *"Fundamental of acoustics"*, John Wiley and Sons, 2000, ISBN 0471847895.

251. **Fottner, L.,** *"Test cases for combustion of internal flows in aero engine components"*, AGARD Advisory Report No 275, 1990, ISBN 9283505735.

252. **Kool, G. A.,** *"Current and future materials in advanced gas turbine engine"*, Journal of Thermal Spray Technology, Vol. 5, 1996, pp. 31-34.

253. **Schilke, P. W.,** *"Advanced gas turbine materials and coatings"*, GE Energy Technical Report, GER-3569G, 2004.

254. **Sporer, D., Refke, A., Dratwinski, M., Dortman, M., Metco, S., Giovannetti, I., Giannozzi, M., Bigi, M.,** *"New high temperature seal system for increased efficiency of gas turbine engines"*, Technical Report on Sealing Technology, GE Oil and Gas, 2008, pp. 9-11.

255. **Carlos, A., Estrada, M.,** *"New technology used in gas turbine engine"*, Scientia et Technica Ano XIII, Vol. 36, 2007, ISSN 01221701.

256. **Berthhold, J. W., Ghering, W. L., Varshneya, D.,** *"Design and characterization of a high temperature fiber optic pressure transducer"*, Journal of Light Wave Technology, Vol. LT-5, 1987, pp. 870-876.

257. **Rooth, R. A., Hiemstra, W.,** *"A fibre optic tip shroud deflection measurement system"*, Journal of Engineering for Gas Turbines and Power, Vol. 23, 2001, pp. 359-362.

258. **Hoffmann, L., Muller, M. S., Kramer, S., Giebel, M., Schwotzer, G., Wieduwilt, T.,** *"Applications of fibre optic temperature measurement"*, Estonian Academy for Science and Engineering, Vol. 13, 2007, pp. 363-378.

259. **Udd, E., Schulz, W. L., Seim, J., Morrell, M., Weaver, T., Bush, J., Adamovsky, G.,** *"Fibre optic distributed sensing systems for harsh aerospace environment"*, SPIE Proceeding in Industrial and Commercial Applications of Smart Structure Technologies, Vol. 3674, New port beach, Ca, USA, 1999, pp. 136-147.

260. **Culshaw, B.,** *"Fibre optics in sensing and measurement"*, IEEE Journal of Selected Topics in Quantum Electronics, Vol. 6, 2000, pp. 1014-1021.

261. **Latini, V., Striano, V., Coppola, G., Rendina, I.,** *"Fibre optic sensors system for high temperature monitoring of aerospace structures"*, Proceedings of SPIE – Photonic Materials, Devices and Applications, Vol. 6593, Maspalomas, Gran Canaria, Spain, 2007, pp. 65930s.1 – 65930s.9.

262. **Hsu, T.R., Moyer, R. G.,** *"Application of holography in high temperature displacement measurements"*, Experimental Mechanics, Vol. 12, 1972, pp. 431-432.

263. **Bates, S. C., Chang, R. S. F.,** *"High temperature fibre optic imaging"*, Fibre and Integrated Optics, Vol. 16, 1997, pp. 387-405.

264. **Archer, D.G.,** *"Thermodynamic properties of synthetic sapphire (á-Al_2O_3) standard reference material 720 and the effect of temperature –scale differences on thermodynamic properties"*, Journal of Physical and Chemical Reference Data, Vol. 22, 1993, pp. 1441-1453.

265. **Zhan, C., Kim, J. H., Yin, S., Ruffin, P., Luo, C.,** *"High temperature sensing using higher order mode rejected sapphire fibre gratings"*, Optical Memory and Neural Networks (Information Optics), Vol. 16, 2007, pp. 204-210.

266. **Grobnic, D., Mihailov, S. J., Smelser, C. W., Ding, H.,** *"Sapphire fiber bragg grating sensor made using femto second laser radiation for ultrahigh temperature applications"*, IEEE Photonics Technology Letters, Vol. 16, 2004, pp. 2505-2507.

267. **Thomas, M. E., Andersson, S. K., Sova, R. M., Joseph R. I.,** *"Frequency and temperature dependence of the refractive index of sapphire"*, Infrared Physics and Technology, Vol. 39, 1998, pp. 235-249.

268. **Murphy, K., Vengsarkar, A., Feth, S., Claus, R., Gollapudi, S., Wang, A.,** *"Sapphire optical fibre interferometer"*, US Patent, Patent Number 5,381,229, 1995.

269. **Marcuse, D.,** *"Curvature loss formula for optical fibres"*, Journal of Optical Society of America, Vol. 66, 1976, pp. 216-220.

270. **Aremco products Inc.,** *"High temperature ceramic adhesives and pastes",* Technical Bulletin A2, 2010, pp. 1-5.

271. **Lattime, S. B., Steinetz, B. M.,** *"Turbine engine clearance control systems: current practices and future directions"*, NASA Technical Report, 211794, 2002, pp. 1-16.

272. **Lord, W. K., Mac Martin, D.G., Tillmann G.,** *"Flow control opportunities in gas turbine engines",* AIAA Conference on Fluids, Denver, Co, USA, 2000, pp. 1-15.